UNIVERSITÀ DEGLI STUDI DI MILANO
Dipartimento di Chimica
Dottorato di Ricerca in Scienze Chimiche, XXVI Ciclo

Point defects and adatoms at surfaces: challenges and opportunities

Tesi di Dottorato di Ricerca di
Marina Casartelli

Tutor: Dott. Rocco Martinazzo
Cotutor: Prof. Gian Franco Tantardini

A.A. 2012-2013

Acknowledgements

First of all I gratefully acknowledge my supervisor, Dr. Rocco Martinazzo, that taught me a lot. In these three years, his guide and enthusiasm allowed me to progress and get fond of my work.

I would also like to thank my co-supervisor Prof. Gian Franco Tantardini, for the confidence and the support he gave me from the very beginning of my PhD.

A great acknowledgement is for Dr. Simone Casolo, who always supported me and felt with me in the hard times of the PhD. I wish him all the best in his new Norwegian life.

I can not forget Dr. Matteo Bonfanti, for the help and the friendship he gave me. I would also like to thank all the other members of the group, Paolo, Simona, Elisabetta, Marta, Davide e Simone. I wish all of them a successful future.

Of course a great acknowledge is for Dr. Stefano Rendine. I'll always keep nice memories of our coffee-times and long lasting breaks, always filled by his funny jokes. I acknowledge also Dr. Shilpi Chaurasia. I sincerely hope that we will meet again in the future.

I am very grateful to Dr. Didier Lemoine, who welcome me in his group during my stay in Toulouse. He taught me a lot not only on molecular dynamics but also about *haute cuisine* and French wines.

I would also like to thank all the people in the LCAR group, in particular Dr. Arunangshu Debnath and Dr. Wesley Unn-Toc for the good times spent together. They made me feel less homesick during my stay in France.

In conclusion, the main acknowledgement is for my family, always close to me in all these years. I can not omit my cat Zorro, for the company and the affection in this last period, writing my thesis.

Abstract

In many occasions defects have been proved to be an opportunity more than a limit, as they may be used to tailor the properties of a given material. To this end, a practical route to introduce a controlled amount of defects as well as a deep knowledge of the defect nature is always desirable. As well, recombinative and dissociative processes involving gas molecules are well known to likely occur on metal surfaces, that may then be used in a number of industrial applications. In this thesis I report on both the isolated carbon atom vacancy, that is a common lattice defect in graphene, and the Eley-Rideal formation of H_2 molecules in the limit of an single adsorbed atom on the Ag(111) surface. In the first part of this thesis I consider the details of the electronic structure in the neighbourhoods of a carbon atom vacancy in graphene by employing magnetization-constrained density-functional theory on periodic slabs, and spin-exact, multi-reference, second-order perturbation theory on a finite cluster. The picture that emerges is that of two local magnetic moments (one σ-like and one π-like) decoupled from the π-band and coupled to each other. The ground state is identified as a triplet with a planar equilibrium geometry resulting upon a Jahn-Teller distortion, in which an apical C atom opposes a pentagonal ring. This state lies 0.2 eV lower in energy than the open-shell singlet with one spin flipped, which is a bistable system with two equivalent equilibrium lattice configurations (for the apical C atom above or below the lattice plane) and a barrier 0.1 eV high separating them. Accordingly, a bare carbon-atom vacancy is predicted to be a spin-one paramagnetic species, but spin-half paramagnetism can be accommodated if binding to foreign species, ripples, coupling to a substrate, or doping are taken into account.
In the second part, I study by DFT means the process of hydrogenation of the carbon vacancy, starting from the bare defect atom up to the case of six hydrogen atoms chemisorbed onto its nearest neighbours. I initially consider the formation of a mono-hydrogenated vacancy, finding a binding energy of $\sim$4.2 eV and no activation barrier to the adsorption. As well, I study a variety of possible mutual arrangements of the adsorbates at higher coverages discussing their reactivity and local magnetic moments. In this way the overall hydrogenation process turns out to be thermodynamically favoured and exothermic with respect to both atomic and molecular hydrogen gas sources at least up to four H atoms. This follows from the fact that the driving force in this process is the saturation of the (3σ+1π) unpaired electrons at the vacancy. Moreover, these DFT energies are used to build a phase diagram in a broad range of temperatures and H_2 partial pressures, thus finding that at room T and p conditions, the magnetic (M=$1\mu_B$) 3H-anti structure is the most stable in agreement with recent magnetic measurements. In addition, by considering the stable phase at TEM conditions, it seems reasonable to identify the recently detected three-fold and distorted vacancy with the 3H-anti and the 1H vacancy, respectively. In the end, in these calculations the 2H-geminal phase detected

in μSR experiments, is found to be unfavoured both from a thermodynamic and a kinetic point of view with respect to other di-hydrogenated structures.
In the third part I consider the formation of hydrogen molecules on the Ag(111) surface by abstraction of the adsorbed H atom according to the Eley-Rideal reaction mechanism. To follow the time evolution of the system, I rely on ab initio molecular dynamics and on the quasiclassical trajectory method based onto an external potential energy surface, originally built for quantum calculations on the same system within the flat and rigid surface approximation. In general the reaction is not activated, in fact it has a sizeable cross section even at collision energies in the order of few meV. In terms of cross sections, the differences between ab initio and quasiclassical results at collision energies below $\sim$0.5 eV are proved to depend on the surface corrugation and the energy exchange between hydrogen atoms and surface atoms, which are ignored in the quasiclassical study, following from the reference PES used. In this energy interval, the target vibration may be safely neglected but this is not the case for higher collision energies where it strongly affects the final outcome. Moreover, by considering the product molecules the reaction mechanism is indentified as mainly based on a non-collinear scheme with the reactive encounter occuring upon a bounce of the incident atom on the surface. By means of all these dynamics calculations a large cross-section (compared to the typical value on transition metals) is found in quite good agreement with a recent experimental estimate at very low coverage. Anyway, in future in order to get closer to the experimental result, it seems to be necessary to account for the initial surface temperature, the surface precoverage and the incident angle of the incoming atoms.

Contents

Chapter 1

Introduction

Surfaces are the natural boundaries of condensed phases, both solid and liquid. An accurate description of chemical and physical surface properties is highly desirable due to the crucial role of surface processes in many technological applications. In the chemical industry most reactions are performed in the presence of a catalyst. This is typically very convenient from many viewpoints compared to reactions performed without a catalytic support, indeed it may allow the use of milder reaction conditions, it may increase the selectivity, thereby reducing the waste of reactants and the generation of by-products, it may improve the yield of the reaction, etc.. The importance of surface studies further increased upon the isolation of truly bidimensional systems composed by a single layer of atoms[76]. Graphene is the prominent example of this new class of materials and it shows a series of peculiar properties that make it different from its three-dimesional counterpart, graphite. Nowadays, a large variety of experimental techniques is available to image surface structures. Some of the most relevant are scanning tunneling microscopy (STM) and atomic force microscopy (AFM) for conductive and nonconductive surfaces respectively; transition electron microscopy (TEM); low energy electron diffraction (LEED); X-ray diffraction (XRD). Different approaches, as thermal desorption spectroscopy (TDS) and thermal programmed desorption (TPD) allow to find the composition and the adsorption energy of foreign species on a given surface. As well, the use of pulsed lasers and ultrafast laser techniques makes possible to follow the pathway of processes occurring on a surface. Along with experimental techniques, there are also theoretical approaches to deal with surfaces, among which the density-functional theory (DFT) is presently the most used to get reliable results on electronic and geometric structure of surfaces. In many cases, the tight inding approximation represents a valid alternative, less accurate than DFT but even cheaper in a computational perspective. On the contrary, ab initio wavefunction approaches provide high quality results at high computational price, thus they come into play only when subtle questions arise. In the end, molecular dynamics techniques are used whenever the interest is in the time evolution of a system and thus on the kinetic aspects of a process.

1.1 General considerations on surfaces

1.1.1 Geometric structure

The description of surface features needs to first introduce the ideal three-dimensional crystal structures. A three-dimensional periodic crystal is given by an infinite repetion of identical cells in the so called Bravais lattice. It is given by the positions vectors $\mathbf{R}$, that in most cases coincide with the atomic positions, and have the form: $\mathbf{R} = n_1\mathbf{a}_1 + n_2\mathbf{a}_2 + n_3\mathbf{a}_3$, where $\mathbf{a}_i$ are three non-collinear unit vectors and n_i are integers. In addition to the translational symmetry, each crystal has its own symmetry elements, like rotation axis, reflection planes, inversion centers that transform the crystal into itself. In the simple limit of a crystal with just spherical atoms at each lattice site, in three dimensions one may distinguish 14 distinct Bravais lattices; they become 230 when each unit cell contains more than one atom. In principle, any cell that generates the crystal upon translation along the lattice vectors may serve as unit cell. Anyway normally one selects the smallest cell with the full symmetry of the lattice, namely the *Wigner-Seitz cell*. Due to its periodicity, a crystal lattice may be defined in the real space as well as in the reciprocal space. This is defined by reciprocal unit vectors $\mathbf{b}_i$ for which the following hold: $\mathbf{a}_i \cdot \mathbf{b}_j = 2\pi\delta_{ij}$ and $\mathbf{b}_1 = 2\pi\frac{\mathbf{a}_2\times\mathbf{a}_3}{|\mathbf{a}_1\cdot(\mathbf{a}_2\times\mathbf{a}_3)|}$, from which $\mathbf{b}_2$ and $\mathbf{b}_3$ follow by cyclic permutation of the indices. The equivalent of the Wigner-Seitz cell in the reciprocal space is the so called *first Brillouin zone*[1]. Reciprocal lattice vectors are used to denote the planes of the real space lattice. Each plane is specified by Miller indices (hkl) that indicate the shortest reciprocal lattice vector $h\mathbf{b}_1 + k\mathbf{b}_2 + l\mathbf{b}_3$ perpendicular to this plane.

A surface can be ideally obtained by cleaving an infinite crystal solid along one surface plane. In this way the periodicity is reduced to two-dimensions along the surface and five two-dimensional Bravais lattices can be defined. At the origin of all the surface properties there is the fact that atoms on the surface are undercoordinated with respect to atoms in the bulk. This generally affects the structure, possibly provoking a *relaxation* or a *reconstruction* of the surface. In the first case the distances between the first few planes change but the overall surface symmetry is preserved; in the second case instead the surface is restructured and both symmetry and periodicity change. Reconstructions are typically more evident in semiconductors than in metals due to the different nature of the chemical bond. Indeed, semiconductors form directional covalent bonds and their surface atoms may have to displace significantly in order to find a new stable arrangement. Differently low index metal structures, namely the (100), (110), (111) faces, do not usually reconstruct. Also the presence of adsorbates may result in a new periodicity as well as in the loss of periodicity, depending on the relative strenght of the adsorbate-substrate and adsorbate-adsorbate interactions. The properties of real surfaces are influenced by the presence of defects. Their creation costs some energy, thereby being an activated process; anyway at non-zero temperature a certain amount of defects is always present because of entropic reasons. There can exist several types of defects, like terraces, steps,

[1] The reciprocal space is also known as k-space and plane waves with wave vectors $\mathbf{k}$ are here represented by single points. The corresponding eigenenergies are usually plotted as a function of their $\mathbf{k}$-vectors in the first Brillouin zone, thus generating the band plot.

kinks, adatoms and islands of adatoms, vacancies... whose concentration and nature can be altered by the method of surface preparation. Defects are currently the object of many theoretical and experimental studies, due to their effects on adsorption and reaction processes at surface that are fundamental in catalysis.

1.1.2 Electronic structure

Naturally, at the surface of a solid the electronic structure is very different compared to that of the bulk. This is due to the fact that a bulk crystal has a three-dimensional periodicity while in a surface only the in-plane periodicity is conserved. A simple way to represent a metal surface is the jellium model[60] in which the positive ion charges are replaced by a uniform charge background. In this framework the electronic charge distribution is evaluated using the density functional theory. It comes out that the electron distribution does not follow the sharp edge of the positive background charge, but it decreases smoothly and the electrons spill out into the vacuum. This means that an excess of negative charge accumulates above the surface, while an equivalent excess of positive charge remains below the jellium edge, finally originating a dipole layer. The electron density inside the jellium oscillates with the so called Friedel oscillations. These result from the behaviour of electrons, that try to screen the sharp edge of the positive charge. Only electrons with wave vectors up to k_F are available, thus the screen is incomplete and the oscillations appear. The work function Φ, namely the work needed to remove one electron from a solid at 0 K, is given by the difference between the energy of the electron in vacuum and the Fermi energy. Accordingly, when a dipole layer is present on the surface, the work function has to account also for the energy needed to carry one electron across such layer. It is known that the work function usually varies of about 10% with respect to the mean value depending on the surface orientation and the smaller value is normally found in the less densely packed surfaces.

A slightly more accurate description is given by the nearly-free electron model[6], where weak periodic pseudopotentials are used to model the screened positive ion cores. At the edges of the Brillouin zone, the periodic potential causes the opening of a band gap; in the gap there are localized states that are called Shockley surface states. These states form a band that does not interact with bulk states if it is either fully localized in the gap or it overlaps with bulk states with different symmetry (as in the case of the surface *d*-state and the bulk *sp*-states). Differently, surface resonances appear when symmetry allows the hybridization of surface states with delocalized bulk states. From the projected density of states, it emerges that the energy band of the first layer is typically narrower than that of the layers below due to lower coordination of the surface atoms. The smaller band width shifts the band center towards the Fermi level to conserve the number of electrons, thus leading to a higher reactivity of the surface[65].

Of course, one needs to spend some energy to cut a crystal along a surface otherwise the crystal would not be stable; this amount of energy is the surface energy γ and strictly depend on the nature of the solid. In the case of metals for a N-layers slab it reads as $\gamma = (E_{slab} - NE_{bulk})/2A$, where

E_{bulk} is the cohesive energy per atom, E_{slab} is the total energy of the slab and $2A$ accounts for the area of both the top and bottom faces of the slab. From a qualitative point of view the surface energy of a given crystal is related to the number of bonds that one needs to break in order to generate a chosen surface, thus closely packed surfaces have usually the lowest surface energy. This is the basis of the so-called bond-cutting model which estimates the surface energy per atom by relating the cohesive energy with the coordination number at the surface and in the bulk. On the other hand, surfaces on semiconductor solids result upon the cleavage of truly directional bonds. In this way dangling bonds, corresponding to unpaired electrons, are left on the surface atoms and the structure is highly unstable. In principle, singly occupied atomic orbitals might combine and generate a band. This would be half-filled and thus have a metallic character, which is generally unfavourable for semiconductors. As an alternative, an electronic transfer may occurr so that one over two orbitals with an unpaired electron becomes doubly occupied while the other is empty. The corresponding energy bands are well-separated in energy and thus the surface behaves as a semiconductor.

1.1.3 Processes at surface

1.1.3.1 Adsorption

The potential energy surface (PES) is the key concept to describe the adsorption of any generic foreign species on a chosen surface. This energy surface is built over the configuration space of the atomic coordinates of the atoms involved. By looking at the PES, usually along a specific direction, one can get information about (i) the adsorption sites and energies, (ii) the vibrational frequencies of the adsorbate, (iii) the barriers for the adsorption. The high symmetry sites are *hollow*, *bridge* and *top* sites, where hollow and top positions give respectively the higher and the lower coordination; typically less coordinated species are further away from the surface. However, the relative stability of the adsorption sites depends on the kind of atoms involved. Depending on the nature of the interaction between the adsorbate and the surface, one can distinguish the physisorption and the chemisorption regime.

Physisorption The physisorption process is controlled by the van der Waals forces and it is characterized by long-range (few Å) and low energy (~ 0.1 eV) interactions between an adsorbate and the surface. For these reasons the formation of a true chemical bond is excluded and the bonding is rather due to a dipole-dipole interaction. This is possible even with nonpolar species, as a dipole may appear due to the fluctuations in the ground state charge distribution. This instantaneous dipole p_{inst} generates an electric field proportional to $-p_{inst}/r^3$ and induces a dipole $p_{ind} \propto -p_{inst}/r^3$ in a given atom at distance r. In the limit of a large surface-adsorbate distance, the physisorption energy is simply given by sum of two-body terms,

$$E_{phys} \propto -\sum_i \frac{1}{|r_i - r_{at}|^6} \tag{1.1}$$

where all the i-th atoms of the solid give a contribution that depends on the distance $r_i - r_{at} = R$. If one also assumes that the charge distribution in the solid is continous, then the sum can be replaced by an integral; this can be conveniently expressed in cylindrical coordinates as

$$E_{phys} \propto -\iiint \frac{1}{|R|^6} dR = \int_d^\infty dz \int_0^{2\pi} d\theta \int_0^\infty \frac{r}{\sqrt{r^2+z^2}}. \tag{1.2}$$

Upon integrating, one finally obtains

$$E_{phys} \propto -\frac{1}{d^3} \tag{1.3}$$

where d is the distance of the atom above the surface. Note that one can obtain this result also in a rigorous derivation of the long-range interaction between a neutral atom and a solid surface by using the second order perturbation theory[35]. Here, the perturbation describes the electrostatic interaction between the atom and the solid.

The position of the physisorption minimum on the potential energy surface derives from the balance between the long-range van der Waals attraction and the short-range Pauli repulsion. This increases exponentially as the distance is reduced. In the well-known Lennard-Jones potential, the two contributions are included as

$$V(R) = V_0 \left\{ \left(\frac{R_0}{R}\right)^{12} - 2\left(\frac{R_0}{R}\right)^6 \right\} \tag{1.4}$$

where V_0 is the potential at the equilibrium distance R_0.

Chemisorption As shown above, atoms may attract each other even without chemical bonding via physisorption. Anyway the physisorption picture is meaningful only in the limit of large distances from the surface, otherwise chemical interactions come into play even in case of rare-gas adsorption. In the chemisorption process, a new chemical bond has to be created upon the hybridization between the adsorbate and the substrate electronic structures. In general, when atomic or molecular systems get close to a transition metal surface, their localized orbitals interact with the bands of the solid. According to the Hammer and Norskov d-band model[37, 38], this interaction may be formally split into a contribution arising from the s and p bands of the metal, and one due to the d band. The sp interaction causes a broadening and a downshift in energy of the orbital level, in a process called *renormalization*. Then the strong hybridization with the metal d-states splits the normalized level into a bonding and an antibonding contribution. The antibonding state may be fully occupied, partially occupied or empty depending on the position of the Fermi level. Note that, when the antibonding state is fully occupied, the metal-adsorbate interaction is repulsive as the upshift of the antibonding level is larger than corresponding downshift of the bonding state. This means that no chemical bond can be formed. As an introductory example, consider the case of Xe on Pt[73]. As the Xe atom approaches the surface, atomic and surface electronic states start to overlap. If only the occupied Xe5p and Pt5d states were involved, no bonding would result. However, by

including also the unoccupied Pt5d states (*polarization states*), an overall downshift of the bonding and antibonding states is observed, and thus a weak chemical bond forms. Moreover, the overlap of Xe5p orbitals with both occupied and unoccupied Pt5d states leads to a charge transfer from the Xe atom to the surface; this justifies the bond formation as well as the lower work function of the solid.
Similarly the adsorption of lithium, chlorine and silicon on an aluminum surface occurs upon a charge transfer[61]. Typically a lithium atom displaces its electronic density towards the surface, while the chlorine atom does the opposite and tends to capture some electron density from the substrate. These correspond respectively to positive and a negative ionic chemisorptions. The case of silicon is different as the charge distribution shows an accumulation of charge density in the region between the adsorbate and the surface, thus proving the formation of true covalent bond. In the density of states of the whole system, the atomic orbitals of the adatoms appear as broad peaks, due to the interaction with the substrate bands. As expected the Li2s state is shifted above the Fermi level and thus it is empty; the Cl2p is shifted below the Fermi level and it is fully occupied; and the Si3p is only half-filled.

In this thesis, the adsorbtion of hydrogen atoms on a silver surface and on defective graphene has been studied. Contrary to the alkali metals, hydrogen has high ionization energy and electronegativity comparable to that of standard transition metals. Thus it generally forms local and covalent chemical bonds with the substrate and it prefers high coordination sites on transition metal surfaces. Molecular hydrogen easily form on several transition metals surfaces and then it is likely released. This means that the chemisorption of H_2 as a molecule is unfavoured; on the other hand physisorption may occur but it is very weak due to the low polarizability of the molecule. In most cases upon adsorbing on a transition metal surface, the hydrogen molecule spontaneously dissociates. This is due to the interaction with the metal surface bands that weaken and finally break the bond in the molecule. This so called *dissociative adsorption* mechanism is very common in many catalytic processes when the release reactive fragments from a large compound is needed.

1.1.3.2 Dynamics at surfaces

When a beam of atoms or molecules with a given energy collides with a surface many events may occur. In this field, theory and experiments are strictly related. Indeed accurate experimental techniques based on particle beams, ultra-high vacuum conditions and pulsed laser light provide *clean* data likely comparable with theoretical outcomes.

Scattering After the collision with a surface, many particles of the incident beam can be scattered back into the gas phase. If the incident particle remains on the surface for a time close to the vibrational period of surface atoms, it may not have time enough to exchange energy with the surface atoms. Thus, the total kinetic energy of the particle is conserved and one refers to this

process as *elastic scattering*; in this case after the scattering event, the component of the wavevector parallel to the surface $K_f^{\parallel}$ is given by

$$K_f^{\parallel} = K_i^{\parallel} + G_{mn} \tag{1.5}$$

where G_{mn} is the two-dimensional reciprocal lattice vector of the periodic surface. As a consequence for a given $K_i^{\parallel}$ and thus for a given incident angle, the scattering angles associated to $K_f^{\parallel}$ are entirely determined by the surface periodicity. This is indeed the basis of diffraction studies.

On the other hand, *inelastic scattering* occurs when the energy exchange between the incident particle and the surface is allowed. The energy transfer usually corresponds to the excitation(+) or deexcitation(−) of the surface phonons, which also carry a momentum Q. Accordingly, the conservation of the parallel momentum carries the additional term $\pm Q^{\parallel}$,

$$K_f^{\parallel} = K_i^{\parallel} + G_{mn} + \sum_{exc.phon.} \pm Q^{\parallel}. \tag{1.6}$$

The simple equations above hold for monoatomic systems, but when dealing with molecules one needs to include the internal degrees of freedom, namely vibrations and rotations, where energy can be stored. Thus the total energy balance is

$$\frac{\hbar^2 K_f^2}{2M} = \frac{\hbar^2 K_i^2}{2M} + \triangle E_{rot} + \triangle E_{vib} + \sum_{exc.phon.} \pm \hbar\omega_{Q,j} \tag{1.7}$$

where the last term accounts for the energy exchange between the molecule and phonons and it is null in case of elastic scattering. Moreover the term $\triangle E_{vib}$ is generally very small, as the excitation of molecular vibrations is usually inefficient with respect to the excitation of both phonons and rotations. This is due to the time scale of molecular vibrations that is much shorter than the scattering time or the rotational period. Therefore the molecular vibrations follow the process almost adiabatically, while the rotations can be quite efficiently excited.

Sticking When a molecular or atomic beam impinges on a surface, the sticking or adsorption probability is given as the fraction of particles that remains on the surface, namely that is not scattered back. In principle, if the surface has a finite temperature, the adsorbed particle will sooner or later desorb due the thermal fluctuations; anyway this usually happens after a long time compared to microscopic time scales. In the sticking process the incident particle becomes trapped into the attractive potential well, upon the transfer of its kinetic energy to the substrate. This causes the excitation of phonos or electron-hole pairs. A simple model to deal with the trapping probability is the *hard cube model*[25], where the surface is represented as a cube with mass M_c moving with velocity v_c sampled from an appropriate distribution. The incoming atom has mass m and velocity v_g; when it feels the attractive potential well E_{ad}, it accelerates and its velocity

becomes

$$v_{well} = -\sqrt{v_g^2 + \frac{2E_{ad}}{m}} \tag{1.8}$$

After the collision, if it has no sufficient energy to overcome the attractive potential, namely $E_f < E_{ad}$, the particle cannot escape the potential well and it remains at the surface. Taking energy and momentum conservation into account, the particle that hits a surface with velocity v_{well} will get trapped if the surface cube velocity does not exceed the limiting value,

$$v_{lim} = v_c < \frac{\mu+1}{2}\sqrt{\frac{2E_{ad}}{m}} + \frac{\mu-1}{2}v_{well} \tag{1.9}$$

where $\mu = m/M_c$. In conclusion, many different aspects may influence the sticking probability, as the mass and the kinetic energy of the incident particle, the adsorbtion energy and the temperature of the surface. In general heavier atoms are favoured as they dissipate the energy more efficiently; for the same reason particles with low kinetic energy can much easily stick on a surface. In case of molecular species, the possibility to store energy in form of vibrations and rotations generally leads to an enhancement of the trapping probability with respect to atoms in the very same conditions. Moreover, for a given particle, a higher adsorption energy means a deeper potential well and thus a higher probability to be trapped. Finally, an increase in the surface temperature enlarges the range of kinetic energies over which the particles can be trapped; more precisely, at high kinetic energy the probability of trapping increases, while at low kinetic energy it decreases . Note that in the hard cube model the surface is assumed to be flat and structureless, thus any scattering and adsorbtion process conserves the incident parallel momentum. However this is a rough approximation, in fact on real surfaces the behaviour of the incident particle is affected by the local environment. This means that the potential energy surface is corrugated, namely that it depends on the lateral position of the incident particle on the surface. It is clear that the excitation of the surface phonons is still the main channel to dissipate the proper amount of energy and allow for the sticking of the particle. Anyway, due to the corrugation and anisotropy of the potential, the particle can also transfer energy into the motion parallel to the surface and, in case of molecules, into the rotational motion. After that this energy won't be available for the backscattering into the gas phase.

The picture proposed so far is based on two assumptions: first of all the system can be described with classical dynamical methods; then, the sticking process is not activated, thus there is no barrier before the adsorption well. Accordingly, in the low kinetic energy regime, namely $E \to 0$, $T_s \to 0$, the trapping probability tends to one, no matter how small is the adsorption well or how small is the mass ratio between the particle and the solid. In fact, for $T_s \to 0$ every particle will transfer energy to the substrate; moreover for $E \to 0$ any energy transfer is sufficient to keep the particle trapped. Anyway, quantum-mechanically there is a nonzero probability for elastic scattering at the surface; hence the sticking probability becomes less than unity in the zero energy limit in particular for light atoms impinging on the surface.

Diffusion and subsurface penetration The diffusion process of adsorbed particles along a surface is driven by thermal fluctuations. Each adsorbate is trapped into a potential well and it vibrates around its equilibrium position. Anyway it may escape from the well once it has enough energy to overcome the barrier. A generic adsorbate can jump from a stable adsorption site to the next with a rate given as

$$k_j = k_0 \exp\left(-\frac{E_a}{k_B T_s}\right)$$

where E_a is the energetic barrier to the nearest neighbours sites and T_s is the surface temperature. In terms of probability the diffusion process along a surface can be described as

$$P\left(\mathbf{R}, t + \triangle t\right) = \sum_{\mathbf{R}'} W\left(\mathbf{R}, \mathbf{R}', \triangle t\right) P\left(\mathbf{R}', t\right)$$

This means that the probability of the adsorbate to be in $\mathbf{R}$ at time $t+\triangle t$, depends on the probability of the adsorbate to be in a generic site $\mathbf{R}'$ at time t, weighted by the transition probability W. In the assuption that the interval $\triangle t$ allows only one jump and that jumps may involve only nearest neighbours sites, the rate of transition to one of these N sites is k_j/N and the probability is $\triangle t \cdot k_j/N$. Accordingly the transition probability reads as

$$W\left(\mathbf{R}, \mathbf{R}', \triangle t\right) = \begin{cases} \triangle t \cdot k_j/N & \text{if } \mathbf{R}, \mathbf{R}' = \text{n.n.} \\ 1 - \sum_{n.n.} \triangle t \cdot k_j/N & \text{if } \mathbf{R} = \mathbf{R}' \\ 0 & \text{else.} \end{cases}$$

In the diffusion process, two alternative mechanisms may be found. In the *hopping diffusion* the adatom hops from one equilibrium site to the next by crossing an intermediate configuration; in the *exchange diffusion* the adatom displaces one atom of the surface and takes its place; upon the displacement, this surface atom adsorbes on to the nearest neighbour site. Note that the exchange process occurs in a concerted way. Many different aspects can influence the diffusion of adatoms along a surface: of course, the type of adsorbates; then their interactions with the surface that mostly depend on the nature of the surface atoms and the exposed face; finally also the surface temperature.

Sometimes the incoming particles may also cross the surface layer and penetrate subsurface, thus dissolving into the bulk; here they can diffuse either parallel to or through the layers, they can adsorbe in stable sites, they can be reflected back to the surface, ... The observed behaviour depends on the energy of the particle as well as on the potential exerted on it by the bulk atoms. Even if a certain amount of subsurface penetration is often possible, this process becomes relevant for open surfaces and small incident particles. As demonstrated by thermal desorption measurements in [52], this is the case of the Ag(100) surface under the fluence of hydrogen or deuterium atoms: at first the incoming atoms are adsorbed on the surface; then, upon further exposure the atoms start to penetrate in the bulk. Interestingly, this process proceeds in a different way for the two atomic species considered, indeed the D atoms occupy the available subsurface sites in addition to the

surface positions, while the H atoms abandone the surface sites and all move subsurface. Anyway, disregarding the surface coverage, the Ag(100) sample shows a clear tendency to host H atoms in the bulk and might be possibly used for the hydrogen storage. On the contrary, the Ag(111) surface under the very same conditions does not allow the penetration of H and D atoms below the surface. This is due to the closer arrangement of the silver atoms in the Ag(111) face compared to Ag(100); this essentially means that on closed-packed surfaces only few entrance channel are available for the incoming particles, while most of the surface offers a repulsive barrier to the penetration.

A further confirm on the importance of the diffusion of particles through the surfaces, from the vacuum space to the bulk region and viceversa, comes from one of the procedure followed to grow graphene on metal surfaces[11]. Currently most of the graphene/metal interfaces are generated after exposure of the clean crystal to hydrocarbons inside the UHV chamber, where the low pressure conditions mainly lead to monolayer graphene formation. After the dehydrogenation on the hydrocarbons occurring at the metal surface, two main growth mechanisms may be distinguished. The first one is the *surface growth*, where the carbon remains on the surface and aggregates to form graphene. Such process ceases once the surface is covered and no more active sites are available to produce new carbon atoms, thus after the deposition of a single layer of graphene. The second one is the *segregation growth*, where the carbon atoms dissolve in the bulk at high temperature and then segregate to the surface at lower temperature. In this case the driving force is the lower free energy of the coated system, which anyway is effective only for the first layer formation. The addition of further layers is not thermodinamically favoured, thus difficult to accomplish in a controlled way. The nature of the metal and the symmetry of the surface not only determine the growth mechanism of the graphene sheet, but are also responsible for the arrangements of the carbon atoms over the surface: in fact different structures can be identified depending on the position of the carbon atoms with respect to the sites of the surface.

1.1.3.3 Reaction: Langmuir-Hinshelwood, Eley-Rideal and hot atoms mechanisms

Reactions at surfaces may ideally occur in terms of three alternative mechanisms[102] as reported in fig.1.1. In the *Langmuir-Hinshelwood* (LH) regime the reaction takes place between two adsorbed species which are in thermal equilibrium with the surface. The reaction path is typically thermoneutral, in fact the energy generated upon the formation of the molecule is almost equal to the energy spent to break the two weak adsorbate-substrate bonds. For this reason the desorbing molecules generally occupy the lower vibrational states, namely $\nu = 0$ and $\nu = 1$. In order to give a reactive encounter, the two fragments have to diffuse on the surface, i.e. they have to overcome the diffusion barrier. In ordinary conditions, this is the dominant mechanism.
The *Eley-Rideal* (ER) mechanism is based on the direct reaction between a gas phase species and an adsorbed species, forming a molecule which immediately desorbs. Due to the fact that one of the two fragments is in gas phase, the reaction is highly exothermic, thus leading to molecules with high translational and internal energies. Moreover the initial state of the gas phase species

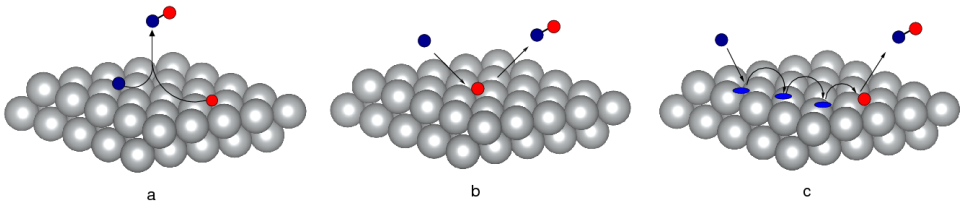

Figure 1.1: Reaction mechanisms between a gas partcile and an adsorbed species. (a) the Langmuir-Hinshelwood scheme; (b) the Eley-Rideal scheme; (c) the hot-atoms scheme.

strongly influences the vibro-rotational distribution of the molecules. Note that in the low kinetic energy regime, the ER reaction probability is affected by the so-called *dynamical steering*. In principle this effect may arise any time a gas phase species interact with a substrate to give a certain outcome, thus for instance it is also observed in molecular dissociative adorptions. The intensity of the steering has to be evaluated for each system depending on both the nature of the substrate and that of the incoming species. To understand the steering phenomenon, one needs to consider the multi-dimensional potential energy surface. For the ER recombination, the typical PES shows non-activated or slightly activated reaction paths. Anyway there are plenty of alternative paths corresponding to different impact points with high energy barriers that hinder the reaction to occur. The point is that at very low kinetic energy the particles are so slow that they can be efficiently steered to a favourable configuration. In this way the number of reactive impact points increases and thus the reaction probability is enhanced. Since the mechanism becomes less effective at higher kinetic energies, the reaction probability decreases.

Unless for strong steering effects or high surface coverage, in general, the Eley-Rideal mechanism is quite improbable as the *direct* encounter between gas and adsorbed species is a rare event. More likely indeed the incident particle hits the surface. Here, this particle may access two main channels: in one case, it dissipates the extra energy, it becomes trapped in a potential well and thus it sticks on the surface; afterwards it might overcome the barrier, diffuse, bump into another adsorbed species and possibly react. In the other case, the dissipative process is almost uneffective, thus the particle will either return into the gas phase or slide along the surface; which of these two possibilities is the real one, depends on wheter the particle momentum has a major component perpendicular or parallel to the surface. When the parallel term prevails, the particle moves along the surface and possibly enters potential wells; here anyway the particle cannot be trapped as its energy is too high. Moreover this high energy particle may finally bump into an adsorbed species, react and form a molecule, with high internal and translational energy. Such molecules are hot ER-like molecules and they contribute to the ER reaction probability as they are not distinguishable from those obtained upon a direct collision of the gas phase species on the adsorbed one. In summary this mechanism differs from the traditional ER scheme only in one aspect: here several non-dissipative bounces on the surface precede the reactive encounters; it is commonly known as *hot atoms* reaction mechanism.

1.2 The case of graphene

Graphene is a two-dimensional crystal of carbon atoms arranged on a honeycomb structure made of hexagons. The existence of free standing graphene has been proved only recently [77], even if it has been known since long time as a model system to study the properties of some carbon allotropes, like graphite, carbon nanotubes and fullerenes. The reason is that the physical structure of such materials is closely related to that of graphene. For instance, the three-dimensional crystal structure of graphite is made by stacked graphene layers that are coupled via weak van der Waals interactions; further on, one-dimensional carbon nanotubes are obtained by rolling up a graphene sheet along one axis; finally fullerenes may form from graphene, by changing some hexagons into pentagons in order to allow the final ball shape.

1.2.1 Lattice of graphene

Carbon atoms in graphene form an hexagonal planar lattice which belong to the simmetry point group D_{6h}. As illustrated in fig.1.2, the unit cell of graphene is defined by two lattice vectors $\mathbf{a}_1$ and $\mathbf{a}_2$ and it contains two atoms. The lattice vectors have coordinates:

$$\mathbf{a}_1 = d\left(\frac{3}{2}, \frac{\sqrt{3}}{2}\right), \qquad \mathbf{a}_2 = d\left(\frac{3}{2}, -\frac{\sqrt{3}}{2}\right) \tag{1.10}$$

where $d = 1.42$ Å is the C-C bond lenght; in direct cell cooordinates, the two carbon atom in cell are located at

$$\mathrm{C}_1 = [0, 0], \qquad \mathrm{C}_2 = \left[\frac{2}{3}, \frac{2}{3}\right] \tag{1.11}$$

and they are nearest neighbours. In graphene each carbon has three nearest neighbours associated to the real plane vectors

$$\delta_1 = d\left(\frac{1}{2}, \frac{\sqrt{3}}{2}\right), \qquad \delta_2 = d\left(\frac{1}{2}, -\frac{\sqrt{3}}{2}\right), \qquad \delta_3 = d\,(-1, 0) \tag{1.12}$$

Note that graphene is formed by two interpenetrating sublattices A and B with triangular symmetry. Due to the alternating character of the two sublattices, the nearest neighbours of a carbon atom in the A sublattice belong to the B sublattice and viceversa. In the same way, a carbon atom will find its six second-nearest-neighbours in its own sublattice located at $\delta_1^{'} = \pm\mathbf{a}_1, \delta_2^{'} = \pm\mathbf{a}_2, \delta_3^{'} = \pm\left(\mathbf{a}_2 - \mathbf{a}_1\right)$.

As shown in fig.1.3, the unit vectors in the momentum k-space are

$$\mathbf{b}_1 = \frac{2\pi}{d}\left(\frac{1}{3}, \frac{1}{\sqrt{3}}\right), \qquad \mathbf{b}_2 = \frac{2\pi}{d}\left(\frac{1}{3}, -\frac{1}{\sqrt{3}}\right). \tag{1.13}$$

From the reciprocal lattice nodes, one can build the first Brillouin zone that is an hexagon. It has the same shape of the Wigner-Seitz cell in the real space even if it is rotated by an angle of 90°. In the Brillouin zone, one may find some special k-points: the Γ point is located at the center of the

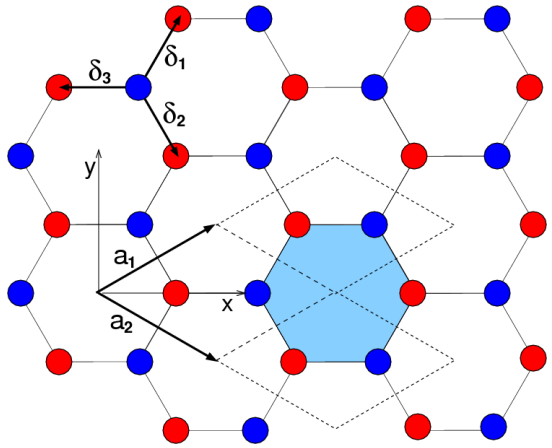

Figure 1.2: The lattice of graphene in real space. The unit cell is defined by the two lattice vectors $\mathbf{a}_1$ and $\mathbf{a}_2$; some unit cells are shown with dashed lines; the light blue area is the Wigner-Seitz cell. Each cell contains two atoms belonging to different sublattices: A (blue) and B (red). The nearest neighbours vectors are shown by vectors δ_i.

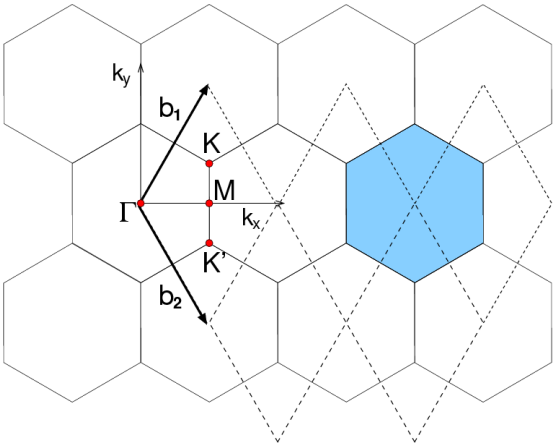

Figure 1.3: The lattice of graphene in reciprocal space. The unit cell is defined by the two lattice vectors $\mathbf{b}_1$ and $\mathbf{b}_2$; some unit cells are shown with dashed lines; the light blue area is the first Brillouin zone.

polygon, the K points are at the corners, while at the center of each side there are the M points. Of course in this Brillouin zone, only three non equivalent special k-points may be found in addition to the Γ point:

$$\mathbf{\Gamma} = [0,0] \qquad \mathbf{K} = \left[\frac{1}{3}, \frac{2}{3}\right] \qquad \mathbf{K}' = \left[\frac{2}{3}, \frac{1}{3}\right] \qquad \mathbf{M} = \left[\frac{1}{2}, \frac{1}{2}\right] \tag{1.14}$$

The $\mathbf{K}$ and $\mathbf{K}'$ sites are important in the band structure of graphene, due to the fact that the Fermi level passes through these points. Here, the point group symmetry is D_{3h} that spans two dimensional irreducible representations; thus, the two points are degenerate in energy.

1.2.2 Electronic structure of graphene

The high flexibility in bonding of carbon atoms is due to the four valence electrons and may give rise to a large variety of structures. In graphene the typical honeycomb structure is due to the in plane σ bonds oriented with angles of 120°. These strong covalent bonds result from the sp^2 hybridization of the $2s$, $2p_x$ and $2p_y$ orbitals on each carbon atom and involve three valence electrons. The resulting $\sigma-$band is fully occupied, it is quite deep in energy, thus it is rarely involved in the electronic processes; similarly also the participation of the empty σ^*-band is rather marginal. Anyway, the fourth electron occupies the p_z orbital perpendicular to the plane and it is involved into a weak and delocalized π bond, resulting from the lateral superposition of the p_z orbitals on each carbon. Note that the π cloud in graphene generates an aromatic network such as in benzene or in policylcic aromatic hydrocarbons. From the linear combination of the singly occupied p_z orbitals, the π (valence) and π^*(conduction) bands arise; they cross exactly at the Fermi energy, thus in ideal graphene the π band is fully occupied, while the π^* band is totally empty. Note that these two bands meet at the so called Dirac points, namely the $\mathbf{K}$ and $\mathbf{K}'$ points in the first Brillouin zone, without any band gap. Graphene is a semimetal due to its intermediate character: in fact at the Fermi energy it behaves both like a metal as it has no band gap, and like a semiconductor with no density of states. Typically the band structure of graphene is handled within the tight binding approximation [4, 17]. In this framework, one basically assumes that the π contribution is sufficient to get a reliable model for the electronic states in the region close to the charge neutrality point. The tight binding hamiltonian in second quantization reads as

$$\hat{\mathcal{H}} = -t \sum_{\langle i,j\rangle\sigma} \left(\hat{a}^\dagger_{i\sigma}\hat{b}_{j\sigma} + h.c.\right) - t' \sum_{\langle\langle i,j\rangle\rangle\sigma} \left(\hat{a}^\dagger_{i\sigma}\hat{a}_{j\sigma} + \hat{b}^\dagger_{i\sigma}\hat{b}_{j\sigma} + h.c.\right) \tag{1.15}$$

Here $\hat{a}^\dagger_{i\sigma}$ creates an electron with spin σ on the lattice site i in the A sublattice, while its conjugate complex $\hat{a}_{i\sigma}$ annichilates it. In the same way, the $\hat{b}^\dagger_{j\sigma}$ and $\hat{b}_{j\sigma}$ operators respectively create and destroy electrons on the j site in the B sublattice. The first term in the hamiltonian mimics the hopping between nearest neighbours sites, thus into different sublattices; the other term instead accounts for the hopping between second nearest neighbours, thus into the same sublattice. Here t (≈ 2.7 eV) and t' represent respectively the energy cost of the two processes. In principle one can include also longer range interactions, but t' is already an order of magnitude smaller than t; hence, they may be reasonably ignored as almost irrelevant to the overall band structure.
The natural choice is then to write the operators in the Hamiltonian in terms of Bloch's function centered on a single sublattice

$$\begin{aligned}
\hat{a}_{\mathbf{r}_A} &= \frac{1}{\sqrt{N}} \sum_{\mathbf{k}\in BZ} e^{-i\mathbf{k}\cdot\mathbf{r}_A}\hat{a}_{\mathbf{k}} \qquad \Longrightarrow \qquad \hat{a}_{\mathbf{k}} = \frac{1}{\sqrt{N}} \sum_{\mathbf{r}_A\in BK} e^{i\mathbf{k}\cdot\mathbf{r}_A}\hat{a}_{\mathbf{r}_A} \\
\hat{b}_{\mathbf{r}_B} &= \frac{1}{\sqrt{N}} \sum_{\mathbf{k}'\in BZ} e^{-i\mathbf{k}'\cdot\mathbf{r}_B}\hat{b}_{\mathbf{k}'} \qquad \Longrightarrow \qquad \hat{b}_{\mathbf{k}'} = \frac{1}{\sqrt{N}} \sum_{\mathbf{r}_B\in BK} e^{i\mathbf{k}'\cdot\mathbf{r}_B}\hat{b}_{\mathbf{r}_B}
\end{aligned} \tag{1.16}$$

where BZ refers to the first Brillouin zone, while BK indicates the Born- von Karman cell that defines the periodic boundary conditions in real space; the spin index has been dropped for the sake of simplicity. Taking into account only the interaction between nearest neighbours, the Hamiltonian reads as

$$\hat{\mathcal{H}} = -\frac{t}{N}\sum_{\mathbf{r}_A,\mathbf{r}_B}\sum_{\mathbf{k},\mathbf{k}'}\left(\hat{a}^{\dagger}_{\mathbf{k}}\hat{b}_{\mathbf{k}'}e^{i\mathbf{k}\mathbf{r}_A}e^{-i\mathbf{k}'\mathbf{r}_B}\right) + h.c. \tag{1.17}$$

then following from the relation between the sites in the two sublattices, $\mathbf{r}_B = \mathbf{r}_A + \delta_j$, the Hamiltonian becomes

$$\begin{aligned}\hat{\mathcal{H}} &= -\frac{t}{N}\sum_{\mathbf{r}_A}\sum_{\mathbf{k},\mathbf{k}'}\sum_{j}^{3}\left(\hat{a}^{\dagger}_{\mathbf{k}}\hat{b}_{\mathbf{k}'}e^{-i(\mathbf{k}'-\mathbf{k})\mathbf{r}_A}e^{i\delta_j\mathbf{k}'}\right) + h.c. \\ &= -t\sum_{\mathbf{k},\mathbf{k}'}\sum_{j}^{3}\left(\hat{a}^{\dagger}_{\mathbf{k}}\hat{b}_{\mathbf{k}'}\delta_{\mathbf{k},\mathbf{k}'}e^{i\delta_j\mathbf{k}'}\right) + h.c. \\ &= -t\sum_{\mathbf{k}}\sum_{j}^{3}\left(\hat{a}^{\dagger}_{\mathbf{k}}\hat{b}_{\mathbf{k}}e^{i\delta_j\mathbf{k}}\right) + h.c.\end{aligned} \tag{1.18}$$

The hamiltonian matrix has only off-diagonal elements due to the fact that an operator applied on a basis function belonging to a different sublattice returns zero, namely

$$\hat{a}_{\mathbf{k}}\left|B\left(\mathbf{k}\right)\right\rangle = 0, \qquad \hat{b}_{\mathbf{k}}\left|A\left(\mathbf{k}\right)\right\rangle = 0 \qquad \text{and} \qquad \hat{a}_{\mathbf{k}}\left|....1^{A}_{\mathbf{k}'}...\right\rangle = \delta_{\mathbf{k},\mathbf{k}'}\left|0\right\rangle \tag{1.19}$$

$$\begin{pmatrix} 0 & H_{AB} \\ H_{BA} & 0 \end{pmatrix}\begin{pmatrix} c_A \\ c_B \end{pmatrix} = \mathcal{E}\left(\mathbf{k}\right)\begin{pmatrix} c_A \\ c_B \end{pmatrix} \tag{1.20}$$

Then by solving the secular equation one finds the eigenvalues,

$$\mathcal{E}\left(\mathbf{k}\right) = \pm t\sqrt{3 + 2\cos\mathbf{k}\left(\delta_1 - \delta_2\right) + 2\cos\mathbf{k}\left(\delta_1 - \delta_3\right) + 2\cos\mathbf{k}\left(\delta_2 - \delta_3\right)} \tag{1.21}$$

that finally read as,

$$\mathcal{E}\left(\mathbf{k}\right) = \pm t\sqrt{3 + 2\cos\sqrt{3}k_y + 4\cos\frac{3}{2}k_x\cos\sqrt{\frac{3}{2}}k_y} = \pm t\sqrt{3 + f\left(\mathbf{k}\right)}. \tag{1.22}$$

where positive and negative eigenvalues refer respectively to the upper (π^*) and the lower (π) band. As reported in ref.[108], when the second nearest neighbours interactions are included the eigenvalues read as

$$\mathcal{E}\left(\mathbf{k}\right) = \pm t\sqrt{3 + f\left(\mathbf{k}\right)} - t^{'}f\left(\mathbf{k}\right). \tag{1.23}$$

Note that for $t^{'} \neq 0$ the two solutions are no more symmetric around zero energy, the electron-hole symmetry is broken and the π^* and π bands become asymmetric.

As already outlined, the Fermi energy is zero at the Dirac points, namely $\mathbf{K}$ or $\mathbf{K}'$ in the first BZ. The low-energy properties of graphene associated to the electronic states close to the Fermi energy, can thus be described by expanding the band structure around the $\mathbf{K}$ point according to $\mathbf{k} = \mathbf{K} + \mathbf{q}$

as in ref.[108],

$$= e^{i\delta_1\cdot\mathbf{K}}e^{i\delta_1\cdot\mathbf{q}} + e^{i\delta_2\cdot\mathbf{K}}e^{i\delta_2\cdot\mathbf{q}} + e^{i\delta_3\cdot\mathbf{K}}e^{i\delta_3\cdot\mathbf{q}} \tag{1.24}$$

then, by using the $\mathbf{K}$ coordinates and projecting the δ_j vectors onto $\mathbf{b}_1$ and $\mathbf{b}_2$, it results

$$\begin{aligned}\sum_j^3 e^{i\delta_j\cdot\mathbf{k}} &= e^{i\delta_1\mathbf{q}} + e^{i\frac{2}{3}\pi}e^{i\delta_2\mathbf{q}} + e^{-i\frac{2}{3}\pi}e^{i\delta_3\mathbf{q}} = \\ &= e^{i\delta_1\mathbf{q}} + \cos\left(\frac{2}{3}\pi\right)\left(e^{i\delta_2\mathbf{q}} + e^{i\delta_3\mathbf{q}}\right) + i\sin\left(\frac{2}{3}\pi\right)\left(e^{i\delta_2\mathbf{q}} - e^{i\delta_3\mathbf{q}}\right).\end{aligned} \tag{1.25}$$

Then by writing each exponential as a Taylor's expansion up to first order, one gets

$$= 1 + i\delta_1\mathbf{q} - \frac{1}{2}\left(2 + i\mathbf{q}\left(\delta_2 + \delta_3\right)\right) + i\frac{\sqrt{3}}{2}\left(i\mathbf{q}\left(\delta_2 - \delta_3\right)\right). \tag{1.26}$$

By noticing that $\delta_2 + \delta_3 = -\delta_1$, one can define new basis vectors

$$\hat{\mathbf{q}}_x = \frac{1}{d}\delta_1, \qquad \hat{\mathbf{q}}_y = \frac{1}{\sqrt{3}d}\left(\delta_2 - \delta_3\right) \tag{1.27}$$

and then rewrite the above expression as

$$= \frac{3d}{2}\mathbf{q}\hat{\mathbf{q}}_x + i\frac{3d}{2}\mathbf{q}\hat{\mathbf{q}}_y = \frac{3d}{2}\left(q_x + iq_y\right) \tag{1.28}$$

Therefore in the vicinity of the $\mathbf{K}$ point the Hamiltonian may be rewritten as

$$\hat{\mathcal{H}}_{\mathbf{K}}\left(\mathbf{q}\right) = v_F\begin{pmatrix} 0 & q_x + iq_y \\ q_x - iq_y & 0 \end{pmatrix} = v_F\boldsymbol{\sigma}\cdot\mathbf{q} \tag{1.29}$$

where $\boldsymbol{\sigma} = (\sigma_x, \sigma_y)$ is a vector of Pauli matrices. The corresponding eigenvalues are $\mathcal{E}\left(\mathbf{q}\right) = \pm v_F\mathbf{q}$, where v_F is the Fermi velocity. This means that in the vicinity of the Dirac points the energy varies linearly with respect to the momentum $\mathbf{q}$; in the same way the density of states has also linear dependence on the energy and it vanishes for $\mathcal{E} = 0$,

$$\rho\left(\mathcal{E}\right) \propto |\mathcal{E}|. \tag{1.30}$$

Accordingly the band structure of graphene shows the peculiar double cones centered at the vertices of the first Brillouin zone; these positions are characterized by no band gap and no density of states. The linear dispersion near K is a direct consequence of the fact that electrons in graphene behave as pseudorelativistic particles. They move at the Fermi velocity v_F that does not depend on the energy or momentum[2] and it is defined as $v_F = \frac{3}{2}dt \simeq 10^6 m/s$. Note also that due to the unusual behaviour of the electrons, many novel effects appear in graphene, like the anomalous integer quantum Hall effect, the Klein's paradox, etc... .

[2]Note that usually $\mathcal{E}\left(\mathbf{q}\right) = \mathbf{q}^2/2m$ where m is the electron mass and the velocity $v = \sqrt{2\mathcal{E}/m}$ changes with energy.

1.2.3 Defects in graphene

In crystalline solids the presence of defects is dictated by the second priciple of thermodynamics. In general defects consist in a perturbation of the crystalline order and they are known as extrinsic defects or intrinsic defects depending whether foreign species are involved or not. Intrinsic defects may be classified in terms of their dimensionality as: (i) zero-dimensional point defects like vacancies and interstitial atoms, (ii) one-dimensional dislocations, (iii) two-dimensional grain boundaries and stacking faults, and finally (iv) three-dimensional voids and inclusions. In a similar way, also foreign species may arrange into different structures. In the production of graphene, defects and impurities are always introduced. Anyway since graphene is a bidimensional crystal, the nature of possible defects in this case is reduced [30]: point defects are usually Stone-Wales defects, single vacancies, multiple vacancies and adatoms. Experimental studies to probe defective structures typically base on transmission electron microscopy (TEM) and scanning tunneling microscopy (STM).

- In *Stone-Wale*s defects the ideal hexagonal lattice is perturbed by a 90° rotation of a C-C bond, that transforms four hexagons into two pentagons and two heptagons. In typical working conditions, the concentration of SW defects is negligible due to the activation energy that is close to 10 eV; thermodinamically the formation energy is $E_f \approx 5$ eV.

- *Vacancies* may be roughly depicted as holes in the lattice due to missing atoms. In graphene upon the removal of a carbon atom four unpaired electrons are left on the vacancy. These electrons represent the key to interpret the destiny of a carbon vacancy in terms of lattice relaxation and electronic structure. Vacancies are typically introduced by irradiation with high energy particles. Indeed the threshold energy to move a carbon atom far from its lattice position is about 18-20 eV, while the formation energy is $E_f \approx 7.5$ eV.

- *Double vacancies* (DV) may form if two adjacent carbon atoms are removed from the lattice or upon coalescence of two single vacancies. They can reconstruct in different ways: in fact they can form two pentagons and one octagon and give the $V_2\,(5-8-5)$ system; alternatively by rotating one bond of the octagon they can form the $V_2\,(555-777)$ structure. The formation energy in the first case is about $E_f \approx 8$ eV, thus close to the value found for the single vacancy; while in the second case, the formation energy is about 1 eV lower. The removal of more than two atoms produces large holes in the lattice that is then required to reconstruct. Commonly the reconstruction implies the bending or warping of the layer, but the formation of pentagon and heptagon rings has also been observed. Note that if an even number of carbon atoms are missing, the vacancy can fully reconstruct and no dangling bonds are left. For this reason such vacancies are typically favoured over structures with an odd number of missing atoms.

- A foreign species adsorbed on the graphene layer is usually referred to as an *adatom*. This is physisorbed on graphene if the bond is weak and mainly due to van der Waals forces; instead it is chemisorbed if it forms a strong covalent bond with graphene. Many bonding

sites are available, normally corresponding to high symmetry points, like on top of a carbon atom, in bridge between two carbons or above the center of a hexagon. In a defective lattice, the adsorption mainly occurs at defective sites, due to the locally higher reactivity of the π-electron system compared to that of perfect graphene. Upon the interaction with foreign species, carbon atoms in the graphene layer may acquire some degree of sp^3-hybridization, thus breaking the symmetry of the lattice. Note that this usually occurs for covalently bound species. Of course, the case of carbon adatoms is unique. In general adsorbed carbon atoms may remain on the graphene surface when a vacancy is created; then they may easily recombine with lattice defects, like vacancies; and finally under the appropriate conditions they can also be incorporated into the sp^2 network at the expense of the local curvature.

- Foreign atoms can also be incorporated in the graphene lattice forming *substitutional impurities*. Boron and nitrogen atoms can easily replace carbon atoms due to their similar atomic radii; moreover they also serve as natural dopants since they have respectively one electron less and one more than carbon. The presence of such impurities not only shift the Fermi level, but also changes the electronic structure of graphene. In substitutional defects based on transition metal atoms, the foreign atom easily exchange electron density with graphene and it is usually accommodated slightly off the lattice plane due to its large volume compared to that of carbon. A common way to introduce transition metals relies on vacancies: here the missing carbon is replaced by the metal which then makes covalent bonds with the undercoordinated atoms.

One-dimensional defects can be thought as lines of point defects that generally separate domains with different lattice orientations. In graphene grown on metal surface one often encounters such domains that result from the growth process. In fact on a chosen metal surface, nucleation starts simultaneously and independently at different points and leads to graphene islands with differing orientations. When two graphene grains coalesce, a line defect appears. Similar line defects can appear also at the edges of a graphene sheet. Indeed edges, either free or passivated with atoms, can possibly reconstruct to achieve a stable nuclear arrangement; note anyway that the presence of non-defective edges affects the electronic structure of graphene by itself.

1.2.3.1 Origin of defects

In general the formation of defects in graphene can follow three alternative mechanisms, namely (i) crystal growth, (ii) irradiation with high energy particles, like electrons or ions, and (iii) chemical treatment. In the first case, defects form while graphene grows on a metal surface; in addition to the expected line defects, also vacancies may form but they are rapidly suppressed due to their high formation energy and to the high mobility of carbon adatoms on the surface. Of course, by reducing the operating temperature, defects can be unlikely annealed and they become a serious problem.
Irradiation of graphene with electrons or ions is the common way to eject carbon atoms and generate point defects[54]. This is a highly activated process, indeed each carbon atom needs approximately

18-20 eV to leave its lattice site. Traditionally, the uniform irradiation of the graphene sample with an electron beam generates a random distribution of vacancies; anyway nowadays more sophisticated techniques based on highly focused electron beams allow to create vacancies with almost atomic selectivity. Alternatively one can generate carbon vacancies by irradiating the graphene sheet with high energy ions, like Ar^+. Note that the number of vacancies depends on the ion energy: in fact it increases up to a maximum value, then it decreases and finally it tends to zero.
In a chemical perspective, in the absence of defects and far from the edges graphene is a quite inert material. At room temperature, by oxidation with HNO_3 or H_2SO_4, hydroxil and carboxyl groups may attach to graphene, thus generating a functionalized defective layer. Under harsh conditions, namely by using plasma, atomic hydrogen may also adsorb on graphene.

1.2.3.2 Properties of defects

Unlike the common way of thinking, the presence of defects is not always undesirable. In materials science indeed it often proved to be an opportunity, possibly showing new and unforeseen ways to use an 'old' material. In principle the controlled and proper generation of defects might allow to act on the properties of the undefective material, so that to tailor them up to the aimed result. To this end, a deep knowledge of the specific nature of a defect, as an isolated state or in a network of defects, is highly desirable and it motivated many theoretical and experimental works. In this way it has been proved that defects have a central role in determining the properties of graphene: accordingly, they are highly reactive sites, they may act as scattering centers for the electron waves, thus inducing a drop of conductance, and they may likely turn graphene into a magnetic material. In a chemical perspective, it is clear that the presence of dangling bonds enhances the reactivity towards foreign species. The same holds also at graphene edges which are normally saturated by hydrogen atoms. Anyway a significant reactivity is also found close to reconstructed vacancies and Stone-Wales defects without dangling bonds. This is due to the modification of the local density of π-electrons that may lead to a higher local reactivity.

Electronic configuration The electronic properties of graphene are determined by the π and π^* bands, generated by the side overlap of the p_z-orbitals. These bands are likely perturbed by the presence of defects. Consider for instance the adsorption of a foreign atom on the carbon lattice that normally induces a local rehybridization of the carbon orbitals from sp^2 to sp^3: in this way a p_z orbital is subtracted from the π-network associated to the two π bands. Also the removal of a carbon atom upon a vacancy formation removes a p_z orbital and has a similar effect on the π bands. Finally the generation of non-hexagonal rings causes a local curvature around defects that may end up in a corresponding orbital rehybridization.
The main effect of such defects is the removal of the equivalence between the A and B sublattices of the graphene sheet, resulting in the so called sublattice imbalance. In turn, this causes the opening of a band gap and the appearence of a number of electronic states within the gap, known as *midgap* states. The existence of such states, predicted by many theoretical studies[88, 89], was confirmed

in experiments[68]. Scanning tunneling microscopy experiments revelead the presence of a sharp resonance at the Fermi energy around each single defects, which was attributed to these midgap states. In general these states show a nonzero amplitude only on the nondefective sublattice, they decay like $\sim 1/r$ as the distance from the defect increases and they show an overall three-fold symmetry.
The presence of defects is also associated with the idea of doping, that modifies the π system and can be pursued in two alternative ways. The first is traditionally based on the addition of foreign atoms which may act as donors or acceptors of electron density and thus give n-doped or p-doped graphene. Here the relative position of the homo and lumo orbitals of the adsorbed species with respect to the π and π^* bands of graphene determines wheter the charge transfer occurs from the adatom to the graphene surface or viceversa. The second way is known as self-doping where intrinsic defects modify the band structure locally. Self-doping arises from the slight electron-hole asimmetry at the Dirac points in perfect graphene, that shifts the Fermi energy of point defects and leads to a transfer of charge from or to the clean regions.

Magnetic configuration The electronic structure of defective graphene is closely related to its magnetic behaviour[114]. In fact, each point defect usually carries a local magnetic moment due to the presence of unpaired electrons. In the case of adatoms, the adsorption process involves one p_z orbital and thus removes one π electron from the π lattice. As a consequence a π unpaired electron is left and a magnetic moment of $\sim 1\,\mu_B$ is generated. Similarly the formation of a carbon vacancy leaves in principle four unpaired electrons, three in the σ and one in the π network. Anyway, upon the reconstruction of the lattice only two unpaired electrons remain and in principle the local magnetic moment is expected to vary between $0 - 2\,\mu_B$ depending on the coupling of the two spins. Of course, the local magnetic moments of adatoms and vacancies vanish if the unpaired electrons are removed from the system, for instance by forming chemical bonds. Moreover the orientation of the π local magnetic moments is different for the two sublattices; this means that the total magnetisation, namely the sum of local magnetic contributions, depends on the distribution of defects between the two sublattices. In the limit of an equal number of defects in the A and B sublattice, the total magnetisation is expected to be zero. In general, ideal graphene is known to be diamagnetic, while a paramagnetic behaviour arises with the introduction of magnetic defects, like vacancies and adatoms; in recent experiments[75] no ferromagnetism has been found down to 2 K in graphene samples obtained by sonic expholiation, thus excluding possible contaminants from the preparation step. This is a significant improvement as in early experiments, additional magnetic moments and ferromagnetic ordering have been measured possibly due to residual impurities left upon the preparation of the graphene sample[100].
From a theoretical perspective the number of midgap states and the spin configuration of a defective graphene sample can be predicted. Actually this is true for a generic system under some fundamental assumptions: (i) it is a perfect bipartite system, thus it consists of two sublattices A and B, with nonzero hopping only between A and B sites; as a consequence, (ii) it may be properly

described within the tight binding approximation by including only the nearest-neighbours interactions, namely with $t \neq 0$ and $t^{'} \sim 0$ in eq.1.23. In this way (iii) the electron-hole symmetry is retained. Graphene fulfills all these requirements as (i) it is composed by two equivalent sublattices A and B and (ii) each carbon atom in the lattice can be represented by just one localized function. This is the singly-occupied p_z orbital, left upon the generation of the sp^2 orbitals that form the σ network in the plane. Note that the σ contribution can be safely neglected as almost irrelevant for the band structure close to the Fermi energy. Finally, (iii) as t' is at least one order of magnitude smaller than t, the next nearest-neighbours term can be reasonably discarded. Within these assumptions, it has been demonstrated that perfect bipartite systems support a number of zero-energy *midgap* states which is greater or equal to the sublattice imbalance $|n_A - n_B|$, where n_A,n_B are the number of sites in the two sublattices[41]. Both theory and experiments proved that midgap states decay like $\sim r^{-1}$ (while other defective states behave as truly localized wavefunctions and decay exponentially) and form quasi-localized π moments which may couple either ferromagnetically or antiferromagnetically. In order to find the nature of the coupling, one refers to the Hubbard model defined by the hamiltonian

$$\mathcal{H} = -t \sum_{\langle i,j \rangle \sigma} \left(\hat{c}^{\dagger}_{i\sigma} \hat{c}_{j\sigma} + h.c. \right) + \sum_i U_i n^{\dagger}_{i\uparrow} n_{i\downarrow} \tag{1.31}$$

where the first term comes from the tight binding hamiltonian, while the second accounts for the on-site interactions: U_i is indeed the on-site energy for the i-th site in the lattice and $n_{i\sigma} = \hat{c}^{\dagger}_{i\sigma} \hat{c}_{i\sigma}$ is a number operator. Under the same assumptions as before, namely perfect electron-hole symmetry and local interactions only, at charge neutrality (half-filling), the spin state of the system exactly matches the sublattice imbalance[64], $S = |n_A - n_B|/2$. This means that the coupling depends on the relative position of defects, thus it is ferromagnetic for defects in the same sublattice and antiferromagnetic otherwise.

1.2.4 Graphene on substrates

In practical applications, free-standing graphene is rarely used as most of synthetic routes lead to supported graphene. Interestingly the presence of a substrate may control the electronic properties of graphene, for instance by means of doping that shifts the Fermi energy and/or by inducing a local change in the lattice that may open a band gap. For graphene on pure metals, the interaction may be strong or weak[11], depending on the relative position of the center of the metal d-band and the Fermi level in free-standing graphene. If the difference is lower than 2 eV, the interaction is expected to be strong, otherwise weak. The weak interaction implies: (i) a distance between graphene and the substrate close to 3.3 Å, i.e. similar to the interlayer distance in graphite which is 3.36 Å; (ii) an almost undisturbed π-band, with no band gap opening. Note that a shift in the Fermi level above or below the Dirac point is possibly observed, deriving from some n- or p-type doping. This shift may be as much as 0.5 eV and it is a consequence of differences between the metal

and the graphene work functions. Therefore, it comes from a charge transfer process and it does not account for any hybridization or chemical bonding. On the other hand, the strong interaction gives rise to: (i) a single rotational domain; (ii) a strong alteration of the graphene π band, with a shift to higher binding energy of 1-3 eV and the opening of a band gap; (iii) a shortest carbon-metal distance close to 2.1-2.2 Å, as found for lattice matched systems, thus graphene on Ni or Co, with the graphene sheet almost flat on the substrate; (iv) a large corrugation of the graphene sheet, if a moiré pattern is formed. The corrugation arises from the mismatch between the metal and the graphene lattice. Indeed the carbon atoms are forced to occupy different sites over the metal surface, namely top, hollow or bridge sites, and thus interact differently with the substrate. As a consequence, the distance from the substrate can vary between 2.1 and 3.6-3.8 Å and in the XPS spectra the splitting of the C-1s signal can be observed, arising from the different enviroment felt by the carbon atoms. Graphene grown on a SiC crystal behaves differently depending on the face of the substrate. On the Si-terminated face, graphene strongly interacts and it forms covalent bonds with the Si atoms. In this way the carbon orbitals rehybridize, a large band gap opens and the typical π-band structure of graphene is lost; moreover a charge transfer from the surface occurs. This perturbed layer of graphene is known as *buffer* layer; anyway on this sheet one may add a further graphene layer that will be n-doped, but with no band gap. On the contrary, graphene makes only weak interactions with the C-terminated surface, thus remaining almost unaffected by the presence of the substrate. A similar dual behaviour is also observed for SiO_2 or BN crystals [4].

Chapter 2

Theoretical methods

This chapter will report on two theoretical approaches to the fundamental problem in quantum chemistry of how to describe in an accurate way an isolated atomic or molecular system. Such approaches, namely the *wavefunction* methods[9, 95, 98, 103] and the *density functional theory*[81] will be presented in sec.2.1 and sec.2.2 .

There is a variety of methods belonging to the first class and they mostly differ in the way chosen to approximate the exact wavefunction of a given system, in the attempt to get as close as possible to the exact solution of the Schrödinger equation. In the Hartree-Fock (HF) method, the approximated wavefunction is an antisymmetrized product of spin orbitals, namely a Slater determinant, that reflects the simple picture of electrons placed in orbitals according to the Pauli principle. The Hartree-Fock wavefunction is the starting point to construct more flexible models, based on different kinds of spin orbitals as well as on a larger number of configurations (determinants), which are expected to closely mirrors the exact wavefunction. Upon a general introduction, we will show the HF approximation, pointing out its limits when dealing with open-shell systems along with the issue of electronic correlation; after that we will present an overview of some representative theoretical methods, some of them directly used in this thesis.

The peculiar aspect of the density functional theory is that the wavefunction is replaced by the electron density and, as a consequence, the total energy turns out to be a functional of the electron density instead of the wavefunction. The theoretical foundation of this choice relies on the Hohemberg-Kohn theorems, that will be demonstrated upon a general introduction on density matrices and their correpondence to wavefunctions. Although in principle exact this theory bases on an universal functional that is unknown, thus making it necessary the Kohn-Sham scheme to find a way to the solution of the eletronic structure problem. In the end, we will present some approximated functional forms and some important theoretical tools that are responsible of the success as well as the versatility of DFT.

2.1 Wavefunction methods

In the Born-Oppenheimer nonrelativistic approximation, the motion of the nuclei along the potential energy surface is obtained by solving the electronic problem, fully described by the time-independent Schrödinger equation

$$\hat{\mathcal{H}}\Psi = \mathcal{E}\Psi. \tag{2.1}$$

The many-body wavefunction $\Psi = \Psi(\mathbf{x}_1, ...\mathbf{x}_N)$ depends on the coordinates of the N electrons in the system, with $\mathbf{x}_i$ giving both the position and spin of the i-th electron; $\mathcal{E}$ is the electronic energy associated to the hamiltonian operator

$$\hat{\mathcal{H}} = \sum_{i=1}^{N_{el}} -\frac{1}{2}\nabla_i^2 + \frac{1}{2}\sum_{i,j}^{N_{el}} \frac{1}{|\mathbf{r}_{ij}|} - \sum_{\alpha}^{N_{at}}\sum_{i}^{N_{el}} \frac{Z_\alpha}{|\mathbf{r}_i - \mathbf{R}_\alpha|} = \hat{T} + \hat{V}_{ee} + \hat{V}_{ext} \tag{2.2}$$

that accounts for the kinetic energy of the electrons, the electron-electron repulsion and the electron-nucleus attraction, represented by the the three operators in eq.2.2 $\hat{T}$, $\hat{V}_{ee}$ and $\hat{V}_{ext}$ respectively. As it is an eigenvalue equation, the solution eq.2.1 gives eigenvalues and eigenstates. Anyway, it is a matter of fact that the exact solution of the Schrodinger equation is not available except for the simplest cases, thereby one generally has to deal with approximate results. In principle, for the given operator $\mathcal{H}$ there are infinite exact solutions of this equation, namely

$$\mathcal{H}\Phi_\alpha = \mathcal{E}_\alpha\Phi_\alpha \tag{2.3}$$

with $\alpha = 0, 1, ...$ and $\mathcal{E}_0 \leq \mathcal{E}_1 \leq \mathcal{E}_2...$ Since $\mathcal{H}$ is hermitian, the eigenvalues are real and the eigenvectors are orthonormal; moreover in the assumption that the eigenstates form a complete set, any trial function Ψ can be represented by a linear combination of $\{\Phi_\alpha\}$, thus $\Psi = \sum_\alpha c_\alpha\Phi_\alpha$ and the energy reads as

$$E[\Psi] = \frac{\langle\Psi| H |\Psi\rangle}{\langle\Psi|\Psi\rangle} = \frac{\sum_\alpha |c_\alpha|^2 \mathcal{E}_\alpha}{\sum_\alpha |c_\alpha|^2} \tag{2.4}$$

where the energy is a functional of the wavefunction. Following from the fact that $\mathcal{E}_0 \leq \mathcal{E}_1 \leq \mathcal{E}_2...$, the variation principle states that the energy of any state $\tilde{\Psi}$ is always an upper bound to the exact ground state energy and it reaches the minimum if and only if $\Psi = c_0\Phi_0$.
In general, every eigenstate of the hamiltonian is an extremum of the functional $E[\Psi]$, thus the Schrödinger equation may be replaced by a minimization of the energy functional with respect to the allowed N-electron wavefunctions under the orthonormality constraint $\langle\Psi|\Psi\rangle = 1$, that is

$$\frac{\partial E[\Psi]}{\partial\Psi} = \frac{\partial}{\partial\Psi}\left[\langle\Psi|H|\Psi\rangle - E\langle\Psi|\Psi\rangle\right] = 0 \tag{2.5}$$

In practice, one chooses an approximate wavefunction, that depends on certain parameters and starts varying these parameters until the expectation value reaches the minimum; this is a variational estimate of the exact ground state energy, namely $E_0 \geq \mathcal{E}_0$ and it is reasonable to expect that

this result depends on the kind of wavefunction, Ψ_0. This means that eq.2.5 returns for a chosen wavefunction the best result achievable for that level of approximation, i.e. for that level of theory.

2.1.1 The Hartree-Fock approximation

The Hartree-Fock many-body wavefunction Ψ^{HF} is described as a Slater determinant, that is the antisymmetrized product of spin orbitals φ_i,

$$\Psi^{HF}(\mathbf{x}_1,\, \mathbf{x}_2, ...\mathbf{x}_N) = \frac{1}{\sqrt{N!}} \begin{vmatrix} \varphi_1(\mathbf{x}_1) & \varphi_2(\mathbf{x}_1) & \dots & \varphi_N(\mathbf{x}_1) \\ \varphi_1(\mathbf{x}_2) & \ddots & & \\ \vdots & & \ddots & \\ \varphi_1(\mathbf{x}_N) & & & \varphi_N(\mathbf{x}_N) \end{vmatrix} \tag{2.6}$$

By applying the hamiltonian operator to this function one obtains the energy $E^{HF} = \left\langle \Psi^{HF} \middle| \mathcal{H} \middle| \Psi^{HF} \right\rangle$ that is a functional of the spin orbitals and reads as

$$E^{HF}[\varphi_i] = \left\langle \Psi^{HF} \middle| \hat{O}_1 + \hat{O}_2 \middle| \Psi^{HF} \right\rangle = \sum_i^N \langle i\,|h|\,i\rangle + \frac{1}{2}\sum_{i,j}^N \langle ij \mid ij\rangle - \langle ij \mid ji\rangle \tag{2.7}$$

where $\hat{O}_1$ accounts for the one-particle terms, namely the kinetic energy of the electron and the attractive interaction with the nuclei,

$$h = -\frac{1}{2}\nabla_i^2 + \sum_\alpha^{N_{at}} \frac{Z_\alpha}{\mathbf{r}_i - \mathbf{R}_\alpha} \tag{2.8}$$

and the operator $\hat{O}_2$ accounts for the two-body terms, that is the electron-electron interaction in terms of Hartree (or Coulomb) energy and exchange energy. Note that the short notation in eq.2.7 corresponds to

$$\langle ij \mid ij\rangle = \int d\mathbf{x} d\mathbf{x}' \varphi_i^*(\mathbf{x}) \varphi_j^*\left(\mathbf{x}'\right) \frac{1}{\mathbf{r} - \mathbf{r}'} \varphi_i(\mathbf{x}) \varphi_j\left(\mathbf{x}'\right) \tag{2.9}$$

and in the same way for $\langle ij \mid ji\rangle$. The ground state energy is found by carrying out a minimization of the energy functional with respect to the spin orbitals, provided they remain orthonormal. In this way, this becomes a constrained minimum search and it reads as

$$\frac{\partial}{\partial \varphi_i^*(\mathbf{x})} \left\{ E^{HF}[\varphi_i] - \sum_{ij} \lambda_{ij} \left[\int d\mathbf{x} \varphi_i^*(\mathbf{x}) \varphi_j(\mathbf{x}) - \delta_{ij} \right] \right\} = 0 \tag{2.10}$$

and finally leads to

$$f\varphi_i(\mathbf{x}) = \sum_j \lambda_{ij} \varphi_j(\mathbf{x})\,. \tag{2.11}$$

where λ_{ij} are the Lagrange multipliers associated to the orthonormality constraint and the one-

particle Fock operator f [1] has been introduced. In general a unitary transformation of spin orbitals in a single determinant wavefunction does not change the wavefunction, that may at most differ from the original determinant by a phase factor; in the same way, as any observable property depends on $|\Psi|^2$, any expectation value is expected to be invariant under an arbitrary unitary transformation of the spin orbitals. This means that the nature of the basis set, e.g. localized or delocalized, does to not affect the features of the system under investigation. In this case a unitary transformation is used to transform the spin orbitals φ_i, into another set of orbitals $\tilde{\varphi}_i$ while leaving the wavefuction unchanged, in such a way to diagonalize the matrix of the Lagrange multipliers λ_{ij} and end up with the canonical form of the eigenvalue equations

$$f\tilde{\varphi}_i(\mathbf{x}) = \varepsilon_i^{HF}\tilde{\varphi}_i(\mathbf{x}) \tag{2.12}$$

where the eigenvalue ε_i^{HF} gives the energy of the i-th orbital. The Koopman's theorem states that $-\varepsilon_i^{HF}$ corresponds to the energy needed to remove one electron from the spin-orbital $\tilde{\varphi}_i$, namely the ionization potential[2].

The solution of the Hartree-Fock equations in eq.2.12 is absolutely not an easy task, as it requires computing the real eigenvalues ε_i^{HF} and the spin orbitals φ_i that depend on both the spatial coordinates and spin. Anyway, in principle one may introduce a set of known N_{basis} spatial basis functions $\{\chi_\mu\}$, that typically are not orthogonal, and represent each spin orbital φ_i as a linear combination of these functions,

$$\varphi_i = \sum_{\mu=1}^{N_{basis}} C_{\mu i}\chi_\mu \tag{2.13}$$

In this way the problem of calculating the Hartree-Fock molecular orbitals reduces to the problem of finding the set of expansion coefficients of each orbital in the chosen basis set; this means that

[1] The one-particle Fock operator for the electron 1 in the field generated by N electrons reads as

$$f(1) = -\frac{1}{2}\nabla_{\mathbf{r}_1}^2 + \sum_a \frac{1}{|\mathbf{r}_1 - \mathbf{R}_a|} + \sum_j^N \int \varphi_j^*(\mathbf{r}_2)\varphi_j(\mathbf{r}_2)\,d\mathbf{r}_2 - \sum_j \int \varphi_j^*(\mathbf{r}_2)\varphi_i(\mathbf{r}_2)\,d\mathbf{r}_2$$

[2] To prove the Koopman theorem one has to write the ground state HF energy E_0^{HF} for a system with N electrons as,

$$E_0^{HF} = \frac{1}{2}\sum_{i=1}^{N}\left(\varepsilon_i^{HF} + t_i\right)$$

where $t_i = \langle i\,|h|\,i\rangle$. The energy difference between the original N electron system and the one with *N-1* electrons, obtained upon removing the m-th electron from its spin-orbital is

$$E_{0,N}^{HF} - E_{0,N-1}^{HF} = t_m + \sum_{l=1}^{N}\langle ml \mid ml\rangle - \langle ml \mid lm\rangle = \varepsilon_m^{HF}$$

When m is the highest occupied orbital, $IP = -\varepsilon_{homo}^{HF}$. Analougously by putting one electron in to the lowest unoccupied orbital, one may compute the electronic affinity (EA),

$$EA = E_{0,N}^{HF} - E_{0,N+1}^{HF} = -\varepsilon_{lumo}^{HF}$$

Note that in both cases the orbital relaxation is not taken into account, since expected to be small when one electron is added or removed from a sufficiently large N electrons system. Hence, the *quasi-particle* gap is equal to the *homo-lumo* gap, i.e. $IP - EA = \varepsilon_{lumo}^{HF} - \varepsilon_{homo}^{HF}$.

the Hartree-Fock energy is now minimized with respect to these coefficients. For the i-th orbital, the eq.2.12 can be rewritten as

$$\sum_{\mu}^{N_{basis}} F_{\nu\mu}^{HF} C_{\mu i} = \varepsilon_i^{HF} \sum_{\mu}^{N_{basis}} S_{\nu\mu} C_{\mu i} \tag{2.14}$$

where $H_{\nu\mu}^{HF}$ and $S_{\nu\mu}$ give respectively the matrix element and the overlap integral between two basis functions μ, ν; more compactly a single matrix equation may also be written

$$\mathbf{HC} = \mathbf{SC}\varepsilon. \tag{2.15}$$

The essence of the Hartree-Fock approximation is that the i-th electron feels a potential due to the presence of the other electrons in an average way; this means that the potential experienced by the i-th electrons depends on the other spin orbitals, thus the potential term in the Fock operator depends on its eigenfunctions. As a consequence, the Hartree-Fock equation in eq.2.12 or equivalently in eq.2.14 is not linear and must be solved iteratively. This iterative procedure starts from a initial guess (for either the spin orbitals or the coefficients of the basis expansion) and goes on with further refinements up to converge on a certain result: this is the self-consistent field (SCF) method.

2.1.1.1 Open shell molecules

When dealing with closed-shell molecules, it is natural to include pairs of spin orbitals, $\varphi_i^{\alpha} = \phi_i^{\alpha}(\mathbf{r})\,\sigma(\alpha)$ and $\varphi_i^{\beta} = \phi_i^{\beta}(\mathbf{r})\,\sigma(\beta)$, that are degenerate in their spatial part, namely $\phi_i^{\alpha}(\mathbf{r}) = \phi_i^{\beta}(\mathbf{r})$. This choice is motivated by the fact that in the ground state the N electrons are coupled in the N/2 α and β lowest energy orbitals and there is no reason why they should differ in their spatial functions. The situation changes in the case of open-shell systems, that is in the presence of unpaired electrons. In the first attempt to generate the ground state wavefunction of an open-shell molecule, a Slater determinant may be set up that contains the appropriate number of singly occupied molecular orbitals in addition to the doubly occupied ones. This type of wavefunction belongs to the *restricted* open-shell HF (ROHF) formalism, that enforces spatial parts of doubly occupied spin orbitals to be identical irrespective for the electron spin. Although conceptually simple, the ROHF wavefunction does not correctly describe the physics of the system as it assumes that α and β electrons respond identically in the presence of unpaired (α or β) electrons, thus excluding any spin-polarization effect. This neglect has several undesirable consequences: of course, correct spin densities are all but unaccessible; moreover the wavefunctions are often unstable towards the symmetry breaking. In a relaxation process, this means that slightly distorted structures surprinsingly turn out to be more stable than the symmetric ones, due to the presence of fake singularities on the potential energy surface at the high symmetry points; of course, one has to be aware that under certain conditions, the lowering of the molecular symmetry is a real effect, enforced by the Jahn-Teller theorem (see for more details Appendix A). The above considerations suggest that a more reliable description

of the system should rely on a more flexible wavefunction. In the *unrestricted* HF formalism, this is attained by allowing the pairs of α and β spin orbitals to differ in their spatial functions, namely $\phi_i^{\alpha}(\mathbf{r}) \neq \phi_i^{\beta}(\mathbf{r})$. In this way, the ground state wavefunction succeeds in reproducing the spin polarization experimentally seen but at the cost of loosing its spin purity, indeed it is still eigenfunction of the operator S_z but not of S^2. More precisely, the expectation value of $\langle S^2 \rangle$ for a UHF wavefunction is always greater than the eigenvalue of the corresponding ROHF wavefunction, due to the contamination of the higher spin states, that eventually may lead to unphysical results.

2.1.1.2 Correlation energy

It is known that the Hartree-Fock approximation, while remarkably successful in many cases, has also some limitations. For instance the dissociation of molecules into open-shell fragments cannot be described by restricted HF method and gives only qualitatively correct but not accurate results with the unrestricted procedure. The origin of such a problem lies in the basic assumption of the Hartree-Fock theory, namely that in a given system each electron moves independently from the others in the static electric field generated by the nuclei and all the other electrons. In reality the electronic motion is strongly influenced by the electron-electron repulsion, as suggested by the fact that the probability of finding two electrons at certain positions $\mathbf{r}_1$ and $\mathbf{r}_2$ tends to zero as the two positions tend to coincide. This observation is consistent with the idea of a hole around each electron that prevents another electron from occupying the same position at the same time: the so called Fermi hole correlates the motion of electrons with parallel spins, while the Coulomb hole is active in the case of electrons with antiparallel spins. Since it is a Slater determinant, by construction the HF wavefuction satisfies the Pauli exclusion principle and thus includes the electronic correlation due to the Fermi hole; on the other hand, it does not account for the correlation of the motion of electrons with opposite spins. In general the correlation energy is quantified as the difference between the exact nonrelativistic energy and Hartree-Fock energy in the limit of a complete basis set, namely $E_{corr} = \mathscr{E}_0 - E_0^{HF}$.

2.1.2 Post-SCF methods

Following from the fact that the Hartree-Fock theory cannot properly account for the electronic correlation, a number of theoretical methods, the so called post-SCF methods, has been developed in the attempt to overcome this limit and recover as much as possible of the correlation energy of a given system. In general the way to improve the HF results passes through the use of a more flexible wavefunction, that is usually derived from the single determinant HF wavefunction. There are two main aspects on which one may operate to increase the flexibility of the wavefunction, namely the number of functions in the basis set and the number of determinants in the wavefunction itself. In the first case, by enlarging the basis set, the quality as well as the total number of the available molecular orbitals increases; this means that for a reasonably sized basis set, a large part of the available molecular orbitals, except for those at lowest energy, will not be occupied in the

ground state HF determinant. Anyway, these virtual orbitals come into play when dealing with the second approach to improve the description of the wavefunction. In this case indeed, the new Slater determinants correspond to excited configurations and represent alternative ways of distributing the electrons among the available molecular orbitals. By mixing the excited configurations Ψ_L and the ground state one $\Psi_0 = \Psi_0^{HF}$, one gets a more flexible and therefore an improved wavefunction $\Psi_{0'}$ with some degree of electron correlation:

$$\Psi_{0'} = \Psi_0 + \sum_L C_L \Psi_L \tag{2.16}$$

If the weighting coefficients C_L of the excited configurations Ψ_L are variationally optimized, $\Psi_{0'}$ is the configuration interaction (CI) wavefunction. In the limit of a complete basis set, if all the possible excited configurations formed with the molecular orbitals are included in the wavefunction, then the procedure is known as *full* CI. Note that given a N-electron system and an arbitrary set of 2K one-electron spin orbitals one can construct $\binom{2K}{N}$ different N-electron Slater determinants.
In general, theoretical methods may be classified depending on: (i) the level of excitations admitted in the calculations, namely on the number of electrons transferred into originally empty orbitals; (ii) the way to compute both the coefficients C_L and the energy of $\Psi_{0'}$, where common alternatives are the variational scheme just introduced for the CI method and the many-body perturbation theory that will be shortly presented in sec.2.1.2.3; (iii) the nature of the reference wavefunction Ψ_0, namely wheter it corresponds to the Hartree-Fock determinant or not.

2.1.2.1 Configuration interaction (CI)

The level of excitations in the configurations Ψ_L constructed from Ψ_0, depend on how many electrons are promoted to virtual orbitals. If only one electron at a time is excited, one speaks of *single excitations* or more simply of *singles*. However, as stated by the Brillouin's theorem this type of configurations may not mix with variationally optimized Ψ_0 wavefunctions in closed-shell molecules and only special types of singly excited Ψ_L can mix with Ψ_0 in open-shell molecules. In case of two electrons being promoted, double excitations are obtained. Unlike singles, *doubles* may directly mix with the ground state determinant through the two-body Coulomb operator, $1/r_{12}$ in a.u. where r_{12} is the distance between the two electrons. In a similar way the process continues, for instance upon the excitation of three and four electrons, *triples* and *quadruples* are generated. Once the excited configurations have been selected, two main quantities need to be evaluated: the electron repulsion integrals $\langle \Psi_0 | V | \Psi_L \rangle$, where V is $1/r_{12}$; and the energy difference $E_L - E_0$ between the excited state Ψ_L and the ground state Ψ_0. After that, once known the values of the integrals and energy differences, the energy of the correlated wavefunction $\Psi_{0'}$ and the coefficients C_L can be calculated.
As noted before, a full CI calculation produces: a correlated wavefunction which includes all the possible excited configuration for a given set of molecular orbitals; for each determinant the corresponding coefficient C_L, obtained upon minimization of the expectation value of the energy of the

correlated wavefuction as a function of C_L. As the number of possible configurations raises quickly with the number of available molecular orbitals, full CI is often not practicable and *truncated* CI is preferred. In this approach excited configurations are built including excitations up to singles, doubles, etc. (namely CISD, CID...). While computationally more feasible with respect to full CI, truncated CI does not recover all correlation energy and it is not size consistent. Note that a computational method is size consistent if the energy of a system of non-interacting molecules is equal to the sum of the energies of each fragment computed separately. Due to the limit over the possible excitations, this is not the case of truncated CI.

2.1.2.2 Complete active space SCF

Wavefuctions like that shown in eq.2.16 are known as multiconfigurational wavefunctions and turn out to be not just useful but absolutely required in calculations on systems with more than one unpaired electron (e.g. diradicals). In general the full CI scheme has been proved to give accurate results, irrespective on the starting molecular orbitals, namely ROHF or UHF, but unfortunately this requires a high computational cost. This means that full CI calculations may be realistically carried out only on systems with very few electrons, thus motivating the development of other theoretical models good for reproduce some of the benefits in full CI without paying the entire cost. This is the case of the complete active space SCF (CASSCF) procedure, in which a sort of full CI wavefunction is generated by accounting for the electronic excitations in and out a (small) number of orbitals in the so-called *active space*. In this way the CASSCF wavefunction turns out to be a linear combination of Slater determinants generated on the basis of the partition of the molecular orbitals into *active*, *inactive* and *external* orbitals. As they are unoccupied, the external orbitals are not present in any of the determinants; on the contrary, the inactive orbitals are always occupied and constitute the 'stable' part shared by all the determinants; finally the remaining electrons in each determinant are placed in active orbitals according to the *full* list of configurations belonging to the active space in a chosen spin and spatial symmetry. The number of electrons and orbitals in the active space determines the number of configurations, namely of Slater determinants, in the CASSCF wavefunction that is conventionally referred as CAS(n,m), where n are the electrons and m the orbitals in the active space[3]. The CI procedure produces variationally optimized weighting coefficients C_L for all the configurations included in CASSCF wavefunction; moreover, differently from standard CI models, also the coefficients of the basis functions of *all* the molecular orbitals are simultaneously optimized. A converged CASSCF calculation thus yields a set of coefficients C_L indicating the contribution of each determinant in the total wavefunction,

[3] The number of configurations depends on the number of n active orbitals and N active electrons and on the total spin S of the function. Accordingly it follows,

$$N_{CAS} = \frac{2S+1}{n+1} \begin{pmatrix} n+1 \\ N/2-S \end{pmatrix} \begin{pmatrix} n+1 \\ N/2+S+1 \end{pmatrix}$$

from which it appears that the number of configurations strongly increases along with the size n of the active space. Therefore, the number of active orbitals is reasonably limited to 10-12 in order to generate computationally manageable wavefunctions.

and a set of coefficients $C_{\mu i}$, where the index μ indicates the basis function and i the molecular orbital. The optimization of the coefficients $C_{\mu i}$ in all the molecular orbitals ensures that the final wavefunction gives the lowest CI energy within that particular active space. The CASSCF method has a number of desirable features. First, it introduces correlation among the electrons in the active space, generating wavefunctions which are eigenfunctions of $\hat{S}^2$. Second, analytical derivatives have been formulated, thus this method may be used for geometry optimizations, location of transition states and vibrational analysis. Third, the CAS wavefunctions are excellent starting points for CI or MBPT calculations that include all occupied and virtual molecular orbitals. This allows to recover the dynamic electron correlation energy which is usually associated to the motion of electrons outside the active space. Finally, CASSCF allows to model systems which may not be described, even to a first approximation, by a single configuration as many excited states and singlet diradicals. Anyway CASSCF calculations present also some disadvantages. First of all, CASSCF can not be considered as a standard method as there is no universal recipe which tells how to build the active space. Indeed in many cases the choice is done with a certain degree of arbitrariness and needs to be guided by good intuition and experience. In geometry optimizations as well as in the comparison of different systems, the choice of a consistent active space may be fundamental. Moreover in CASSCF calculations the simultaneous optimization of the basis set coefficients $C_{\mu i}$ and that of C_L, may cause the shapes of the molecular orbitals to strongly depend on the choice of the active space and to greatly differ among different electronic states (configurations) of a molecule. This means a loss of transparency with respect to standard CI calculations where all the excited configurations are described in terms of the same set of molecular orbitals. Finally in a CASSCF study, only the electrons in the active space are correlated while the dynamic correlation energy for the remaining electrons is not recovered.

2.1.2.3 Many-body perturbation theory (MBPT)

The basic concept behind the MBPT is to model the effects of the correlation energy by treating them as a perturbation to the zero-order reference wavefuction Ψ_0. To this end, the correlated wavefunction $\Psi_{0'}$ is expanded as $\Psi_{0'} = \Psi_0 + \Psi^{(1)} + \Psi^{(2)} + ...$ and the total energy is $E = E_0 + E^{(1)} + E^{(2)} + ...$, where the apices indicate the order of the perturbation. For all the $\Psi^{(m)}$ orthogonal to Ψ_0 (namely $\left\langle \Psi_0 \mid \Psi^{(m)} \right\rangle = 0$), it can be shown that

$$E^{(1)} = \langle \Psi_0 | \, V \, | \Psi_0 \rangle \qquad E^{(2)} = \langle \Psi_0 | \, V \left| \Psi^{(1)} \right\rangle \qquad E^{(3)} = \langle \Psi_0 | \, V \left| \Psi^{(2)} \right\rangle ... \tag{2.17}$$

where V is again the electron repulsion operator, $1/r_{12}$. If the perturbation theory works well the correction to the energy is expected to decrease as the perturbation order increases, thus $E^{(1)} \gg E^{(2)} \gg E^{(3)}...$ Accordingly, a second order correction is usually sufficient to get good results. Similarly to the CI procedure, each perturbed wavefunction $\Psi^{(m)}$ is composed by excited configurations Ψ_L formed from the molecular orbitals (occupied and virtual) of the unperturbed reference wavefunction Ψ_0. By contrast, the weighting coefficients C_L are here determined within

the perturbation theory and not variationally. For instance, when $\Psi^{(m)} = \Psi^{(1)} = \sum_L C_L \Psi_L$, the coefficients C_L are defined as

$$C_L = \frac{\langle \Psi_0 | V | \Psi_L \rangle}{E_L - E_0}. \tag{2.18}$$

Therefore C_L is directly proportional to the interaction energy between Ψ_0 and Ψ_L expressed by the off-diagonal matrix element, and inversely proportional to the energy difference between these two electronic states. The contribution of $E^{(1)}$ to the total energy is ignored as it is already included in the energy of Ψ_0, which is the Hartree-Fock energy. Thus the first correction to the Hartree-Fock energy occurs in the second order perturbation theory. This is defined as

$$E^{(2)} = \sum_L \frac{|\langle \Psi_0 | V | \Psi_L \rangle|^2}{E_0 - E_L} \tag{2.19}$$

and it is always negative, as $E_0 - E_L < 0$. In order to calculate $E^{(2)}$ and $\Psi^{(1)}$, the repulsion integrals need to be computed. In a CISD calculation, the same matrix elements need to be evaluated but they must be stored to set up the CI matrix; in the so-called direct CI there is no storage but such elements must be recomputed whenever they are needed. By contrast in computing $E^{(2)}$, once $\langle \Psi_0 | V | \Psi_L \rangle$ has been processed (computed, squared, divided by the energy difference and added to the sum), it is discarded. Conceptually, higher order corrections are included in a similar way. Obviously, methods based on the perturbation theory are computationally less demanding than similar levels of variational CI; they are also size consistent by virtue of to the so-called linked diagram theorem. Note anyway that MBPT methods implicity assume that electron correlation may be regarded as a small perturbation to the average field model on which HF-SCF theory is based. For this approach to work, the unperturbed wavefunction needs to be a reasonable zero-order approximation, otherwise a variational CI treatment is preferred. The perturbation theory is thus expected to fail if the reference state is a highly spin-contaminated or a symmetry-broken wavefunction; moreover it cannot deal with systems, like singlet diradicals, which may not be adequately described by single-configuration models.

2.1.2.4 Multi-reference perturbation theory

As noted before, MBPT works well if the reference HF-SCF wavefunction is a good zero-order approximation. Poor results are thus expected for open-shell systems, due to the problematic ROHF and UHF wavefunctions, and in general for all the systems which cannot be well characterized by a single-determinantal description. For such kind of systems the use of multiconfigurational reference wavefunctions represents a significant improvement as it allows to overcome many of these problems. The second order perturbation treatment applied to CASSCF wavefunctions results in the CASPT2 procedure. This method has some useful features. First, CASPT2 has the advantage over CASSCF that the final result is less affected by the choice of the active space, as in CASPT2 excitations over all the virtual orbitals are included. Second, it allows to recover a large part of the correlation energy in addition to that already included in the CASSCF wavefunction; for this

reason, CASPT2 is a very successful method in dealing with excited states, as (i) they often require a multideterminantal description and (ii) the energy differences among them are usually small and thus correlation energy may become crucial in determining the correct ordering. Finally, the CASPT2 method is substantially less computationally demanding compared to CAS-CISD with the same set of configurations. Anyway, a serious problem associated to CASPT2 calculations comes from the so called *intruder states*. These are excitations outside the active space whose contributions to the CASPT2 wavefunctions are blown out of proportion due to the small energy difference $(E_0 - E_L)$ at the denominator in the expression for C_L. As a consenquence of the presence of such states, the energy evaluation becomes very inaccurate and the weight of the CASSCF determinants in the resulting CASPT2 wavefunction becomes small.

The best theoretical approach to study a molecule is mainly determined by the molecule itself. Single-reference theoretical methods, as truncated CI, CASSCF, MBPT methods..., are adequate to describe most radicals and closed-shell molecules, as their wavefunctions are well represented by single configurations. Differently, singlet diradicals and some excited states of both radicals and closed-shell molecules are associated to multideterminantal wavefunctions and are better treated by multi-reference computational methods, as MR-CI, CASPT2,...

2.2 Fundamentals of Density Functional Theory

The density functional theory (DFT) is a theoretical approach to electronic structure calculations that is becoming a standard in condensed matter and materials physics. It allows to deal with the hamiltonian of a many body system composed by N_{el} electrons and N_{at} atoms, working with the electron density $\rho(\mathbf{r})$, defined as just the three-dimensional single-particle density, instead of the $3N-$dimensional ($4N$ if spin is taken into account) wavefunction $\Psi(\mathbf{r}_1, ..\mathbf{r}_N)$. Within the density-fuctional theory a practical computation scheme is offered by the Kohn-Sham (KS) equations, which are formally similar to the Hartree-Fock (HF) equations.

2.2.1 Density matrices

In a physical system, the number of electrons per unit volume in a given state is the electron density of that state. We consider a generic quantum state $|\Psi\rangle$ of a single-particle system represented by a vector in the Hilbert space. Such state may be described by $\Psi(r)$ in coordinate space. Once chosen a complete basis set $\{|n\rangle\}$ where the orthogonality condition $\langle n \mid m\rangle = \delta_{nm}$ holds, then any state $|\Psi\rangle$ can be expressed in terms of the basis set functions $|n\rangle$

$$|\Psi\rangle = \sum_n \Psi_n |n\rangle \tag{2.20}$$

The inner product of $|\Psi\rangle$ with $\langle m|$ gives the m-th component of $|\Psi\rangle$ in the representation of the $|n\rangle$,

$$\Psi_m = \langle m \mid \Psi\rangle \tag{2.21}$$

For a continuous basis set the orthogonality condition reads as $\left\langle \mathbf{r} \mid \mathbf{r}' \right\rangle = \delta\left(\mathbf{r} - \mathbf{r}'\right)$ and the state $|\Psi\rangle$ with its components can be expressed as

$$|\Psi\rangle = \int \Psi(\mathbf{r}) |\mathbf{r}\rangle \, d\mathbf{r} \qquad \Psi(\mathbf{r}) = \langle \mathbf{r} \mid \Psi \rangle \tag{2.22}$$

where $\Psi(\mathbf{r})$ is precisely the ordinary wavefunction in coordinate space. A generic operator $\hat{A}$ trasforms the state $|\Psi\rangle$ into another state in the Hilbert space

$$\hat{A} |\Psi\rangle = \left|\hat{A}\Psi\right\rangle = \left|\Psi'\right\rangle \tag{2.23}$$

while its adjoint gives

$$\langle\Psi| \hat{A}^\dagger = \left\langle \hat{A}\Psi\right| = \left\langle \Psi'\right| \tag{2.24}$$

Finally we define the projection operator $\hat{P}_n$ on a generic state $|n\rangle$, as

$$\hat{P}_n = |n\rangle \langle n| \tag{2.25}$$

If we apply $\hat{P}_n$ on the state $|\Psi\rangle$

$$\hat{P}_n |\Psi\rangle = |n\rangle \langle n \mid \Psi\rangle = \Psi_n |n\rangle \tag{2.26}$$

It can be shown that projector operators are idempotent

$$\hat{P}_n \cdot \hat{P}_n = \hat{P}_n \tag{2.27}$$

and that they satisfies the closure relation, indeed being $\hat{I}$ the identity operator,

$$\sum_n |n\rangle \langle n| = \sum_n \hat{P}_n = \hat{I} \tag{2.28}$$

In the continuous, the closure relation reads as

$$\int |\mathbf{r}\rangle \langle \mathbf{r}| \, d\mathbf{r} = \int \hat{P}_r d\mathbf{r} = \hat{I} \tag{2.29}$$

If we consider the effect of the operator $\hat{A}$ in eq.2.23

$$\left\langle n \left|\hat{A}\right| \Psi \right\rangle = \sum_n \left\langle n \left|\hat{A}\right| n \right\rangle \langle n \mid \Psi\rangle = \sum_n \left\langle n \left|\hat{A}\right| n \right\rangle \Psi_n = \left\langle n \mid \Psi' \right\rangle \tag{2.30}$$

where $\left\langle n \left|\hat{A}\right| n \right\rangle$ is the matrix representation of $\hat{A}$ in the basis set $|n\rangle$. The same relations hold when the quantum state $|\Psi\rangle$ describes a N-particles system, i.e. $|\Psi\rangle = |\Psi_N\rangle$. In this case the nature of such particles (fermions or bosons) determines the symmetry of the quantum state $|\Psi\rangle$ (symmetric

or antisymmetric). For a pure quantum state $|\Psi\rangle$, the density operator is usually defined as:

$$\hat{\rho} = |\Psi\rangle \langle\Psi| \tag{2.31}$$

In the coordinate space this can be viewed as an element of a matrix, which is usually call the density matrix

$$\rho\left(\mathbf{r}_1^{'}, \mathbf{r}_2^{'}, ...\mathbf{r}_N^{'}, \mathbf{r}_1, \mathbf{r}_2 ... \mathbf{r}_N\right) = \Psi\left(\mathbf{r}_1^{'}, \mathbf{r}_2^{'}, ...\mathbf{r}_N^{'}\right) \Psi^*\left(\mathbf{r}_1, \mathbf{r}_2 ... \mathbf{r}_N\right) \tag{2.32}$$

Note that while $|\Psi\rangle$ is defined only up to an arbitrary phase factor, $\hat{\rho}$ is unique for a given state:

$$\hat{\rho} = e^{i\phi} |\Psi\rangle \langle\Psi| e^{-i\phi} = |\Psi\rangle \langle\Psi| \tag{2.33}$$

According to the definition in eq.2.25, $\hat{\rho}$ is a projection operator on the subspace $S \subseteq \mathcal{H}$ spanned by the state $|\Psi\rangle$ itself. Hence, $\hat{\rho}$ is idempotent and hermitian, indeed

$$\langle n \left|\hat{\rho}^2\right| n\rangle = \langle n \mid \Psi\rangle \langle\Psi \mid \Psi\rangle \langle\Psi \mid n\rangle = \langle n \mid \Psi\rangle \langle\Psi \mid n\rangle = \langle n \left|\hat{\rho}\right| n\rangle$$

$$\Rightarrow \hat{\rho}^2 = \hat{\rho}^\dagger = \hat{\rho} \tag{2.34}$$

where the state $|\Psi\rangle$ is normalized and $|n\rangle$ (e.g. $|n\rangle = |\mathbf{r}_1, ...\mathbf{r}_N\rangle$ is a basis set in which $|\Psi\rangle$ can be decomposed. Since it also satisfies the closure relation, its trace is one

$$\mathrm{Tr}\hat{\rho} = \langle n \mid \Psi\rangle \langle\Psi \mid n\rangle = \int \Psi^*\left(\mathbf{r}_1, ...\mathbf{r}_N\right) \Psi\left(\mathbf{r}_1, ...\mathbf{r}_N\right) d\mathbf{r}_1 ... d\mathbf{r}_N = 1 \tag{2.35}$$

and in the same way $\mathrm{Tr}\hat{\rho}^2 = 1$.
The expectation value for a generic operator $\hat{A}$, according to the definition for a normalized state $|\Psi\rangle$ is

$$\left\langle \hat{A} \right\rangle = \left\langle \Psi \left| \hat{A} \right| \Psi \right\rangle = \langle\Psi \mid n\rangle \left\langle n \left| \hat{A} \right| n \right\rangle \langle n \mid \Psi\rangle = \langle n \mid \Psi\rangle \langle\Psi \mid n\rangle \left\langle n \left| \hat{A} \right| n \right\rangle \tag{2.36}$$

where $\left\langle n \left| \hat{A} \right| n \right\rangle$ are the matrix elements of $\hat{A}$ in the basis $|n\rangle$ and thus

$$\left\langle \hat{A} \right\rangle = \mathrm{Tr}\left(\hat{\rho}\hat{A}\right) = \mathrm{Tr}\left(\hat{A}\hat{\rho}\right) \tag{2.37}$$

When a physical system is not a pure state, it is addressed as a mixed state and it can be characterized by a probability distribution over all the accessible pure states. Its density operator is known as *ensemble* density operator and it reads as

$$\hat{\rho} = \sum_i p_i |\Psi_i\rangle \langle\Psi_i| \tag{2.38}$$

where p_i is the probability of the system to be found in the state $|\Psi_i\rangle$ and the sum is over all the accessible pure states. The rule of probability requires that for normalized pure states

$$p_i \geq 0 \qquad \sum_i p_i = 1 \tag{2.39}$$

The trace of $\hat{\rho}$ is equal to one, indeed chosen an arbitrary complete basis $|n\rangle$,

$$\mathrm{Tr}\hat{\rho} = \sum_i \sum_n p_i \langle n \mid \Psi_i\rangle \langle \Psi_i \mid n\rangle = \sum_i \sum_n p_i \langle \Psi_i \mid n\rangle \langle n \mid \Psi_i\rangle = \sum_i p_i = 1 \tag{2.40}$$

It is also positive semidefinite in fact

$$\langle n \,|\hat{\rho}|\, n\rangle = \sum_i p_i \langle n \mid \Psi_i\rangle \langle \Psi_i \mid n\rangle = \sum_i p_i \left|\langle n \mid \Psi_i\rangle\right|^2 \geq 0 \tag{2.41}$$

Differently from the pure state, the density operator for a mixed state is not idempotent indeed

$$\hat{\rho}^2 = \sum_i p_i \,|\Psi_i\rangle \langle\Psi_i|\, \hat{\rho} = \sum_{ij} p_i p_j \,|\Psi_i\rangle \langle \Psi_i \mid \Psi_j\rangle \langle\Psi_j| =$$

$$= \sum_{ij} p_i p_j \,|\Psi_i\rangle \langle\Psi_j|\, \delta_{ij} = \sum_i p_i^2 \,|\Psi_i\rangle \langle\Psi_i| \neq \hat{\rho} \tag{2.42}$$

In the same way the trace of $\hat{\rho}^2$ is less than one if $p_i \neq 0$ for more than one state $|\Psi_i\rangle$

$$\mathrm{Tr}\hat{\rho}^2 = \sum_{ij} \sum_n p_i p_j \langle n \mid \Psi_i\rangle \langle \Psi_i \mid \Psi_j\rangle \langle \Psi_j \mid n\rangle =$$

$$\sum_{ij} \sum_n p_i p_j \langle \Psi_j \mid n\rangle \langle n \mid \Psi_i\rangle \langle \Psi_i \mid \Psi_j\rangle = \sum_{ij} p_i p_j \left|\langle \Psi_i \mid \Psi_j\rangle\right|^2 = \sum_i p_i^2$$

$$\Rightarrow \begin{cases} \mathrm{Tr}\hat{\rho}^2 = 1 & \exists \text{ only one } |\Psi_i\rangle\,, p_i \neq 0 \\ 0 \leq \mathrm{Tr}\hat{\rho}^2 \leq 1 & \text{otherwise} \end{cases} \tag{2.43}$$

So the idempotency condition is necessary and sufficient to identify a physical system as a pure state. For a mixed state, the expectation value for the observable $\hat{A}$ is given by a natural generalization of eq.2.36,

$$\left\langle \Psi \left| \hat{A} \right| \Psi \right\rangle = \sum_i p_i \left\langle \Psi_i \left| \hat{A} \right| \Psi_i \right\rangle = \sum_i \sum_n p_i \langle \Psi_i \mid n\rangle \left\langle n \left| \hat{A} \right| n \right\rangle \langle n \mid \Psi_i\rangle = \mathrm{Tr}\left(\hat{\rho}\hat{A}\right) \tag{2.44}$$

2.2.1.1 Reduced density matrices

Up to here, it has been shown that the coordinate representation of the density operator $\hat{\rho}$, equivalent to the density matrix ρ in eq.2.32, namely a square matrix with the dimensions equal to the number of degrees of freedom in the system, contains all the information (observables) of the physical system. Anyway, since the basic hamiltonian operator is the sum of only 'one-electron' and 'two-electron'

operators, it is now useful to introduce the concept of the reduced density matrix of order p.

$$\rho_p\left(\mathbf{x}_1^{'}\mathbf{x}_2^{'},...\mathbf{x}_p^{'},\mathbf{x}_1\mathbf{x}_2...\mathbf{x}_p\right)=\left(\begin{array}{c}N\\p\end{array}\right)\int...\int\rho_N\left(\mathbf{x}_1^{'}...\mathbf{x}_p^{'}...\mathbf{x}_N,\mathbf{x}_1...\mathbf{x}_p...\mathbf{x}_N\right)d\mathbf{x}_{p+1}...d\mathbf{x}_N \tag{2.45}$$

where $\left(\begin{array}{c}N\\p\end{array}\right)=\frac{N!}{p!(N-p)!}$ is a binomial coefficient. In particular,

$$\rho_1\left(\mathbf{x}_1^{'},\mathbf{x}_1\right)=N\int...\int\Psi\left(\mathbf{x}_1^{'}\mathbf{x}_2...\mathbf{x}_N\right)\Psi^*\left(\mathbf{x}_1\mathbf{x}_2...\mathbf{x}_N\right)d\mathbf{x}_2..d\mathbf{x}_N \tag{2.46}$$

and,

$$\rho_2\left(\mathbf{x}_1^{'}\mathbf{x}_2^{'},\mathbf{x}_1\mathbf{x}_2\right)=\frac{N\left(N-1\right)}{2}\int...\int\Psi\left(\mathbf{x}_1^{'}\mathbf{x}_2^{'},...\mathbf{x}_N\right)\Psi^*\left(\mathbf{x}_1\mathbf{x}_2...\mathbf{x}_N\right)d\mathbf{x}_3..d\mathbf{x}_N \tag{2.47}$$

They normalize respectively to

$$\begin{aligned}\mathrm{Tr}\rho_1\left(\mathbf{x}_1^{'},\mathbf{x}_1\right)&=\int\rho_1\left(\mathbf{x}_1,\mathbf{x}_1\right)d\mathbf{x}_1=N\\\mathrm{Tr}\rho_2\left(\mathbf{x}_1^{'}\mathbf{x}_2^{'},\mathbf{x}_1\mathbf{x}_2\right)&=\int\int\rho_2\left(\mathbf{x}_1\mathbf{x}_2,\mathbf{x}_1\mathbf{x}_2\right)d\mathbf{x}_1d\mathbf{x}_2=\frac{N\left(N-1\right)}{2}\end{aligned} \tag{2.48}$$

Note that the matrices ρ_1 and ρ_2 correspond to the coordinate space representations of the density operators $\hat{\rho}_1$ and $\hat{\rho}_2$ acting on the one-particle and two-particle Hilbert spaces. Like $\hat{\rho}$, $\hat{\rho}_1$ and $\hat{\rho}_2$ are positive semidefinite and hermitian. Antisymmetry of the wavefunction for a fermionic system requires that the reduced density matrices reflect this property; thus

$$\rho_2\left(\mathbf{x}_1^{'}\mathbf{x}_2^{'},\mathbf{x}_1\mathbf{x}_2\right)=-\rho_2\left(\mathbf{x}_2^{'}\mathbf{x}_1^{'},\mathbf{x}_1\mathbf{x}_2\right) \tag{2.49}$$

$$\rho_2\left(\mathbf{x}_1^{'}\mathbf{x}_2^{'},\mathbf{x}_1\mathbf{x}_2\right)=-\rho_2\left(\mathbf{x}_1^{'}\mathbf{x}_2^{'},\mathbf{x}_2\mathbf{x}_1\right) \tag{2.50}$$

This implies

$$\rho_2\left(\mathbf{x}_1^{'}\mathbf{x}_2^{'},\mathbf{x}_1\mathbf{x}_2\right)=0\qquad\text{if}\qquad\mathbf{x}_1^{'}=\mathbf{x}_2^{'}\text{ or }\mathbf{x}_1=\mathbf{x}_2 \tag{2.51}$$

This is due to the repulsion between two electrons with the same spin and give rise to the Fermi correlation hole: this is the probability of finding two fermions as a function of their separation. This function goes to zero when the two electrons with the same spin are in the same point, in agreement with the Pauli exclusion principle. Finally the two operators $\hat{\rho}_1$ and $\hat{\rho}_2$ also admit eigenfuctions and eigenvalues, indeed

$$\hat{\rho}_1\left|\psi_i\right\rangle=n_i\left|\psi_i\right\rangle\qquad\qquad\hat{\rho}_2\left|\theta_i\right\rangle=g_i\left|\theta_i\right\rangle \tag{2.52}$$

where the eigenvalues n_i and g_i are called occupation numbers, while the eigenvectors for $\hat{\rho}_1$ and $\hat{\rho}_2$ are respectively natural and geminal orbitals. Note that for a mixed state the same properties hold.

Now consider the expectation value of a generic one-electron operator related to an antisymmetric

N-body wavefunction Ψ,

$$\left\langle \hat{O}_1 \right\rangle = \mathrm{Tr}\left(\hat{O}_1 \rho_1\right) = \int O_1\left(\mathbf{x}_1^{'}, \mathbf{x}_1\right) \rho_1\left(\mathbf{x}_1^{'}, \mathbf{x}_1\right) d\mathbf{x}_1^{'} d\mathbf{x}_1 \tag{2.53}$$

If the one-electron operator is local then

$$\left\langle \hat{O}_1 \right\rangle = \int \left[O_1\left(\mathbf{x}_1\right) \rho_1\left(\mathbf{x}_1^{'}, \mathbf{x}_1\right)\right]_{\mathbf{x}_1 = \mathbf{x}_1^{'}} d\mathbf{x}_1 = \int O_1\left(\mathbf{x}_1\right) \rho\left(\mathbf{x}_1\right) d\mathbf{x}_1 \tag{2.54}$$

In the same way for a two-electron operator $\hat{O}_2$

$$\left\langle \hat{O}_2 \right\rangle = \mathrm{Tr}\left(\hat{O}_2 \rho_2\right) = \int O_2\left(\mathbf{x}_1^{'}\mathbf{x}_2^{'}, \mathbf{x}_1\mathbf{x}_2\right) \rho_2\left(\mathbf{x}_1^{'}\mathbf{x}_2^{'}, \mathbf{x}_1\mathbf{x}_2\right) d\mathbf{x}_1^{'} d\mathbf{x}_2^{'} d\mathbf{x}_1 d\mathbf{x}_2 \tag{2.55}$$

If it is local then

$$\begin{aligned} \left\langle \hat{O}_2 \right\rangle &= \int \left[O_2\left(\mathbf{x}_1, \mathbf{x}_2, \right) \rho_2\left(\mathbf{x}_1^{'}\mathbf{x}_2^{'}, \mathbf{x}_1\mathbf{x}_2\right)\right]_{\mathbf{x}_1 = \mathbf{x}_1^{'}, \mathbf{x}_2 = \mathbf{x}_2^{'}} d\mathbf{x}_1 d\mathbf{x}_2 \\ &= \int O_2\left(\mathbf{x}_1, \mathbf{x}_2, \right) \rho_2\left(\mathbf{x}_1, \mathbf{x}_2\right) d\mathbf{x}_1 d\mathbf{x}_2 \end{aligned} \tag{2.56}$$

2.2.1.2 Hartree-Fock theory with the density matrix formalism

By using the concepts of reduced density matrices at the first and the second order, one can now write the expectation value of the hamiltonian associated to a system of N_{el} electrons and N_{at} nuclei.

$$\hat{\mathcal{H}} = \sum_{i=1}^{N_{el}} -\frac{1}{2}\nabla_i^2 + \frac{1}{2}\sum_{i,j}^{N_{el}} \frac{1}{|\mathbf{r}_{ij}|} - \sum_{\alpha}^{N_{at}} \sum_{i}^{N_{el}} \frac{Z_\alpha}{|\mathbf{r}_i - \mathbf{R}_\alpha|} = \hat{T} + \hat{V}_{ee} + \hat{V}_{ext} \tag{2.57}$$

Since its expression does not show any explicit dependence on spin variables, one may use here the spinless density matrices where all the spin coordinates have been ruled out by integration and get

$$E = -\frac{1}{2}\int \left[\nabla_1^2 \rho_1\left(\mathbf{r}_1, \mathbf{r}_1^{'}\right) d\mathbf{r}_1\right]_{\mathbf{r}_1 = \mathbf{r}_1^{'}} - \sum_{\alpha} \int \frac{Z_\alpha}{\mathbf{r}_{1\alpha}} \rho\left(\mathbf{r}_1\right) d\mathbf{r}_1 + \frac{1}{2}\int\int d\mathbf{r}_1 d\mathbf{r}_2 \frac{\rho_2\left(\mathbf{r}_1, \mathbf{r}_2\right)}{\mathbf{r}_{12}} \tag{2.58}$$

In particular, in the Hartree-Fock approximation, the energy eigenvalue reads as

$$\begin{aligned} E^{HF} = \left\langle \Psi^{HF} \left| \hat{O}_1 + \hat{O}_2 \right| \Psi^{HF} \right\rangle &= \int dr \left[\left(-\frac{\nabla_{\mathbf{r}}^2}{2} + V_{ext}\left(\mathbf{r}\right)\right) \rho\left(\mathbf{r}, \mathbf{r}^{'}\right)\right]_{\mathbf{r}=\mathbf{r}^{'}} + \\ &+ \frac{1}{2}\left\{ \iint d\mathbf{r} d\mathbf{r}^{'} \frac{\rho\left(\mathbf{r}\right)\rho\left(\mathbf{r}^{'}\right)}{|\mathbf{r} - \mathbf{r}^{'}|} - \iint d\mathbf{r} d\mathbf{r}^{'} \frac{\tilde{\rho}\left(\mathbf{r}, \mathbf{r}^{'}\right)\tilde{\rho}\left(\mathbf{r}^{'}, \mathbf{r}\right)}{|\mathbf{r} - \mathbf{r}^{'}|} \right\} \end{aligned} \tag{2.59}$$

Equivalently the total energy E_0^{HF} reads as

$$E_0^{HF} = \sum_i \varepsilon_i^{HF} - \frac{1}{2}\left\{ \iint d\mathbf{r} d\mathbf{r}^{'} \frac{\rho\left(\mathbf{r}\right)\rho\left(\mathbf{r}^{'}\right)}{|\mathbf{r} - \mathbf{r}^{'}|} - \iint d\mathbf{r} d\mathbf{r}^{'} \frac{\tilde{\rho}\left(\mathbf{r}, \mathbf{r}^{'}\right)\tilde{\rho}\left(\mathbf{r}^{'}, \mathbf{r}\right)}{|\mathbf{r} - \mathbf{r}^{'}|} \right\} \tag{2.60}$$

where $\rho(\mathbf{r})$ is the local first order reduced density matrix,

$$\rho(\mathbf{r}) = \sum_{i}^{N} \varphi_i(\mathbf{r}) \varphi_i^*(\mathbf{r}) \tag{2.61}$$

and $\tilde{\rho}\left(\mathbf{r}, \mathbf{r}^{'}\right)$ is the non-local first order reduced density matrix,

$$\tilde{\rho}\left(\mathbf{r}, \mathbf{r}'\right) = \sum_{i}^{N} \varphi_i(\mathbf{r}) \varphi_i^*\left(\mathbf{r}^{'}\right). \tag{2.62}$$

It is evident that in the calculation of E^{HF}, the second-order reduced matrices are not require as expected from eq.2.58. Indeed the density matrix of any order is calculable from first-order density matrices,

$$\rho_p\left(\mathbf{r}_1^{'}, ...\mathbf{r}_p^{'}, \mathbf{r}_1 ... \mathbf{r}_p\right) = \frac{1}{p!} \begin{vmatrix} \rho_1\left(\mathbf{r}_1, \mathbf{r}_1^{'}\right) & \rho_1\left(\mathbf{r}_1, \mathbf{r}_2^{'}\right) & \dots & \rho_1\left(\mathbf{r}_1, \mathbf{r}_p^{'}\right) \\ \rho_1\left(\mathbf{r}_2, \mathbf{r}_1^{'}\right) & \rho_1\left(\mathbf{r}_2, \mathbf{r}_2^{'}\right) & \dots & \rho_1\left(\mathbf{r}_2, \mathbf{r}_p^{'}\right) \\ \vdots & \vdots & \ddots & \vdots \\ \rho_1\left(\mathbf{r}_p, \mathbf{r}_1^{'}\right) & \rho_1\left(\mathbf{r}_p, \mathbf{r}_2^{'}\right) & \dots & \rho_1\left(\mathbf{r}_p, \mathbf{r}_p^{'}\right) \end{vmatrix} \tag{2.63}$$

As shown in eqs.2.61 and 2.62 density matrices assume very simple forms when they are derived from a single determinant. In can be shown that this is consequence of the one to one mapping existing between a Slater determinant and a density matrix of the form in eq.2.62.

2.2.2 The Hohemberg-Kohn theorems

Recall that for an electronic system described by the hamiltonian in eq.2.57, both the ground state energy and the ground state wavefuction are determined by the minimization of the energy functional $E[\Psi]$ with respect to Ψ; moreover, the hamiltonian for a N-electron system is completely fixed by the the external potential $V_{ext}(\mathbf{r})$, thus N and $V_{ext}(\mathbf{r})$ determine all the ground state properties. In principle, this means that all the information about the system (observables) may be obtained by applying the suitable operator to the wavefunction Ψ; anyway in practice, it is very difficult to deal with Ψ except for very small systems, as it is a large object depending on $3N$ variables ($4N$ if the spin index is included in addition to the spatial coordinates $\{x, y, z\}$ for all the particles). The use of density matrices in place of wavefunctions is possible, as they still contain all the information of the system, but not much easier. So the need of a method based on some smaller representation of Ψ arose very early in the history of quantum chemistry. The use of the electron density $\rho(\mathbf{r})$ instead of Ψ would be computationally much more convenient, indeed $\rho(\mathbf{r})$ is a purely three-dimensional function, compared to the $3N$ dimensions of Ψ; of course, the integration over all but one spatial coordinate in the full density matrix induces some loss of information.

The first Hohemberg-Kohn theorem legitimizes the use of electron density $\rho(\mathbf{r})$ instead of N and $V_{ext}(\mathbf{r})$ as basic variable: indeed it assures that a given ρ corresponds to only one physical system, hence two different V_{ext} will never give the same $\rho(\mathbf{r})$. Moreover, since ρ determines the number

of electrons, it follows that $\rho(\mathbf{r})$ also determines the ground state wavefunction Ψ and then all the other properties of the system. The proof of this theorem is very simple. Consider two external potentials differing by more than a constant, $V_{ext} \neq V_{ext}^{'} + c$ and the two Hamiltonian $\mathcal{H} \neq \mathcal{H}^{'}$ with their ground state eigenfunctions, $\Psi_0 \neq \Psi_0^{'}$. The theorem shows that $\rho_0 \neq \rho_0^{'}$ within these hypothesis. Indeed

$$E_0 = \langle \Psi_0 | \mathcal{H} | \Psi_0 \rangle \qquad E_0^{'} = \left\langle \Psi_0^{'} \middle| \mathcal{H}^{'} \middle| \Psi_0^{'} \right\rangle \tag{2.64}$$

and thus,

$$\begin{aligned} E_0 = \langle \Psi_0 | \mathcal{H} | \Psi_0 \rangle < \left\langle \Psi_0^{'} \middle| \mathcal{H} \middle| \Psi_0^{'} \right\rangle = \left\langle \Psi_0^{'} \middle| \mathcal{H}^{'} - V_{ext}^{'} + V_{ext} \middle| \Psi_0^{'} \right\rangle = \\ = \left\langle \Psi_0^{'} \middle| \mathcal{H}^{'} \middle| \Psi_0^{'} \right\rangle + \left\langle \Psi_0^{'} \middle| V_{ext} - V_{ext}^{'} \middle| \Psi_0^{'} \right\rangle = E_0^{'} + \int \rho_0(\mathbf{r}) \left(V_{ext} - V_{ext}^{'} \right) d\mathbf{r} \end{aligned} \tag{2.65}$$

In the same way

$$\begin{aligned} E_0^{'} = \left\langle \Psi_0^{'} \middle| H^{'} \middle| \Psi_0^{'} \right\rangle < \left\langle \Psi_0 \middle| H^{'} \middle| \Psi_0 \right\rangle = \left\langle \Psi_0 \middle| H - V_{ext} + V_{ext}^{'} \middle| \Psi_0 \right\rangle = \\ = \langle \Psi_0 | H | \Psi_0 \rangle - \left\langle \Psi_0 \middle| V_{ext} - V_{ext}^{'} \middle| \Psi_0 \right\rangle = E_0 - \int \rho_0^{'}(\mathbf{r}) \left(V_{ext} - V_{ext}^{'} \right) d\mathbf{r} \end{aligned} \tag{2.66}$$

By summing eqs.2.65 and 2.66 one finally obtains

$$\int dr \left(\rho_0^{'}(\mathbf{r}) - \rho_0(\mathbf{r}) \right) \left(V_{ext} - V_{ext}^{'} \right) > 0 \tag{2.67}$$

which requires $V_{ext} \neq V_{ext}^{'}$ and $\rho_0^{'}(\mathbf{r}) \neq \rho_0(\mathbf{r})$. This result can be summarized as follows:

$$\Psi_0 \leftrightarrow \rho_0 \leftrightarrow V_{ext}(\mathbf{r}) \tag{2.68}$$

thus showing the one to one correspondence between the ground state electron density and the ground state wavefunction in a given external potential. In this way, the electron density appears as an extremely powerful tool to describe a certain system, though one has to be aware that $\rho(\mathbf{r})$ can be easily generate once Ψ is known, but the reverse is not the case. Indeed there exists an infinite number of antisymmetric wavefunctions that all give the same $\rho(\mathbf{r})$. The point here is that one needs to identify the ground state wavefunction Ψ_ρ among those that integrate at a given $\rho(\mathbf{r})$; then recognize the ground state density $\rho_0(\mathbf{r})$ among all the accessible $\rho(\mathbf{r})$. This procedure can be performed in two steps. First the space of Ψ is partitioned into subsets of wavefunctions that give by quadrature the same electron density $\rho(\mathbf{r})$. For each of these subsets, one searches the ground state Ψ:

$$\begin{aligned} E_\rho[\rho] = \min_{\Psi \to \rho} \left\langle \Psi \middle| \hat{H} \middle| \Psi \right\rangle = \min_{\Psi \to \rho} \left\langle \Psi \middle| \hat{T} + \hat{V}_{ee} + \hat{V}_{ext} \middle| \Psi \right\rangle \\ = \min_{\Psi \to \rho} \left\langle \Psi \middle| \hat{T} + \hat{V}_{ee} \middle| \Psi \right\rangle + \int dr \rho(\mathbf{r}) V_{ext}(\mathbf{r}) = F[\rho] + \int dr \rho(\mathbf{r}) V_{ext}(\mathbf{r}) \end{aligned} \tag{2.69}$$

where it has been introduced the *universal* functional $F[\rho]$ of $\rho(\mathbf{r})$

$$F[\rho] = \min_{\Psi \to \rho} \left\langle \Psi \left| \hat{T} + \hat{V}_{ee} \right| \Psi \right\rangle \tag{2.70}$$

Note that $F[\rho]$ is definited independently on the external potential, which is peculiar of each system, therefore it is universally valid for every physical system. Once obtained the variational energy for a given $\rho(\mathbf{r})$, i.e. $E_\rho[\rho]$, the constraint over $\rho(\mathbf{r})$ is released and the search proceeds over all the electron densities:

$$\begin{aligned} E_0 = \min_\rho E_\rho[\rho] = \min_\rho \left\{ F[\rho] + \int d\mathbf{r} \rho(\mathbf{r}) V_{ext}(\mathbf{r}) \right\} = \\ = \min_\rho \left\{ \min_{\Psi \to \rho} \left\langle \Psi \left| \hat{T} + \hat{V}_{ee} \right| \Psi \right\rangle + \int d\mathbf{r} \rho(\mathbf{r}) V_{ext}(\mathbf{r}) \right\} \end{aligned} \tag{2.71}$$

This procedure is known as Levy constrained search and it defines immediately a variatonal principle based upon the electron density equivalent to the Rayleigh-Ritz one. It is also an alternative version (more general) of the second theorem by Hohemberg-Kohn. The variational principle may also be written as a Lagrange multipliers problem:

$$\frac{\delta \left[E_\rho[\rho] - \mu \left(\int d\mathbf{r} \rho(\mathbf{r}) - N \right) \right]}{\delta \rho} = 0 \tag{2.72}$$

$$\frac{\delta E_\rho[\rho]}{\delta \rho} - \mu = 0 \tag{2.73}$$

By substituting $E_\rho[\rho]$ with eq.2.69, one gets the final Euler-Lagrange equation

$$\frac{\partial F[\rho]}{\partial \rho} + V_{ext}(\mathbf{r}) = \mu \tag{2.74}$$

where μ is the chemical potential, introduced as a Lagrange multiplier.
In conclusion, the first theorem states the key role of the electron density, that fully determines the external potential and thus the hamiltonian; moreover, since it determines the number of electrons, it follows that also Ψ is determined. In addition, the second theorem shows that all the ground state properties, particularly the ground state energy, are obtained variationally from $\rho(\mathbf{r})$.

2.2.2.1 *v*- and *N*-representability problems

The set of all possible trial electron densities has to be carefully chosen, indeed the ground state electron density must obey some conditions. In the original formulation of the density functional theory by Hohemberg and Kohn, the electron density is requested to be v-representable. This means that it has to be associated with the antisymmetric ground state wavefunction of a hamiltonian with some external potential $V_{ext}(\mathbf{r})$. From a mathematic point of view this is a very difficult problem, indeed the general conditions for a density to be v-representable are still unknown, and

only for some specific densities the v-representability has been proved. However the constrained-search approach overcomes this issue, since the universal functional $F[\rho]$ used in eq.2.71 results from the minimization over a set of wavefunctions, that originate from a hamiltonian (which by definition contains an external potential). Hence, the electron densities need only to be associated with antisymmetric wavefunctions. This is known as the condition of N-representability and it is satisfied by any reasonable density. It is consider a weaker condition than the v-representability one, indeed the former is necessary for the latter.

2.2.3 The Kohn-Sham scheme

The density-functional theory is an exact theory, which proves the existence of an universal functional of the electron density $F[\rho]$ but does not provide any explicit form for it. If one knew the exact expression of the universal functional $F[\rho]$ then equations eq.2.71 and eq.2.73 would be exact for the ground state electron density. Unfortunately, $F[\rho]$ is unknown, thus for practical calculations some approximations are needed. From Hohemberg-Kohn theorems one may write

$$E[\rho] = T[\rho] + V_{ee}[\rho] + \int d\mathbf{r}\rho(\mathbf{r}) V_{ext}(\mathbf{r}) \tag{2.75}$$

where $T[\rho]$ and $V_{ee}[\rho]$ are not explicitely known. Within the Thomas-Fermi (TF) approximation, the expression in eq.2.75 is greatily simplified, with of course a great loss of accuracy, and it reads as

$$E_{V_{ext}}^{DFT-TF}[\rho] = c\int d\mathbf{r}\rho^{\frac{5}{3}}(\mathbf{r}) + E_{Hartree}[\rho] + \int d\mathbf{r}\rho(\mathbf{r}) V_{ext}(\mathbf{r}) \tag{2.76}$$

where

$$\begin{aligned} T[\rho] &= c\int d\mathbf{r}\rho^{\frac{5}{3}}(\mathbf{r}) \\ V_{ee}[\rho] &= E_{Hartree}[\rho] = \int d\mathbf{r}d\mathbf{r}' \frac{\rho(\mathbf{r})\rho\left(\mathbf{r}'\right)}{|\mathbf{r}-\mathbf{r}'|} \end{aligned} \tag{2.77}$$

The solution of eq.2.76 reads as,

$$\frac{\partial}{\partial\rho} E_{V_{ext}}^{DFT-TF}[\rho] = \frac{5}{3}c\rho^{\frac{2}{3}} + V_{Hartree}^{[\rho]}(\mathbf{r}) + V_{ext}(\mathbf{r}) - \lambda = 0 \tag{2.78}$$

where λ is the Lagrange multiplier coming from the constraint on the density $\rho(\mathbf{r})$, which is requested to satisfy $\int \rho(\mathbf{r})\, d\mathbf{r} = N$. The solution of Thomas-Fermi equations provides a good description for high density systems, but not for atoms where the approximations introduced become inadequate. To solve this problem, one has to refer to the Kohn-Sham scheme. It introduces a new physical system, an *auxiliary* system, closely related to the *real* system, but such that its energy functional may be easily computed. All the differences between the two systems are then collected in a corrective term. The Kohn-Sham *ansatz* assumes that for every physical system of interacting particles exists a dummy auxiliary system of noninteracting particles and that they share the same electron

density ρ. The monodeterminant wavefunction exactly describes N noninteracting electrons, thus the electron density for the auxiliary system reads as

$$\rho(\mathbf{r}) = \sum_{i}^{N} \left|\varphi_i^{KS}(\mathbf{r})\right|^2 \tag{2.79}$$

where $\varphi_i^{KS}(\mathbf{r})$ are the Kohn-Sham orbitals. The kinetic energy functional $T_s[\rho]$ is then given by

$$T_s[\rho] = \sum_{i} \left\langle \varphi_i^{KS} \left| -\frac{\hbar^2}{2m}\nabla^2 \right| \varphi_i^{KS} \right\rangle. \tag{2.80}$$

One can now rewrite the energy functional for the real system as follows

$$E_{V_{ext}}^{DFT-KS}[\rho] = T_s[\rho] + J[\rho] + \int d\mathbf{r}\rho(\mathbf{r}) V_{ext}(\mathbf{r}) + E_{xc}[\rho] \tag{2.81}$$

where

$$\begin{aligned} J[\rho] = E_{Hartree}[\rho] &= \int d\mathbf{r}d\mathbf{r}' \frac{\rho(\mathbf{r})\rho\left(\mathbf{r}'\right)}{|\mathbf{r}-\mathbf{r}'|} \\ E_{xc}[\rho] &= T[\rho] - T_s[\rho] + V_{ee}[\rho] - J[\rho] \end{aligned} \tag{2.82}$$

The quantity $E_{xc}[\rho]$ is called the exchange-correlation energy: it contains the difference between the kinetic energy of the two systems ($T[\rho] - T_s[\rho]$), also known as dynamical correlation, and the nonclassical part of the electron-electron interaction, ($V_{ee}[\rho] - J[\rho]$). By minimizing eq.2.81 with respect to the KS orbitals within the usual constraint on the electronic density, it follows

$$\frac{\partial E_{V_{ext}}^{DFT-KS}}{\left\langle \partial\varphi_i^{KS}\right|} = \frac{\partial T_s}{\partial\left\langle\varphi_i^{KS}\right|} + \left[\frac{\partial J}{\partial\rho} + \frac{\partial E_{ext}}{\partial\rho} + \frac{\partial E_{xc}}{\partial\rho}\right]\frac{\partial\rho}{\partial\left\langle\varphi_i^{KS}\right|} = 0 \tag{2.83}$$

where $E_{ext} = \int d\mathbf{r}\rho(\mathbf{r}) V_{ext}(\mathbf{r})$ and $\frac{\partial E_{XC}[\rho]}{\partial\rho} = V_{xc}^{[\rho]}$ is the exchange-correlation potential that acts locally on the wavefuction. The effective potential acting on the real system is then defined as

$$V_{eff}^{[\rho]} = V_{Hartree}^{[\rho]} + V_{ext} + V_{xc}^{[\rho]} \tag{2.84}$$

It is important to notice that the first Hohemberg-Kohn theorem implies $V_{eff}^{[\rho]} = \tilde{V}_{ext}$, where $\tilde{V}_{ext}$ is the external potential in the *auxiliary* system. The minimization of the energy functional leads to

$$\left\{-\frac{\hbar^2}{2m}\nabla^2 + V_{Hartree}^{[\rho]}(\mathbf{r}) + V_{ext}(\mathbf{r}) + \frac{\partial E_{XC}[\rho]}{\partial\varphi_i^{KS*}(\mathbf{r})}\right\}\varphi_i^{KS}(\mathbf{r}) = \sum_j \lambda_{ij}\varphi_j^{KS}(\mathbf{r}) \tag{2.85}$$

and after diagonalization, the Kohn-Sham equations are obtained in their canonical form:

$$H_{eff}^{KS}\varphi_i^{KS}(\mathbf{r}) = \left\{-\frac{1}{2}\nabla^2 + V_{eff}^{[\rho]}\right\}\varphi_i^{KS}(\mathbf{r}) = \varepsilon_i^{KS}\varphi_i^{KS}(\mathbf{r}) \tag{2.86}$$

where φ_i^{KS} in eqs.2.85-2.86 may be different. The total energy E_0^{DFT-KS} of the system can then

be expressed as

$$E_0^{DFT-KS} = \sum_i \varepsilon_i^{KS} - \frac{1}{2} E_{Hartree}[\rho] - \int d\mathbf{r} \rho(\mathbf{r}) V_{xc}^{[\rho]}(\mathbf{r}) + E_{xc}[\rho] \tag{2.87}$$

where the last two terms are added since the functional form of the exchange correlation energy is unknown (possibly being linear, quadratic...in ρ). Before concluding this section on the Kohn-Sham scheme it is useful to add some remarks: first, by introducing the KS orbitals one may exactly handle $T_s[\rho]$, which represents the dominant part of the kinetic energy in the real system; this of course increases the accuracy with respect to the Thomas-Fermi approximation, but it also implies a larger number of calculations, that is N equations to solve instead of only one. Second, the KS equations are very similar to Hartree equations, except for the local $V_{eff}(\mathbf{r})$ term, which is more general in the KS case; thus the two methods need almost the same computational effort to deal with the characteristic equations. This is not true within the Hartree-Fock approximation that is indeed computationally more expensive because of the nonlocal exchange operator. Finally, one should be aware that the KS theory is exact in principle and once known the exact form of $E_{xc}[\rho]$, it would be possible to achieve the exact ρ and E; of course, this is not the case of the HF theory which, by construction, does not account for the electron correlation effects.

According to the original formulation by Kohn and Sham, the electron density shared by the auxiliary and the real system is defined by the set of N lowest eigenstates φ_i with energy ε_i, solution of eq.2.86: this assumption holds only for non-interacting v-representable densities and implies that the two systems share the ground state density. Anyway the variational search for the true ground state needs to be carried out on functionals defined for the larger domain composed of N-representable densities; this is done within the constrained-search formulation, initially developed for the Hohemberg-Kohn definition of $F[\rho]$. Accordingly, $T_s[\rho]$ can be written as

$$T_s[\rho] = \min_{\Psi_D \to \rho} \left\langle \Psi_D \left| \hat{T} \right| \Psi_D \right\rangle \tag{2.88}$$

where the search is over all the monodeterminant antisymmetric functions Ψ_D. Note that this definition is applicable for all N-representable densities (for the very same reasons shown for $F[\rho]$ in eq.2.70). By including also multideterminant wavefunctions, one obtains $\tilde{T}_s[\rho]$ and, due to the larger set of functions involved, the following relation holds

$$\tilde{T}_s[\rho] \leq T_s[\rho] \tag{2.89}$$

Anyway it can be shown that for any density ρ that is noninteracting v-representable and is associated to a nondegenerate ground state, the minimum solution does not change if multideterminant wavefunctions are included in the search, thus $\tilde{T}_s[\rho] = T_s[\rho]$. Indeed if ρ is v-representable, there will always be a $V(\mathbf{r})$ for which $\rho(\mathbf{r})$ is the non-interacting N-electron ground state density (corresponding to a monodeterminant wavefunction). The N orbitals, coming from the variational search

in eq.2.88 must fulfill some conditions, indeed $\Omega[\{\varphi_i\}] =$

$$\sum_i^N \int \varphi_i^*(\mathbf{r}) \left[-\frac{1}{2}\nabla^2\right] \varphi_i(\mathbf{r})\, d\mathbf{r} + \int \lambda(\mathbf{r}) \left\{\sum_i^N |\varphi_i(\mathbf{r})|^2 - \rho(\mathbf{r})\right\} d\mathbf{r} - \sum_{ij}^N \varepsilon_{ij} \int \varphi_i^*(\mathbf{r})\, \varphi_j(\mathbf{r})\, d\mathbf{r} \tag{2.90}$$

where the function $\lambda(\mathbf{r})$ and ε_{ij} are Lagrange multipliers. The former asks that the sum of orbital densities is equal to the given density $\rho(\mathbf{r})$, while the latter represents the orthonormality constraint. From the minimization condition $\frac{\delta\Omega}{\delta\varphi_k^*(\mathbf{r})} = 0$, there result the equations

$$\left[-\frac{1}{2}\nabla^2 + \lambda(\mathbf{r})\right] \varphi_k(\mathbf{r}) = \sum_j^N \varepsilon_{jk}\varphi_k(\mathbf{r}) \tag{2.91}$$

and after diagonalization

$$\hat{h}_s\varphi_k(\mathbf{r}) = \varepsilon_k\varphi_k(\mathbf{r}) \tag{2.92}$$

This shows that the orbitals involved in the minimization are eigenstates of the one-electron hamiltonian with a local potential exactly equal to the lagrangian multiplier $\lambda(\mathbf{r})$. For any noninteracting v-representable density, there exists a potential $V_{eff}(\mathbf{r})$ related to $\rho(\mathbf{r})$ and such that $\lambda(\mathbf{r}) = V_{eff}(\mathbf{r})$. In this case the eq.2.92 reduces exactly to the original definition by Kohn-Sham; of course the optimized φ_k orbitals in eq.2.92 are the same as the KS orbitals in eq.2.86. If, on the other hand, ρ is not noninteracting v-representable, then $\lambda(\mathbf{r})$ is not the potential related to $\rho(\mathbf{r})$ and equations in eq.2.92 can not be reduced to the KS equations. In this case, since $\lambda(\mathbf{r}) \neq V_{eff}(\mathbf{r})$, the φ_k orbitals in eq.2.92 are not equal to the N lowest eigenstates solutions of the KS equations eq.2.86 for the noninteracting system. Hence, these φ_k orbitals do not describe the ground state density of the auxiliary system, but some excited configuration. One may conclude that the real and the auxiliary system share the density $\rho(\mathbf{r})$, but this is the ground state density only for the real system. Only if $\rho(\mathbf{r})$ is v-representable, one can be sure that it is the ground state density for both of them. Equivalently, if $\rho(\mathbf{r})$ is the true ground state of an N-electron interacting system with a given potential $V_{eff}(\mathbf{r})$, then it is of course v-representable and equations eq.2.92 are precisely the Kohn-Sham equations, with $\lambda(\mathbf{r}) = V_{eff}(\mathbf{r})$. Because of their auxiliary nature, the Kohn-Sham orbitals have in principle no-physical meaning, indeed they are related to the real system only because their squares are expected to sum up at the true electron density. In the same way, no physical meaning is carried by the orbital energies ε_i and there is no equivalent of the Koopman's theorem, which could relate the orbital energies to ionization energies. In the limit of exact DFT, there is one exception though: the eigenvalue of the highest occupied orbital ε_{max} equals the negative of the ionization energy, because of the exact long-range behaviour of the exact electron density (as shown in sec. 2.2.4). While the above considerations are all true in a very strict sense, anyway one should also point out that KS orbitals are eigenfunctions of an one-particle hamiltonian, which includes all the non-classical effects. In this sense, the HF orbitals are much farther away from the real system, since they neither contain any correlation nor could in principle provide the exact

electron density. For this reason, KS orbitals should be legitimated as well as HF orbitals for, *e.g.*, reactivity considerations. At last, one has to remark that both KS and HF schemes are based on a monodeterminant wavefunction, nevertheless, they significantly differ. In fact the HF method does not include any non-classical effect and correlation can be introduced only through the interaction among different Slater determinants each of those representing an excited electronic configuration (as in CASSCF, CI...). On the other hand, in the KS approach some correlation effects are included: the dynamic correlation comes from the term $T[\rho] - T_s[\rho]$ in the exchange-correlation functional; while, for the static correlation the issue is more subtle. Indeed here the question about the sense of using a multi-determinant wavefunction is closely related to whether or not it is correct to use the lowest N orbitals of the non-interacting system to build the Slater determinant. This is closely related to the v-representability problem, described above.

2.2.3.1 Kohn-Sham equations in plane wave basis

For finite systems, like atoms and molecules, it is natural to represent the KS orbitals using a localized basis set. In the same way, for ideally infinite periodic systems, like crystalline solids, the use of a plane waves basis set comes straightforwardly. Plane waves are defined as

$$f_{\mathbf{G}}^{PW}(\mathbf{r}) = \frac{1}{\sqrt{\Omega}} e^{i\mathbf{G}\mathbf{r}} \tag{2.93}$$

where Ω is the volume of a periodic (super-) cell and $\mathbf{G}$ is a vector in the reciprocal space. Note that plane waves do not depend on the nuclear positions and they are delocalized in space; as a consequence they form a very unbiased basis set which do not favour certain areas over others. According to the Bloch's theorem, the eigenstates of a monoelectronic hamiltonian defined within a periodic potential are described by a plane wave $e^{i\mathbf{k}\cdot\mathbf{r}} = |\mathbf{k}\rangle$ times a periodic function $u_{i\mathbf{k}}(\mathbf{r})$. Hence they have the form

$$\varphi_{i\mathbf{k}}(\mathbf{r}) = \frac{1}{\sqrt{N_{cell}}} u_{i\mathbf{k}}(\mathbf{r})\, e^{i\mathbf{k}\cdot\mathbf{r}} \tag{2.94}$$

where N_{cell} gives the number of cells, $\mathbf{r}$ is a real space vector, while the wavevector $\mathbf{k}$ is defined in the first Brillouin zone. The function $u_{i\mathbf{k}}(\mathbf{r})$ has the same periodicity of the crystal, namely $u_{i\mathbf{k}}(\mathbf{r}) = u_{i\mathbf{k}}(\mathbf{r}+\mathbf{L})$; thus its plane waves expansion is a sum over the vectors in the reciprocal space:

$$u_{i\mathbf{k}}(\mathbf{r}) = \frac{1}{\sqrt{\Omega_{cell}}} \sum_{\mathbf{G}} c_{i\mathbf{G}} e^{i\mathbf{G}\cdot\mathbf{r}} = \sum_{\mathbf{G}} c_{i\mathbf{G}} |\mathbf{G}\rangle \tag{2.95}$$

where $\{\mathbf{G}\}$ is the set of reciprocal lattice vectors and Ω_{cell} is the volume of a single cell; note that the total volume of the crystal is $\Omega = \Omega_{cell} N_{cell}$. Note that the subscript i in $u_{i\mathbf{k}}(\mathbf{r})$ comes from its periodicity. Indeed $u_{i\mathbf{k}}(\mathbf{r})$ satisfies the periodic boundary conditions and this generates for each $\mathbf{k}$ a set of i eigenfunctions which are directly connected to the concept of energy bands and form the set of KS solutions for the given $\mathbf{k}$. Therefore, $\varphi_i(\mathbf{r}, \mathbf{k})$ in eq.2.94 can be rewritten as:

$$\varphi_{i\mathbf{k}}(\mathbf{r}) = \frac{1}{\sqrt{\Omega}} \sum_{\mathbf{G}} c_{i,\mathbf{k}+\mathbf{G}}(\mathbf{k})\, e^{i\mathbf{G}\cdot\mathbf{r}} e^{i\mathbf{k}\cdot\mathbf{r}} = \sum_{\mathbf{G}} c_{i,\mathbf{k}+\mathbf{G}} |\mathbf{k}+\mathbf{G}\rangle \tag{2.96}$$

Accordingly, the matrix element of the hamiltonian is

$$\sum_{\mathbf{G}} c_{i,\mathbf{k}+\mathbf{G}} \left\langle \mathbf{k}+\mathbf{G}^{'} \left| H \right| \mathbf{k}+\mathbf{G} \right\rangle = \varepsilon_i c_{i,\mathbf{k}+\mathbf{G}^{'}} \tag{2.97}$$

where all the $\mathbf{k}$ vectors belong to the first Brillouin zone. Each plane wave in the expansion eq.2.96 corresponds to a $\mathbf{k}^{'}$ outside the Brillouin zone and connected to $\mathbf{k}$ by a reciprocal lattice vector $\mathbf{G}$, thus the following relation holds: $\mathbf{k}^{'} = \mathbf{k}+\mathbf{G}$. In actual calculations the infinite sums over $\mathbf{G}$ vectors have to be truncated. Moreover the integral over the Brillouin zone has to be approximated by a finite sum over a set of $\mathbf{k}$-points as follows,

$$\int_{BZ} d\mathbf{k} = \sum_{\mathbf{k}} w_{\mathbf{k}} \tag{2.98}$$

where the contribution of each $\mathbf{k}$ is weighted by a coefficient $w_{\mathbf{k}}$. The number of plane waves in the basis set is controlled by the *energy cutoff*, which gives the upper limit to the kinetic energy of the $\mathbf{G}$ vectors. In plane waves the matrix elements of the kinetic energy operator are simply

$$\left\langle \mathbf{k}+\mathbf{G}^{'} \left| -\frac{\nabla^2}{2} \right| \mathbf{k}+\mathbf{G} \right\rangle = \frac{1}{2} \left| \mathbf{k}+\mathbf{G} \right|^2 . \tag{2.99}$$

thus the $\mathbf{G}$ vectors included in the basis are those for which the relation $\frac{1}{2} \left| \mathbf{k}+\mathbf{G} \right|^2 \leq E_{cut}$ holds. Note that the appropriate value E_{cut} has to be chosen upon evaluating the convergence of the calculations. Moreover any periodic local potential can be expanded as a Fourier series

$$V(\mathbf{r}) = \sum_{\mathbf{G}} V(\mathbf{G}) e^{i\mathbf{G}\cdot\mathbf{r}} \qquad \text{and} \qquad V(\mathbf{G}) = \frac{1}{\Omega_{cell}} \int_{\Omega_{cell}} dr V(\mathbf{r}) e^{-i\mathbf{G}\cdot\mathbf{r}} \tag{2.100}$$

and then its matrix elements read as

$$\left\langle \mathbf{k}+\mathbf{G}^{'} \left| V \right| \mathbf{k}+\mathbf{G} \right\rangle = \sum_{\mathbf{G}} V(\mathbf{G}) \delta_{\mathbf{G}^{'}-\mathbf{G},\mathbf{G}} = \sum_{\mathbf{G}} V\left(\mathbf{G}^{'}-\mathbf{G}\right) \tag{2.101}$$

where from the condition in the δ-function, i.e. $\mathbf{G} = \mathbf{G}^{'} - \mathbf{G}$, it is clear that they are nonzero only when they differ by a unitary reciprocal lattice vector $\mathbf{G}$. Concluding, for each $\mathbf{k}$ in the Brillouin zone the electronic problem reads as

$$\sum_{\mathbf{G}} H_{\mathbf{k}+\mathbf{G}^{'},\mathbf{k}+\mathbf{G}} c_{i,\mathbf{k}+\mathbf{G}} = \varepsilon_{i\mathbf{k}} c_{i,\mathbf{k}+\mathbf{G}^{'}} \tag{2.102}$$

in which

$$H_{\mathbf{k}+\mathbf{G}^{'},\mathbf{k}+\mathbf{G}} = \left\langle \mathbf{k}+\mathbf{G}^{'} \left| H \right| \mathbf{k}+\mathbf{G} \right\rangle = \frac{1}{2} \left| \mathbf{k}+\mathbf{G} \right|^2 + V\left(\mathbf{G}^{'}-\mathbf{G}\right) \tag{2.103}$$

In the same framework, the total energy from the Kohn-Sham scheme reads as

$$E = \frac{1}{N_k} \sum_{i\mathbf{k}} w_{i\mathbf{k}} \left\{ \sum_{\mathbf{G}} c^{*}_{i,\mathbf{k}+\mathbf{G}^{'}} c_{i,\mathbf{k}+\mathbf{G}} \left[\frac{1}{2} \left| \mathbf{k}+\mathbf{G} \right|^2 + V_{ext}\left(\mathbf{G}^{'}-\mathbf{G}\right) \right] \right\} +$$

$$+\Omega_{cell}\sum_{\mathbf{G}}\varepsilon_{xc}\left(\mathbf{G}\right)\rho\left(\mathbf{G}\right)+2\pi\Omega_{cell}\sum_{\mathbf{G}\neq 0}\frac{\rho\left(\mathbf{G}\right)^{2}}{G^{2}}+\gamma_{Ewald}+\frac{N_{e}}{\Omega}\sum_{\kappa}\alpha_{\kappa} \tag{2.104}$$

where

$$\rho_{i\mathbf{k}}\left(\mathbf{G}\right)=\sum_{\mathbf{G},\mathbf{G}'}c^{*}_{i,\mathbf{k}+\mathbf{G}'}c_{i,\mathbf{k}+\mathbf{G}}\qquad\Rightarrow\qquad\rho\left(\mathbf{G}\right)=\frac{1}{N_{k}}\sum_{i,\mathbf{k}}w_{i\mathbf{k}}\rho_{i\mathbf{k}}\left(\mathbf{G}\right) \tag{2.105}$$

Remember that there is a different system of KS equations for each $\mathbf{k}$, therefore the total energy comes from the summation over all the $\mathbf{k}$ vectors in the Brillouin zone. Actually, to speed up the calculations and without loosing accuracy, one may deal only with the $\mathbf{k}$ vectors belonging to the *irreducible* Brillouin zone and then weigth their contributions by the appropriate factor $w_{i\mathbf{k}}$. Note that this is allowed by the symmetry of the Brillouin zone: in fact the non-equivalent $\mathbf{k}$ vectors are only those within the *irreducible* Brillouin zone, which by symmetry transformations generate all the other $\mathbf{k}$ vectors. Consider now the last three terms in eq.2.104. The Coulomb potential and the Ewald term (γ_{Ewald}) are both ill-defined sums, indeed they diverge at some points. Anyway γ_{Ewald} is built in such a way that, when combined with the Coulomb potential, they compensate each other finally giving a regular expression. The last term instead accounts for the energies of the core electrons; due to the frozen core approximation, one may avoid to treat them explicitly in the calculation but their effects need anyway to be included. More details on this topic will be presented in sec.2.2.8.

2.2.4 Janak theorem and quasiparticle gap

In the Kohn-Sham scheme discussed before it has been supposed that the ground state for a N-electron system is described by N orbitals only. Actually this is only a special case of more general forms involving an arbitrary number of orbitals and fractional occupation numbers. In this case the derivation of the KS equations is not very different since most of the terms depend on the electron density and not on the orbitals. However the generalized kinetic energy becomes

$$T_{J}\left[\rho\right]=\sum_{i}n_{i}\int dr\varphi_{i}^{KS*}\left(\mathbf{r}\right)\left[-\frac{1}{2}\nabla^{2}\right]\varphi_{i}^{KS}\left(\mathbf{r}\right) \tag{2.106}$$

where $T_{s}\left[\rho\right]$ in eq.2.81 has been substituted by $T_{J}\left[\rho\right]$, J for Janak, who first dealt with the generalized KS equations; n_{i} is the occupation of the i-th orbital, which satisfies

$$\sum_{i}n_{i}=N\qquad\qquad n_{i}\in\left[0,1\right] \tag{2.107}$$

and the density $\rho\left(r\right)$ is now defined as

$$\rho\left(\mathbf{r}\right)=\sum_{i}n_{i}\varphi_{i}^{KS*}\left(\mathbf{r}\right)\varphi_{i}^{KS}\left(\mathbf{r}\right) \tag{2.108}$$

The generalized energy functional is thus given by

$$\begin{aligned}\tilde{E}^{DFT-KS}[\rho] = &\sum_i n_i \int d\mathbf{r}\varphi_i^{KS*}(\mathbf{r})\left[-\frac{1}{2}\nabla^2\right]\varphi_i^{KS}(\mathbf{r}) + \\ &+ \int d\mathbf{r}\rho(\mathbf{r})V_{ext}(\mathbf{r}) + \frac{1}{2}\iint d\mathbf{r}d\mathbf{r}'\frac{\rho(\mathbf{r})\rho(\mathbf{r}')}{|\mathbf{r}-\mathbf{r}'|} + E_{XC}[\rho]\end{aligned} \tag{2.109}$$

Thus, the ground state energy can be obtained by minimizing $\tilde{E}^{DFT-KS}[\rho]$ with respect to both φ_i^{KS} and n_i. For a fixed set of n_i, the energy is minimized by a set of φ_i^{KS}, as follows

$$\frac{\partial}{\partial\varphi_i^{KS*}(\mathbf{r})}\left\{\tilde{E}^{DFT-KS}[\rho] - \sum_{ij}\lambda_{ij}\left[\int\varphi_i^{KS*}(\mathbf{r})\varphi_j^{KS}(\mathbf{r}) - \delta_{ij}\right]\right\} = 0 \tag{2.110}$$

which leads to

$$\left[-\frac{1}{2}n_i\nabla^2 + n_i V_{eff}(\mathbf{r})\right]\varphi_i^{KS}(\mathbf{r}) = \varepsilon_i^{KS'}\varphi_i^{KS}(\mathbf{r}) \tag{2.111}$$

where $\varepsilon_i^{KS'} = n_i\varepsilon_i$. Then the equation eq.2.111 reduces to a canonical KS equation

$$\left[-\frac{1}{2}\nabla^2 + V_{eff}(\mathbf{r})\right]\varphi_i^{KS}(\mathbf{r}) = \varepsilon_i^{KS}\varphi_i^{KS}(\mathbf{r}) \tag{2.112}$$

To examine the dependence of the energy on the orbital occupation, $\tilde{E}^{DFT-KS}[\rho]$ is differentiated with respect to the occupation number as follows

$$\begin{aligned}\frac{\partial\tilde{E}^{DFT-KS}[\rho]}{\partial n_i} &= \left\langle\varphi_i^{KS}\left|-\frac{\nabla^2}{2}\right|\varphi_i^{KS}\right\rangle + \int\left\{\frac{\partial}{\partial\rho(\mathbf{r})}[J[\rho] + E_{xc}[\rho] + E_{ext}[\rho]]\frac{\partial\rho(\mathbf{r})}{\partial n_i}\right\}d\mathbf{r} = \\ &= \left\langle\varphi_i^{KS}\left|-\frac{\nabla^2}{2}\right|\varphi_i^{KS}\right\rangle + \left\langle\varphi_i^{KS}\left|V_{eff}(\mathbf{r})\right|\varphi_i^{KS}\right\rangle = \varepsilon_i\end{aligned} \tag{2.113}$$

This result is known as the Janak theorem: it is independent on the approximation to the exchange correlation functional and it holds also when the total number of electrons $N = \sum_i n_i$ is not integer. It is absolutely not trivial to infer the distribution of n_i which minimize the energy. One can try by setting $n_i = \cos^2\theta_i$ in agreement with eq.2.107 and then performing the minimization with respect to θ_i. The constraint in eq.2.107 is included with the lagrangian multiplier μ representing the chemical potential at $T = 0\,K$.

$$\frac{\partial}{\partial\theta_i}\left\{n_i\left\langle\varphi_i^{KS}\left|H_{eff}^{KS}\right|\varphi_i^{KS}\right\rangle - \mu\sum_j n_j\right\} = \frac{\partial}{\partial\theta_i}\left\{\cos^2\theta_i\varepsilon_i^{KS} - \mu\sum_j\cos^2\theta_j\right\} = 0 \tag{2.114}$$

Hence,

$$\sin(2\theta_i)\left[\mu - \varepsilon_i^{KS}\right] = 0 \tag{2.115}$$

If $\varepsilon_i^{KS} \neq \mu$ then $\theta_i = 0, \frac{\pi}{2}$ and n_i can assume only two values $n_i = 1, 0$ for occupied or unoccupied orbitals. Only in case the eigenvalue ε_i^{KS} corresponds to the highest eigenvalue, i.e. $\varepsilon_i^{KS} = \mu$, then fractional values of n_i are allowed. Using the Janak's theorem, the energy of the highest orbital is expressed as

$$\tilde{E}_N^{n_N=1} - \tilde{E}_{N-1}^{n_N=0} = \int_0^1 dn_N \frac{\partial \tilde{E}_N(n_N)}{\partial n_N} = \int_0^1 dn_N \varepsilon_N^{KS}(n_N) \tag{2.116}$$

where n_N is the occupation number of the highest orbital, the subscript of $\tilde{E}$ gives the total number of electrons in the system and the subscript of ε^{KS} is the label of the orbital to which the energy refers. In the exact DFT, this finally gives

$$\int_0^1 dn_N \varepsilon_N^{KS}(n_N) = \varepsilon_N^{KS,n_N=1} = \varepsilon_N^{KS} = -IP \tag{2.117}$$

and it is known as Perdew result. In a similar way for *N+1* electrons the energy of the highest orbital reads as,

$$\tilde{E}_{N+1}^{n_{N+1}=1} - \tilde{E}_N^{n_{N+1}=0} = \varepsilon_{N+1}^{KS,n_{N+1}=1} = \varepsilon_{N+1}^{KS} = -EA \tag{2.118}$$

The *quasiparticle* gap, by definition $(IP - EA)$, does not match with the *homo-lumo* gap,

$$IP - EA = \varepsilon_{N+1}^{KS} - \varepsilon_N^{KS} \neq \varepsilon_{lumo} - \varepsilon_{homo} \tag{2.119}$$

since the orbitalic energies ε_N^{KS} and ε_{N+1}^{KS} refer to occupied orbitals, while ε_{lumo} is the energy of the *(N+1)*-th orbital in a system composed by N electrons. Thus

$$\varepsilon_{lumo} = \varepsilon_{N+1}^{n_{N+1}=0} = \varepsilon_{N+1}^{n_{N+1}=1} - \triangle V_{xc} \tag{2.120}$$

where $\triangle V_{xc}$ is a correction related to the exchange-correlation potential, which is included in the energy of the orbital when it is occupied. Thus it follows that the *quasiparticle* gap is underestimated in the *homo-lumo* (Kohn-Sham) gap by a quantity $\triangle V_{xc}$,

$$IP - AE = \varepsilon_{N+1}^{KS} - \varepsilon_N^{KS} = \varepsilon_{lumo} - \varepsilon_{homo} + \triangle V_{xc} \tag{2.121}$$

2.2.5 Spin-density functional theory

The spin-density functional theory is the natural extension of the density functional theory in the presence of an external magnetic field. It also give important contributions in the absence of magnetic field since it allows to improve the description of the exchange-correlation functional, through its spin dependence. Indeed the basic variables are the α and β electron densities, $\rho^\alpha(\mathbf{r})$ and $\rho^\beta(\mathbf{r})$. Thus, the constrained-search for the ground state energy, reads as

$$E_0 = \min_{\rho^\alpha, \rho^\beta} \left\{ F\left[\rho^\alpha, \rho^\beta\right] + \int d\mathbf{r} V_{ext}(\mathbf{r}) \left(\rho^\alpha(\mathbf{r}) + \rho^\beta(\mathbf{r})\right) \right\} \tag{2.122}$$

where

$$F\left[\rho^{\alpha},\rho^{\beta}\right]=\min_{\Psi\to\rho^{\alpha},\rho^{\beta}}\left\langle\Psi\left|\hat{T}+\hat{V}_{ee}\right|\Psi\right\rangle \tag{2.123}$$

According to the Kohn-Sham scheme, the universal functional allows to rigorously handle the kinetic-energy contribution $T_s\left[\rho^{\alpha},\rho^{\beta}\right]$ and to gather all the unknown terms in the exchange-correlation energy. In this case the constrained-search definition of the kinetic energy term, T_s reads as

$$T_s\left[\rho^{\alpha},\rho^{\beta}\right]=\min\left[\sum_{i\sigma}n_{i\sigma}\left\langle\varphi_{i\sigma}\left|-\frac{\nabla^2}{2}\right|\varphi_{i\sigma}\right\rangle\right] \tag{2.124}$$

where $\sigma=\alpha,\beta$ and the constraint over the $\sigma-$electron density ($\rho^{\sigma}=\sum_{i\sigma}n_{i\sigma}\left|\varphi_{i\sigma}\right|^2$) holds. In practice, the occupation numbers $n_{i\sigma}$ are chosen so that the N lowest eigenstates are occupied ($n_{i\sigma}=1$) and the rest are empty ($n_{i\sigma}=0$). In the same fashion as in sec.2.2.4 for a fixed set of $n_{i\sigma}$, the energy functional is minimized with respect to the orbitals $\phi_{i\sigma}$, that must satisfy the normalization constraint. The final result are the two following sets of KS equations for α and β electrons:

$$\hat{h}^{\sigma}_{eff}\varphi_{i\sigma}\left(\mathbf{r}\right)=\left[-\frac{1}{2}\nabla^2+V^{\sigma}_{eff}\left(\mathbf{r}\right)\right]\varphi_{i\sigma}\left(\mathbf{r}\right)=\varepsilon_{i\sigma}\varphi_{i\sigma}\left(\mathbf{r}\right)\qquad\begin{matrix}i=1,...N^{\sigma}\\\sigma=\alpha,\beta\end{matrix} \tag{2.125}$$

where

$$V^{\alpha}_{eff}=\int\frac{\rho^{\alpha}\left(\mathbf{r}'\right)}{\left|\mathbf{r}-\mathbf{r}'\right|}d\mathbf{r}'+V_{ext}\left(\mathbf{r}\right)+\frac{\partial E_{xc}\left[\rho^{\alpha},\rho^{\beta}\right]}{\partial\rho^{\alpha}\left(\mathbf{r}\right)} \tag{2.126}$$

and analogously for V^{β}_{eff}. Note also that the number of α and β electrons is

$$N^{\alpha}=\int d\mathbf{r}\rho^{\alpha}\left(\mathbf{r}\right)\qquad N^{\beta}=\int d\mathbf{r}\rho^{\beta}\left(\mathbf{r}\right)\qquad N=N^{\alpha}+N^{\beta} \tag{2.127}$$

There is also a spin polarized version of the Janak's theorem that reads as $\partial E/\partial n_{i\sigma}=\varepsilon_{i\sigma}$.
The spin-polarized density-functional theory compared to the original (spin-compensated) version has the obvious advantage to be capable of treating many-electron systems when a magnetic field is present. However the major advantage appears with no magnetic field. In this case, in the limit of an exact exchange-correlation functional $E_{xc}\left[\rho^{\alpha},\rho^{\beta}\right]$ the spin-polarized Kohn-Sham results reduce to those expected from spin-compensated version. But the exact functional is not known and the approximated spin-density functional $E_{xc}\left[\rho^{\alpha},\rho^{\beta}\right]$ is usually a better description of the real system than $E_{xc}\left[\rho\right]$; this is surely the case of spin-polarized systems, such as open-shell atoms and molecules. Moreover, the α and β orbitals are obtained self-consistently from eq.2.125, and in principle are allowed to be different. This flexibility is very useful when dealing with large bond lenghts, providing an accurate description of molecules close to their dissociation limit. In the presence of a perfect matching between α and β orbitals, that is the paramagnetic case, the non-interacting kinetic term

is spin-independent, in fact

$$T_s\left[\rho^\alpha,\rho^\beta\right]=T_s\left[\rho^\alpha\right]+T_s\left[\rho^\beta\right]=T_s\left[\frac{1}{2}\rho,\frac{1}{2}\rho\right]=T_s\left[\rho\right] \tag{2.128}$$

On the other hand, the exact exchange-correlation energy functional $E_{xc}\left[\rho^\alpha,\rho^\beta\right]$ separates into its components, $E_x\left[\rho^\alpha,\rho^\beta\right]$ and $E_c\left[\rho^\alpha,\rho^\beta\right]$. The exchange term, like the non-interacting kinetic term, can be easily written as a sum of spin-α and β contributions

$$E_x\left[\rho^\alpha,\rho^\beta\right]=E_x\left[\frac{1}{2}\rho,\frac{1}{2}\rho\right]=E_x\left[\rho\right] \tag{2.129}$$

while the correlation term cannot be decomposed into a sum of two different spin contributions, because the correlation energy contains the effects of both like-spin and unlike-spin electron-electron interactions.

2.2.6 Describing the exchange-correlation functional

2.2.6.1 Local density approximation

With the KS equations the kinetic energy is handled exactly and only the exchange-correlation energy remains to be determined. It is very important to realize that if the exact form of the exchange and correlation functional were known, the solution of the KS equations would finally lead to the exact ground state energy and the exact electron density, since the method is exact in principle. The search for an accurate $E_{xc}\left[\rho\right]$ has encountered tremendous difficulty and up to now the exact explicit expression for $E_{xc}\left[\rho\right]$ is still not available. Nevertheless many approximated forms have been proposed in order to specify the KS equations. The simplest approximation is the so called local-density approximation (LDA) for exchange and correlation energy, based on the assumption that the real system behaves locally as an homogeneus electron gas, known as the Fermi gas. This turns out to be a good approximation for metallic systems, but it fails badly for insulators and semiconductors. Within this approach, the real system is divided into infinitesimal portions, each having $\int\rho\left(\mathbf{r}\right)d\mathbf{r}$ electrons and behaving as an homogeneus gas. The exchange-correlation energy of the real non uniform system is then obtained as the sum of the contributions from all these parts.

$$E_{xc}^{LDA}\left[\rho\right]=\int\rho\left(\mathbf{r}\right)\varepsilon_{xc}\left(\rho\right)d\mathbf{r} \tag{2.130}$$

where $\varepsilon_{xc}\left(\rho\right)$ is the exchange and correlation energy per particle of a uniform electron gas of density ρ. The corresponding exchange-correlation potential is given by

$$V_{xc}^{LDA}\left(r\right)=\frac{\partial E_{xc}^{LDA}\left[\rho\right]}{\partial\rho\left(\mathbf{r}\right)}=\varepsilon_{xc}\left(\rho\left(\mathbf{r}\right)\right)+\rho\left(\mathbf{r}\right)\frac{\partial\varepsilon_{xc}\left(\rho\right)}{\partial\rho\left(\mathbf{r}\right)}. \tag{2.131}$$

where ε_{xc} is a function and not a functional of the electron density. Its analytic form is unknown but it has been parametrized in several ways, usually based on the separation between the exchange and correlation contributions, respectively ε_x and ε_c. The first can be derived from the Dirac exchange

energy functional, while accurate values for ε_c come from accurate Monte Carlo calculations by Adler-Ceperley[19].

In the same fashion, the local spin density approximation (LSDA) has been developed to approximate the exchange-correlation energy functional for open-shell systems, which are usually treated within the spin-DFT. In LSDA the real system is described locally by an homogeneous spin-polarized electron gas and the polarization effects are taken into account through the spin polarization parameter ζ defined as

$$\zeta = \frac{\rho^{\alpha} - \rho^{\beta}}{\rho^{\alpha} + \rho^{\beta}} \tag{2.132}$$

Accordingly, two limit cases may be thought, namely $\zeta = 0$ for spin-compensated systems and $\zeta = 1$ for spin-completely-polarized systems. Like within the LDA scheme, in the LSDA the exchange and correlation contributions to the total functional $E_{xc}^{LSDA}\left[\rho^{\alpha}, \rho^{\beta}\right]$ are separated in $E_{x}^{LSDA}\left[\rho^{\alpha}, \rho^{\beta}\right]$ and $E_{c}^{LSDA}\left[\rho^{\alpha}, \rho^{\beta}\right]$ and then treated independently.

2.2.6.2 Other approaches

The local density approximation is expected to fail when applied to systems with less homogeneus electron density. More sophisticated functionals are for instance those depending on both the electron density $\rho(\mathbf{r})$ and the electron density gradient $\nabla\rho(\mathbf{r})$. They are still local and are usually addressed as generalized gradient approximation (GGA) functionals:

$$E_{xc}^{GGA}[\rho] = \int \rho(\mathbf{r})\, \varepsilon_{xc}(\rho, \nabla\rho)\, d\mathbf{r} \tag{2.133}$$

Instead of making local approximations of both the exchange and the correlation energy, another possibility is to include the exchange effects exactly, leaving only the correlation energy to be approximated. By introducing the exchange energy in the same way as in the HF approximation, the exchange-correlation energy functional reads as

$$E_{xc}[\rho] = -\frac{1}{2} \iint \frac{\rho_1\left(\mathbf{r}, \mathbf{r}^{'}\right) \rho_1\left(\mathbf{r}^{'}, \mathbf{r}\right)}{|\mathbf{r} - \mathbf{r}^{'}|} d\mathbf{r} d\mathbf{r}^{'} + E_c[\rho] \tag{2.134}$$

and the resulting effective potential is

$$V_{eff}\left(\mathbf{r}, \mathbf{r}'\right) = \left[V_{ext}(\mathbf{r}) + \int \frac{\rho\left(\mathbf{r}^{''}\right)}{|\mathbf{r} - \mathbf{r}^{''}|} d\mathbf{r}^{''} + \frac{\delta E_c[\rho]}{\delta\rho(\mathbf{r})} \right] \delta\left(\mathbf{r} - \mathbf{r}^{'}\right) - \int \frac{\rho_1\left(\mathbf{r}^{'}, \mathbf{r}\right)}{|\mathbf{r} - \mathbf{r}^{'}|} d\mathbf{r}^{'} \tag{2.135}$$

Within this scheme, known as Hartree-Fock-Kohn-Sham method, the characteristic eigenvalue equations differ from both the KS equations, due to the presence of a non-local effective potential, and from the Hartree-Fock equations, due to the correlation energy contribution. Interestingly, if the last were know exactly, the exact energy and electron density would be achieved; moreover by keeping only a fraction of the exact exchange energy, one generates a slightly different class of methods

based on the so called *hybrid* functionals. In conclusion, note anyway that due to the high computational cost in computing the exchange energy, these methods are still not so popular. Of course many other approximated descriptions exist and an exenstive discussion about several exchange and correlation functional can be found in literature[24, 81, 87]. For this reason when starting with a new system, one should know that there is not a functional better than another one, but the suitable functional can be chosen only after a careful screening over the several possibilities.

2.2.7 Self-interaction correction

It is very important to be aware of the fact that many good results of L(S)DA are due to a cancellation of errors, since it was shown that this approximation underestimates E_x, while overestimating E_c. To get improvements upon the local (spin) density approximation, it is important to look at the problem of self-interaction, namely the interaction of one electron with itself via the Coulomb potential. In the hamiltonian in eq.2.57 the electron-electron interaction term excludes the self-interaction, as it is clearly shown in the Hartree-Fock approximation: in this case indeed the self-interaction in the Coulomb term cancels exactly with the one in the exchange term. Differently, in the approximated DFT (including LDA, LSDA,..) a spurious self-interaction is contained that can not be easily ruled out. This problem comes from the classical expression of the Coulomb energy for a given electron density $J[\rho]$, which allows the unphysical interaction of one electron with itself. Naturally, the exact expression of $E_{xc}[\rho]$ in the KS equations is expected to perfectly compensate this error, but for approximate functionals this is not the case. In the limit of no self-interaction the following requirement over a one-electron system is fulfilled:

$$V_{ee}[\rho_i^\alpha, 0] = J[\rho_i^\alpha] + E_{xc}[\rho_i^\alpha, 0] = 0 \tag{2.136}$$

where ρ_i^α is the single electron density for the i-th orbital and $\rho_i^\beta = 0$. Unfortunately the expression in eq.2.136 is true only for the exact functional, otherwise representing an estimate of the self-interaction contribution and it can be used in the self-interaction corrected (SIC) version of $E_{xc}[\rho]$ as follows

$$E_{xc}^{SIC}\left[\rho^\alpha, \rho^\beta\right] = E_{xc}\left[\rho^\alpha, \rho^\beta\right] - \sum_i \left[J[\rho_i^\alpha] + E_{xc}[\rho_i^\alpha, 0]\right] \tag{2.137}$$

where the SIC procedure would not change the exact functional, if it were known, since in that case eq.2.136 would be zero.

2.2.8 The pseudopotential method

It is not trivial to map the electronic wavefunction over the volume of interest for the system under investigation. Indeed even in case of few tens of atoms, a significant effort is needed as for each atom of the system, one has to represent each Kohn-Sham orbital φ_i^{KS} throughout the volume. Furthermore in the atomic core region, the wavefunctions oscillate strongly due to the high kinetic energy. This means that one should use a very dense uniform grid or alternatively a very large

plane wave basis set to be able to give an accurate representation of such wavefunctions. Anyway it is clear that from a chemical point of view not all the electrons have the same importance. Indeed the inner (core) electrons are almost chemically inert while the most of reactivity is ruled by the outer (valence) electrons. A consequence of this observation is the frozen core approximation which states that the core orbitals can be held fixed while the total energy is minimised. These orbitals are usually kept in the form they have in the isolated atom as they are almost unaffected by any external perturbation. The pseudopotential method is widely used to represent the electronic wavefunction within the DFT theory and it has its foundation on the frozen-core approximation. The key-point of the pseudopotential method is the substitution of the strong potential exerted by the core electrons on the valence electrons by a much weaker pseudopotential so that: (i) the core orbitals are taken out from the explicit treatment, and (ii) the pseudo valence orbitals become smooth with no oscillations close to the nuclei. In general the potential of an atom is the sum of a nuclear part and two electronic parts, due to core and valence electrons. The sum of the nuclear plus the core electron potentials gives the ionic potential. Due to the frozen core approximation, one can just retain this term and forget about the core wavefunctions and orbital energies. Anyway in the all-electron framework, the core electrons do not only participate in the potential acting on the valence electrons, but core orbitals also contribute to the orthogonality constraint. Note that this constraint is crucial to prevent valence orbitals from collapsing into the core regions during the minimisation processes. The solution proposed by the pseudopotential method is to replace the true ionic potential with an ionic pseudopotential, where the valence wavefunctions become pseudo valence wavefunctions. The pseudopotential is chosen in such a way that the all-electron and pseudo wavefunctions have the same energies, so that the orthogonality effect from the core electrons is retained even without treating them explicitely. The crucial parameter in the generation of a pseudopotential is the core radius r_c beyond which the true ionic potential and the pseudopotential are equivalent. Inside r_c the all-electron valence orbitals and the pseudo valence orbitals behave differently as the last are nodeless and therefore they do not have oscillations. However both the functions have the same energy and outside r_c they have also the same form. In general a single-atom pseudopotential is given by

$$V^{PP}\left(\mathbf{r},\mathbf{r}^{'}\right)=\sum_{l=1}^{\infty}\sum_{l=-m}^{m}Y_{lm}^{*}\left(\omega\right)V_{l}\left(\mathbf{r}\right)\delta\left(\mathbf{r}-\mathbf{r}^{'}\right)Y_{lm}\left(\omega^{'}\right) \tag{2.138}$$

where $Y_{lm}\left(\omega\right)$ are spherical harmonics and ω Euler angles of the position vector $\mathbf{r}$. Note that the radial dependence of the potential V^{PP} is given by the radial function $V_l\left(\mathbf{r}\right)$ that depends on both the radius $\mathbf{r}$ and the angular momentum. This feature is typical of *nonlocal* pseudopotentials (also known as angular momemtum-dependent pseudopotentials) while a *local* pseudopotential only depends on $\mathbf{r}$.

In order to get the above features, a pseudopotential must satisfy a number of conditions: (i) it has to be weak compared to the true ionic potential inside r_c; (ii) it has to be smooth, thus at the core radius r_c the potential and its derivative should be continous; (iii) finally it has to be transferable, thus it has to work properly in different situations, for instance in different chemical environments.

2.2.8.1 Norm-conserving pseudopotentials

The norm-conserving pseudopotentials as originally introduced by Haman, Schluter and Chiang[8, 36] meet all the general requirements listed above. More precisely, (i) the all-electron wavefunction ψ_l and the pseudo wavefunction ϕ_l are identical outside r_c and (ii) they have equal eigenvalues. In addition (iii) the pseudo wavefunction and the all-electron wavefunction have the same norm inside the core region even if they have different form; (iv) also the logarithmic derivatives of the two wavefunctions and their first energy derivatives are equal in the region outside the core radius.
In general the pseudopotential reproduces exactly the all-electron wavefunction only in the reference configuration in which it was generated. Anyway it is requested to closely reproduce all-electron calculations even in different environments. This means that it has to be transferable. A straightforward method to check transferability is to compare the logarithmic derivatives of all-electron and pseudo wavefunctions in different systems; anyway more advanced approaches have been developed[32, 33, 105]. The easiest way to enhance transferability is to reduce the core radius r_c used to generate the pseudopotential and the pseudo wavefunction. However, there are practical limits on how far one can reduce r_c; indeed it must be larger as the outermost node of the all electron wavefunction in order to generate a nodeless pseudo wavefunction. In fact for r_c too close to the node, the pseudopotential starts to oscillate and thus a larger plane wave basis set is needed to describe the pseudo wavefunction.

2.2.8.2 PAW and ultrasoft pseudopotentials

For elements with highly localized orbitals, as first row and 3d elements, the appropriate core radius is small and the resulting pseudopotentials require large plane waves basis sets. In the attempt to avoid large basis sets, compromises are often necessary. One possibility is to reduce the plane wave cutoff, thus however sacrificing accuracy and reliability; alternatively the core radius can be enlarged, but in this way the transferability is diminished.
The ultrasoft pseudopotential method proposed by Vanderbilt[107] gives a possible solution to the problem. In this method the norm-conservation constraint is relaxed and localized atom-centered augmentation charges are introduced to make up the resulting wrong charge distribution. These augmentation charges are defined as the charge difference between the all-electron and pseudo wavefunctions, and they are usually transformed into pseudo charges. The core radius of the pseudopotential can here be chosen close to the nearest-neighbours distance independently on the position of the outermost node of the all-electron wavefunction. This allow to significantly reduce the size of the basis set needed to get reliable results. Only the core radius of the pseudo charges has to be small enough to reproduce the charge distribution of the all-electron wavefunction accurately. The pseudo augmentation charges are usually mapped onto a regular grid in real space, which is not necessarily the same grid used to describe the wavefunctions.
The ultrasoft pseudopotentials can be formally derived from the projector augmented-wave (PAW) method[58]. In this derivation the key-point is to transform the all-electron external potential of the

PAW into a norm-conserving pseudopotential. Differently from the techniques described above, the projector augmented-wave method[14] proposes an alternative way to represent the wavefunction which does not make use of any pseudopotential. The PAW method divides the whole space Ω into non-overlapping spherical regions around each atom Ω_a and interstitial space Ω_I, thus giving $\Omega = \Omega_I + \cup_a \Omega_a$. It is clear that the plane waves description is the ideal choice for the interstitial region but not for the atomic spheres. To solve the problem, auxilary wavefunctions $\tilde{\phi}_i(\mathbf{r})$ are generated from the all-electron wavefunction $\phi_i(\mathbf{r})$ via an invertible linear transformation. The new wavefunctions $\tilde{\phi}_i(\mathbf{r})$ are smooth, so that they can be expanded into a practicable number of plane waves. It thus comes straightforwardly that the Kohn-Sham problem can be reformulated in terms of $\tilde{\phi}_i(\mathbf{r})$ and the whole problem can be treated within the plane waves basis set. Moreover in a given atomic space Ω_a, the all-electron wavefunction $\phi_i(\mathbf{r})$ may be described in terms of atomic centered functions $\{\chi^a_\alpha\}$; similarly the auxiliary wavefunction $\tilde{\phi}_i(\mathbf{r})$ is associated to the auxiliary set of atomic centered functions $\{\tilde{\chi}^a_\alpha\}$. Note that $\tilde{\chi}^a_\alpha(\mathbf{r})$ merges into $\chi^a_\alpha(\mathbf{r})$ in the interstitial region, while in the atomic region $\tilde{\chi}^a_\alpha(\mathbf{r})$ is smooth, thus it can be expanded in terms of plane waves with a practicable cutoff. Given these properties of the basis set $\{\tilde{\chi}^a_\alpha\}$, the resulting wavefunction $\tilde{\phi}_i(\mathbf{r})$ is smooth inside the atomic sphere, while it equals $\phi_i(\mathbf{r})$ in the interstitial space. The peculiar feature of the PAW method is that it is in principle an all-electron approach. For practical reasons, the dimensionality of the system is typically reduced by the frozen core approximation; therefore the sum over states is restricted to valence electrons only. Anyway the electronic density always includes contributions from the core electrons and the $\tilde{\chi}^a_\alpha$ basis functions have to be orthogonal to the core states of the atom. The potential term in the total energy expression refers to an arbitrary local potential localized in the augmentation regions, i.e. inside the atomic spheres Ω_a. This contribution vanishes if a complete expansion in plane waves is done; therefore it can be used to minimise the truncation errors. In addition in PAW the point charge density of the nuclei and the compensation charge density inside the atomic regions are introduced.

Chapter 3

Spin coupling around a carbon vacancy in graphene

In this chapter we investigate the details of the electronic structure in the neighborhoods of a carbon atom vacancy in graphene by employing magnetisation-constrained density-functional theory on periodic slabs, and spin-exact, multi-reference, second-order perturbation theory on a finite cluster. The picture that emerges is that of two local magnetic moments (one π-like and one σ-like) decoupled from the π band and coupled to each other. We find that the ground state is a triplet with a planar equilibrium geometry where an apical C atom opposes a pentagonal ring. This state lies $\sim$0.2 eV lower in energy than the open-shell singlet with one spin flipped, which is a bistable system with two equivalent equilibrium lattice configurations (for the apical C atom above or below the lattice plane) and a barrier $\sim$0.1 eV high separating them. Accordingly, a bare carbon-atom vacancy is predicted to be a spin-one paramagnetic species, but spin-half paramagnetism can be accommodated if binding to foreign species, ripples, coupling to a substrate, or doping are taken into account.

3.1 Magnetism in graphene: theoretical background and experiments

Magnetism in graphene is a fascinating and highly controversial matter[50]. Early reports on ferromagnetic ordering in graphite and graphene[10, 28, 29, 109] have been questioned in the light of the ubiquitous presence of magnetic contaminants, and measurements under carefully controlled conditions showed that graphene, like graphite, is strongly diamagnetic with a weak paramagnetic contribution from adatoms and/or carbon atom vacancies[99]. Simple adsorbates such as fluorine and missing carbon atoms have been shown to provide a spin-1/2 paramagnetic response[74], though spin-1 paramagnetism has been reported upon N^+ irradiation[3].

In the theoretical perspective, perfect bipartite systems support a number of zero-energy "midgap" states which is greater or equal than the sublattice imbalance $|n_A - n_B|$, where n_A,n_B are the number of sites in the two sublattices[31, 41]. When imbalance results from isolated missing p_z orbitals (*e.g.* for low concentrations of covalently bound adatoms or vacancies) these states decay

slowly ($\sim 1/r$) from the defects and localize on the locally majority sites[88, 89], as also found by scanning tunneling microscopy/spectroscopy measurements on irradiated graphite[68]. Thus, these defects form quasi-localized π moments, which couple to each other either ferromagnetically or antiferromagnetically depending on their lattice position. In fact, with local interactions only, at charge neutrality (half-filling) the spin state of the system exactly matches the sublattice imbalance[64], $S = |n_A - n_B|/2$, and thus coupling is ferromagnetic for defects in the same sublattice and antiferromagnetic otherwise. Within the same assumptions (perfect electron-hole symmetry, local interactions only) coupling between π moments and conduction states has been investigated beyond mean-field approaches by means of dynamical mean field theory and found to be ferromagnetic[79], thereby confirming that simple adatoms covalently bound to the substrate (*e.g.* H, F species) behave as spin-1/2 localized moments. In turn, this also affects chemical properties and favours formation of dimers of balanced type[16, 40].

This simple picture has to be revised for a carbon atom vacancy where, in addition to the above π midgap state, three σ orbitals are left singly occupied upon vacancy formation, and a structural instability (Jahn-Teller distortion) arises which breaks electron-hole symmetry, even if nearest neighbors interactions only are retained. The ensuing lattice re-arrangement leaves two unpaired electrons, and a magnetic moment in the range $2.0 - 1.0\,\mu_B$ has been found by (ensemble) density functional theory (DFT) calculations[2, 22, 63, 80, 113, 115], with a tendency to $1.0\,\mu_B$ in the low-density limit[80]. The latter result (along with the observed vanishing dependence of the energy on the magnetisation[80]) signals the absence of any magnetic order at experimentally relevant concentrations, and only apparently conflicts with the the presence of both a σ and a π moment (see below). Recent experiments have indeed shown that the spin$-1/2$ paramagnetism of missing carbon atoms has two contributions[75], from σ and π states respectively, and one of them can be quenched upon molecular doping and possibly by means of the electric field effect[75]. Yet, this remarkable result requires that the unpaired electrons around a vacancy negligibly interact with each other, in contrast with early reports on spin-1 paramagnetism of irradiated graphene samples[3]. Proper consideration of σ states, and their possible hybridization with π states when the substrate is no longer locally planar, *e.g.* because of ripples or interaction with a substrate[69], has led to reconsidering the issue of the interaction between the localized magnetic moments and the conduction electrons[66, 72], though the above mentioned recent experiments[75] seem to rule out this possibility.

Here, in order to help shed light on the above issues we re-consider in detail the electronic structure around a carbon atom vacancy in graphene, by employing both conventional DFT methods in periodic models and accurate, spin-exact quantum chemistry methods in a finite cluster. Such combined analysis was motivated by the fact that current DFT approaches often prove to be unsatisfactory to discuss the spin-properties of many-electronic systems, for reasons which essentially lie in the common *abuse* of the theory in describing properties other than the ground-state energy by means of the reference Kohn-Sham non-interacting system. Among the latter, the correct spin state of very simple systems such as open-shell atoms or the dissociating ground-state H_2 molecule, cannot be

encoded in a single (Kohn-Sham) determinant, irrespectively of the functional used. To this we add that if fractional occupation of single-particle levels is allowed, as done in ensemble-DFT[1], further problems may arise from the ensemble average, which may cause non-zero magnetic moments to be apparently quenched when they are actually rotationally averaged, where this case is signaled by a vanishing dependence of the energy on the magnetic moment. All these problems are easily detected (and cured) in finite systems but might also be relevant for localized electrons in extended systems where their identification is not always trivial, as we argue is here the case for a carbon atom vacancy in graphene.

To address this kind of problems methods which explicitly handle electron correlations are more appropriate. Among these, the above mentioned dynamical mean field theory[34, 53] seems to be the most promising in condensed phases, especially if used in conjunction with first-principles determination of lattice parameters and interaction energies [39], and has been successfully applied to a number of strongly correlated electron problems[34, 53]. In the method one replaces a lattice model with local interactions by a single-site, open-system problem to be determined self-consistently, which in turn is conveniently mapped into an Anderson impurity model[2] and solved by various means[34, 53]. In this way, though freezing spatial fluctuations, one captures the important temporal fluctuations beyond Hartree-Fock theory which dominate for large coordination numbers.

[1]The ensemble-DFT is a theoretical approach particularly useful to deal with degenerate states, namely in open shell systems, and with metals, where a number of unoccupied orbitals appear close to the Fermi level. These systems are considered as mixed states as they cannot be described by a single wavefunction but they need an *ensemble* of wavefunctions on which it is possible to define the ensemble density,

$$\rho^e = \sum_i p_i \left|\Psi_i\right\rangle \left\langle\Psi_i\right|$$

where p_i is the probability to find the system in $|\Psi_i\rangle$ and the sum is over all the accessible pure states. For $|\Psi_i\rangle$ orthonormal, p_i has to be: $p_i \geq 0$ and $\sum_i p_i = 1$. According to the ensemble minimum principle, $\sum_i E_i \leq \sum_i p_i \left\langle\Psi_i\right| \mathcal{H}_V \left|\Psi_i\right\rangle$, where $\mathcal{H}_V$ is the hamiltonian operator in the external potential V. Then the procedure is in two steps: at first one has to find the energy by minimizing with respect to the wavefunctions in the ensemble, that give a certain ensemble density ρ^e

$$E_V^e\left[\rho^e\right] = \min_{\Psi_i \to \rho^e} \sum_i p_i \left\langle\Psi_i\right| \mathcal{H}_V \left|\Psi_i\right\rangle$$

then, one has to minimize the energy with respect to an ensemble density ρ^e that accounts for the N electrons in the system

$$E_V^e = \min_{\rho^e \to N} E_V^e\left[\rho^e\right]$$

thereby leading to the optimized partial occupation of the spin orbitals.

[2]The Anderson model is useful to deal with a system in which cohexist an *impurity*, namely a localized state ϕ_d, and a band of states ϕ_k. The associated hamiltonian within the second quantization formalism reads as

$$\mathcal{H} = \sum_k \varepsilon_k a_k^\dagger a_k + \sum_{i=\alpha,\beta} \varepsilon_d d_i^\dagger d_i + \sum_k V_{kd}\left(a_k^\dagger d + d^\dagger a_k\right) + U\left(d_\alpha^\dagger d_\alpha + d_\beta^\dagger d_\beta\right)$$

where $a_k^\dagger$ and a_k are the creation and annihilation operators in the state ϕ_k with on-site energy ε_k and $d_i^\dagger$ and d_i are the creation and annihilation operators for α and β electrons in the impurity ϕ_d state with on-site energy ε_d. Moreover, V_{kd} accounts for the hopping between ϕ_k and ϕ_d and is responsible for the broadening of the impurity level ϕ_d, while U represents the on-site repulsion due to the double occupation of the ϕ_d state. This term U accounts for the existence of singly occupied states below the Fermi level, in case the double occupation is so repulsive as to shift them above the Fermi level. This description applies to the case of the carbon vacancy, where the bands of graphene interact with the localized σ or quasi-localized π states. These behave like impurities and correspond to singly occupied orbitals placed below the Fermi level; in this case, for a wide interval of geometries of the reconstructed vacancy, the double occupation is prevented as too much repulsive.

Occasionally, one may also make profitably use of well-developed quantum chemistry methods to describe atomic-like features at the expense of introducing a finite-size model of the system under investigation. Such methods focus on the full system wavefunction of the zero-temperature case, and aim at recovering as much correlation energy as possible by means of multi-determinantal functions, typically following either a variational or a perturbative scheme, or a combination thereof. They have been recently used, for instance, to investigate the spin state and energetics of a transition metal atom on graphene [96].
The approach we chose in this work (called CASPT2) belongs to this second class and likely represents nowadays the best compromise between accuracy and manageability. It is a second-order perturbative method which differs from conventional Möller-Plesset perturbation theory (MPn) in the choice of the reference problem. Indeed, it uses a multi-determinant reference function to solve, with a few determinants, the near-degeneracy problems which typically spoil MPn, thus making a perturbative approach reliable. More accurate methods, from exact diagonalization (in a truncated single-particle space) to coupled-cluster theory (the gold-standard in quantum chemistry), suffer from awful scaling problems which prevent their application to any reliable finite-size graphene model with a missing carbon atom.
Admittedly, even for CASPT2 the system size one can manage is rather modest and, therefore, in order to assess the role that extended states may have on the problem, we performed in parallel the magnetisation constrained DFT study mentioned above. Our approach is thus validated *a posteriori* by the ensuing semi-quantitative agreement between the two sets of results, on the light of the complementary limitations of the two strategies. Specifically, as detailed below in the following sections, we investigated the energetics of several substrate geometries close to the equilibrium one, focusing in particular on the out-of-plane movement of the carbon atom where most of the unpaired electron density resides. We considered the lowest-energy spin states and found, as expected, that the triplet is the ground-state and has a planar equilibrium geometry. However, we also found that the singlet (previously noticed in DFT calculations[69]) is only ~ 0.2 eV above it, it is stable out-of-plane and becomes the ground-state for a reasonably small out-of-plane distortion. Hence, we conclude that both spin-1 and spin-1/2 paramagnetism may in principle arise in irradiated graphene, depending on local interactions, curvature, etc. of the graphene sheet, in addition to doping or chemical interactions with foreign species.
This chapter is organized as follows: in section 3.2 we outline the Jahn-Teller distortion occurring in the system and associated to the reconstruction of the vacancy; then in section 3.3 we report the details of the electronic structure methods adopted in this work and the obtained results are reported and discussed in sections 3.4 and 3.5.

3.2 Jahn-Teller distortion

The formation of a carbon atom vacancy gives rise to localized states around the vacancy, namely one π (semilocalized) *midgap* state and three dangling orbitals in the σ network which result from

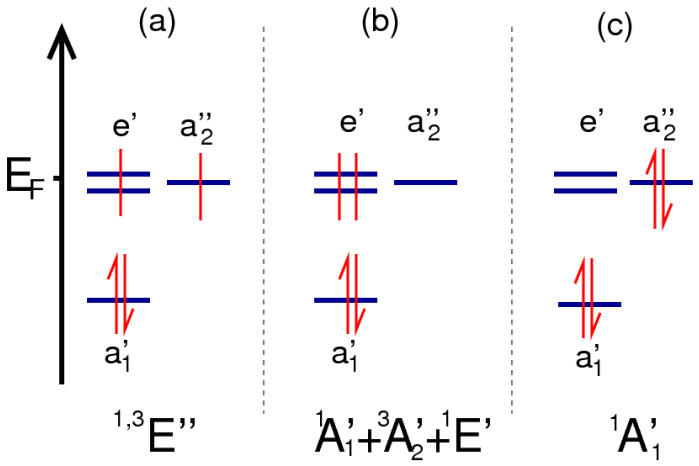

Figure 3.1: lowest energy configurations arising from different arrangements of the four unpaired electron on the vacancy: (a) is the ground state; (b) is based on the electronic transfer from $\pi\,(a_2'') \rightarrow \sigma(e')$ orbitals; (c) is based on the electronic transfer from $\sigma(e') \rightarrow \pi\,(a_2'')$ orbitals.

breaking the sp^2 bonds which hold the carbon atom in place. In the local D_{3h} point symmetry group which is appropriate to discuss proper and pseudo Jahn-Teller distortions, the first belongs to a_2'' symmetry species, and the latter span $a'_1 + e'$ irreducible representations, a'_1 being lowest in energy since it contains a purely bonding combination of σ orbitals. As illustarted in fig.3.1, the lowest energy scenarios for the many-body electronic state can be obtained by distributing two electrons in the e' and a_2'' states, *i.e.* starting from configurations of the type $..(a'_1)^2(e')^{n_1}(a''_2)^{n_2}$ with $n_1 + n_2 = 2$. Among these, the one with $n_1 = n_2 = 1$ is expected to be lowest in energy and gives rise to many-body states of E'' symmetry for both the parallel and antiparallel alignment. The remaining possibilities with two electrons in the same set of states are pushed up in energy by a larger Coulomb repulsion and have symmetries ${}^1A'_1 + {}^3A'_2 + {}^1E'$ for $n_1 = 2$ and ${}^1A'_1$ for $n_2 = 2$. So that, the ground-state is doubly degenerate for both spin alignments and undergoes (proper or pseudo) Jahn-Teller distortion. As summarized in fig.3.2, this occurs because of coupling with in-plane e' vibrations ($[E'']^2 = [E']^2 = A' + E'$) which distort the symmetric arrangement of the carbon atoms around the vacancy. This is a standard $E \otimes e$ problem which is described by the so-called *tricorn* when such vibrations are included up to second-order[12, 13]. This peculiar shape of the potential energy surface is due to the presence of three degenerate equilibrium configurations with distorted geometries produced by a combination of the two vibrational components Q_ε and Q_θ. In several recent investigations[2, 22, 63, 80, 113, 115] a reconstructed vacancy with a pentagonal ring in front of an apical carbon (atom 1 in Fig.3.4) has been found; this is likely associated to the minimum geometry located along Q_θ axis.

Out of plane, e'' vibrations do not lift degeneracy at first-order, but may affect energetics at higher orders, especially if coupling to the low-lying excited states is considered[13]. In this way a pseudo Jahn-Teller distortion is observed, that here comes along with the traditional one; this means that the carbon atoms in planar distorted geometry start to vibrate in the normal direction to the molecular plane, as reported in fig.3.3. This is particularly important here since such distortions are

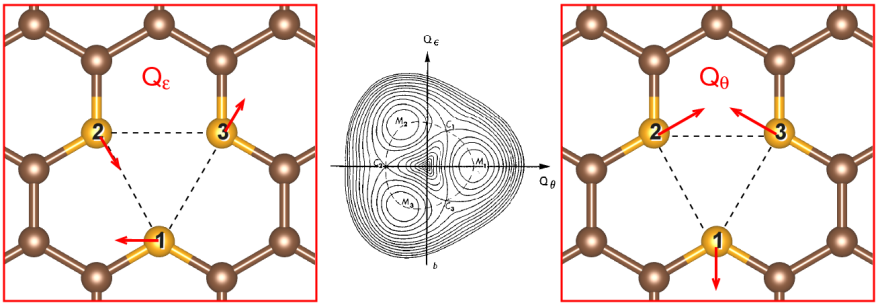

Figure 3.2: Q_ε(left panel) and Q_θ(right panel) are the degenerate components of the e' vibration; equipotential sections of the adiabatic potential energy surface (APES) of the electronic state E'' as a function of Q_ε and Q_θ (central panel).

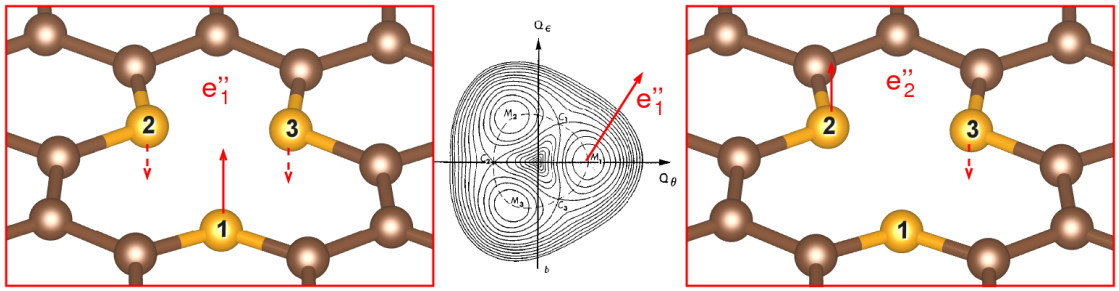

Figure 3.3: (left and right panel) normal modes of the degenerate out of plane vibration e''; (central panel) the e_1'' vibration applied to a standard $E \otimes e$ problem leading to a so called pseudo-JT problem. Note that the axes representing different normal modes are mutually orthogonal.

qualitatively different for the states $..\pi^1\sigma^1$ depending on whether the spins are parallel or antiparallel to each other. This is evident for the out-of-plane movement of the apical carbon atom, shown as the e_1'' normal mode in fig.3.3, in the distorted configuration: the σ and the π states may hybridize to some extent (and gain energy from double filling) if the two electrons couple at low-spin, otherwise they require extra energy to reduce their overlap. As a consequence, the planar structure is expected to be stable in the triplet state only; in the singlet, a non-planar configuration with the apical carbon atom slightly above (or below) the surface plane appears to be more stable. This means that upon taking into account the distortion along e_1'' in fig.3.3, the adiabatic potential energy surface for the triplet state still shows three equivalent minima corresponding to planar geometries, while for the singlet state six equivalent minima corresponding to non-planar geometries are expected. Because of that, the relative stability of the two spin states is geometry-dependent and its analysis requires at least investigating the out-of-plane movement of the apical carbon atom. This is described in sec.3.4, after sec.3.3 has introduced the electronic structures methods and setups adopted, along with the structural models chosen to investigate the vacancy. The Jahn-Teller theory is introduced in the appendix A; moreover in appendix B the D_{3h} point symmetry group is described in terms of symmetry orbitals, normal modes and spin states symmetry for the specific case of the carbon vacancy.

n	$\triangle E$ (meV)	$M_p(\mu_B)$	d^p_{CC}(Å)	$M_{np}(\mu_B)$	d^n_{CC}(Å)	h_C(Å)
4	27.0	1.642	2.212	0.411	2.232	0.25
5	38.2	1.889	2.126	0.111	2.169	0.28
6	36.3	1.556	2.007	0.444	2.075	0.25
7	30.2	1.556	1.999	0.444	2.026	0.24
8	28.3	1.556	1.985	0.450	1.958	0.23
9	26.9	1.556	1.978	0.446	1.969	0.23
10	27.9	1.556	1.962	0.463	1.952	0.25

Table 3.1: Results of full structural relaxation without constraints on the magnetisation, for a vacancy in several $n \times n$ supercells. ΔE is the energy separation between the metastable non-planar (C_s) structure and the planar (C_{2v}) minimum, M_{np} is the magnetisation of the former and M_p that of the latter. Also reported the length of newly formed CC bond closing the pentagon (d^p_{CC} and d^n_{CC} for planar and non-planar geometries, respectively) and the height h_C of the apical carbon atom in the non-planar configuration.

3.3 Methods and models

Electronic structure calculations were performed at different correlation levels for different structural models. Periodic arrangements of vacancies in large unit cells were investigated with standard, plane-wave based density functional theory calculations, whereas a finite-size (cluster) model was judiciously selected and studied with correlated wavefunction methods described below. As already mentioned, the two models are best considered as complementary to each other, and none of them is free of problems. On the one hand, the cluster approach suffers from unvoidable finite-size effects and related discreteness of the energy spectrum; on the other hand, the periodic arrangement of defects always favors their ferromagnetic alignment and, in addition, generates -in some regions of the superlattice Brillouin zone- anomalous midgap states which have truly delocalized character, *i.e.* that do not decay as $1/r$ from the defect position.

3.3.1 Periodic models

Periodic models were studied with plane-wave DFT as implemented in the Vienna *ab initio* package suite (VASP)[55, 57]. The exchange-correlation effects were treated with the Perdew-Burke-Ernzerhof (PBE)[84, 85] functional within the generalized gradient approximation (GGA), in the spin-polarized framework. Kohn-Sham orbitals were expanded on a plane-wave set limited to a 500 eV energy cutoff and core electrons were frozen and replaced by projector-augmented wave (PAW) potentials[14, 58]. Several $n \times n$ graphene supercells with a 20 Å vacuum were initially considered to model the defective system, from $n = 2$ to $n = 10$, by using Γ centered $k-$point meshes ranging from $15 \times 15 \times 1$ (for $n = 2$) to $3 \times 3 \times 1$ for $n = 6 - 10$, in conjunction with a 0.02 eV wide Gaussian smearing of the one-particle occupation numbers. These parameters were carefully tested to give well converged results on the 6×6 supercell and take the same reasonable values for larger unit cells. The structure of a vacancy in such cells was fully optimized without constraints on the

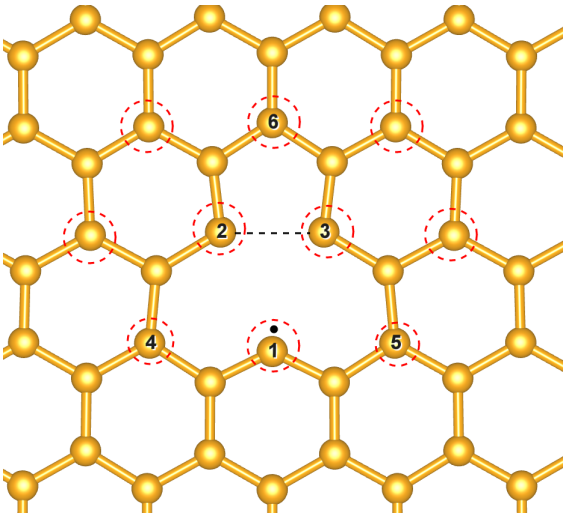

Figure 3.4: Optimized structure of a carbon vacancy in a 6x6 unit cell. A σ electron (black dots) is left on the apical carbon 1; the π electron is semilocalized on the majority sites (red dashed circles).

magnetisation and gave a Jahn-Teller distorted planar minimum, with a local[3] symmetry C_{2v} and a $C-C$ bond length in the pentagon of about 2 Å, *i.e.* smaller than the graphene lattice constant $a = 2.46$ Å but much larger than a typical (single) $C-C$ bond (1.54 Å). A total magnetisation of $\sim 1.5\ \mu_B$ was found, in agreement with previous studies[2, 22, 63, 80, 113, 115], and decomposed into atomic contributions by integrating the magnetisation density over Bader's atomic basins: these 'site integrated' magnetisations (M_{SI}) show that the spin-density localizes around the vacancy (with reference to the labels in fig.3.4 and for $n = 6$, we obtained $M_{SI} = 0.896$ for the apical carbon atom, $M_{SI} = 0.148$ for atoms 2 and 3, $M_{SI} = 0.084$ for atoms 4 and 5 and $M_{SI} = 0.079$ for atom 6), in a way that is consistent with the presence of both a σ and a π contribution. Additionally, starting with a low-magnetisation guess, for $n \geq 4$ we invariably found a *metastable* spin-polarized solution with a much smaller magnetisation which converges to a non-planar equilibrium configuration with a local symmetry C_s if not carefully handled during the optimization run. Clearly, the presence of such spurious solution signals the existence of a low-lying energy state with different magnetisation. The energy separation ΔE between the metastable configuration and the planar minimum in the same supercells, along with the resulting magnetisations M and the main geometrical parameters of the two structures (the length of the newly formed CC bond and the height of the apical C atom above the surface) are given in table 3.1. Results for the global minimum compare well with those found in previous studies[2, 22, 63, 80, 113, 115]. Based on table 3.1 we concluded that a 6×6 supercell with a $6 \times 6 \times 1$ $k-$point mesh was a good compromise between the need of reducing interaction between periodic images and computational manageability. Therefore, further investigations were performed with this setup.

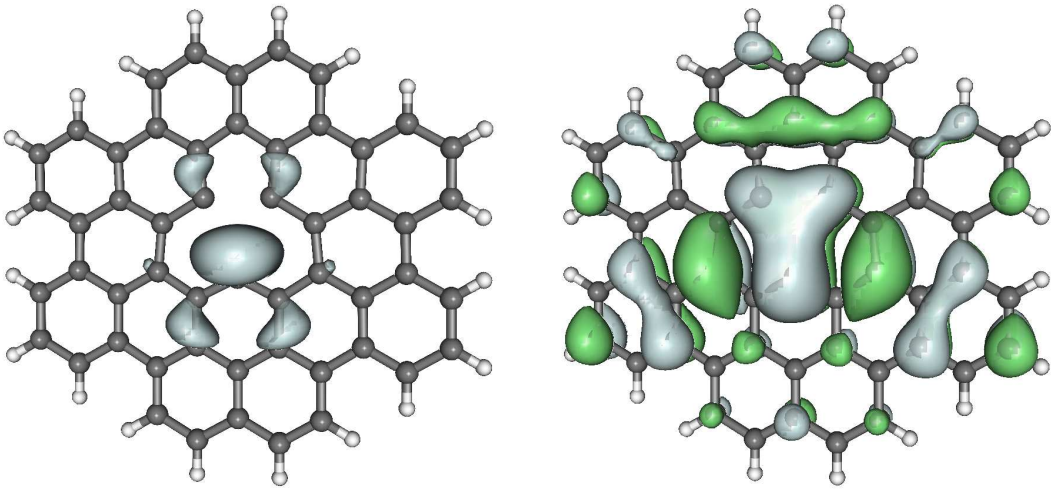

Figure 3.5: The molecular model adopted for the wavefunction calculations, along with isosurfaces of singly occupied σ (left) and π -midgap (right) orbitals for $|\phi| = 0.015$ Å$^{-3/2}$, as obtained at the restricted open-shell Hartree-Fock level ($S = 1$) for the minimum structure.

3.3.2 Finite-size model

The semi-localized character of the electronic states induced by the vacancy makes it realistic the study of finite-size models by means of all-electron, correlated wavefunction calculations. The size (and shape) of the cluster had to be carefully chosen to minimize the effects that edges have on the details of the electronic structure, and small enough that complex many-body wavefunctions were yet tractable. To this end we considered a reasonably sized Polycyclic Aromatic Hydrocarbon (PAH) ($C_{53}H_{20}$), a carbon cluster with a central vacant site which is hydrogen-terminated at the edges (fig.3.5). Its actual shape was chosen, following the line of reasoning of ref.[67], with the help of Tight-Binding (TB) calculations in such a way to limit the edge localization which does interfere with the defect-induced states at the Fermi level. In the chosen structure, edge states were found sufficiently far in energy from the vacancy-induced states (both at the TB and at the Hartree-Fock (HF) level) to make us confident that the resulting energetics accurately describes the vacancy. Cluster geometries were selected with a 'cut-out process' starting from the above mentioned 6×6 supercells, and adding hydrogen atoms to the undercoordinated edge C atoms, without further geometry refinement. In this way, comparison between the periodic and the cluster model with the same local arrangement close to the vacancy was possible.

Accurate results on the finite model were achieved through all-electron, correlated wavefunction calculations based on atom-centered basis-sets of the correlation consistent type[106] (cc-pVDZ). Energy was obtained with the help of the MOLPRO suite of codes[111] by correcting to second order in perturbation theory a 'reference' wavefunction of the Complete Active Space Self-Consistent Field (CASSCF) type, according to what is known as CASPT2[18, 110]. The CASSCF(n,m) wave-

[3]In this chapter, all considerations on the symmetry of the pristine and the distorted vacancy have only a local character that does not apply neither to the whole periodic system nor to the finite cluster.

function, which acts as zero-th order state in the perturbation scheme, is a multi-determinant wavefunction containing all possible excitations of n 'active' electrons in m 'active' orbitals, where all the orbitals and expansion coefficients are variationally optimized[51, 112]. For our purposes, we started with a minimal active space containing the σ and π orbitals localized around the vacancy (see fig.3.5) and the two electrons occupying them at the HF level, and enlarged it by including two further π orbitals (one below and one above the Fermi level), *i.e.* CAS(4,4). Starting from the Hartree-Fock guess, we fully optimized the active orbitals and the thirty doubly-occupied orbitals higher in energy, and kept the lowest-lying (doubly occupied) orbitals frozen at the Hartree-Fock level. With the optimized CASSCF wavefunctions at hand, dynamic correlation was introduced by including perturbatively the effect of single and double excitations out of the configurations contained in the selected CAS 'reference' space. More details on CASSCF and CASPT2 theoretical methods can be found in the chapter 2.

3.4 Results

3.4.1 Periodic calculations

Potential energy curves As shown in tab.3.1 the optimized minimum structure shows an appreciable magnetisation, in agreement with previous studies [2, 22, 63, 80, 113, 115], which is compatible with a spin state where two unpaired electrons couple at high spin. The existence of a metastable solution, on the other hand, signals the presence of a low-energy solution with different spin coupling, a solution which, in a DFT setting, can only be identified by constraining the magnetisation, so that it turns out to be the low spin ground-state. This procedure, though not sufficient for representing definite spin states, allows one to mimic as much as possible the desired electron configurations, while keeping the advantages of DFT of dealing with extended states.
We thus performed magnetisation-constrained DFT calculations on the 6×6 supercell, setting the (projection of the) magnetic moment to two (zero) Bohr magnetons for the triplet (singlet) case. Full structural optimizations were then performed for different out-of-plane displacements h_C of the apical carbon, for each 'spin' state, to investigate how these states evolve out of the plane.
The results of such calculations are shown in fig.3.6, referenced to the planar configuration in the triplet state, along with the magnetisation-unconstrained curve referenced to its minimum (which is only 29 meV below that of the constrained triplet curve). It is clear that the latter is a mixture of the two electronic states, with the triplet prevailing for $h_C \approx 0$ and the singlet dominant for $h_C \gg 0$. Notice here that no miminum other than the planar one appears in fig.3.6 in the spin-relaxed curve, since care was taken for each h_C to obtain the lowest energy solution.
From fig.3.6, we also see that the global minimum belongs to the triplet curve and has a flat geometry (of C_{2v} symmetry). The singlet curve instead shows two equivalent minima (of C_s symmetry) for the carbon atom above and below the plane, respectively, ~ 0.4 Å away from the surface. The latter thus represents a bi-stable system that crosses the triplet when the carbon atom moves out by about ~ 0.5 Å, but is otherwise higher in energy. The energy difference between the singlet and

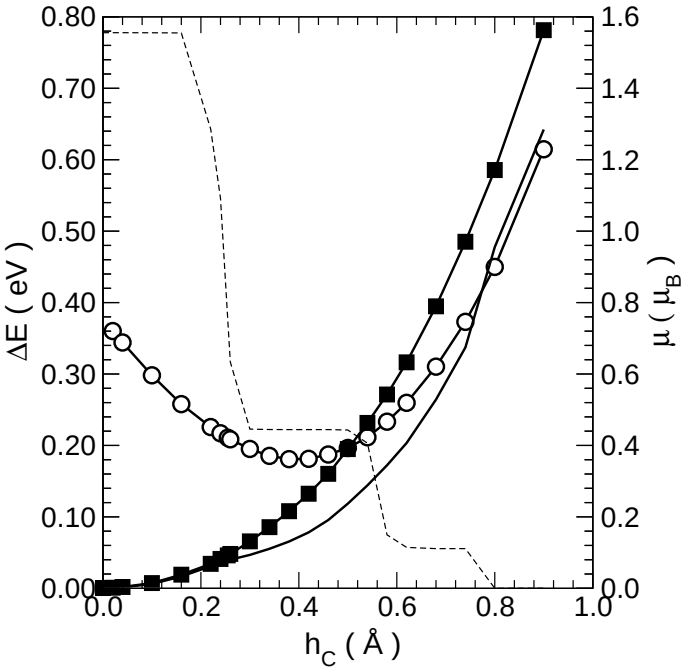

Figure 3.6: Magnetisation-constrained energies as functions of the height h_C of the apical carbon atom above the surface. Filled and empty symbols for $M = 2,0\,\mu_B$, referenced to the minimum of the $M = 2\,\mu_B$ case. Also reported as a thick line the results of magnetisation-unconstrained calculations, referenced to their minimum, and the corresponding magnetisation (dashed line, right scale).

triplet minima is ~ 0.18 eV, thus significantly larger than the (unconstrained) $\triangle E$ for the same 6×6 supercell reported in table 3.1, which referred to 'mixed' electronic states. The singlet minima are separated by a barrier ~ 0.2 eV high which lies ~ 0.4 eV above the triplet. This estimate will be refined in the next section on the basis of more accurate wavefunction calculations.
Before leaving this section we only stress that the curves reported in fig.3.6 refer to a full structural relaxation (in the given electronic state) with respect to all the degrees of freedom but the height of the apical carbon atom, and thus different geometries for the triplet and for the singlet typically result for the *same* h_C value. The differences though are minimal as the height of the apical carbon atom is the main geometrical parameter controlling spin alignment in this system, hence graphs such as those of fig.3.6 are also representative of vertical energy differences. For instance, the pentagon CC bond length is 2.035 Å in the triplet equilibrium configuration and increases to 2.081 Å in the singlet minima, to be compared with $d_{CC} = 2.007$ Å for the magnetisation-free planar structure (table 3.1) and $d_{CC} = 2.467$ Å in pristine graphene.

Potential energy surfaces As outlined in table 3.1, along with the out-of-plane displacement h_C of the apical carbon, the carbon-carbon distance d_{CC} in the pentagonal ring is a relevant aspect in the reconstructed the vacancy. Indeed the equilibrium geometry of the carbon vacancy results from an in-plane distortion, that leads to the formation of the weak CC bond in the pentagon; as shown in fig.3.6, in the low spin configuration, the in-plane relaxation is accompained by an out-of

plane distortion that acts on the apical carbon. In the same way as for the h_C displacement , we proceeded to analyse the effect of the CC distance in the pentagon on the stability of the system. To this end, we performed magnetisation-constrained DFT calculations on the 6×6 supercell to find the equilibrium geometry of the two spin states for chosen carbon-carbon distances d_{CC} at certain (fixed) out-of-plane displacements h_C of the apical carbon. This led in the end to obtain two potential energy surfaces (PES) as a function of the height h_C and the bond length d_{CC}, respectively h and q in the plots in fig.3.7. Note that each surface results from a bicubic spline interpolation of the grid of data, in which each node has coordinates (h, q). We chose h points in the interval $0.0-0.58$Å and q points in the interval from $0.0-1.2$ that corresponds to $2.467-1.949$Å in a way to include all the minima previously found. In the reasonable assumption that d_{CC} and h_C are representative of the collective distortion Q_θ and e_1'' in fig.3.3 and that V is the potential energy, one may associate the relevant configurations in the Q_θ, Q_ϵ, V space to the ones in the q, h, V space as signalled by coloured dots in fig.3.7. On the potential energy surface generated by Q_θ, Q_ϵ, the blue dot represents the undistorted geometry while the red dot sits in one of the equivalent minima; note that this PES is qualitatively correct for both the spin states. Of course, the plot of such points in the q, h, V space leads to different results since the equilibrium geometry of the triplet state is planar, while that of the singlet state is not. Accordingly, it is interesting to notice that on the singlet surface, close to high symmetry point, the surface is slightly corrugated for both positive and negative h values. This effect is due to the presence of the two other minima on the tricorn surface, both splitted along the h coordinate in the singlet state.

3.4.2 Wavefunction calculations

As mentioned in section 3.3.2 correlated wavefunction calculations were performed on the geometries obtained at the DFT level, fit to the cluster model of fig.3.5. We first checked that the singlet had the expected open-shell character at the planar geometry, namely that the wavefunctions read approximately as

$$\Psi^S_{h=0} \propto |...\phi^\alpha_\sigma \phi^\beta_\pi| \pm |...\phi^\beta_\sigma \phi^\alpha_\pi| \tag{3.1}$$

where ϕ_σ and ϕ_π are σ-like and π-like orbitals on the apical carbon atoms, respectively, α and β denote up and down spin states, $|..|$ is a shorthand for a Slater determinant and the plus (minus) sign holds for the triplet (singlet) state. For non-planar geometries $\sigma-$like and $\pi-$like orbitals get generally mixed, and the singlet displays both open- and closed-shell character. Only if the first dominates the singlet can be considered to be the "same" electronic state of the triplet but with one spin flipped, and the singlet-triplet energy separation is meaningful of an exchange coupling.
To check this, we exploited the invariance of the CASSCF wavefunction with respect to rotations of the active orbitals, and chose orbitals which maximize the overlap (while keeping orthogonality) with the above ϕ_σ and ϕ_π states of the planar case. In this case

$$\Psi^{S=0}_h \approx c_1|...\phi^\alpha_\sigma \phi^\beta_\pi| + c_2|...\phi^\beta_\sigma \phi^\alpha_\pi| + c_3|...\phi^\alpha_\sigma \phi^\beta_\sigma| + c_4|...\phi^\alpha_\pi \phi^\beta_\pi| \tag{3.2}$$

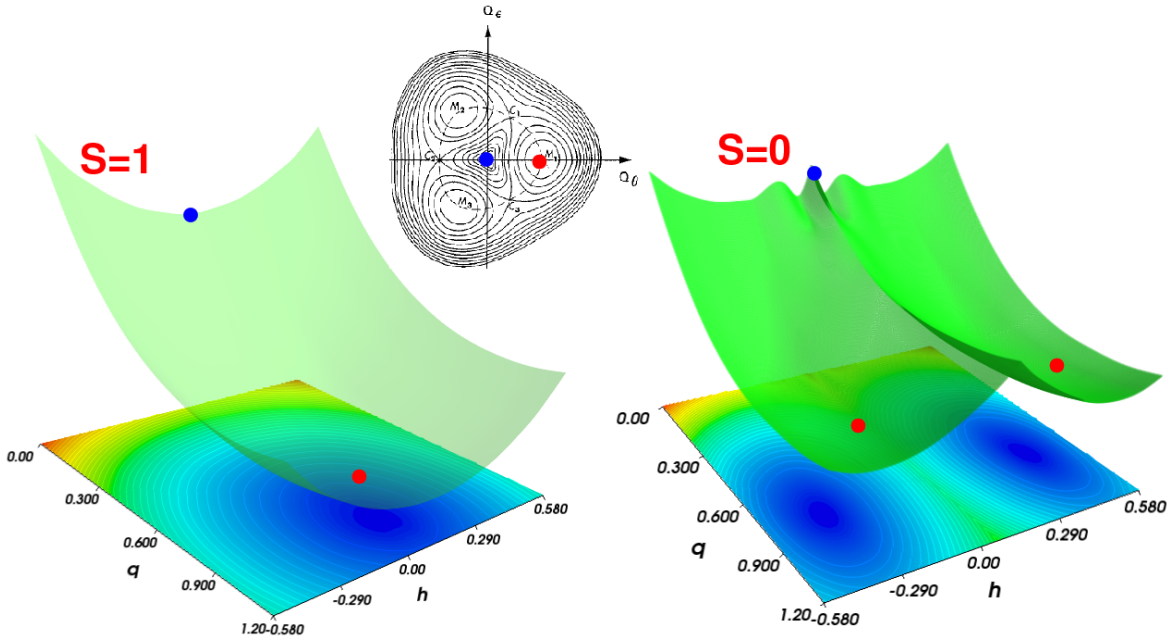

Figure 3.7: 2D and 3D plot of the potential energy surface for the triplet (left panel) and the singlet (right panel) state computed as function of the height of the apical carbon h and of the pentagon CC bond length d_{CC}. In the plot d_{CC} is replaced by q, with $q = 1$ and $q = 0$ for the CC distance in the triplet ground state and in the undistorted geometry, respectively. Coloured dots on the tricorn surface (central panel) defined by Q_θ, Q_ϵ are projected in the q, h, V space with $q \sim Q_\theta$ and V the potential energy.

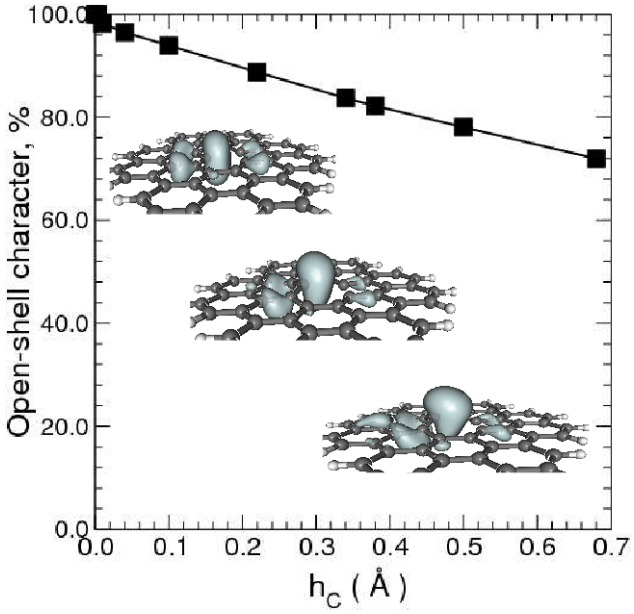

Figure 3.8: Variation of the open-shell character of the singlet state as the apical carbon atom moves out of plane. The symbols give the weight $(c_1^2 + c_2^2) \times 100$ of the coefficients in the minimal CAS(2,2) wavefunction with diabatized orbitals described in the main text. The insets show isosurfaces at $|\phi| = 0.015$ Å$^{-3/2}$ of the corresponding σ-like CASSCF orbitals for representative values of $h_C = 0.0$, 0.32, 0.68 Å, from left to right, respectively.

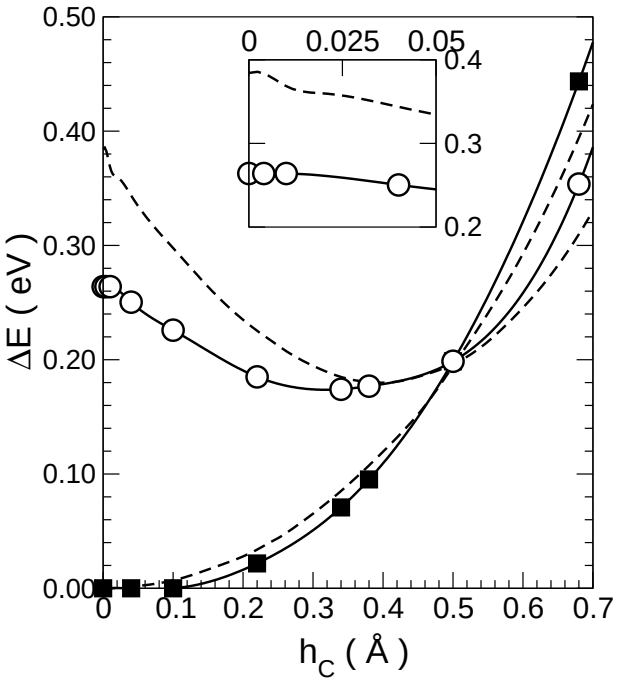

Figure 3.9: CASPT2 energies as a function of the displacement (h_C) of the apical carbon atom out of the surface plane, for the singlet (open symbols) and the triplet (filled symbols) states. Also reported for comparison the magnetisation constrained DFT results of fig.3.6 (dashed lines). Energies are referenced to the triplet minimum at the corresponding theory level. The inset shows a blow-up of the $h_C \approx 0$ region for the singlet.

where c_1 and $c_2 = -c_1$ represent the open-shell contribution, and c_3 and c_4 account for the closed-shell character ($c_3 = c_4 = 0$ and $c_2 = c_1$ in the triplet). In fig.3.8 we report the evolution of the weight $|c_1|^2+|c_2|^2$ in the normalized wavefunction, as a measure of the open-shell character in singlet state. They were obtained from simple CAS(2,2) calculations on the singlet-optimized geometries -*i.e.* using just the four-determinant wavefunction described in eq.3.2- but we checked that similar results hold for more elaborate functions. Evidently, the system is of open-shell type for a wide range of h_C values, comprising the equilibrium one. Only for very large values of h_C the system prefers a closed-shell configuration with "magnetic" properties turned off and, correspondingly, the triplet is pushed higher in energy.

Multi-configuration SCF wavefunctions obtained distributing 4-electrons in 4-orbitals (CAS(4,4)) were then optimized for several geometries sampled from the singlet and the triplet curves in fig.3.6, and used as references for perturbative (CASPT2) calculations. The results are shown in fig.3.9, together with DFT ones for comparison, for several values of the h_C coordinate, referenced to the triplet minimum.

It is evident from fig.3.9 that CASPT2 and DFT results closely parallel each other for the triplet but differ substantially in the singlet. In the latter case, a cusp (due to a likely interaction with higher lying electronic states) is only present at the DFT level, and smooth out at the CASPT2 level, thereby signaling the presence of an avoided crossing. In fact, the CAS(4,4) space is sufficiently large to allow us to properly describe a number of quasi-degenerate states, *i.e.* those obtained by

placing all the four unpaired electrons of the vacancy in low-lying states.
As expected, ferromagnetic coupling is preferred for most values of the height of the carbon above the surface, and a crossing results at about $h_C = 0.5$Å; for larger values of h_C, the gain in hybridization energy overcomes Coulomb repulsion, and the system show increased closed-shell character. A minimum occurs in the singlet at $h_C = h_0 = 0.38$ Å ($h_0 \approx 0.4$ Å at the DFT level), and is actually a double minimum, $h_C = \pm h_0$, on account of the meaning of the h_C coordinate. The singlet is thus a symmetric bistable system with a barrier height of $E_b = 0.09$ eV.
Exchange (Hund) coupling was obtained by the vertical singlet-triplet energy separation, $J_H = \Delta E_{ST}$, using the geometries optimized for the triplet, and is shown in fig.3.10 as a function of the angle θ subtended by the σ dangling bond and the graphene plane. The results closely parallel those reported in fig.3.9 since, as observed above, the difference between singlet and triplet geometries are minimal. The coupling ranges from $J_H \sim 0.27$ eV in the planar configuration to about $J_H \sim 0.1$ eV in the equilibrium configuration of the singlet. Accounting for the zero-point motion of the apical carbon atom out of the plane, which turns out to have a frequency $\omega_\perp \approx 200 cm^{-1}$, $J_H \sim 0.27 - 0.25$ eV seems to be appropriate for the ground-state system.
It is worth stressing at this point, that J_H defined in this way is the Hund coupling constant related to the geometry-dependent σ-like and π-like orbitals hosting the unpaired electrons. Its value in the planar structure, $J_H^0 = J_H(\theta \equiv 0)$, gives the Hund coupling constant in the Anderson impurity model for the vacancy[66], while its dependence on θ (at small angles) simply reflects the behavior of the hybridization strength[82] $V_{\sigma\pi} = \sqrt{2}\tan(\theta)\sqrt{(1 - 2\tan^2(\theta))/3}\,\Delta\epsilon_{sp}$ ($\Delta\epsilon_{sp}$ being the carbon $s-p$ splitting), as confirmed by the dashed line in fig.3.10.
Furthermore, despite the limited size (and discreteness of the energy spectrum) we found no indication that the π-midgap state is only marginally occupied, thereby suggesting that the limit $U_{\sigma\pi} \ll J_H/4$ applies in the above mentioned Anderson model ($U_{\sigma\pi}$ is the Coulomb repulsion between electrons in the σ and in the π midgap states).

3.5 Discussion

Computed exchange coupling constants are clearly too large to have a decoupled response from the two localized electrons to external magnetic fields. The presence of a low-lying singlet at energy Δ above a J-paramagnetic ground-state does affect the magnetisation, but only to the extent it modifies thermal populations, that is introducing a temperature- and field- dependent correction factor $f(\beta, H) = A(Be^{-\beta\Delta} + A)^{-1}$ to the thermally averaged magnetic moment (here $A = \sinh[\beta\gamma H\left(J + \frac{1}{2}\right)]$ and $B = \sinh[\frac{\beta\gamma H}{2}]$, $\beta = 1/k_B T$ as usual, H is the magnetic field and γ is the relevant gyromagnetic ratio). This factor has a distinguishing feature of making the moment no longer dependent on the reduced field βH only, but is hardly appreciable for $\beta\Delta \gtrsim 1$ (*i.e.* $T \lesssim 2000$ K(!) for $\Delta \sim 0.2$ eV). Only for $\beta\Delta \ll 1$ this factor transforms the $J = 1$ ground-state magnetisation density into twice that of a $J = 1/2$ moment. In practice, this limit attains only if Δ is vanishing

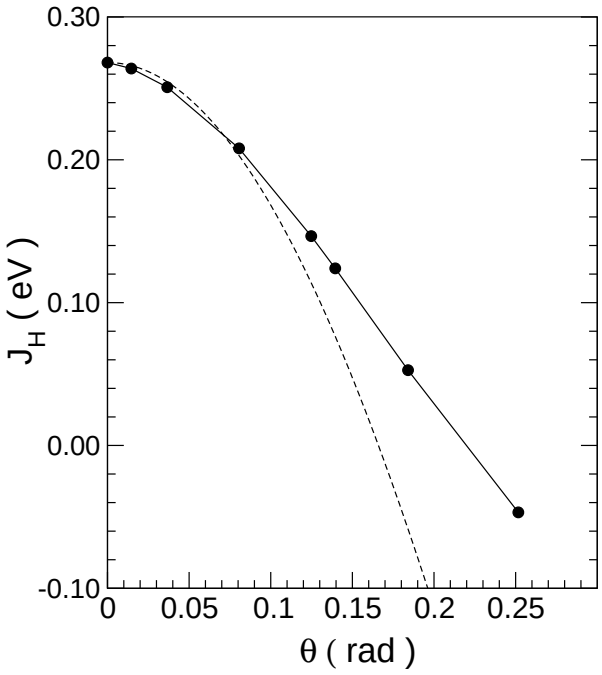

Figure 3.10: Variation of the Hund coupling constant as a function of the angle subtended by the σ dangling bond and the graphene plane (filled symbols). Dashed line is a low-angle weighted-fit of the data to $J_H = J_H^0 - 4A\,\tan^2(\theta)\left(1 - 2\tan^2(\theta)\right)/3$, which gives $J_H^0 = 0.268$ eV and $A = 7.59$ eV.

small[4], since the above (2-electron) 'atomic' picture is challenged at much lower temperatures by thermal excitations out of/into the π midgap state[5]. Likewise for doping which can be used to tune the π state population, as it has been recently shown by molecular adsorption[75].

All this suggests that the bare vacancy in free-standing graphene at low temperature should display a $J = 1$ paramagnetic response and results reported by ref.[3] are consistent with this picture. Decoupled σ and π moments, as those observed under better-controlled conditions by Nair *et al.*[74, 75], though, are still plausible since the apical carbon atom may be easily stabilized out of the

[4]This follows from

$$e^{-\beta F_1} = e^{-\beta\triangle} + \sum_{J_z=-1}^{+1} e^{-\beta\gamma H J_z} = 1 + e^{-\beta\gamma H} + 1 + e^{+\beta\gamma H} \equiv$$

$$\equiv \left(e^{-\frac{\beta\gamma H}{2}} + e^{\frac{\beta\gamma H}{2}}\right)^2 = \left(e^{-\beta F_{1/2}}\right)^2$$

where $e^{-\beta F_1}$ is the partition function of the system with $J = 1$ in the presence of a state with $J = 0$ at energy $\triangle$ and F_1 is the Helmotz free energy. In this limit, $F_1 = 2F_{1/2}$ and total magnetic moment is obtained from

$$\langle m_1 \rangle = -\frac{\partial F_1}{\partial H} = -2\frac{\partial F_{1/2}}{\partial H} \equiv 2\langle m_{1/2} \rangle$$

This situation may occur at very high temperatures even for non vanishing Δ: in this case, low temperature curves for $\Delta \neq 0$ resemble $J = 1$ behaviour and high temperature curves resemble (twice) $J = \frac{1}{2}$ behaviour.

[5]Notice though that thermal excitations are not relevant to magnetometry experiments since they are performed at very low temperatures. This is confirmed by the fact that, under similar conditions, flourinated graphene gives the expected spin$-\frac{1}{2}$ response of π moments[74]. Double occupation of the σ state, on the other hand, is prevented by the large Coulomb repulsion[66], $U_{\sigma\sigma} \approx 10$ eV, and the binding energy in this state is substantial[80] ($\epsilon_\sigma \approx -0.75$ eV) to rule out possible excitations out of this state.

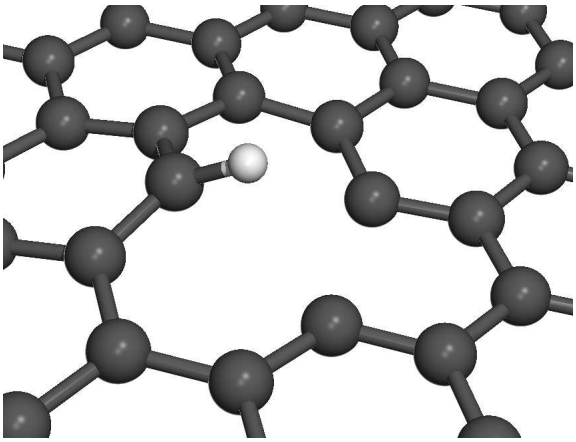

Figure 3.11: Optimized structure of a single hydrogenated vacancy. The CH bond is 1.080 Å long, and its carbon end lies 0.694 Å above the graphene plane.

surface plane (at about $h \sim 0.3$ Å where $J_H \approx 0$), for instance in the presence of a (weakly-binding) substrate[69] or ripples.

With the same token, spin-half residual moments may arise because of interaction with foreign species. Vacancies are highly reactive species which easily saturate their dangling σ bonds and leave a π magnetic moment only. We have checked this by considering adsorption of a single hydrogen atom, and found that such a process is both thermodynamically and kinetically favoured at any temperature. A rather large value (typical of a CH bond in saturated hydrocarbons, $E_b \approx 4$ eV) is found for the binding energy E_b of a single H atom ($E_b = 4.226$ eV at the DFT level of theory in the 6×6 supercell setup), and no barrier appears in the adsorption profile, indicating that the vacancy is a site where facile sticking may occur. The resulting structure is shown in fig.3.11 and has magnetisation $M = 0.676\mu_B$, compatible with a residual unpaired electron localized into a hybrid $\pi - \sigma$ state. A deeper analysis of single and multiple hydrogenation comprising static and dynamical aspects will be presented in chapter 4.

Screening of the magnetic impurity (the vacancy) by $\pi-$band states (Kondo effect) is a more subtle issue. DFT is not able to handle such highly correlated situations, and the finite model adopted for the wavefunction calculations, along with the limited excitations included in the wavefunction, prevent observation of any pairing between the "impurity" and the π band states. In the finite size model, such pairing would be signaled by the presence of singly excited configurations where π states singlet-couple with the impurity π-midgap or σ state. Our wavefunction does include a number of excitations out of the occupied states in the CAS space and, perturbatively, excitations of the "core" states at the CASPT2 level, but a detailed analysis of the wavefunction such that presented above at the CASSCF level is out of question. In the overall triplet state, Kondo singlet-pairing would be signaled by an increasing delocalization of the spin-density when enlarging the cluster size (as a consequence of the mixing with band states) but computational cost becomes prohibitive to check this. Notice though that dynamical mean-field theory with local interactions showed no evidence of quenching of the $\pi-$related local magnetic moment[79], in accordance with observations

of spin-$\frac{1}{2}$ paramagnetism in fluorinated graphene[74]. In the case of vacancies, screening of the σ moment is expected only for non planar geometries and, if any, is not compatible with the Curie-law behaviour observed in refs. [74, 75]. Metallic Kondo screening of spin-$\frac{1}{2}$ impurities has been used to explain transport measurements in irradiated graphene at different doping levels[42], including charge neutrality, but the interpretation has been questioned[43, 47], and the observed logarithmic increase of resistivity at low temperatures related instead to electron-electron interactions in the disordered system[5, 48].

3.6 Conclusions

We reported on a detailed analysis of the electronic and geometric changes that occur upon vacancy formation in graphene, using both DFT and a high-level quantum chemistry method (CASPT2) to overcome known limitations of DFT. The picture that emerges is that of two local magnetic moments coupled to each other to give a triplet ground-state, in accordance with a report of spin-1 paramagnetic species[3]. Spin-half paramagnetism[74, 75], though, can arise in many instances. Vacancies are highly reactive and easily saturate their σ dangling bond in the presence of foreign species. Also, ripples or (weak) coupling to a substrate may stabilize a non-planar configuration of the apical carbon atom, thereby reducing the effective Hund coupling constant of the two-electron system and decoupling the corresponding local moments. This is the likely source of spin-half paramagnetic behavior observed in refs.[74, 75], where doping has been shown to effectively halve the magnetisation density.

We could not deal with the possible pairing of the magnetic moment with the "conduction" π-band states, because of the limitations of DFT on one hand and the use of a finite cluster model (and limited excitation in the wavefunction) on the other hand. At the above level of theory we do not have indication, however, of such a coupling. This is consistent with the absence of anomalies in the measured susceptibility of refs.[74, 75], also at finite densities, and in that computed (for π-moments only) with dynamical mean field theory in the presence of local interactions[79], and suggests that further investigation on the transport data measured by ref.[42] is required for the Kondo effect in graphene to be unambiguously identified.

Chapter 4

Poly-hydrogenation of a carbon vacancy in graphene

In this chapter we study by DFT means the process of hydrogenation of the carbon vacancy, starting from the bare defect atom up to the case of six hydrogen atoms chemisorbed onto its nearest neighbours. We initially consider the formation of a mono-hydrogenated vacancy, looking at the binding energy and the activation barrier. As well, we study a variety of possible mutual arrangements of the adsorbates at higher coverages discussing their reactivity and local magnetic moments. Moreover, by using these DFT energies, we build a phase diagram in a broad range of temperatures and H_2 partial pressures and we find that the first few hydrogen stickings are the most energetically favourable steps, making defective graphene extremely sensitive to hydrogenation. At room T and p conditions, the magnetic ($M = 1\mu_B$) 3H-anti structure is the most stable in agreement with recent magnetic measurements. In addition, we discuss and compare our results with recent TEM, STM and μSR experiments and, motivated by the comparison with a μSR experiment, we carry out a dynamics study on the addition of a second hydrogen atom on a mono-hydrogenated vacancy as reported in the last part of this chapter. This permits us to find the statistically more relevant configurations for the two hydrogen atoms and to further confirm our results.

4.1 Structure and energetics

4.1.1 Method and system

The structure and the energetics of several possible hydrogenated vacancies in graphene has been investigated with plane-wave DFT as implemented in the Vienna ab initio package suite (VASP)[55, 57]. To this end, we chose a setup that is a good compromise between the need of a reliable description of isolated (non-interacting) vacancies and the computational manageability. The exchange-correlation effects for both carbon and hydrogen atoms were introduced by the Perdew-Burke-Ernzerhof (PBE)[84, 85] functional within the generalized gradient approximation (GGA), in the spin-polarized framework. The Kohn-Sham orbitals were expanded in a plane-wave basis set limited to a 500 eV energy cutoff, the electrons were described by the projector augmented-wave

(PAW)[14, 58] method, in the limit of frozen core electrons. The hydrogenated carbon vacancy was modeled by a 6×6 supercell with 20 Å vacuum by using a $6 \times 6 \times 1$, Γ centered k-points mesh, introducing up to six hydrogen atoms. The structure of each hydrogenated vacancy was fully optimized in terms of geometry and spin, and minimum structures were obtained. The binding energy for the poly-hydrogenation of the bare C vacancy was computed as

$$\Delta E^{H}_{VnH} = E_{VnH} - (E_V + nE_H) \tag{4.1}$$

$$\Delta E^{H_2}_{VnH} = E_{VnH} - \left(E_V + \frac{n}{2}E_{H_2}\right) \tag{4.2}$$

depending on the reference state being either the H radical in eq.4.1 or gas phase H_2 molecules in eq.4.2. In the same equations, E_V is the DFT energy of the isolated vacancy in graphene and E_{VnH} is the energy of the n-hydrogenated vacancy, with $n = 1..6$. The reference bare vacancy is in its equilibrium state obtained upon a relaxation of both the nuclear positions and the total magnetisation. Both atomic and molecular hydrogen, chosen as hydrogen source, have been modeled by a cubic cell with a 20 Å side using one Γ centered k-point; the exchange-correlation functional and the basis set are the same used for the hydrogenated vacancy. The progressive hydrogenation steps were computed accordingly,

$$\Delta E^{H}_{VnH-1H} = E_{VnH} - \left(E_{V(n-1)H} + E_H\right) \tag{4.3}$$

$$\Delta E^{H_2}_{VnH-1H} = E_{VnH} - \left(E_{V(n-1)H} + \frac{1}{2}E_{H_2}\right) \tag{4.4}$$

where E_{VnH} and $E_{V(n-1)H}$ are the DFT energies of the carbon vacancy with $n-$ and $n-1$ H atoms chemisorbed, respectively.

As described in details in chapter 3, a vacancy in graphene forms upon the extraction of a carbon atom that implies the cleavage of four bonds and leaves four unpaired electrons, three σ and one π, on the lattice. The σ electrons are tightly localized on the sites C1, C2, C3 in fig.4.1 and behave as dangling bonds; the π electron instead behaves similarly to π electrons left upon the chemisorption of monovalent species (H, F, etc.)[16] and in analogy with them it is usually referred as *midgap* state. The origin of these states relies on the inherent nature of graphene, that is a bipartite system, composed by two interpenetrating and equivalent sublattices A and B. Such equivalency is broken after the introduction of a defect, like a C-vacancy or a chemisorbed species, which removes one p_z orbital from the π-network. In this way the sublattice imbalance turns out to be also an electronic imbalance and gives rise to singly-occupied electronic states, namely the *midgap* states. The number of midgap states is expected to be greater or equal than $|n_A - n_B|$, where n_A and n_B are the number of sites in the two sublattices[41]. Both theory and experiments proved that these states localize on the majority sites and decay as $\sim r^{-1}$ from the defect[68, 88, 89]. Moreover, in recent magnetisation measurements[74], graphene samples with adsorbed fluorine atoms showed an itinerant spin-1/2 paramagnetic response due to the presence of these π unpaired electrons. However, on the carbon vacancy this simple picture is complicated by the presence of three σ

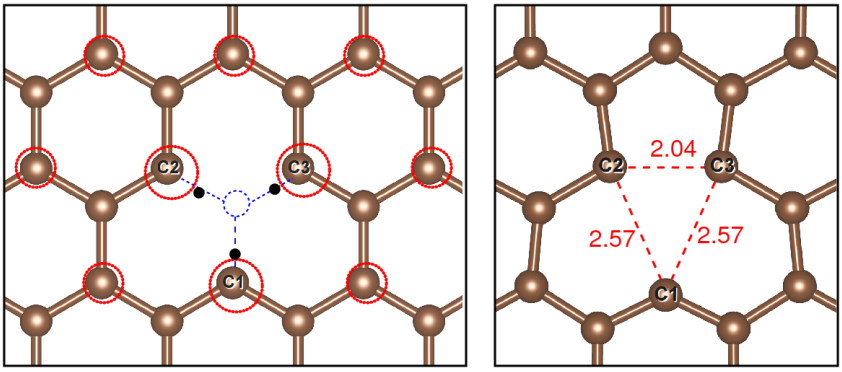

Figure 4.1: three σ electrons (black dots) localized on as many carbon atoms and one π electron (red dotted circles) delocalized on the non defective sublattice. Note that the probability to find the π electron decays like $\sim 1/r$ with r the distance from the center of the vacancy.

electrons in addition to the π one. Indeed within the D_{3h} symmetry of the pristine vacancy, these electrons give rise to a doubly degenerate electronic configuration that in turn implies a Jahn-Teller instability. As a consequence two carbon atoms on the vacancy get close forming a pentagonal ring, while the third (apical C) possibly shifts out of the lattice plane. Along with this nuclear displacement, two σ electrons turn out to be coupled in a low-lying orbital referable to the weak C-C bond, while the remaining σ and π electron are host by the apical carbon. As reported in chapter 3, in the ideal situation of a bare vacancy in a free-standing graphene sample, these two unpaired electrons give rise to a magnetisation of 1.56 μ_B in the equilibrium planar geometry. It is important to point out that this non-integer value does not have a real physical meaning, being due to the intrinsic features of spin-polarized ensemble-DFT calculations. To overcome this limit we relied on magnetisation-constrained DFT calculations and we found in the end that the ground state equilibrium geometry is planar and it correponds to a triplet state; anyway,we found also a non-planar minimum solution corresponding to an open-shell singlet. It is interesting to notice that recent experiments in refs.[3],[75] have proved the existence of a vacancy magnetism, that originates from two unpaired electrons. In ref.[75] these have been clearly identified as a π electron and a σ dangling bond, leading to a decoupled magnetic response that makes the C-vacancy a spin-1/2 paramagnetic center. On the other hand, in ref.[3] the two electrons are found to be coupled in a triplet configuration thereby leading to a spin-1 paramagnetic signal. Irrespective of the way they interact, that strongly depends on the "environment" in which the graphene sample is kept, the σ and π are expected to be highly reactive towards foreign monovalent species due to their radical nature. As well, also the two σ electrons coupled in the weak C-C bond in the pentagonal ring, are predicted to be likely available to react as the carbon-carbon interaction is very weak, as suggested by relatively long bond length ~ 2 Å, compared to the usual ~ 1.54 Å of the single C-C bond. This means that four unpaired electrons sit at the vacancy nearest neighbours sites, thereby permitting the multiple adsorption of hydrogen atoms to easily occur and explaining why the sticking process is more favoured on such sites than elsewhere around the vacancy or onto 'bulk' carbon atoms.

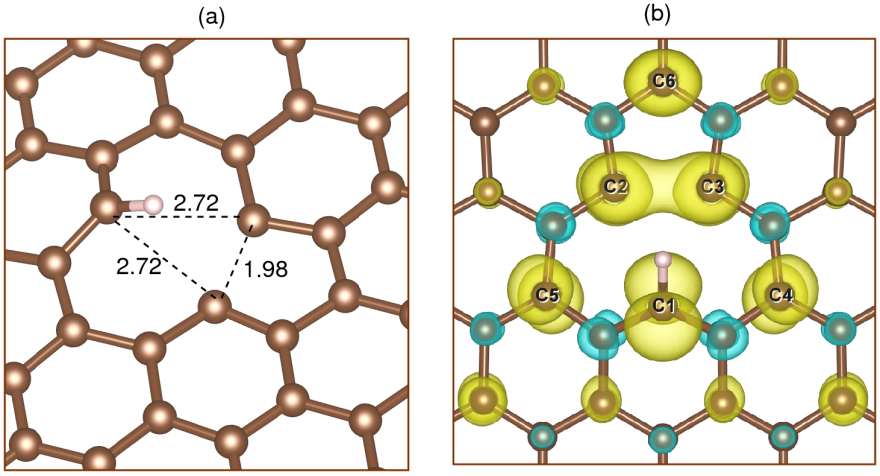

Figure 4.2: (a) geometry of the mono-hydrogenated vacancy and (b) electron spin density, mainly localized on the non defective lattice with a dominant π character.

4.1.2 Adsorption of the first hydrogen atom

We start considering the adsorption of the first hydrogen atom on the bare vacancy. The binding energy is ΔE^H_{V1H}=4.19 eV which accounts for the formation of the bond between the hydrogen atom and a carbon atom of the surface and for the distortion of the graphene lattice, with the hydrogenated carbon shifted $\sim$ 0.35 Å out of the surface plane, that drags along its neighbouring atoms. As shown in fig.4.2a, the pentagonal ring associated to the in-plane reconstruction of the bare vacancy is still present as the H atom binds to the apical carbon. After the adsorption, a single π electron is left as shown by the spin density plot in fig.4.2b, and it is responsible for the nonzero magnetisation equal to 0.56 μ_B.

In order to get a comprehensive picture of the single hydrogen adsorption, we computed the potential energy curve as a function of the z coordinate of the hydrogen atom, in such a way to determine whether the process is activated or not. To this end, both the nuclear positions and the spin structure of the 6×6 supercell with a carbon vacancy and an hydrogen atom on top of C1 have been relaxed to find the equilibrium configuration for a number of different heigths of the hydrogen atom. Accordingly, its position was fully optimized in the xy plane, while the z coordinate was constrained; in the graphene lattice, only the nuclei close to the vacancy were allowed to relax while all the other were kept fixed. Note anyway that the initial geometry of the graphene lattice was taken from a previous optimization of the bare system. The chosen setup is equivalent to that used to study the hydrogenation of the vacancy and reported in sec.4.1.1, except for two aspects: (i) the empty space that isolates the periodic images along the c axis has been cut from 20 to 10 Å to reduce the computational cost; (ii) the smearing procedure has been changed from the gaussian smearing to the tetrahedron method to obtain more accurate energies. In fig.4.3 the energy profile as a function of the z coordinate of the hydrogen atom is shown as a green line and it is referenced to the energy of the system with the hydrogen atom 4.5 Å far above the surface. It is possible to notice that the chemisorption is barrierless as a consequence of the crossing at z $\sim$3.5 Å between a diabatic

potential energy curve in an asymptotic "high spin" manifold (red line in fig.4.3, with magnetisation $M = 2.7\mu_B$) and a diabatic bound "low spin" manifold (blue line in fig.4.3, with magnetisation $M \leq 1\mu_B$). By following the minimum energy profile, one finds that in the interval between 4.5 and 3.5 Å, the incoming hydrogen has almost no interactions with the surface, indeed the energy of any equilibrium structure is almost independent on the z value and close to zero. Here, the graphene sheet remains flat as shown in the inset b and the high magnetisation accounts for the unpaired electron on the hydrogen atom in addition to the two unpaired electrons on the vacancy (in the triplet state). When the hydrogen moves beyond the threshold of 3.5 Å, the situation dramatically changes: the drop in energy accounts for the formation of a C-H bond and for a strong distortion of the graphene lattice, as indicated by the illustrative geometry in fig.4.3(inset a). In the end, the residual magnetisation, below 1 μ_B, is due to the unpaired π electron as apparent from fig.4.2.

4.1.3 Multiple hydrogen adsorption

We have computed equilibrium structures and binding energies for the chemisorption of up to six H atoms on the three C atoms (C1,C2,C3 in fig.4.1) nearest neighbours of the vacant site. In this way several different configurations can be achieved that can be classified in terms of relative positions of hydrogen atoms. Accordingly, the *geminal* configuration consists of two hydrogen atoms bound to the same carbon atom, while in the *syn* or *anti* arrangements the two hydrogen atoms are on different carbon atoms and span respectively either the same or the opposite faces of the graphene layer. Similarly, three hydrogen atoms are syn when they sit on the same face of the graphene sheet, anti when two of them sit on the opposite faces, geminal when these two are bound to the same carbon. With four hydrogen atoms on the vacancy, the formation of a geminal pair is unavoidable; anyway the relative arrangement of the other two hydrogen atoms may still be syn, anti or geminal. Finally, for the higher hydrogenation levels, namely with five and six atoms adsorbed, the possible arrangement is just one. All these possibilities have been explored, with the only exception of the tri-hydrogenated syn vacancy for which we could not find any stable solution.

4.1.3.1 Lattice structure

The geometrical structure of each hydrogenated vacancy is analysed in terms of hydrogen-carbon, carbon-carbon and hydrogen-hydrogen bond lenghts; moreover also the displacement of the hydrogenated carbon out of the lattice plane is considered. In table 4.1, the C-H bond lenghts are listed and they vary in the range $1.07 - 1.12$ Å, where the highest values in this interval refer to the geminal pairs as longer bonds permit a reduction of the steric repulsion. It is interesting to notice that, in any case, such distances are shorter than those found for H chemisorbed on perfect graphene (1.13 Å in [16]). The spatial configuration is the most significant parameter in determining the C-H bond lenght, which is otherwise almost unaffected by the number of hydrogen atoms bound to the vacancy. The sticking of hydrogen atoms induces a further reconstruction of the C-vacancy as shown in table 4.2 and table 4.3. The C atom involved in the C-H bond usually

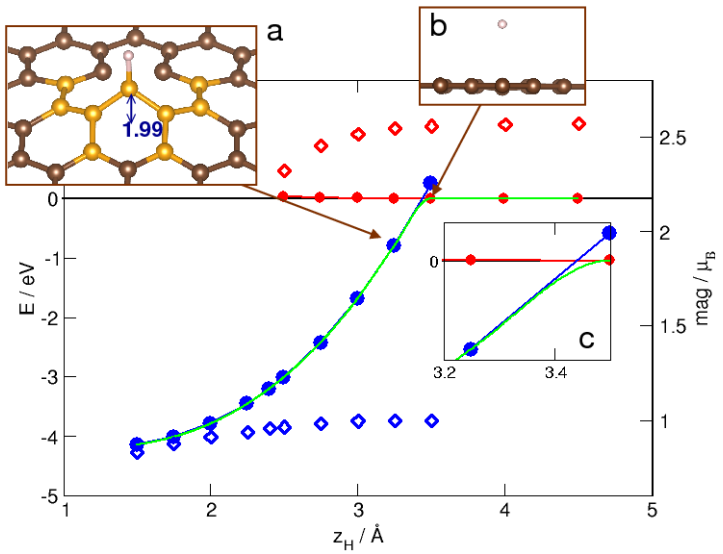

Figure 4.3: the energy (left axis) and the total magnetisation (right axis) as a function of the z coordinate of the H atom above the graphene plane. For each optimized geometry, solid and empty symbols give the energy and the magnetisation, respectively; red and blue symbols are for non-interacting and strongly interacting systems, respectively. In (a) an illustrative case of the lattice distortion to form a C-H bond, with the hydrogenated carbon shifted 1.99 Å out of the lattice plane along with its neighbours and $z_H = 3.25$ Å. In (b) the undistorted structure. In (c) the crossing of the curves.

moves out of the layer plane as a consequence of its partial rehybridization from sp^2 to sp^3. When poly-hydrogenation occurs, the direction of the displacement is determined by the configuration: reasonably the carbons are pulled in the same direction for the syn case and in opposite direction for the anti case. Note that the carbon atom with a geminal pair of hydrogen atoms usually undergoes a smaller displacement than the mono-hydrogenated carbon, because of the opposed effect of the two hydrogen atoms. The C-C distances in table 4.3 suggest that different outcomes should be encountered depending on the number of hydrogen atoms and their relative positions. We also note that in the mono-hydrogenated vacancy as well as in the geminal di-hydrogenated vacancy, the two carbon atoms not involved in the C-H bond form the pentagonal ring by making a weak C-C bond, whose bond lenght is close to 2 Å, compared to the 2.47 Å of ideal graphene. This structure is analogous to that of the bare vacancy due to the Jahn-Teller effect. In all the other cases, the presence of at least two hydrogenated carbon atoms prevents the formation of the weak C-C bond and the pentagonal ring. Here the structural relaxation finally results in a vacancy where the C-C distances are all larger than the reference unrelaxed value (2.47 Å). This clearly accounts for the steric repulsion associated to the presence of several hydrogen atoms. However, in addition to the in-plane relaxation of the carbon atoms, the hydrogenated vacancy often shows a significant displacement of the hydrogenated carbons (and their closest neighbours) out of the molecular plane mainly motivated by their partial orbital rehybridization. Some of these observations are summarized in fig.4.4. The hydrogen-hydrogen distances are reported in table 4.4. In geminal pairs, the H-H distance is almost unaffected by the total number of atoms adsorbed, in fact it varies between

	C_1-H	C_2-H	C_3-H
1H	1.08		
2H gem	1.11 1.11		
2H anti	1.09	1.09	
2H syn	1.08	1.08	
3H gem	1.11 1.12	1.08	
3H anti	1.08	1.07	1.09
4H gem	1.11 1.09		1.10 1.11
4H anti	1.07	1.07	1.10 1.10
4H syn	1.07	1.07	1.11 1.11
5H	1.07	1.11 1.08	1.09 1.10
6H	1.11 1.10	1.11 1.08	1.10 1.09

Table 4.1: C-H bond lenght in Å for hydrogen atoms adsorbed on the carbon atoms of the vacancy.

	position C_1	position C_2	position C_3
1H	0.69	-0.03	-0.03
2H gem	**0.30**	0.07	0.05
2H anti	0.48	-0.44	0.00
2H syn	0.60	0.60	-0.09
3H gem	**0.36**	0.60	0.12
3H anti	0.68	0.49	-0.34
4H gem	**0.29**	0.03	**−0.09**
4H anti	0.48	-0.41	**0.05**
4H syn	0.80	0.80	**0.54**
5H	0.79	**0.66**	**0.18**
6H	**0.32**	**−0.23**	**0.00**

Table 4.2: out of plane displacement of C atoms along the z coordinate, in Å. In bold type the C atoms that carry a geminal pair of hydrogen atoms.

$1.73 - 1.79$ Å, where the lowest and the highest value accounts for the di-hydrogenated and the fully hydrogenated vacancy respectively. This is consistent with the behaviour of C-H distances in table 4.1 which was found to be essentially independent on the degree of hydrogenation. On the other hand, general considerations on the distances between syn and anti hydrogen atoms are of course more complicated and less reliable, since they follow from the reconstruction of the vacancy that depends on both the number of hydrogen atoms and their spatial configuration. For this reason each case needs to be investigated individually.

4.1.3.2 Electronic properties

The magnetisation and the orbital character of the possible unpaired electrons in the C-vacancy at different stages of hydrogenation is summarized in table 4.5 together with the corresponding spin densities shown in fig.4.5.

Except for the mono-hydrogenated vacancy, all the other cases correspond to almost pure spin states, with the total magnetisation between 0 and 2 μ_B depending on the degree of hydrogenation. Our calculations show that the residual π^C electron, left upon the first H adsorption, would couple

	C_1-C_2	C_1-C_3	C_3-C_2
1H	2.72	2.72	**1.98**
2H gem	2.58	2.58	**2.06**
2H anti	2.81	2.73	2.72
2H syn	2.80	2.65	2.65
3H gem	2.72	2.62	2.75
3H anti	2.85	2.86	2.81
4H gem	2.64	2.65	2.62
4H anti	2.84	2.73	2.73
4H syn	2.89	2.74	2.74
5H	2.77	2.78	2.70
6H	2.71	2.68	2.67

Table 4.3: C-C distances around the C vacancy, in Å. In bold the C-C distance in the pentagonal ring that appears when two carbon atoms get close.

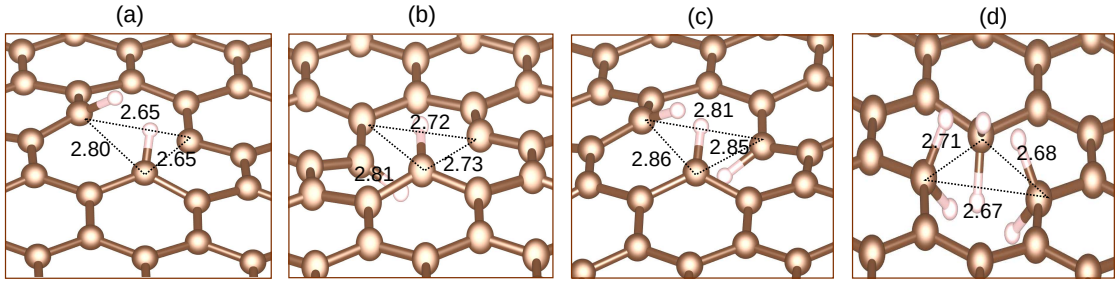

Figure 4.4: Different aspects of the carbon vacancy in graphene. Note that all the distances are in Å and carbon and hydrogen atoms are respectively brown and pink. In (a) 2H-syn, (b) 2H-anti, (c) 3H-anti and (d) the 6H structures.

H-H distance	gem	anti	syn
2H gem	1.73		
2H anti		1.92	
2H syn			1.51
3H gem	1.74	1.81	1.65
3H anti		1.87 2.20	1.42
4H gem	1.75 1.76	1.85 2.85	1.70 1.62
4H anti	1.76	2.14 2.01 2.21	1.47 1.48
4H syn	1.75	1.87 1.87	1.48 1.74 1.74
5H	1.74 1.78	2.94 1.82 2.38 1.75	1.97 1.88 1.58
6H	1.79 1.76 1.77	1.67 2.08 2.67 3.08 1.94 2.80	1.79 1.78 1.49 1.72 1.71 1.50

Table 4.4: H-H distances for geminal, anti and syn pairs, in Å. In the geminal case the values are quite uniform and essentially independent on the total degree of hydrogenation.

	magnetisation (μ_B)	unpaired electrons left
1H	0.56	π^C
2H gem	0.00	none
2H anti	2.00	σ, π^C
2H syn	0.00	σ, π^C
3H gem	1.00	σ
3H anti	1.00	π^C
4H gem	1.92	σ, π^H
4H anti	0.00	none
4H syn	0.00	none
5H	1.00	π^H
6H	2.00	π^H, π^H

Table 4.5: total magnetisation in μ_B and unpaired electrons left on the C-vacancy after the hydrogenation process.

with that of an H atom giving rise to a closed shell electronic structure only when the latter forms a geminal pair. On the contrary, an open-shell character is associated to both the anti and syn dimer configurations, where the spin alignment of the two electrons is respectively parallel and antiparallel. Further on, in presence of three hydrogen atoms, just a single unpaired electron is left; it occupies the π^C or σ orbital depending on the relative arrangement of the adsorbed atoms, respectively anti or geminal. As expected, when four hydrogen atoms are on the vacancy in anti or syn configuration, there are no unpaired electrons left; differently the geminal structure involves two σ dangling bonds on the three available, the midgap π^C electron and a further π electron (π^H) made available upon the break of a π bond in the graphene lattice. This means that two unpaired electrons are left on the vacancy: a σ and a π^H. Finally, from this observation it follows that the fifth hydrogen atom reasonably makes a bond with the σ electron left; moreover, the sixth hydrogen may be accommodated at the vacancy only upon breaking a further π bond. These results are shown in fig.4.5, where it is easy to see the π^H electrons left on the highly hydrogenated vacancy as they belong to the defective sublattice unlike the π^C electron that localizes on the non-defective one.

4.1.3.3 Energetic aspects

We consider now the energy balance of the hydrogenation process of the C-vacancy with respect to atomic and molecular hydrogen. The formation of a C-H bond is always an exothermic process which generates a certain amount of energy, therefore the difference between the DFT energies of products and reactants (ΔE^H_{VnH}) with respect to atomic hydrogen is always negative. This is not true for molecular hydrogen, since in this case the energy balance $\Delta E^{H_2}_{VnH}$ also includes the energy required to break the H_2 molecule, ~ 4.55 eV.

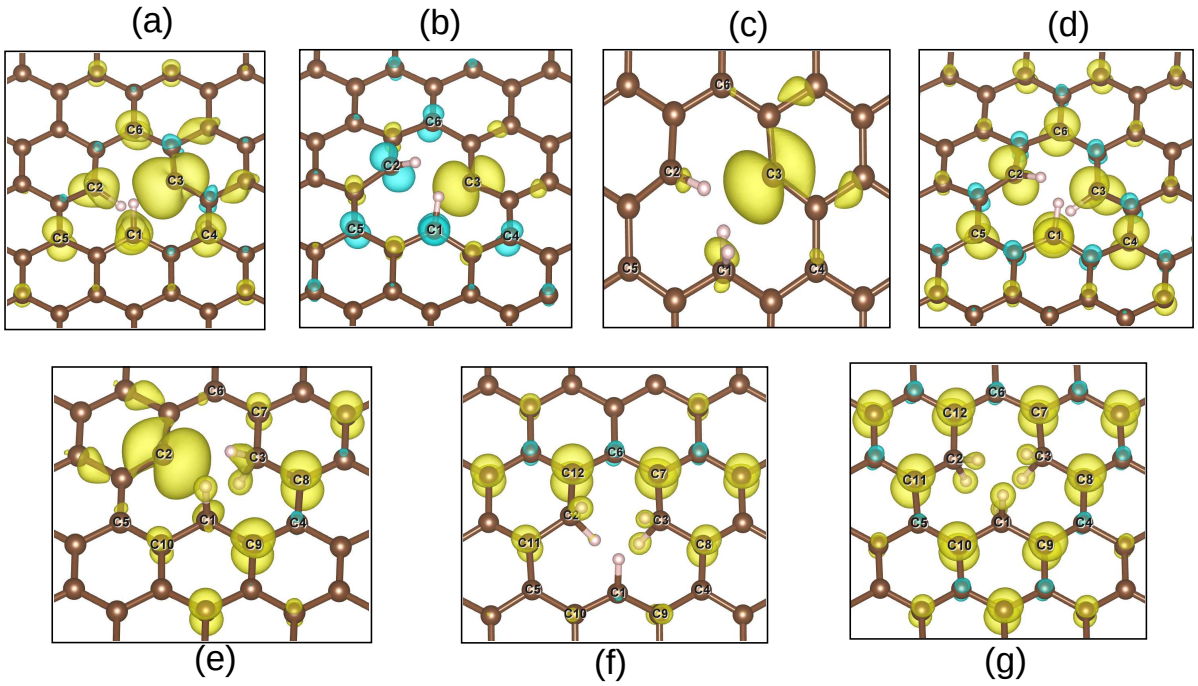

Figure 4.5: spin density for different hydrogenation degrees, due to α (yellow) and β (blue) electrons; C and H atoms are respectively brown and pink. (a) 1H-vacancy; 2H-vacancy with (b) geminal, (c) anti and (d) syn arragement of the two H atoms; 3H-vacancy in (e) geminal and (f) anti configuration; (g) 4H-vacancy in a global geminal configuration; (h)-(i) 5H- and 6H-vacancy.

Hydrogenation with H atoms We consider first the hydrogenation process with atomic hydrogen. In table 4.6 we report the energy difference between the bare vacancy, in its ground state (M=1.56 μ_B) and the hydrogenated vacancy. Depending on the degree of hydrogenation as well as on the final configuration, ΔE_{VnH} varies. The largest value is observed for the first H atom, where steric effects are minimal; then the energy gain raises up to ~ 16 eV in the 6H-vacancy. This process is also illustrated in the scheme in fig.4.6, which shows a detailed landscape of the energy differences for each progressive step of the hydrogenation. Here it is clear how the highest energy gain is obtained by adsorbing the first hydrogen atom, while the lowest is for the adsorption of the last (sixth) hydrogen to produce the 6H-vacancy. It is interesting to note that the formation of a geminal pair at each level of the scheme is always the less exothermic event due to steric and electronic effects. Nevertheless some differences should be pointed out: indeed when the geminal pair involves a σ and the π^C electron the energy release is close to ~ 2.40 eV; on the other hand when a σ and a π^H electron are involved the amount of energy is significantly lower and varies between $1.20 - 1.70$ eV. Such difference can not only be related to steric factors but reasonably accounts for the energy needed to break a π-bond and generate the π^H electron.

Hydrogenation with H_2 molecules The energetics of hydrogenation with respect to molecular hydrogen is instead shown in table 4.7. From this table, it is possible to recognize the same trend found for the atomic hydrogen, where the largest *average* energy per H atom is still associated to the monohydrogenated vacancy, while the smallest one is for the fully hydrogenated vacancy. The

	$\triangle E^{H}_{VnH}$
1H	-4.19
2H gem	-6.61
2H anti	-7.53
2H syn	-7.28
3H gem	-9.96
3H anti	-11.36
4H gem	-11.53
4H anti	-13.74
4H syn	-13.75
5H	-15.43
6H	-16.65

Table 4.6: total energy in eV for poly-hydrogenation computed from eq.4.1 with respect to H atoms gas as source and the bare vacancy with magnetisation M=1.56 μ_B.

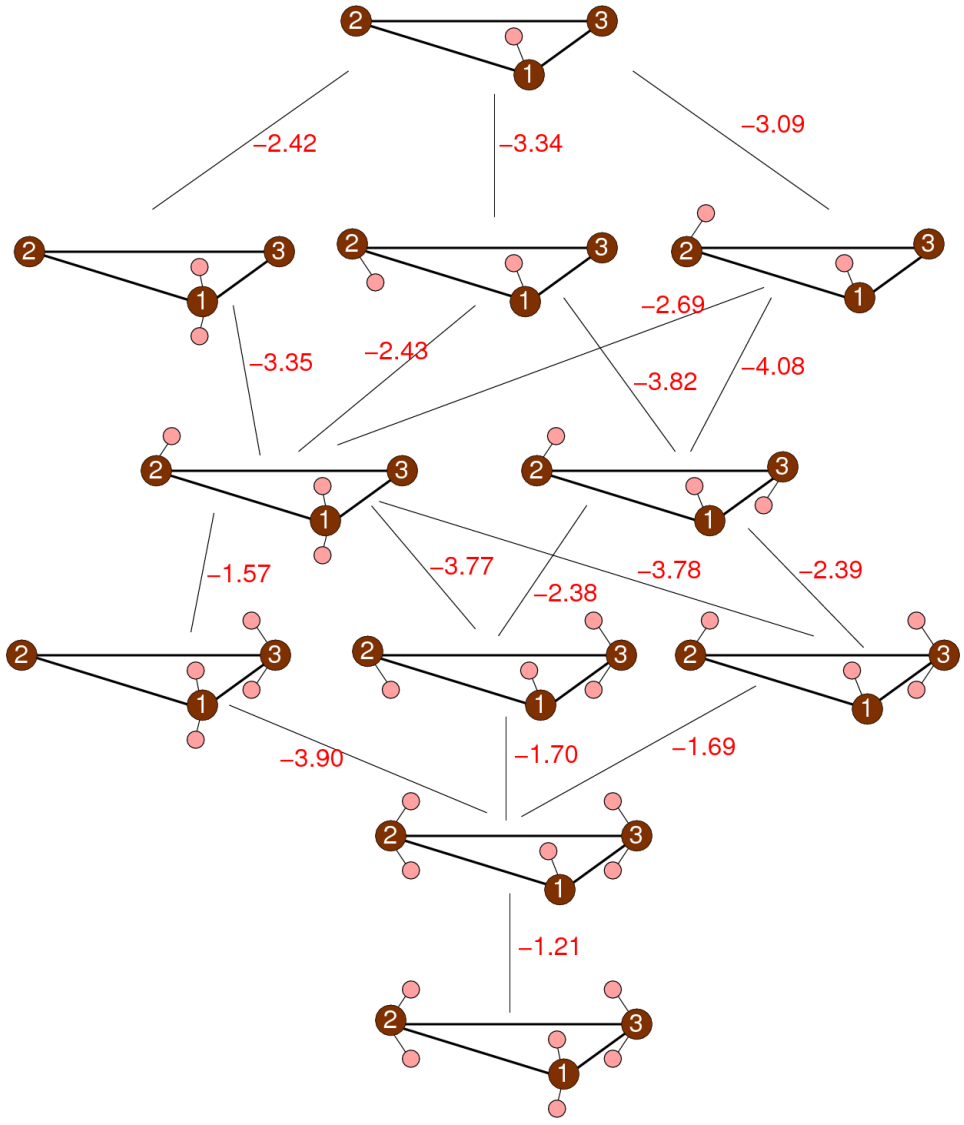

Figure 4.6: detailed energy differences in eV computed according to eq.4.3 for each step in the hydrogenation process with respect to the configurations. Atomic hydrogen is used. The vacancy is shown as a triangle, the three C atoms are in brown while the adsorbed H atoms are pink.

	$\triangle E_{VnH}^{H_2}$
1H	-1.94
2H gem	-2.11
2H anti	-3.03
2H syn	-2.77
3H gem	-3.20
3H anti	-4.60
4H gem	-2.52
4H anti	-4.72
4H syn	-4.73
5H	-4.17
6H	-3.13

Table 4.7: total energy in eV for poly-hydrogenation computed from eq.4.2 with respect to H_2 gas as source and a bare vacancy with magnetisation M=1.56 μ_B.

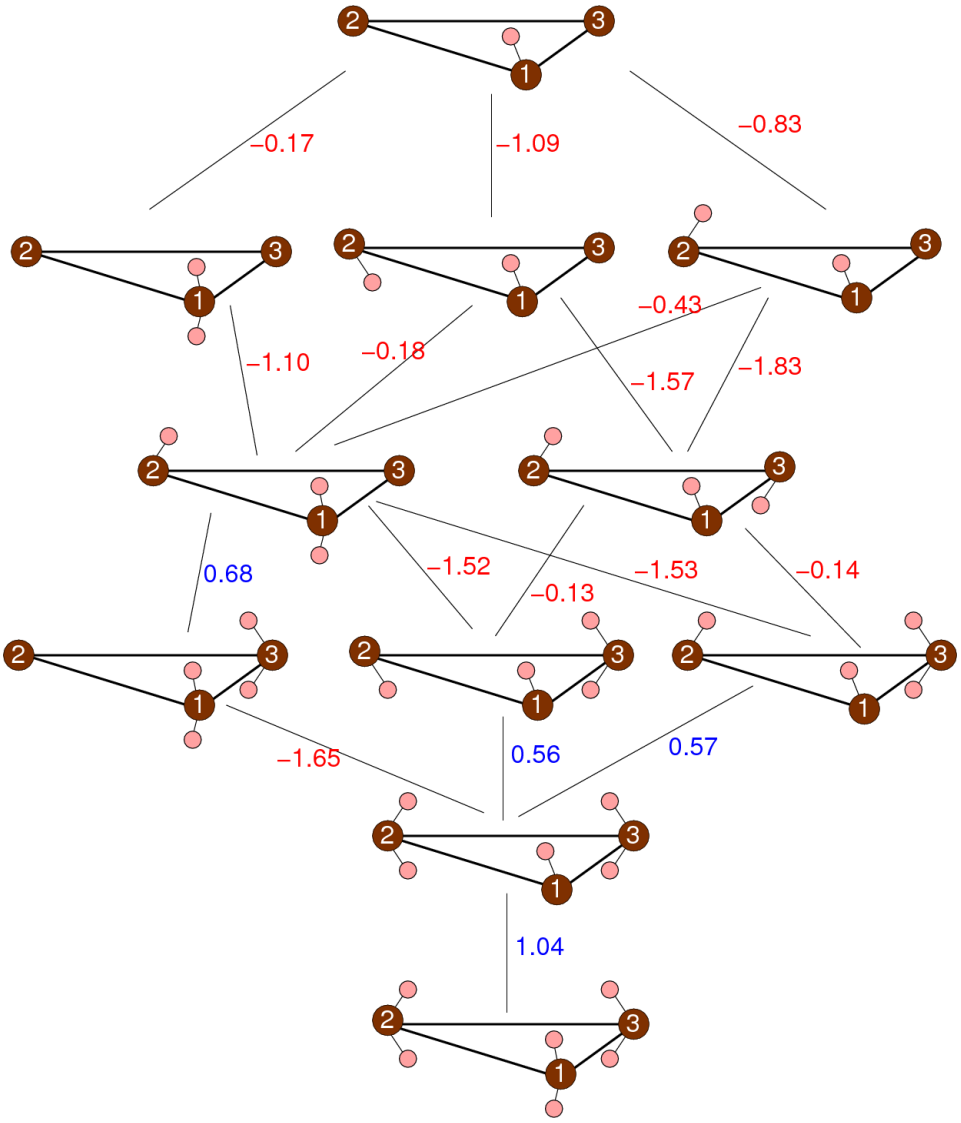

Figure 4.7: detailed energy differences in eV computed according to eq.4.4 for each step in the hydrogenation process, by using gaseous H_2 as source. The vacancy is shown as in fig.4.6. In blue positive energy differences associated to endothermic adsorption steps.

absolute values are anyway significantly smaller because of the binding energy of H_2. The detailed energy differences reported in fig.4.7 show that, up to the third hydrogen atom, the hydrogenation process is always enthalpically favoured. On the other hand, for the more hydrogenated vacancies the energy balance may depend on the final configuration. Indeed the 4H-vacancy is enthalpically favoured with respect to the 3H-vacancy in the syn and anti configurations but is unfavoured in the geminal one. In the same way, the 5H-vacancy is favoured with respect to the geminal 4H-vacancy but not to the syn and anti structures. Finally the production of the 6H-vacancy from the 5H one is anyway endothermic. Note that, as already remarked for the adsorption of atomic hydrogen, whenever the cleavage of a π-bond is required, an extra-amount of energy is spent.

4.1.4 Discussion

From our results it is clear, that the hydrogenation of a carbon vacancy is a spontaneous process from both a thermodynamic and a kinetic point of view. The first hydrogenation step is barrierless, and it could occur even at very low H_2 partial pressures[46]. As the mono-hydrogenated vacancy carries one unpaired electron, this process could explain the detection of S=1/2 magnetism in irradiated graphene samples[74, 75]. In all the cases considered, the adsorption of a second H atom seems to be preferred in a *dimer* (either syn or anti) configuration over the geminal one, as binding energies are more favourable in the former case, while barriers are very similar, as will be shown in sec.4.2. This scenario is contradicting recent muon spin resonance (μSR) measurements, which have found the geminal structure to form preferentially from irradiation of hydrogenated C vacancies[93]. Anyway, by assuming that the three-fold vacancy observed in STM and TEM images may account for the average over the three possible orientations of the pentagon ring[59, 94], the formation of a geminal pair that fixes the position of the pentagon might justify the simultaneous detection of a reconstructed vacancy in ref.[94]. To clarify this issue and find out a possible kinetic effect on the formation of a 2H geminal structure, we carried out a molecular dynamics simulation to follow the entrance of the second hydrogen on both the same (syn entrance) or on the other face (anti entrance) with respect to the first hydrogen adsorbed, as presented in sec.4.2.

In the adsorption of further H atoms, the energy landscape is governed by both geometric and electronic effects, with the latter being dominant. The general trend is to minimize the number of unpaired electrons at the vacancy site, in the end favouring closed shell (non-magnetic) states. Thereby, the incoming hydrogen atom preferably binds to one of the σ dangling bonds as these are tightly localized, thus more likely available to react than the π electrons, delocalized on many carbon atoms. Once no unpaired σ electrons are left or in the case of a geminal arrangement, the π electrons come into play. Accordingly, the closed-shell 4H-syn and 4H-anti structures are found to be thermodynamically more stable then the other structures ($\triangle E^H_{VnH} = -4.7$ eV), with the only exception of the 3H-anti case ($\triangle E^H_{VnH} = -4.6$ eV), as shown in table 4.7. In this latter structure the three H atom saturates the dangling bonds, leaving only the midgap electron unpaired.

To evaluate the thermodynamic stability of each n-hydrogenated phase at a chosen temperature

and pressure, we needed to consider the Gibbs free energy of formation $\triangle G_{form}(p,T)$, which was computed following the formula

$$\triangle G^{n}_{form}(p,T) = G_{VnH}(p,T) - G_{V}(p,T) - \frac{n}{2} \times G(p,T)_{H_2} \tag{4.5}$$

Where $G_{VnH}(p,T)$, $G_V(p,T)$ and $G(p,T)_{H_2}$ are the Gibbs free energies for the n-hydrogenated vacancy, the bare defect and the H_2 molecule respectively. As condensed phases usually show a much lower dependence on temperature and pressure conditions than the gas phase, we simply use DFT energies for the first two terms in eq.4.5. Assuming for hydrogen an ideal gas dependence on its partial pressure p, it follows

$$\triangle G_{form}(T,p) \sim E_{VnH} - E_V - \frac{n}{2} \times \left[E_{H_2} + H_{H_2}\left(p^0,T\right) - TS_{H_2}\left(p^0,T\right) + RT\ln\left(\frac{p}{p^0}\right)\right] \tag{4.6}$$

where E_{H_2} is the DFT energy of H_2, R is the perfect gas constant, $S_{H_2}\left(p^0,T\right)$ is the standard entropy at temperature T and standard pressure p^0 =1 bar[1] and the enthalpy is written as $H_{H_2} = \frac{5}{2}RT^0 + \triangle H^0_{H_2}\left(p^0,T\right)$ where $\triangle H^0_{H_2}\left(p^0,T\right)$ is the H_2 molar enthalpy change from T = T^0 =298.15 K and T at the standard pressure p^0[1]. With these taken, at first we computed the Gibbs free energies of formation for the various hydrogenated phases under a reasonable H_2 pressure and temperature conditions. Then we consider the lowest Gibbs molar free energies of formation at each temperature T and pressure p to build a phase diagram. The result is shown in fig.4.8, in which appears that the bare vacancy is stable in an ideal circular sector spanning the region of high temperature and low pressure. From this region, by moving along with a decrease of the temperature and/or an increase of the pressure, the system has the consecutive transitions towards the 1H, the 3H anti and the 4H syn phases. It is interesting to notice that, in these conditions, the 2H phase was not found. Moreover also high coverage phases were not found, as expected from the energy differences shown in fig.4.7, where, above the third hydrogen, the energy gain starts to reduce up to eventually become unfavourable. At the typical room-temperature (T$\sim$300 K) and pressure p(H_2)=0.55×10^{-6} bar the 3H-anti structure is the most stable and it would be a possible explanation for the detection of S=1/2 magnetic moments in irradiated graphene samples[74]. At the typical STM and TEM working conditions the column pressure is in the order of p=10^{-10} bar, but it is not easy to determine the composition of the gas mixture. Assuming a p(H_2)$\simeq 10^{-16} - 10^{-18}$ bar our calculations predict different scenarios depending on the system temperature. STM experiments are often performed at low temperatures (T $\sim$ 10 K) where the stable phase is hydrogenated, and to obtain a clean vacancy defect the samples usually undergo thermal annealing. For TEM instead, assuming a temperature T=300 K, the 3H-anti phase is still the most favorable and it might correspond to the three-fold symmetric vacancy recently observed by Robertson and co-workers[94], although the C-C distances shown in table 4.3 are sensibly larger than those found in the experiment (d_{CC}=2.8 Å vs. $d^{TEM}_{CC} = 2.5 \pm 0.1$ Å). We also note that the phase boundary with the 1H phase lays not far from these conditions, suggesting that the reconstructed vacancy also found in the same study [94], could

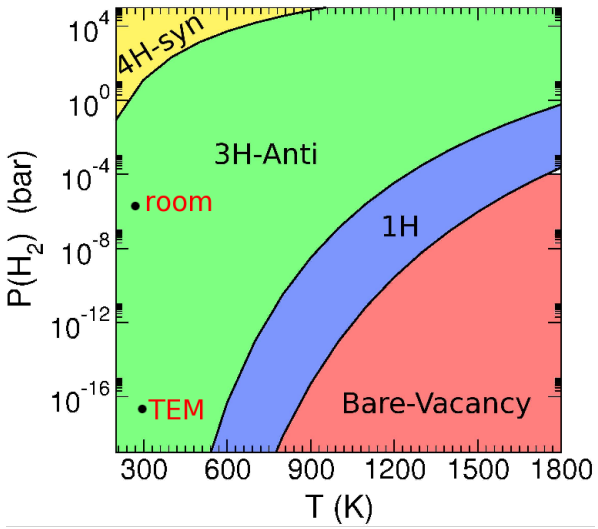

Figure 4.8: phase diagram for the hydrogenated C-vacancy in graphene. The diagram was built including all the structures reported in table 4.5.

be a mono-hydrogenated defect (d_{CC}=1.98-2.72 Å) in which, the presence of the H atom hinders the switching of the pentagon ring between the three possible orientations. Nevertheless the TEM experimental conditions are somewhat different from those used in our simulations, especially in terms of temperature, hence the identification of our computed structures with the observed defects, though reasonable, remains arguable.

4.2 Dynamics study of hydrogen adsorption on a 1H-vacancy

4.2.1 Method

We studied the entrance of a second hydrogen atom on a mono-hydrogenated carbon vacancy with ab initio molecular dynamics (AIMD) by using the VASP code[55, 57]. With respect to the position of the first hydrogen atom relatively to the graphene layer, namely above or below the plane, we considered the entrance of the second hydrogen atom from the same side or from the opposite side. We refer to these two possibilities as *syn* and *anti*, as shown in fig.4.9. Dynamical simulations were performed sampling the microcanonical (NVE) ensemble with classical trajectories. The Hellmann-Feynman forces were computed on-the-fly with DFT while the Newton equations of motion were integrated using the Verlet algorithm with a time step of 0.40 fs for projectile collision energy E_{coll}=0.1 eV. At the beginning of each trajectory the incident atom was set at 4 Å above the surface plane with monochromatic initial velocity directed along the surface normal. The aiming points were generated by sampling the xy coordinates of the incident hydrogen within a symmetry irreducible sector $\theta = \pi$ of the circular area of radius $r = 4.2$ Å centered on the vacancy. The surface initial conditions were not sampled in these calculations, in fact the surface atoms and the adsorbed hydrogen were initially set at rest at their equilibrium positions, determined by a geometry optimization run using a 0.01 eV/Å threshold on each atomic force, and left free to move during the

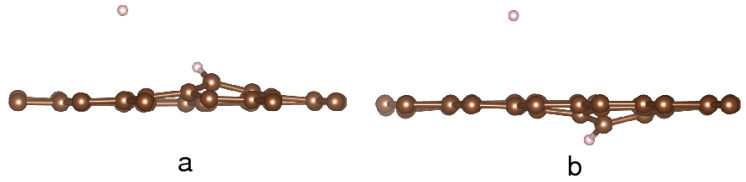

Figure 4.9: C and H atoms are respectively brown and pink. (a) *syn* entrance: the adsorbed H atom points towards the incoming H. (b) *anti* entrance: the adsorbed H atom points in the opposite direction with respect to the incident H.

whole simulation. These initial conditions imply a surface temperature T_s=0 K. Here the need of a large number of calculations required to significantly reduce the computational setup. Therefore, we chose a 4×4 supercell consisting of 31 C atoms, with the vacant site at the center of the cell and one hydrogen atom bound to carbon C1 in fig.4.1 and we set 10 Å of vacuum along the c axis to isolate the periodic images. A $3 \times 3 \times 1$, Γ centered k-points mesh was used, with a small (0.05 eV) Gaussian smearing to ensure a fast electronic convergence and correct forces; moreover the true ionic potential in the frozen core approximation was modeled by ultra-soft pseudopotentials that allowed to limit the energy cutoff of the plane waves expansion to 300 eV. The exchange and correlation energy was introduced via the Perdew-Wang (PW91)[86] functional within the generalized gradient approximation (GGA) in the spin polarized framework. On each of the two faces of the graphene layer, we run 1192 trajectories, equivalent to 2384 trajectories on the whole circular area surrounding the center of the vacancy.

4.2.2 Results

When an incident atom hits a generic surface many possible events may occurr and many of them are described in chapter 1. In the specific case of a mono-hydrogenated vacancy, the incoming hydrogen atom comes close to the surface and then it may be scattered back; alternatively it may access a reactive channel and form a chemical bond with a carbon atom of the lattice. The relative position of the two chemisorbed atoms, namely bound to the same carbon or not, allows to classify the possible outcome as either dimer or geminal pair.

The analysis of the trajectories shows that the incident hydrogen typically makes a bond with C1, C2 and C3 while no adsorption has been found on C4, C5 and C6. These sites are not nearest neighbours to the vacancy but they still bear spin density as consequence of the midgap state, i.e. of the π unpaired electron (see fig.4.2). Accordingly, the absence of sticking in these positions cannot be justified only by electronic arguments as a sizeable amount of spin density is anyway available to bind the projectile H atom. Anyway if one consider that the hydrogen adsorption on graphene implies a partial orbital rehybridization from sp^2 to sp^3, then it is reasonable to expect that the undercoordinated sites are favoured over the other sites. Note that the carbon C1 with the

cross section σ/Å^2	HH syn	HH anti
geminal	3.58	0.09
dimer	5.72	8.41

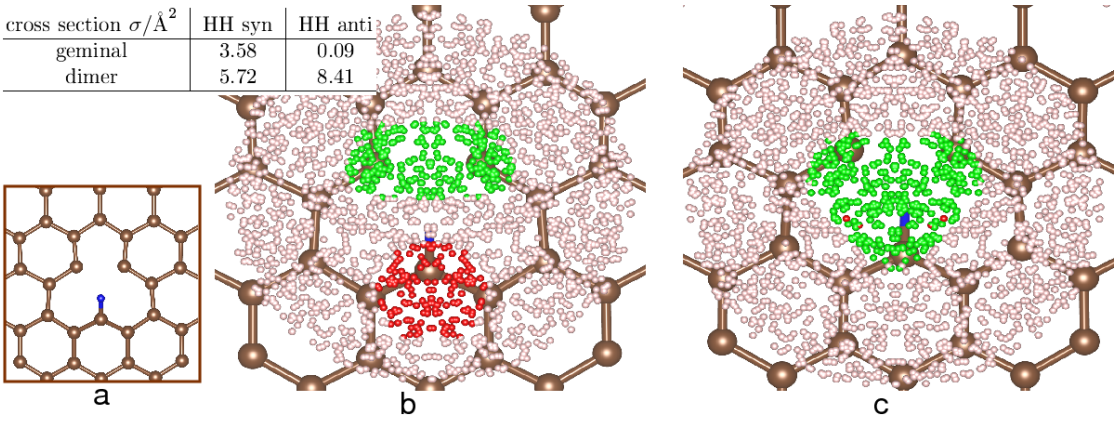

Figure 4.10: the aiming points of the incident H atoms span a circle centered on the vacancy. In red the impact coordinates of the incident H that lead to the formation of a geminal pair; in green those that result in the formation of a dimer; in pink the non reactive aiming points. The chemisorbed H is blue. In (a) the mono-hydrogenated vacancy in the equilibrium configuration. In (b) the syn configuration and in (c) the anti configuration.

chemisorbed hydrogen has already an sp^3 character and it is located out of the molecular plane as apparent in fig.4.2.

In the syn entrance, the geminal attachment has a cross section (*i.e.* a surface area around the target site in which the reaction occurs) of 3.58 Å^2, comparable to that of the dimer formation equal to 5.72 Å^2. On the other hand in the anti entrance, the incoming hydrogen may only access the dimer arrangement while the geminal one is almost inaccessible. This observation can be justified by considering the relative position of the hydrogenated carbon atom C1 with respect to the lattice plane and to the incoming hydrogen. Indeed the graphene plane acts somehow as a screen that deviates the incoming atoms towards the adsorption on C2 and C3. The resulting cross section on these sites is thus very large, 8.41 Å^2.

In fig.4.10 the initial coordinates (aiming points) of the incident atoms are shown with different colours depending on whether they enter a reactive channel or not. It can be clearly seen that syn and anti configurations are characterized by different reactive areas. More precisely in the syn case in fig.4.10b two reactive regions appear: one above the C1 carbon leads to the geminal arrangement, while that between C2 and C3 accounts for the dimers formation. On the other hand in the anti case in fig.4.10c only one reactive area is found above the vacancy that produces almost exclusively pairs of dimers. However, the two faces of graphene are both associated to large cross sections, mainly due to the presence of a remarkable steering effect. This implies the existence of a force that deviates the projectile from its linear motion perpendicular to the surface towards a certain target.

4.2.2.1 Reaction mechanisms

By following few trajectories in details one may deduce the mechanism through which a certain process occurs. In the following we examine the case of the reactive outcomes upon both the syn

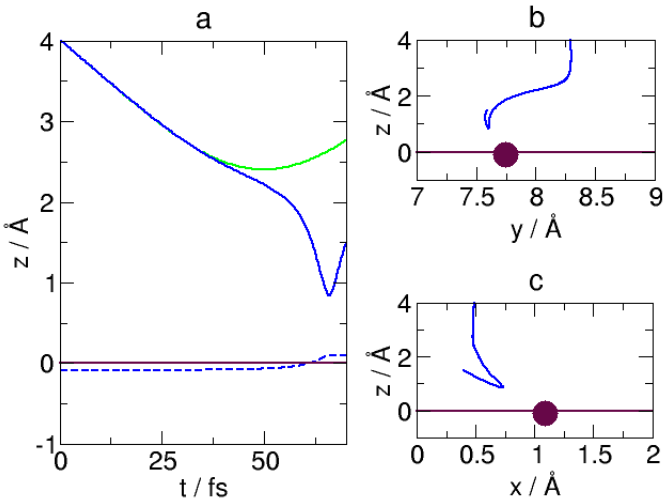

Figure 4.11: formation of a dimer upon the syn entrance. In (a) the time evolution of the z coordinate: the incident atom (solid blue line) proceeds toward the surface, it induces a displacement of the C atom (dashed blue line) on which finally it gets adsorbed. Incident atoms that do not enter the reactive channels are normally scattered back (solid green line). In (b) and (c) the xz and yz planes with the target C atom as a purple circle. The lattice plane is set to 0.

and the anti entrance. In general, when the incoming particle approaches the molecular surface two alternative processes may occur, namely it may access a reactive channel or it may be scattered back into the gas phase. In the case of the mono-hydrogenated vacancy the choice occurs at ~ 2.5 Å above the lattice plane as it is clear from fig.4.11a and fig.4.13a. Anyway if the incident atom succeeds in entering the reactive channel, then it gets close to the surface and it may induce a relaxation of the lattice and of the chemisorbed hydrogen; in the end it is trapped on one of the adsorption sites. Note that the incident hydrogen in syn with the adsorbed one is typically stopped $1 - 1.5$ Å above the molecular plane and does not penetrate closer to the surface, as shown in fig.4.11a and fig.4.12a; on the other hand in the anti configuration it may reach the surface and possibly cross it through the hole of the vacancy, before getting adsorbed. Of course, the relative position of the target and the projectile determines whether the projectile may cross the hole or it is reflected back; anyway the higher mobility of the projectile upon the anti entrance originates from the lower hindrance of the face. A common aspect to all these situations is the presence of a large amount of steering, that strongly deviates the incident hydrogen from its normal direction towards the target carbon. This effect justifies the large cross sections and can be clearly seen in fig.4.11b,c and fig.4.12b and fig.4.13b.

4.2.2.2 Energy barriers for the syn facial adsorption

The energy barriers for the entrance of a second hydrogen atom in the syn-facial configuration have been computed by using the nudged elastic band (NEB)[49, 71] method as implemented in VASP.

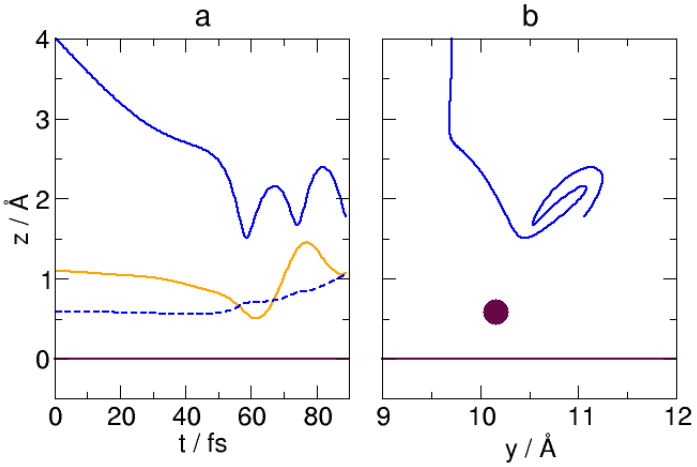

Figure 4.12: formation of a geminal pair upon the syn entrance. In (a) the time evolution of the z coordinate of the C atom (dashed blue line) that is pulled further away from the molecular plane by interacting with the incident H atom (solid blue line) that finally makes a bond. The effect on the chemisorbed H (orange solid line) is also shown. The lattice plane is set to 0. In (b) the trajectory in the yz plane with the C atom as a purple circle.

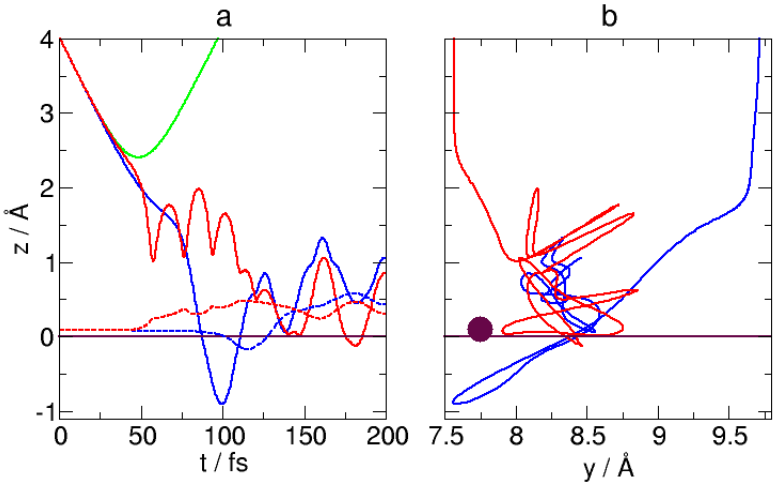

Figure 4.13: formation of a dimer upon the anti entrance. In (a) the time evolution of the z coordinate is shown for two trajectories, (i) blue and (ii) red. In (i) the incident H atom (solid line) passes through the surface before getting adsorbed on its target C (dashed line); while in (ii) this not occurs. Incident atoms that do not enter the reactive channels are normally scattered back (solid green line). In (b) the trajectories in yz plane with the C atom as a purple circle. The lattice plane is set to 0.

In principle this method allows to find the minimum energy path between an initial and a final state by acting on the intermediate configurations (images). Each image corresponds to a point on the energy hyperplane and it is associated to a specific geometry of the atoms on their way from the initial to the final state. Each image is allowed to move into the direction perpendicular to the hypertangent, defined as the normal vector between two neighbouring images. In this way the energy of the images is minimized and the minimum energy path is found. Note that the tangential motion is impeded only up to first order; anyway the introduction of *springs* allows to control this motion at higher orders and prevents the images from drifting.
Within the syn-facial scheme for the entrance of the second hydrogen atom, we computed the energy barriers to form a dimer or a geminal pair, corresponding to the blue and red curve in fig.4.14, respectively. To this end we chose two trajectories with the appropriate final outcome and we selected as intermediate images a number of geometries visited in the dynamics. In both cases the initial state consists of the mono-hydrogenated vacancy with the incoming hydrogen at 4 Å from the lattice plane. In principle the initial and final state should be two real minimum structures, but actually this is not the case for configurations reached within a dynamics simulation, thus only the initial state can be hold really equilibrated, while the final state cannot. Anyway this is not expected to have any relevant influence on the position and the shape of the energy barrier for two main resons: (i) we are interested in the hypothetical energy barrier in the entrance channel, thus far away from the surface and from the final state; (ii) we used a large number of images (sixteen) between the two reference states. The fig.4.14a shows the energy profile as a function of the z coordinate of the incoming hydrogen, chosen as the reaction coordinate for both the geminal and the dimer final configuration. In the same frame, the dotted lines represent the magnetisation profiles, that go to zero as the incoming hydrogen and the hydrogenated graphene start to interact. It is interesting to note from fig.4.14b that the incident atom has to overcome an energy barrier to form the dimer as well as the geminal structure. Due to the small height of the barrier, $\sim$20 meV, at room temperature the projectile may always access the reactive channel. As expected, the two barriers are shifted with respect to the z coordinate of the incident atom and this reflects the local geometry of the system, indeed the distortion of the lattice close to the hydrogenated carbon displaces the barrier at higher z values compared to the planar regions. This simply means that the hydrogen atoms directed towards the hydrogenated carbon C1 (the red area of the geminal product in fig.4.10a) will enter the reactive channel further away from the surface than those directed upon C2 or C3 (the green area of the dimer product in fig.4.10a).

4.3 Conclusions

We have studied the energy landscape and the magnetic properties of each of the structures involved in the hydrogenation of a carbon vacancy in free-standing graphene. The driving force for the hydrogenation process is given by the saturation of σ-dangling bonds and midgap states of the

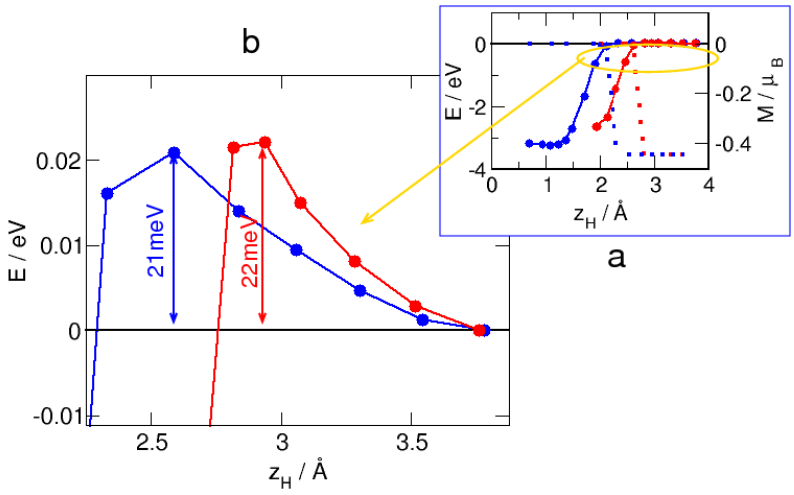

Figure 4.14: (a) energy (solid line) and magnetisation (dotted line) with respect to the z coordinate of the projectile for both the dimer (blue) and the geminal (red) arrangements. The solid circles on the energy profiles correspond to the optimized 'images' in the NEB calculation. (b) inset of the energy curves between 2-4 Å and evidence of the energy barriers.

graphene defect, which can readily couple with incoming radical H atoms to form progressively hydrogenated structures. Our calculations showed that the overall hydrogenation process is thermodynamically favoured and exothermic with respect to both atomic and molecular hydrogen gas sources at least up to four H atoms. In general we found that at each level of hydrogenation, the formation of the geminal structure is always less favoured than that of syn or anti configurations in contrast to recent a μSR study on the di-hydrogenated vacancy. In this case we carried out AIMD simulations to check if the geminal pair was somehow kinetically favoured, but we didn't find any evidence in this sense. Moreover, by extending our DFT results to a thermodynamic modelling, we found that at room temperature and pressure conditions the magnetic 3H-anti structure (M=1μ_B) is the most favoured phase, while the 2H phase cannot be dectected.

Chapter 5

Eley-Rideal formation of H_2 on Ag(111)

The study presented in this chapter inserts in the research field on nuclear fusion, as it aims to describe an important aspect of the production of negative ions, required in the process of plasma heating. In general, a nuclear fusion reactor needs a heated plasma to work. Many ways are known to heat plasma, like electric discharges, microwaves and neutral beam injection, where the latter appears as the best choice, once considered the large volume of plasma to heat. In this way, the plasma, which is usually confined by strong magnetic fields in a toroidal reactor known as tokamak, is heated up to desired level by two fluxes of high energy atoms, typically hydrogen isotopes. These atoms are injected as neutral species (otherwise they could not penetrate the strong magnetic field that confines fully ionized plasmas), but they are soon ionized upon bouncing off the ions already in the plasma. In this way they transfer energy to the plasma, thus increasing its temperature. The energetic neutral atom beam is obtained by acceleration and collisional neutralization of negative ions extracted from a low-temperature plasma source[1]. In principle both positive and negative ions might be used, but at the high operation energies ($\sim$ 1 MeV) at which current research aims, the choice of negative ions seems to be more practicable. This is related to the final neutralization step, that is more easily achieved in case of negative charges. Presently, the generation of negative ions from cold plasma is based on both a *volume* and a *surface* mechanism. In the first case, H^- ions are generated in the bulk plasma, where cold electrons (e^-_{cold} $\sim$1 eV) attach vibrationally excited hydrogen molecules H_2^v, thus inducing the dissociation of these molecules in the so-called dissociative attachment, namely $H_2^v + e^-_{cold} \rightarrow H + H^-$. The point is that this process is reversible, thus to prevent H from killing H^-, it would be useful to remove these H atoms from the bulk, so that to minimize the losses and possibly improve the gain of negative ions. To this end, two alternative routes are possible: in the present models, H atoms impinge on the internal walls of the reaction chamber, which are covered by cesium, likely forming H^- ions by electron capture. This process, known as *surface* production, easily occurs due to the low ionization energy of the metal, but it has an important shortcoming following from the volatile nature of cesium: indeed it can easily desorb and

[1]This is also known as *cold* plasma and it is usually defined at one atmosphere and near room temperature. This is usually a non-thermal plasma, namely the ions and neutral atoms temperature is significantly lower than the electronic temperature, $T_{ion} \ll T_e$, which indeed may be in the order of one eV.

diffuse into the accelerator. Not only does this mean that the cesium coverage has to be replenished continously, but it may also induce breakdowns and unwanted side-effects in the accelarator. In the attempt to find a cesium-free route, an alternative method has been considered aiming to remove H atoms possibly by sticking on a proper surface. To this end, the use of tantalum, graphite, silver... has been taken into account. Ideally, this process, known as *surface vicinity* production, should be as follows: H atoms easily stick on the surface which has to be stable and sustain a long operation time; then, through the mediation of the surface, H_2 molecules form, possibly in highly excited states; in the end, upon the desorption, these molecules are available to interact with cold electrons in the bulk. In general transition metals are a practicable choice as they are stable towards the erosion of cold plasma and H atoms may easily stick on them[15]. Anyway, if the metal-H binding energy is too high, the release of H_2 molecules is difficult as indicated by a low cross section[44]. This means that by using this kind of surface the loss of H^- ions is minimal due to the trapping of H atoms, but also the gain of H^- ions is minimal as the adsorbed H are not reused. On the other hand, by using graphite instead of a transition metal, one may likely achieve a large cross section and a high vibrational excitation for the molecular hydrogen recombination[44, 116], but at the price of a very small stability under the operative conditions. In this scenario, silver has many interesting features, indeed it is stable and it has the weakest H-metal binding energy ($\sim$ 2 eV), that is high enough to favour the sticking of H atoms, as well as low enough to allow the formation of H_2 molecules with a sizeable cross section that mainly accounts for Eley-Rideal and hot-atoms reaction mechanisms. In the following, upon a general presentation of H-metal systems, we consider the theoretical methods used to study the formation of H_2 molecules on metal surfaces according to Eley-Rideal reaction mechanism, pointing out both benefits and shortcomings. Then we report and compare the results obtained in terms of reactive cross sections and product molecules.

5.1 Hydrogen atoms on metal surfaces

The abstraction of hydrogen atoms adsorbed on a single crystal surface by means of gaseous hydrogen atoms impinging on that surface leads to the formation of H_2 molecules, $H_{(g)}+H_{(a)} \rightarrow H_2$, and it has been the object of many theoretical as well as experimental studies. This process is expected to occur according to the Eley-Rideal reaction mechanism[26] that exhibits energetics, kinetics and dynamics features that are not common to reactions following the alternative and more familiar Langmuir-Hinshelwood scheme. The energetics of the hydrogen abstraction from metal surfaces may be roughly estimated by considering that the formation of the H-H bond releases about twice as the energy in the H-metal bond, thus the reaction is strongly exothermic (over 2 eV). Note that this energy is available to the product molecule if the dissipation into phonons is not effiecient; in this way, the dynamics of the reaction leads to product molecules that immediately desorb from the surface due the high translational energy and that are vibrationally and rotationally excited. Both experiments[92] and theory[62] proved that the exothermicity of the reaction is typically distributed into the internal degrees of freedom of the product molecules.

In terms of kinetics, the formation of product molecules upon a direct reactive encounter between the two hydrogen atoms is expected to obeys the exponential rate equation $R(t) = R_0 exp(-\sigma\phi t)$, where R is the rate, σ is the abstraction cross-section, ϕ is the flux of gaseous atoms and t is the time. This means that the product rate is maximun when the flux of gaseous atoms starts, then it decays exponentially. Anyway, discrepancies from this ideal behaviour are quite usual: in some cases for instance the maximum of the product rate is delayed over a finite time after the opening of the gaseous flux; moreover in the D by H abstraction homonuclear product (D_2) may form in addition to the HD molecules.

Upon these observations a new reaction model was proposed based on the concept of hot atoms. These form when the incident atoms, possibly accelerated by the attractive potential of the surface, approach that surface. Here, the corrugation of the potential energy surface may cause a mixing of the translational degrees of freedom of the atoms that finally ends up with a substantial kinetic energy parallel to the surface. In ref.[52] it is clearly pointed out that these hot atoms may either stick on the surface or react with adsorbed species depending on the nature of the metal surface. Of course, hot atoms can stick only if they loose the excess of energy via phonons or electron-hole excitations. Anyway, the mass mismatch prevents from an effective energy exchange with phonons; moreover metals with similar mass often show substantially different phenomenologies. Therefore the energy dissipation more likely occurs via the electronic mechanism, with an electron-hole excitation probability that is proportional to the squared density of states at the Fermi level $\rho^2_{E_F}$. Accordingly, on metals with a low ρ_{E_F} the sticking is unfavoured and the abstraction kinetics proceeds along the hot atoms pathway that produces molecules almost indistinguishable from those obtained in the direct Eley-Rideal scheme. Note that the encounter of hot atoms with adsorbed particles can open an alternative channel to dissipate energy. Indeed the collision is not always reactive, but it may simply induce an energy transfer towards the adsorbed species that possibly start to diffuse on the surface as 'secondary' hot atoms.

In this chapter, we report on the formation of hydrogen molecules on the face (111) of crystalline silver within the Eley-Rideal reaction scheme. This surface is closely packed and it has hexagonal symmetry. In a recent experimental study[52] the formation of HD molecules by abstration of deuterium adsorbed on Ag(111) with gaseous hydrogen has been investigated. The choice of the (111) instead for instance of the (100) face, derives from the experimental fact that the dense arrangement of nuclei in (111) rules out any complication possibly due to the presence of subsurface species as well to the surface reconstruction, in the limit of a controlled exposure to gaseous atoms. Moreover, the product rates measured for a variety of coverages with fixed surface temperature $T_s = 80K$ and flux of H atoms $\phi = 16ML/s$, all show the exponential decay common to Eley-Rideal and hot atom pathways.

An interesting feature, already found for HD formation of graphite, is that a lower surface coverage implies a larger cross-section. In the case of graphite a cross-section[2] of about 10 $Å^2$ was predicted

[2]The concept of cross section is used in physics to indicate the surface area around a target in which a certain event is expected to occur. For instance in the case of recombinative processes between an adsorbed atom and a gas

in theory[101] and measured in experiments[116]. This huge value is due to three main reasons: (i) deuterium forms a weak bond of only ∼0.7 eV with carbon; (ii) the carbon atom has to pucker out of the plane to bind H or D. This means that this process is activated, thus the sticking of hot atoms is unfavoured. Moreover this also implies that (iii) the adsorbed atom on top of a puckered carbon is nearly 1.8 Å far above the surface. Therefore the incident hydrogen feels the attraction of this atom very soon approaching the surface and it is steered towards it eventually increasing the reactive cross section. Note that at high coverage this effect is reduced due to the competition between adjacent adsorbed atoms.

By considering the abstraction of adsorbed hydrogen by gaseous hydrogen as a prototypical case, in general one may identify two limiting situations[62]: if the incident hydrogen is weakly attracted by the surface, namely the adsorption energy (D_a) is lower than one half of the energy released by forming a molecule (D_m), i.e. $D_a < D_m/2$, then the reaction is favoured over the trapping; on the contrary, when $D_a > D_m/2$ the trapping channel becomes energetically more favourable. In the case of metals, usually $D_a \sim D_m/2$, thus the trapping and the reactive channels are energetically similar and the final results varies from metal to metal. Note that here the reaction usually occurs within the hot atom scenario. For small D_a, namely when the Eley-Rideal scenario likely applies, the steering effect begins to operate and to increase the reactivity. Here in fact the incoming atom feels a less strong attraction towards the substrate, thus it is less accelerated and it can more likely access the minimum energy path towards the product state; note that, as for graphite, the effectiveness of the steering is maximum at low surface coverage where the adsorbed atoms are far apart and do not overlap their reactive spaces. In a similar way, also the energy of the incident atom E_i may act on the reaction cross section. In this case, when $E_i < D_a$ the reactivity is little affected by the choice of E_i due the acceleration felt by the incoming atom while approaching the surface; on the other hand once $E_i > D_a$, the reactivity decreases as the incident atom moves too fast to feel any steering effect. The case of Ag-H is somehow borderline indeed it shows both an Ag-H bond energy of ∼2 eV that should favours the hot atoms scenario and a remarkable enhancement of the cross section at low coverage that is consistent with the steering effect and the Eley-Rideal scheme. Moreover, the large reaction cross section encountered on the silver surface is also determined by the small density of states at the Fermi level that makes the energy dissipation unefficient and the sticking unfavourable[52].

The model system The crystalline structure of silver is face-centered cubic (fcc) and the lattice constant is $a = 4.163$Å. The face (111) results from the ABC stacking of the lattice planes, it is closely packed and it has hexagonal symmetry. On this face there are four high symmetry sites, namely top, bridge, hollow fcc and hollow hcp as shown in fig.5.1. This means that the hydrogen atom may stick on the silver surface directly above a silver atom (on top), between two adjacent

phase particle, the reactive cross section correspond to a region, such as, if the incident atom impinges on it, the reaction takes place otherwise not. Note that the reactive region does not necessarily include the target, for instance in the limit of non collinear reactions, the cross section usually accounts for the area of a ring possibly centered on the target atom.

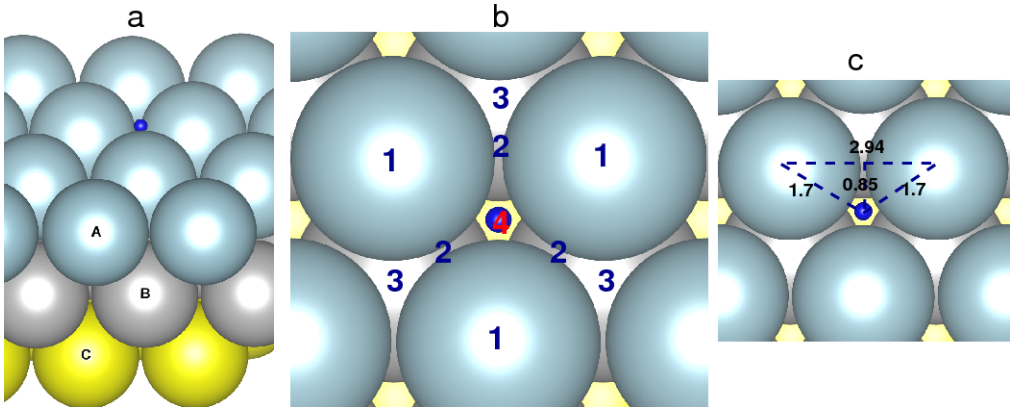

Figure 5.1: (a) side view of the Ag layers with ABC stacking. (b) In evidence the high symmetry sites (1) top, (2) bridge, (3) hollow hcp and (4) hollow fcc where target hydrogen sits. (c) Significative distances.

silver atoms (in bridge), in a threefold hollow site eclipsed with a silver atom either in the second layer (hcp) or in the third layer (fcc). In this way the coordination increases, thereby it is reasonable that the hydrogen adsorbs preferably in the hollow site with the fcc configuration sligthly favoured ($\sim 16\,\text{meV}$) over the hcp one. With respect to the bridge and the top positions, the hollow fcc site is favoured of nearly $\sim$0.15 eV and $\sim$0.61 eV respectively[3]. Of course the adsorption in intermediate positions is also possible.

5.2 Theory of gas-surface systems

Traditionally the study of gas surface processes is done with the help of molecular dynamics methods where the positions of the nuclei in the system evolve in time driven by the forces acting on them. Two alternative perspectives may be identified, that differ on the way these forces are handled: in one case, the forces are obtained at each step from the potential energy surface of the system computed before running the simulation; in the other case, the forces acting on the nuclei are computed on-the-fly over the simulation, thus for each istantaneous nuclear arrangement.

5.2.1 The quasiclassical trajectory method

In this chapter we report quantum dynamics and quasiclassical trajectory (QCT) results obtained on the basis of the same external potential energy surface. This has an analytical form and it is defined with a limited number of degrees of freedom chosen as relevant for the system under investigation. In the case of the Eley-Rideal recombination between an incident gaseous hydrogen (projectile) and an hydrogen adsorbed in a given site (target) on a rigid surface, in principle the potential energy surface should be defined upon two position vectors $\mathbf{r}_i$ and $\mathbf{r}_t$ for the incident and the target hydrogen atoms. As the interest is on the state of the product molecule, these

[3]The energy differences have been computed in the plane-wave density functional theory approach, by using the setup described in sec.5.4.1: three layers of silver atoms described by PAW potentials; the exchange-correlation energy introduced by the PBE functional; the energy cutoff set at 270 eV and a $6 \times 6 \times 1$ k-points grid.

positions can be redefined in terms of relative position $\mathbf{r} = \mathbf{r}_t - \mathbf{r}_i$ and center-of-mass position, $\mathbf{R} = (m_t\mathbf{r}_t - m_i\mathbf{r}_i) / (m_t + m_i)$ with m_t and m_i the two masses. At this point the six-dimensional problem may be reduced to a three-dimensional case by introducing the flat surface approximation, based on the assumption that the interaction between the atoms and the surface is translationally invariant on the surface and thus rotationally invariant around a normal axis to the surface; this means that the diffusion of atoms on this model surface is a non activated process. In the limit of this approximation, the potential energy can be specified as $V(\rho, z_t, z_i)$ where ρ is the distance between the target and the incident atom in the xy plane, while z_t and z_i are the positions of the atoms along the z axis. At last, the analytic expression of the potential energy surface is given by a model potential in which a number of parameters has been optimized to fit in the potential energy data $V(\rho, z_t, z_i)$.

5.2.1.1 The potential energy surface

A common type of model potential appropriate to deal with gas-surface processes like recombinative desorption as well as dissociative adsorption is the modified LEPS (London-Eyring-Polanyi-Sato) potential[27, 97]. To build the modified LEPS potential of interest in this work, the energy values for the fitting were obtained by varying the coordinate z_i from 0 to 4 Å for each chosen value of z_t and ρ, more precisely for z_t equal to 0.91, 1.11 and 1.31 Å and ρ set at 0.00, 0.75 and 0.95Å along the hollow (fcc) to top direction in fig.5.1. It is crucial to point out here that this choice of ρ implies that the peculiar features of this high symmetry direction are actually extended to the whole xy plane as the flat-surface model applies. This is of course a strong approximation but the error introduced is often acceptable as on metal surfaces (i) the diffusion barriers for hydrogen atoms are low, just few tenths of eV[90], and (ii) the reactive encounters take place relatively quite far above the surface where the corrugation effects are minimal[91]. Reasonably one might choose more than one representative direction and make a rotational average over the results obtained along each direction (weighted for the probability of each direction). The natural choice, in the case of the Ag(111) surface, would be to investigate the potential energy surface for ρ values along the hollow to hollow direction in addition to the one hollow to top. In this way the obtained potential energy surface is no longer attributable to one specific direction, but it indirectly accounts for the surface corrugation even in the flat surface model.
However in this case, for each set of coordinates, the corresponding energy $V(\rho, z_t, z_i)$ is computed with plane-wave density functional theory (DFT) as implemented in the VASP package[55, 57]. To this end, the metal surface has been modeled by five stacked layers of silver atoms, in which each layer is a 2×2 supercell with four atoms; above the top layer ~ 22 Å of vacuum were set along the c axis to prevent any unphysical interactions with the adjacent images. Note that the positions of the nuclei in the highest two layers were allowed to relax during the calculation. The exchange-correlation effects for both silver and hydrogen atoms were introduced by the Perdew-Burke-Ernzerhof (PBE) functional[84, 85] within the generalized gradient approximation (GGA),

in the spin-polarized framework. Moreover, the expansion of Kohn-Sham orbitals in a plane-wave basis set was limited to a 425 eV energy cutoff; the electrons were described by the projector augmented-wave (PAW) method[14, 58], in the limit of frozen core electrons. The wave function in the reciprocal space was defined by a $10 \times 10 \times 1$, M centered k-points mesh[4].

5.2.1.2 Main differences between quantum and quasiclassical dynamics

It is important to point out that this potential energy surface has been originally constructed in the group of D. Lemoine[20] to perform quantum dynamics calculations and for this reason only three degrees of freedom have been taken in account. In this thesis, we chose to keep the same potential energy surface so that to be able to reproduce those quantum results by using our own code; moreover this choice allowed us to compare exactly quasiclassical and quantum results so that to find out the possible quantum effects in the formation of H_2 according to the Eley-Rideal mechanism. To this end it is useful to sketch out the main differences existing between the quantum and the (quasi)classical approach as used in this thesis. The main point relies on the nature of the atoms in the system: in the quantum approach they are described in terms of wavefunctions, while in the quasiclassical approach they are treated as classical objects. Accordingly, in quantum dynamics:

- the dynamics of the system is fully described by the time-dependent Schrödinger equation[5] and depends on the potential energy surface of the system itself.
- the target atom initially bound to the surface is represented by an appropriate eigenstate, corresponding to a certain vibrational state v, while the incoming atom at the starting point is represented by a wavepacket fully localized in space, namely a set of waves all in phase at the initial time. Due to the uncertainty principle, this implies that the corresponding momentum of each wave cannot be determined, namely the wavepacket spreads over a wide range of energies; as a consequence, the propagation of the wavepacket occurs with some interference among its components.

[4]The optimized parameters of the LEPS model potential used in this work, taken from the group of D. Lemoine[20]:

	$D_j\,(eV)$	$r_j^{eq}\,(\text{Å})$	$a_j\,(\text{Å})$	$\alpha_j\left(\text{Å}^{-1}\right)$	$b_j\,(\text{Å})$	$\beta_j\left(\text{Å}^{-1}\right)$	Δ_j
i	1.153	1.156	0.805	0.718	2.058	4.056	-0.210
t	2.052	0.944	0.874	0.144	1.622	13.006	-0.002
m	4.821	0.767	1.753	0.134	1.627	9.672	0.095

The root mean square of the final fit is 14 meV .

[5]The time dependent Schrödinger equation read as

$$i\hbar\frac{\partial\Psi\left(\mathbf{R},t\right)}{\partial t}=\mathcal{H}\Psi\left(\mathbf{R},t\right)$$

and upon integration it gives

$$\Psi\left(\mathbf{R},t\right)=\exp\left(-\frac{i}{\hbar}\mathcal{H}t\right)\Psi_0\left(\mathbf{R}\right)$$

where the time-dependent wavefunction is splitted into a time evolution operator, i.e. the exponential function, and in a spatial part corresponding to the initial wavefunction.

- in the presence of an energy barrier to the formation of the product molecule, a certain amount of tunneling may be observed; this effect allows to obtain a nonzero reaction cross section even when the incident particle approaches the surface with an amount of energy smaller than such energy barrier.

- in the end, reactive encounters in quantum dynamics lead to the formation of molecules in a well-definite quantum state, characterized by vibrational and rotational quantum numbers.

On the other hand, in quasiclassical dynamics:

- the dynamics of the nuclei occurs along the same potential energy surface used in the quantum case, but the nuclear coordinates are propagated by solving either the Newton's or the Hamilton's equations of motion, equivalently[6]. The output of this process is known as a trajectory.

- each trajectory corresponds to a specific initial state of the incident atom with a well-defined position and momentum; for this reason a classical trajectory has a completely definite outcome, strictly determined by these initial conditions. Naturally, to get quantities of physical interest (i.e. cross-sections, rates...), one may not refer to a single specific situation as it has no statistical meaning, but it is necessary to average over a number of initial conditions, usually generated in a random way. By the way this allows also to reflect the quantum uncertainty, in the classical limit.

- each trajectory is run independently from the other ones, thus there is no way to account for the interference among the wavefunctions, observed in the quantum case. In principle, in the attempt to mimic the quantum interference at the classical level, one might propagate all together a number of incident atoms with different initial conditions, in such a way that they can feel each other during the dynamics.

- the classical nature of the particles excludes any tunnelling effect, thus in the presence of a potential energy barrier the quasiclassical cross-section is irremediable doomed to vanish at sufficently small collision energies.

- the quantum effects are partially recovered by assigning an initial position and velocity to the adsorbed atom, taken from the proper phase space. This choice, that defines the quasiclassical approach, is due to the assumption that the main limit of the classical dynamics comes from neglecting the vibration of the adsorbed atom, indeed supposed to be at rest in its equilibrium position. In the quasiclassical model, at the initial time the adsorbed atom has a quantum

[6]The classical evolution of the nuclear coordinates of each particle is obtained by using the Newton's law $-\nabla V(\mathbf{R}) = M\ddot{\mathbf{R}}$. An alternative method relies on the Hamilton's equations for the position and the momentum:

$$\frac{d\mathbf{p}}{dt} = -\frac{\partial \mathcal{H}}{\partial \mathbf{q}}; \qquad \frac{d\mathbf{q}}{dt} = \frac{\partial \mathcal{H}}{\partial \mathbf{p}}$$

where $\mathcal{H} = \mathcal{H}(\mathbf{p}, \mathbf{q}, t)$ is the hamiltonian, corresponding to the total energy of the system.

nature; anyway over the dynamics this atom moves in a continuum of energies as predicted by the classical equation of motions, thereby loosing its quantum character. In the same way, the product molecules may explore any energy and any configuration along the potential energy surface, thus behaving as classical species. However, in this case, the quantum nature of the molecules is usually recovered by associating each of them to the closest quantum level, specified by the vibrational and rotational quantum numbers.

5.2.2 The ab initio molecular dynamics approach

In ab initio molecular dynamics the forces that act on the nuclei are computed at each step of the simulation and depend on the actual nuclear arrangement. This means that it is fundamental to reach the electronic convergence at each step to prevent the system from evolving under the action of fake forces. Of course, this implies a dramatic enhancement of the computational cost compared to those methods that rely on the external potential energy surface; therefore a key point in AIMD is often to determine the best setup in terms of model system and computational accuracy to get reliable results while reducing as much as possible the timings. It is obvious that the main novelty in AIMD rests on the description of the potential energy for two main reasons: the first is a consequence of the type of potential energy surface chosen for our quantum and quasiclassical studies, while the second is more general. More precisely, with respect to the flat surface model, the AIMD approach fully accounts for the surface corrugation, that is the computed energy values for each configuration depend on 3N degrees of freedom with N the number of atoms in the system. In this way a more realistic picture of the system is obtained, that goes beyond the limits of the flat surface approximation: namely the fact that the features of a chosen direction along the surface, for instance hollow to top, are overemphasized as this direction is assumed to be rotationally invariant throughout the xy plane. Anyway, it is important to point out that in principle not only AIMD can model the surface corrugation, indeed at least in the (quasi)classical trajectory method the dimensionality of the reference potential energy surface can be likely increased to this end. This means that the peculiar aspect in AIMD in general does not rely on the proper description of the surface, but on the fact that the forces computed on-the-fly are able to account for any instantaneous variation of the system possibly leading to unforeseen outcomes. For further details on this method the reader is referred to appendix C.

5.3 Formation of H_2 molecules: the QCT approach

We used the quasiclassical trajectory method to study the formation of hydrogen molecules on a silver surface. The QCT method leans on a potential energy surface built in a previous calculation and included as a set of parameters in the dynamics; as outlined in sec.5.2.1.1 in this case the potential energy surface has three degrees of freedom and accounts only for the hollow to top direction across the xy plane. This means that no corrugation is introduced and the flat surface approximation holds; moreover, the lattice vibrations are not taken into account as the surface

is assumed to be rigid. It is important to point out that the use of a rigid surface rules out the possibility of an hydrogen-to-silver energy transfer and this has two main consequences: (i) it introduces an error, that anyway is expected to be small due to the mass mismatch of the two species; (ii) it prevents the adsorbate from dissipating its vibrational energy into the substrate. From this last point it follows that, whenever the vibrational excitation of the adsorbate is taken into account, e.g. in the quasiclassical model, the substrate has to be described as a rigid surface to avoid fluctuations in the energy of the target atom. On the other hand, simple classical mechanics without any zero point-effect is appropriate to deal with a non rigid surface. Note that following from the experimental evidences in ref.[52], here the role of the electron-hole excitations in the metal atoms is neglected and a simple adiabatic picture of the collision dynamics is given.
The quasiclassical dynamics method was used to study the system composed by an adsorbate either at rest or in its vibrational ground state $v = 0$ and an incident atom initially moving along the surface normal with collision energy in the interval 0.01-4.0 eV. It was found that while approaching the substrate, the incident atom may (i) react, (ii) be trapped on the surface, (iii) induce the desorption of the adsorbate or (iv) be scattered back into the gas phase. In each case the actual outcome depends on a number of factors, like the collision energy, the impact parameter and the efficiency of the energy transfer. Note that in the assumption of a rigid surface, the incident atom has only one way to dissipate part of its energy, that is by transfer to the adsorbate. In this process, the adsorbate may simply start to vibrate in its place or it may acquire energy enough to diffuse on the surface, form a molecule or desorb escaping from the potential well. In the meanwhile, if the incident atom has dissipated the proper amount of its energy, it may populate a truly bound state, otherwise it is doomed to return into the gas phase: note that such event possibly occurs after some time in which the atom is temporatily trapped into an unstable state. It is quite obvious that this metastable species can be addressed as hot atom; anyway, also the bound species has an hot atom character as it is not in thermal equilibrium with the substrate: this means that its energy is below the dissociation threshold but above the diffusion barrier[70]. Note that the flat surface approximation assumes that no barrier to diffusion exists, thus that the surface is flat.

5.3.1 Computational details

The Eley-Rideal formation of hydrogen molecules is studied with the homemade code TRAJ[83, 104]. For each energy in the interval $0.025 - 4.0$ eV we run 10^5 trajectories with a uniform sampling of the $8 \times 8\,\text{Å}^2$ unit cell. The projectile atom was initially placed 10 Å above the surface with the velocity vector along the surface normal; each trajectory is propagated until the final analysis returns the same final state for five consecutive times. The first analysis is performed after about ~ 726 fs ($3 \cdot 10^4$ a.u.) when the projectile has initial energy in the interval $0.025 - 1.0$ eV and after ~ 242 fs (10^4 a.u.) in the interval $1.025 - 4.0$ eV. The hamilton equations of motion were integrated using the Nordsieck numerical integrator with a time step of 0.006 fs (0.25 a.u.) for all the projectile collision energies.

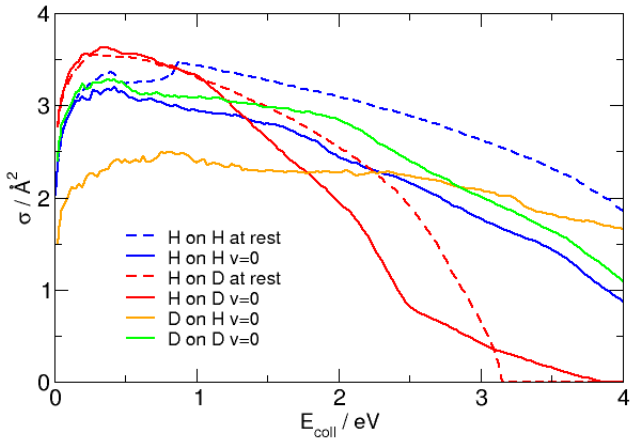

Figure 5.2: The Eley-Rideal cross-section as a function of the collision energy of the incident particle. Solid lines result from quasiclassical ($v = 0$) initial conditions of the target atom, while dashed lines accounts for classical trajectories with the target atom initially at rest ($ZPE = 0$).

5.3.2 Results

Both hydrogen and deuterium atoms were chosen as incident and adsorbed species and all the possible combinations were considered. The initial conditions of the target were sampled only in the vibrational ground state $v = 0$, as the excited states are not accessible in the ordinary experimental conditions; indeed in ref.[52], the adsorption of hydrogen and deuterium on the surface was achieved upon admitting a flux of atoms to the silver surface at ~ 80 K.

The cross sections of the Eley-Rideal reaction are reported in fig.5.2. In general the curves differ depending on the nature of the incident and the target atom; anyway the formation of homonuclear products, namely H_2 and D_2, shows a similar tendency. Note anyway that in a qualitative perspective, the reaction cross section behaves in the same way in all the cases: at low collision energy, below ~ 0.4 eV, it rapidly increases up to a maximum value and then it decreases. More precisely, the cross section vanishes at high collision energy in the case of the abstraction of deuterium by an incident hydrogen; on the other hand, in the reversed case the cross section only slightly decreases by increasing the collision energy. The classical situation was studied in the case of hydrogen impinging on the surface with either hydrogen or deuterium adsorbed on it. Here the target atom is assumed to be at rest in its equilibrium position 0.944 Å above the surface, as taken from the potential energy surface. Of course, this approximation introduces an error that has been evaluated in the case of the abstraction of either hydrogen or deuterium leading to H_2 and HD molecules. Accordingly, the vibrational motion of the atom on the surface seems to be almost irrelevant at low collision energy, that is below ~ 0.5 eV in the case of hydrogen and below ~ 1.1 eV for deuterium; on the other hand at higher energies, the classical model returns a cross section that follows almost parallely the quasiclassical one up to ~ 4 eV for the H_2 formation and at least up to ~ 3 eV in the case of HD, but that overestimates the quasiclassical cross section up to $\sim 50\%$.

5.3.2.1 Reaction mechanisms

As can be seen in fig.5.3a, at low collision energy, the incident atom feels the corrugation of the potential as it moves slowly towards the surface and it may possibly access the minimum energy path. In this way the cross section increases since more trajectories with high impact parameter, namely $r_{eq} < b < 2r_{eq}$ where $r_{eq} = 0.767$Å is the equilibrium distance in the H_2 molecule, can be captured by the adsorbed hydrogen. On the other hand, at small b, the incident hydrogen is initially attracted towards the target; then by further approaching the surface the distance between the two atoms becomes smaller than r_{eq} and eventually the incident hydrogen is scattered away from the target. Anyway, the projectile has probably trasferred part of its energy to the target, thus it unlikely returns into the gas phase while it more probably becomes trapped on the surface with a hot atom character. In the end, for $b \geq 2r_{eq}$ the incident hydrogen still slightly deviates from the normal direction possibly following the minimum energy path and it is finally back reflected into the gas phase by the repulsive potential once the distance between this hydrogen and the surface has become smaller than about ~ 1Å.

In general, by increasing the collision energy, the incident atom feels the corrugation of the potential energy surface more weakly in the entrance channel, so that it unlikely will be able to find out the minimum energy path leading to a certain outcome. As shown in fig.5.3b-c the increase of the collision energy up to 1 eV and further on up to 4 eV results in a decrease of the reaction cross section due to the fact that fast-moving projectiles with high impact parameter cannot be captured by the attractive potential of the target atom. Normally at high b the incoming hydrogen proceeds along the normal direction up to the surface, then it is reflected back by the repulsive potential and it returns into the gas phase; in a similar way, at small b while approaching the surface, the projectile gets close to the target atom and it is scattered away by the repulsive potential when the distance between them becomes smaller than r_{eq}. Trajectories with impact parameter in the interval $r_{eq} < b < 2r_{eq}$ are typically slightly deviated towards the target while the projectile approaches the surface, then they may lead to a reactive encounter that typically occurs upon a bounce of the projectile on the surface.

In general at normal incidence, the use of a flat surface, that is rotationally invariant around the normal to the surface, allows to define the probability of reaction as a function of the impact parameter. This reaction probability, also known as opacity function, is related to the reactive cross section by $\sigma_r = 2\pi \int_0^\infty P_r(b)\, bdb$ where $P_r(b)$ is the opacity and b is the impact parameter. Note that the integral is actually limited to the sampled area and that b acts as a weighting factor, thereby trajectories at high impact parameters are responsible for most of the reactivity. The opacity function for a given collision energy in fig.5.3d represents the fraction of reactive trajectories for each impact parameter in the interval from 0 to 3 Å from the target, being 0.01 Å the separation between the impact parameters. For each of them, we run 400 trajectories by randomly sampling the phase space of the target atom in the vibrational ground state $v = 0$ (on the potential energy surface in ref.[20]) in terms of position and velocity along the z axis normal to the surface. In the

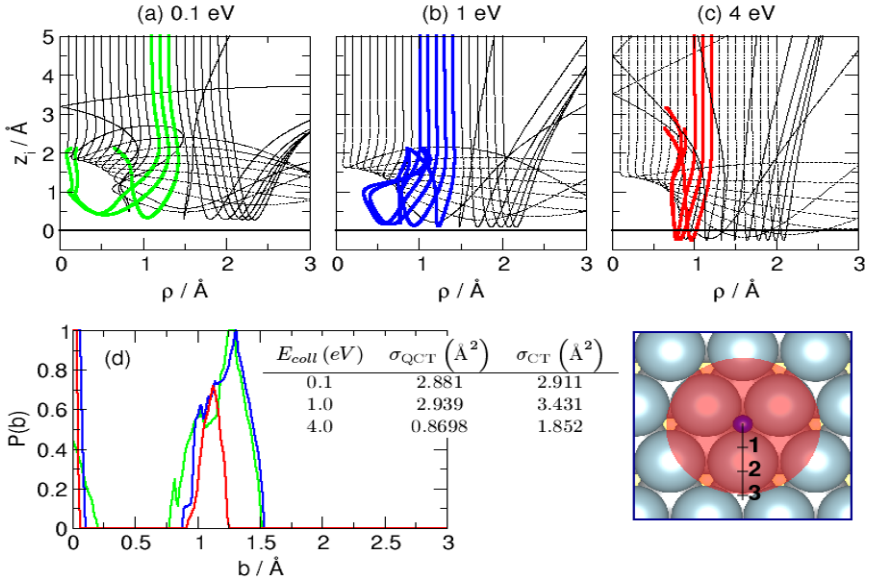

Figure 5.3: (a)(b)(c) representatives set of classical trajectories in the (ρ, z_i) plane for different collision energies; solid bold and dashed lines are for reactive and nonreactive trajectories, respectively. (d) QCT ($v = 0$) opacity functions computed at the same collision energies as for the trajectories (with the same choice of colours). The surface level is set to zero. In the inset on right the lenght scale in Å drawn along the hollow to top direction; as indicated by the red shaded area, this peculiar direction is assumed to generate the xy plane by rotation around the surface normal.

end, as illustrated in fig.5.3d the increase in the collision energy narrows the reactive interval in terms of impact parameter and it reduces the reaction probability. Note that at all the energies considered a nonzero contribution to the quasicollinear reactivity is present that anyway has an almost negligible influence on the total cross section.

The effect of the initial energy of the projectile on the reactivity, for instance on the formation of H_2 molecules, has been studied at collision energy equal to 0.1, 1 or 4 eV and impact parameter equal to $b = 0.95$ Å with the adsorbed atom in $v = 0$; for each value of E_{coll}, we followed 400 quasiclassical trajectories by choosing at random the initial conditions of the target, in terms of position and velocity along the z axis normal to the surface. These coordinates give an energy equal to that of the desired quantum vibrational state, in this case $v = 0$, and are obtained from the potential used for the dynamics. Moreover, the choice of this impact parameter is appropriate to investigate the reasons of the narrowing of the reactive interval with the increase of the energy; this is because such b falls on the region where clear differences on the three collision energies appear.

In fig.5.4 we plot phase space points of the target hydrogen at the initial time $t = 0$ (blue ellipse) and in correspondence of the first turning point of the incident atom (orange non regular shape) for all the energies considered; the green dots indicate the position and velocity of trajectories with an eventual reactive outcome. Note that due to the anharmonicity of the potential, the phase space points at $t = 0$ with the target atom in $v = 0$ do not have a perfect elliptical shape, that would be indeed typical of the harmonic case; anyway here the deviation is small since close to the bottom of the well the anharmonicity is very weak. On the other hand, at the time the projectile has its

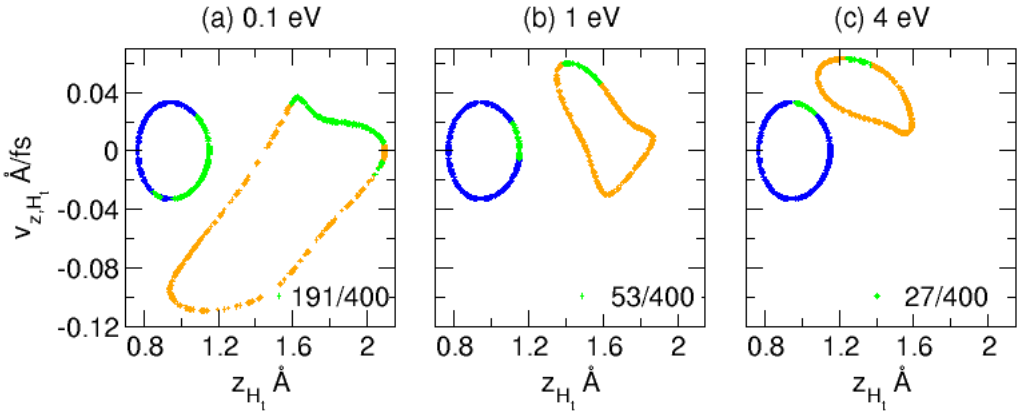

Figure 5.4: phase space points of the target hydrogen as found in 400 quasiclassical trajectories: the target hydrogen is in $v = 0$; the impact parameter of the incoming hydrogen is $b = 0.95$Å at different collision energies. The regular shape (almost elliptical) contains the initial conditions of the target randomly chosen (blue and green dots); in the other shape, each point gives position and velocity of the target at the first turning point of the incident H (orange and green dots); in any case, green dots define the target H in trajectories with an eventual reactive outcome.

first bounce on the surface, the phase space points of the target atom are distributed in different ways depending on the collision energy of the projectile. This energy indeed determines the speed at which the incident atom proceeds, thus the path to the surface followed by this atom and its interaction with the target. Naturally as shown in fig.5.3b-c at high collision energy, the incident hydrogen moves too fast to be able to find out the minimum energy path to the surface, so that it typically proceeds along the normal direction and a reaction may occur upon a bounce on the surface. More precisely, at $E_{coll} \sim 4$ eV, the projectile has the turning point located below the surface level, where it may penetrate due to its large energy; in the same time the target hydrogen moves away from the surface with a positive velocity. To react this atom needs to be ~ 1.2 Å far above the surface with a velocity of at least~ 0.06 Å/fs. Similarly, at $E_{coll} = 1$ eV the reaction occurs for the target atom placed at least ~ 1.4 Å far on the surface with a speed above ~ 0.04 Å/fs. As shown in fig.5.3a, upon a further decrease in the collision energy down to $E_{coll} = 0.1$ eV, the incoming atom feels the corrugation of the potential energy surface and it deviates towards the target while getting close to the surface. This induces the target atom to step away from the surface, in such a way that the reaction likely occurs for atoms above ~ 1.6 Å and with a velocity of ~ 0.02 Å/fs.

In conclusion a fast-moving projectile hits the surface and it is rapidly back reflected; while returning into the gas phase, it can capture the target atom provided this is not too tightly bound and it has a sufficiently large speed along the z axis. The energy transfer is fundamental for a slow-moving projectile: this is generally deviated from its direction by the attraction of the target, thus it hits the surface and bounces off it in the nearby of the target; for this reason the reactive encounter may take place only if the target atom has a z coordinate large enough that does not hinder the rebound of the projectile and does not deflect it away in a trapped state with a main speed component

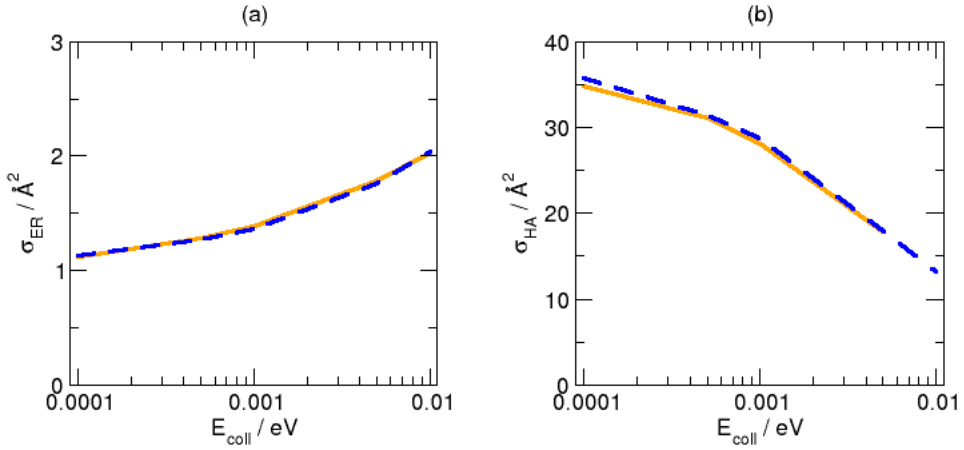

Figure 5.5: (a) reaction cross section as function of E_{coll} on a logaritmic scale for 10^5 classical trajectories (dashed blue line) and 10^5 quasiclassical trajectories for $v = 0$ (orange solid line); (b) cross section for the trapping of hot atoms as function of E_{coll} on a logaritmic scale with the same sets of trajectories as in (a).

parallel to the surface. Of course in all these cases the formation of a molecule implies an energy transfer from the incoming atom to the adsorbed one in the entrance channel; anyway this process is expected to be quite inefficient at $E_{coll} \gtrsim 1$ eV where the high energy incident particle 'glides' above the surface corrugation. Note that in this regime, as the collision energy increases, the position and velocity of the target become more and more relevant for the efficiency of the energy transfer, as can be deduced from the distribution of the reactive coordinates (green dots) in fig.5.4; this observation may reasonably justify the increasingly (huge) difference between the classical and the quasiclassical cross section in the same energy interval.

5.3.2.2 The drop in cross section at low collision energy

On the basis of the above considerations the drop in the cross section at low collision energy is somehow unexpected. In the attempt to understand the origin of such behaviour we performed classical and quasiclassical ($v = 0$) calculations to study the formation of hydrogen molecules in the energy interval $E_{coll} = 0.1 - 10$ meV. We chose the same parameters used for the higher collision energies except for the time of the final analysis that has been delayed (the first analysis is done after 7257 fs from the beginnig) in order to handle the slow rate of the projectile. The decrease in the collision energy up to 0.1 meV results in a decrease of the reactive cross section that anyway remains sizeable as shown in fig.5.5a. This allowed us to exclude the existence of any energy barrier as in that case the cross section would have vanished; moreover the result appears to be almost independent on the initial conditions of the adsorbed hydrogen as the inclusion of the zero point energy has not changed the picture. Interestingly, fig.5.5b shows that the drop in the reaction cross section is accompained by an increase in the cross section for the trapping of hot atoms on the surface. These species are free to move along the surface as in the limit of a flat surface the diffusion process is not activated, anyway they do not have enough energy to leave the surface and

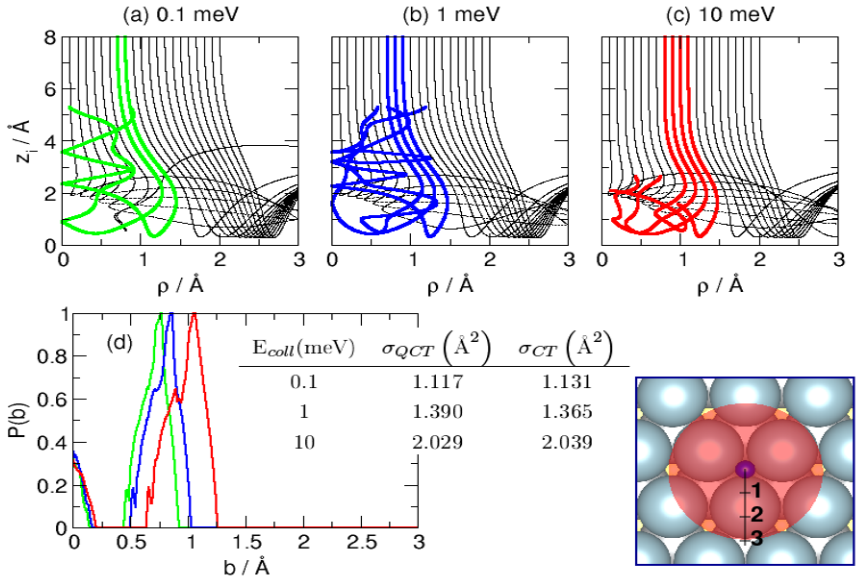

Figure 5.6: Representative trajectories in the very low collision energy regime. The plots are the same as in fig.5.3.

return into the gas phase. By considering fig.5.6 some conclusions may be drawn. First, the opacity function is nonzero in the quasicollinear case, that anyway hardly affects the reaction cross section, and in the region close to r_{eq}. Note that in this case the increase in the collision energy results in a shift of the opacity fuction at higher impact parameters. Second, in this very low energy regime the incident atom moves slowly and it can always access the minimum energy path towards the surface; in this way it possibly deviates from the normal direction. This implies that for impact parameters slightly above the equilibrium distance r_{eq}, the projectile is driven far away from the target atom and it presumably becomes trapped on the surface in the form of an hot atom. So that, the drop of the cross section at low collision energy indicates the presence of an alternative path that becomes accessible only in this energy range and that carries the projectile far away from the adsorbed atom.

5.3.2.3 Comparison between quasiclassical and quantum results

As introduced in sec.5.2.1.2 by comparing quasiclassical and quantum results obtained on the same potential energy surface one may find some differences that have a quantum origin. In this way, from fig.5.7 it emerges that quantum and quasiclassical methods give the same result in terms of formation of HD molecules upon the reaction between an adsorbed deuterium atom and an incident hydrogen atom; on the other hand in the case of H_2 molecules, the agreement between the two approaches is quite good up to collision energies of ~ 0.5 eV, as shown in the inset in fig.5.7 then the two cross sections become clearly different: up to ~ 2 eV, the quasiclassical cross section is lower than the quantum one, beyond this threshold the situation is reversed. This observation is consistent with the fact that, being lighter, the hydrogen atom is predicted to show a quantum nature more pronounced that the deuterium atom. As well, quantum and QCT results are almost equivalent in the low energy regime, thus indicating that the ER process is not activated: indeed, in the presence

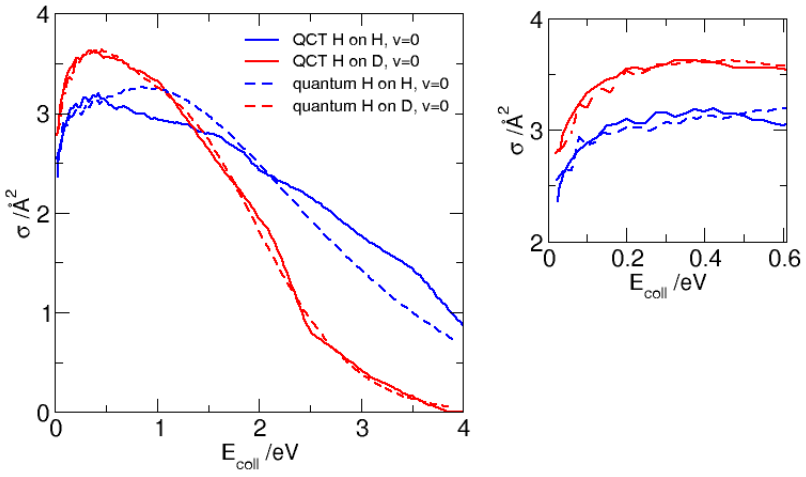

Figure 5.7: The Eley-Rideal cross-section as a function of the collision energy of the incident particle. Solid and dashed lines account for quasiclassical and quantum results respectively, with the target (hydrogen or deuterium) atom in $v = 0$. The inset show the region at low collision energy.

of a barrier, a certain amount of tunneling would have affected the quantum description. Once excluded the presence of an activation barrier, the origin of the discrepancy between quantum and quasiclassical results may be found in the fact that both bond formation and bond breaking involves quantized states, especially in the presence of light atoms. For these reason, clear differences are predicted (i) in the reactive case, where the adsorbed atom passes from a bound state on the surface to another bound state in the molecule, (ii) in the formation of hot atoms, where the incident atom initially unbound becomes trapped in a high energy state of the potential well and (iii) in the collision induced desorption, where the adsorbed atom is pushed out from its bound state upon the collision with the incoming atom.

In the end, we chose to investigate the possible effect of the vibrational excitation of the target on both quantum and QCT final results. Of course, this aspect does not have a real physical interest as in the ordinary experimental conditions only the vibrational ground state is populated, anyway an intriguing observation has been done upon placing the adsorbed atom in an excited vibrational state, that is from $v = 1$ to $v = 5$. As shown in fig.5.8, it turns out that the two theroretical methods produce almost equivalent results, provided the adsorbed atom belongs to a vibrational odd state, while the agreement is much worse if the target atom is in a vibrational even state. Up to now an explanation of this effect is still lacking.

5.4 Formation of H_2 molecules: the AIMD approach

5.4.1 The choice of the setup

In parallel to the quasiclassical trajectory method we also investigated the Eley-Rideal formation of hydrogen molecules with ab initio molecular dynamics (AIMD) as implemented in the VASP[56, 57]

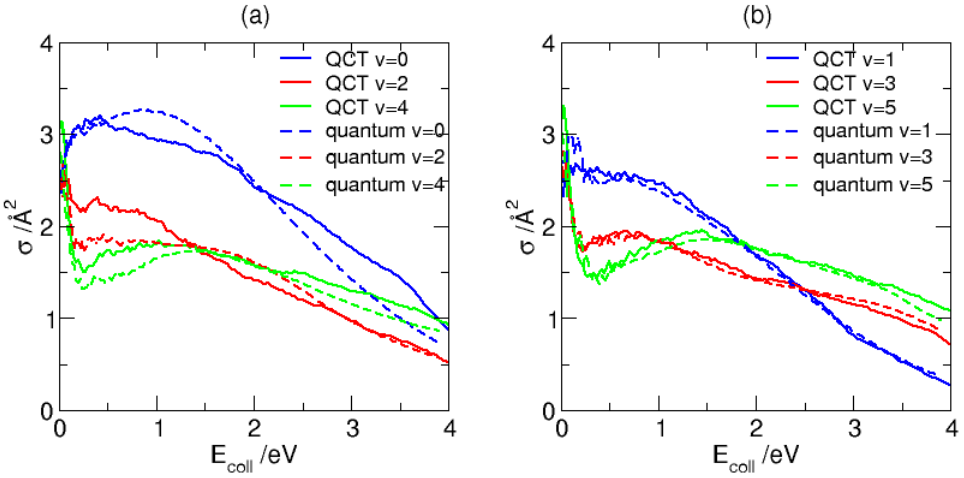

Figure 5.8: reaction cross section as a function of the collision energy of the incident hydrogen; the target hydrogen is in a vibrational state with (a) even quantum number or (b) odd quantum number.

package. Dynamical simulations were performed sampling the microcanonical (NVE) ensemble with classical trajectories. The Hellmann-Feynman forces were computed on-the-fly with DFT while the Newton equations of motion were integrated using a Verlet algorithm with a time step of 0.40 fs for all the projectile collision energies in the interval E_{coll}=0.01-0.4 eV. At the beginning of each trajectory the incident atom was set at ~ 4 Å above the surface plane with monochromatic initial velocity directed along the surface normal. The aiming points were generated by sampling at random the xy coordinates of the incident hydrogen within a symmetry irreducible sector $\theta = \pi/3$ of the hexagonal area of side $r = 1.7$ Å centered on the target in the adsorption site. The initial conditions of the surface atoms and of the adsorbed hydrogen were not sampled in these calculations, in fact they both were initially set at rest at their equilibrium positions. These were determined by a geometry optimization run using a 1 meV threshold on the total free energy relaxing the positions of the top layer atoms and the position of the hydrogen; these atoms were also left free to move during the whole simulation. Note that these initial conditions imply a surface temperature T_s=0 K.

Here the need of a large number of calculations to get statistically meaningful data required to reduce the computational setup and this has been done on the basis of a careful selection of the number of layers in the slab and the number of k-points as will be shown in sec.5.4.1.2. Eventually, we chose a 2×2 supercell to model each layer of the metal and we ended up with 12 silver atoms in a sample composed by three layers; the target hydrogen atom was seated in the fcc hollow site and the vacuum along the c axis was set to ~ 12 Å to isolate the periodic images. A $6 \times 6 \times 1$, Γ centered k-points mesh was chosen upon a careful selection, with 1 eV Gaussian smearing that is appropriate when dealing with metals. Moreover the Kohn-Sham orbitals were expanded in a plane-wave basis set limited to a 270 eV energy cutoff and the electrons were described by the projector augmented-wave (PAW) method, in the limit of frozen core electrons. The exchange and correlation energy

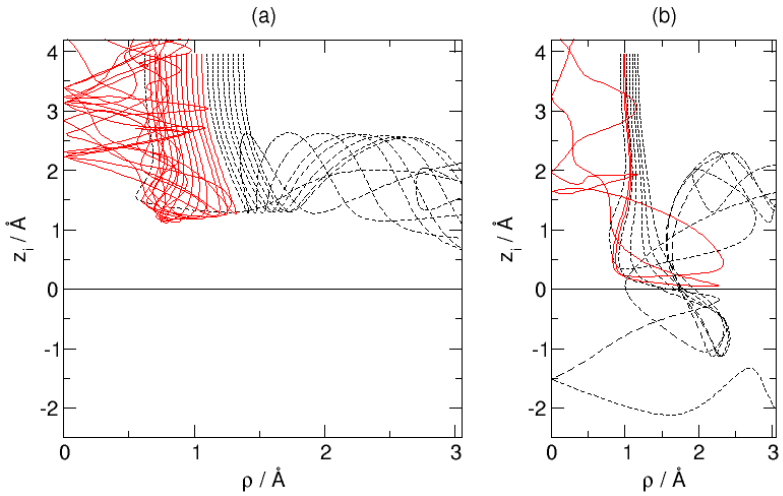

Figure 5.9: (a) top direction and (b) bridge direction. Only trajectories close to the reactive zone are shown: solid red lines and dashed black lines are for reactive and non reactive trajectories respectively. The surface level is set to zero.

was introduced via the Perdew-Burke-Ernzerhof (PBE) functional within the generalized gradient approximation (GGA), in the spin-polarized framework. In the chosen surface sector we run 400 trajectories equivalent to 2400 trajectories on the whole hexagonal area surrounding the target hydrogen.

5.4.1.1 The two limiting directions

The Ag(111) surface has two nonequivalent directions corresponding to symmetry axes in the xy plane: hollow to hollow (fcc to hcp) and hollow to top. In our case, we investigated these two directions in terms of reactivity in order to evaluate the importance of the surface corrugation, thus to estimate the implicit error in the flat surface approximation. As shown in fig.5.9, we found that most of the reactivity is concentrated along the hollow to top direction, 0.65-1.10 Å far from the target atom, seated in the fcc hollow site. In fact, by considering the other direction, we only found a small amount of reactivity beyond the bridge at around one Å from the target; note that in this region the surface is more open in correspondence of the hollow hcp site, thus the incident hydrogen may likely cross the surface and possibly either be reflected by the atoms in the second layer or diffuse subsurface. Also the reaction is found to occur in a different way along the two directions due to the different surface structure; a detailed description of the reaction mechanisms will be given in sec.5.4.2 for different initial collision energies.
At last, note that a small amount of reactivity is always encountered in the quasi collinear region, for $\rho \to 0$; anyway this contribution has almost no effect on the reaction cross section and it is almost equivalent in both the directions.

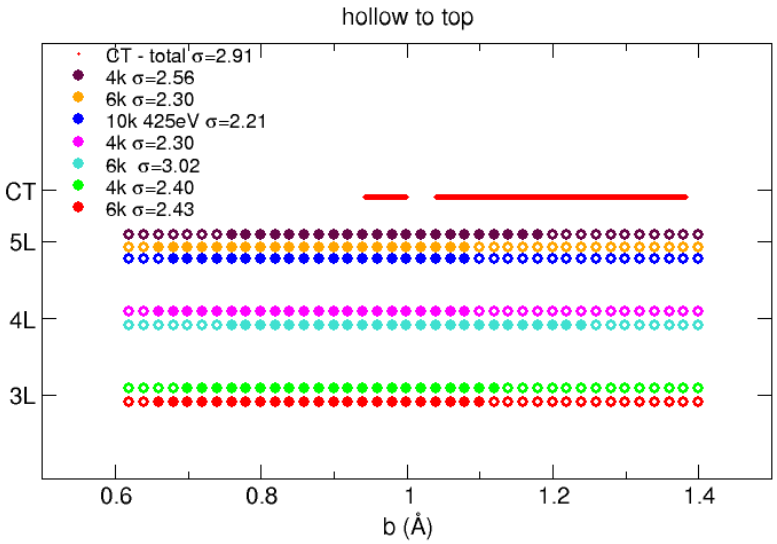

Figure 5.10: reactivity in the hollow to top direction for $E_{coll} = 0.1$ eV as a function of b (the quasicollinear contribution is ignored). AIMD reactive impact parameters (filled dots) along the hollow to top direction on a silver slab composed by three, four and five layers of atoms, respectively 3L, 4L, 5L in the figure; each of them is described by a $4 \times 4 \times 1$ and $6 \times 6 \times 1$ k-points meshes, respectively 4k and 6k in the figure; the blue dots have been computed according to the same setup in sec.5.2.1.1, namely a cutoff of 425 eV and a$10 \times 10 \times 1$ k-points mesh, 10k in the figure; the line of small red dots indicates the reactive interval obtained with the CT method. All the AIMD reactive cross sections σ in Å^2 are compared with the CT result (this accounts also for the quasicollinear contribution).

5.4.1.2 The number of layers and k-points

Of course the forces acting on the atoms are responsible for the final outcome of each trajectory, thus they are requested to be as accurate as possible to get a reliable picture of the system. For this reason we proved the number of k-points and the number of layers as expected to affect the description of the potential felt by the atoms and we found that both the aspects are relevant. Indeed, in the case of $E_{coll} = 0.1$ eV, we studied the reactivity towards the formation of hydrogen molecules along the most reactive hollow to top direction at impact parameters b in the interval $r_{eq} < b < 2r_{eq}$ and we found that the reactive region is shifted by varying the number of layers in the metal slab, namely three, four or five layers, and the k-points mesh, namely $4 \times 4 \times 1$ and $6 \times 6 \times 1$. The results are reported in fig.5.10. For each case the reactive cross section is computed[7] in the assumption that the result in terms of reaction probability along the specific hollow to top direction might be valid throughout the whole surface. This is somehow related to the flat surface approximation used to construct the PES for the CT method. Anyway here the motion of any incident atom is driven by forces computed on-the-fly, thus in principle the particle may experience

[7] The reaction cross section is computed as

$$\sigma_r = \pi P_r(b_1)\, b_1 \triangle b + \pi P_r(b_N)\, b_N \triangle b + 2\pi \sum_{i=2}^{N-1} P_r(b_i)\, b_i \triangle b$$

where i labels the impact parameters in interval considered, $P_r(b_i)$ is the reaction probability, that here is just 1 or 0 for each b_i depending on the final outcome of the trajectory, whether it is reactive or not, and $\triangle b$ is the width of the interval centered on b_i.

the surface corrugation as soon as it deviates from the given direction. Upon comparing the different setups, the natural choice is the slab made by three layers of silver with $6 \times 6 \times 1$ k-points: in fact this well reproduces the five layers system with the same k-points grid, taken as a benchmark, at a significantly lower computational cost.

It is important to notice that independently on the number of metal layers in the slab and by using a $6 \times 6 \times 1$ grid of k-points, the reactive cross section computed in the interval $r_{eq} - 2r_{eq}$ differs up to $\sim 20\%$ from the one found with the CT method taken as reference, that anyway includes also the small quasicollinear contribution. In the attempt to explain the origin of this different reactivity along the same direction, at first we looked for the possible drawbacks in the reduced setup. To this end, we computed a number of trajectories by using a setup equal to the one originally adopted to generate the potential energy surface in sec.5.2.1.1, except for the position of the $10\times10\times1$ k-points grid that here is centered in the Γ point on the surface, in order to better exploit the hexagonal symmetry of the lattice, while originally was M-centered. As shown by the blue dots in fig.5.10 the result is almost equivalent to the one obtained from both the three and the five layers system, with an energy cutoff of 270 eV and a $6 \times 6 \times 1$ grid of k-points, thus making unlikely the idea that the chosen setup may account for the different response from the ab initio MD and the classical trajectory study. Once redimensioned the influence of the reduced setup on our final results and considering that the surface corrugation might not be so relevant in the limit of the specific hollow to top direction, we looked at the possible consequences in the use of a non rigid surface. In our ab initio MD approach the surface atoms are allowed to move, thus the incident atom may trasfer part of its energy to them, while bouncing on the surface. This energy loss is expected to contribute to the observed displacement of the reactive interval as suggested by fig.5.3 and fig.5.6, in which it is shown that, at least at collision energies below $\sim$1 eV, the decrease in the collision energy shifts the reactive region at lower impact parameters. As a further check, we considered the H_2 formation on a rigid surface and we found that the cross section is increased by $\sim$0.3 Å^2 in the case of a five layers slab with a $6 \times 6 \times 1$ k-points grid. Accordingly, the energy dissipation into the surface degrees of freedom, though rather inefficient due to the mass mismatch between hydrogen and metal atoms, turned out to be relevant in the final outcome.

At last, to validate our setup over the whole surface, we considered the reactivity of hydrogen atoms impinging around the target in the xy plane at E_{coll}=0.1eV in the case of a three layers and a five layers slab and we found that the reaction cross sections are $1.52 \pm 0.15\text{Å}^2$ and $1.93 \pm 0.16\text{Å}^2$respectively. Thus, by taking as a benchmark the five layers system, at this collision energy the smaller setup underestimates the reaction cross section of about 20%, thus meaning that the reactive area is closer to the target. This is evident in fig.5.11 in which the initial coordinates (i.e. aiming points) of the incident atom leading to an eventual reactive outcome are reported for both the systems.

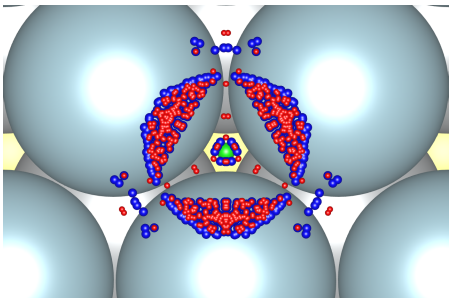

Figure 5.11: comparison of the reactive aiming points on a five layers slab (blue dots) and on a three layers slab (red dots). The target hydrogen in the hollow fcc site (green atom).

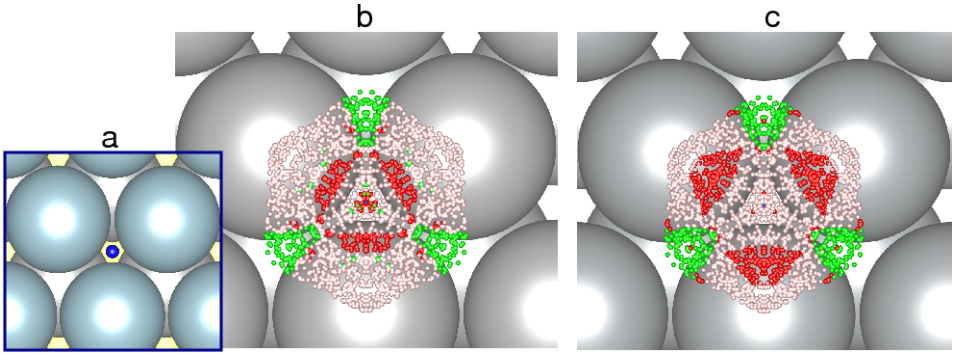

Figure 5.12: (a) position of the target H in blue in the fcc hollow site. (b) and (c) aiming points for the incident H with energy 0.01 and 0.4 eV respectively. Different colours indicate incoming H atoms that react (red) with the target, diffuse along the surface more that ~ 3Å far away from the target (pink) possibly spending some time also below the surface layer (green).

5.4.2 Results

Once chosen the starting setup, we followed 400 trajectories for different collision energies between 0.01-0.4 eV to evaluate the variation of the reaction cross section. As evident from fig.5.12, at low collision energy (0.01 eV) the reactive region is small and it slightly varies throughout the xy plane; on the contrary, at higher collision energies the reactive region is gradually broadened and in the meanwhile it tends to gather around the hollow to top direction while the region close to the bridge becomes almost non reactive. This suggests that the effect of the surface corrugation is different depending on the energy of the incoming particle. This observation is not unexpected and it can reasonably be explained considering that, by increasing the collision energy, the projectile may get closer to the surface, in such a way to feel more closely the potential of the surface atoms.

To better understand the variation in terms of reactivity across the surface, we followed in details few representative cases, chosen as close to the two limiting directions, for different energies of the incident hydrogen, E_{coll}=0.01,0.1 and 0.4 eV. As shown in fig.5.13, differences in the reaction mechanisms are encountered that depend on the initial position as well as on the energy of the incident atom.

In general, the atom directed along the hollow to top direction proceeds towards the surface up to ~ 1 Å far above it, then it may either react with the adsorbed hydrogen or be reflected far away

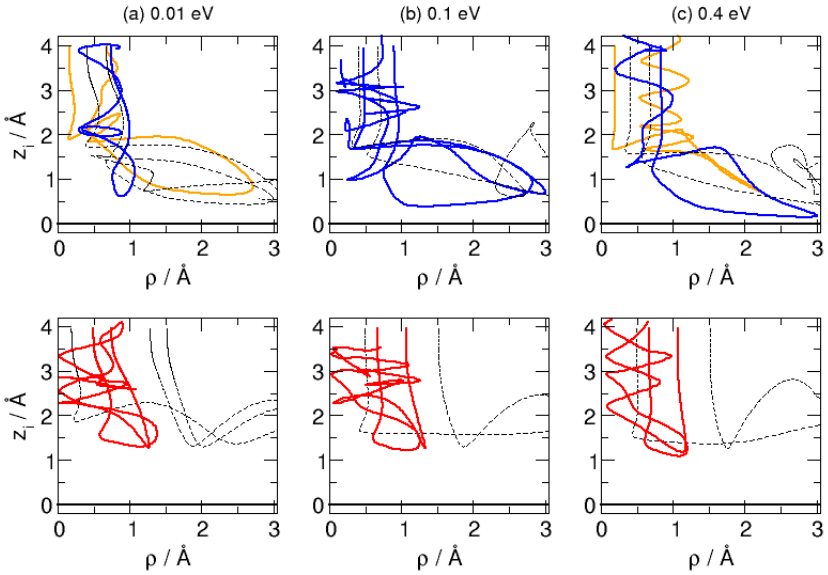

Figure 5.13: plots of the z coordinate of the incident atom as a function of the distance between the two hydrogens in the xy plane. The top line shows reactive (red solid line) and non reactive (black dashed line) trajectories along the hollow to top direction; the bottom line shows reactive trajectories close to the bridge (blue solid line) for an incident atom with (a) E_{coll}=0.01eV , (b)E_{coll}=0.1eV and (c) E_{coll}=0.4eV . The surface level is set to zero.

from it; on the other hand, the particle directed along hollow to hollow direction may get closer to the surface, typically less than ~ 1 Å far above it, before either reacting or going away. Note that in this second direction for $\rho > 0.85$ Å, thus in the region beyond the bridge, the incident hydrogen may possibly glide on the surface driven by the energy gradient towards the hcp hollow site and then be reflected back to target by the repulsive potentials of a surface atom. Of course, all the events along this direction are quite rare especially at high collision energy. It is important to point out that in all the cases, while approaching the surface the incident atom interacts with the adsorbed hydrogen, thereby deviating from the normal direction; this effect is found to be more evident at low collision energy.

5.5 Formation of H_2 molecules: comparison of AIMD and CT results

Results obtained with ab initio molecular dynamics and with the classical trajectory method have been compared in fig.5.14. It is clear that the choice of one rather than the other method gives remarkably different cross sections at the same collision energy. Of course, this is not unexpected and it mainly derives from the two alternative ways to deal with the potential energy and thus to find the forces acting on the atoms. As outlined in sec.5.2.2, in AIMD the forces are computed on-the-fly, thus they account for the instantaneous position of all the atoms and they reflect the corrugation of the surface. This allows to get a realistic description of the motion of the (hydrogen) atoms, including energy barriers to the diffusion throughout the surface and permitting the energy transfer

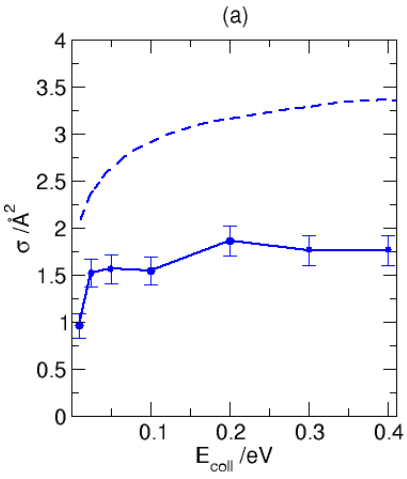

$E_{coll}\,(eV)$	$\sigma_{\mathrm{CT}}\left(\text{Å}^2\right)$	$\sigma_{\mathrm{AIMD}}\left(\text{Å}^2\right)$
0.010	2.039	0.96 ± 0.13
0.025	2.364	1.52± 0.15
0.050	2.622	1.56± 0.15
0.100	2.911	1.54± 0.15
0.200	3.158	1.86± 0.16
0.300	3.284	1.76± 0.16
0.400	3.356	1.76± 0.16

Figure 5.14: (a)reactive cross section from CT (dashed line) and AIMD (solid line) calculations; (b) differences in the cross section between these two approaches.

to phonons. On the other hand, in the classical trajectory method the potential energy surface is computed before running the trajectories and it is assumed to be flat and rigid; by construction this potential is defined along the hollow to top direction, that generates the whole surface by rotation around the z axis normal to the surface itself (see par.5.2.1.1). Of course this is an approximation, that anyway allows to dramatically reduce the computational cost; moreover the AIMD approach is in principle more accurate, but in practice it becomes computationally feasible only upon a drastic reduction of the setup quality, thus including a certain amount of approximation also in this case.
As illustrated in fig.5.14 we limited our comparison to the low energy regime, where the classical trajectory method has been found to well reproduce the quasiclassical ($v = 0$) results, thereby we coud reasonably assume the target to be at rest in its equilibrium position. In fig.5.14a classical and AIMD cross sections are reported and both reproduce the drop in the cross section at low collision energy. Anyway, the reactive cross sections found by the two methods differ of ∼1-1.5 Å^2 in the interval of energy considered. As shown in fig.5.14b, such difference tends to increase together with the collision energy of the incident atom; this is consistent with the observation that the surface corrugation becomes more relevant as the collision energy increases.
In fig.5.15 both CT and AIMD reactive aiming points are reported at $E_{coll} = 0.01$ and E_{coll}=0.4 eV. On the basis of the potential energy surface used in the CT method, it is not surprising that the reactive region in this case forms a ring, whose width and radius depends on the initial energy of the projectile. On the contrary, the AIMD method clearly accounts for the effect of the surface corrugation: this is more pronounced at collision energy E_{coll}=0.4 eV, where it produces a clear localization of the reactive region around the hollow to top direction along with a reduction of the reactivity close to the hollow to hollow direction. However, it is evident from fig.5.15 that the two methods do not only differ in terms of surface corrugation included, but even in terms of reactive impact parameters, as already outlined in fig.5.10. Indeed within the CT method, the

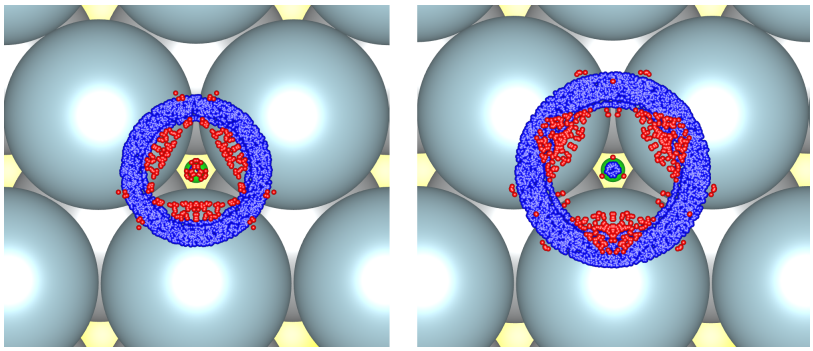

Figure 5.15: reactive aiming points for the formation of H_2 in classical trajectory dynamics (blue dots) and ab initio molecular dynamics (red dots) at collision energy, $E_{coll} = 0.01$ eV (left panel) and $E_{coll} = 0.4$ eV (right panel). In green the target hydrogen in the hollow fcc site.

reactive interval is placed farther away from the target atom compared to the reactive region found in AIMD, as in this last case, the incoming hydrogen transfers part of its energy to the surface upon bouncing on it. Obviously, this contributes to the difference between the two cross sections. Anyway, in the energy range considered here, the increase in the collision energy enhances the overlap between the two reactive regions. Accordingly, it is reasonable to affirm that an increase of the collision energy up to 0.4 eV allows the incoming atom to have a stronger feeling of the surface corrugation, that thereby becomes the main responsible for the difference between AIMD and CT cross sections. On the other hand, the flat surface approximation becomes at least qualitatively correct at very low collision energy ~ 0.01 eV, as the incident atom may not get too close to the surface so that to feel the corrugation of the surface potential. In this limit the two methods give different responses mainly due to the relative positions of the reactive impact parameters.

5.6 Analysis of H_2 molecules

5.6.1 H_2 molecules in the QCT method

Along with the reaction cross section shown in fig.5.2, we also obtained the average vibrational ($\langle v \rangle$) and rotational ($\langle j \rangle$) quantum numbers for the homonuclear, H_2 and D_2, and heteronuclear HD molecules; these results are reported in fig.5.16 as a function of the collision energy of the projectile. In general, an increase in the collision energy results into an increase of the average vibrational and rotational excitation. For instance, quasiclassical ($v = 0$) calculations show that, in H_2 molecules, $\langle v \rangle$ increases from $\sim$1 to $\sim$8 when the collision energy of the projectile passes from few tenths of eV up to 4 eV; in the same energy range, $\langle j \rangle$ varies from $\sim$8 to $\sim$14. On the other hand, in the classical approach, the average vibrational excitation of H_2 molecules varies from less than $\sim$1 to $\sim$6, while the average rotational excitation ranges between $\sim$7 and $\sim$18. Moreover, in fig.5.17 we plotted the vibrational and rotational quantum numbers as a function of the impact parameter b for some representative values of the collision energy, namely 0.1, 1 and 4 eV. In the quasiclassical scheme, $v\,(b, E_{coll})$ and $j\,(b, E_{coll})$ are obtained by averaging over 400 trajectories generated for

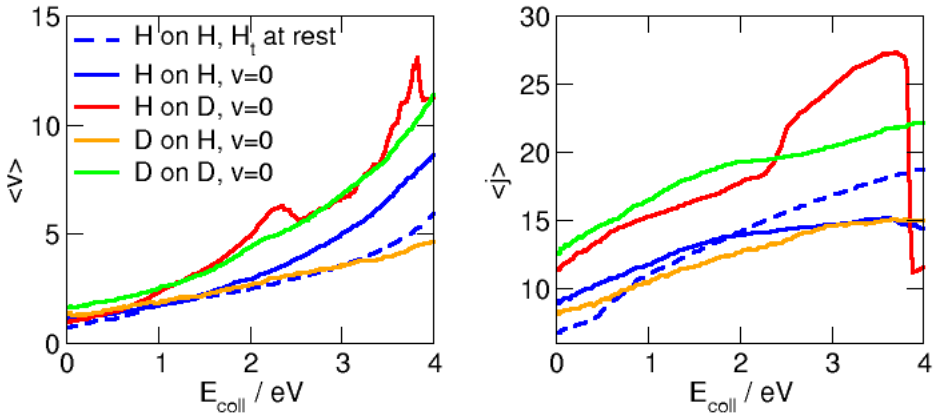

Figure 5.16: average vibrational (a) and rotational (b) quantum numbers as a function of the collision energy.

each b and E_{coll} by randomly choosing the initial conditions (position and velocity) of the target atom in the ground vibrational state. Of course, in the classical scheme the average over the initial conditions of the target is not involved, as it is assumed to be initially at rest in the equilibrium position. These results are reported in fig.5.17; here the plateau correspond to regions in which the reaction probability is null, and do not actually represent molecules belonging to $v = 0$ or $j = 0$. As shown in this figure, if the vibrational energy of the target atom in $v = 0$ is taken into account, the reactive interval in terms of impact parameter b is found to be larger than the corresponding classical result, for each of the collision energies considered. Note that the probability to form H_2 molecules is nonzero for impact parameters in $r_{eq} < b < 2r_{eq}$ and in the quasicollinear region and, as already outlined, the reactive interval broadens when the collision energy decreases. Moreover, fig.5.17 shows that, for a given impact parameter, the vibrational and rotational excitation increases, as the collision energy increases; also, for a given energy, molecules in highly excited rotational and vibrational states usually form at the boundaries of the reactive interval.

5.6.1.1 Comparison with H_2 and HD molecules from quantum dynamics

The analysis of the product molecules H_2 and HD in terms of vibrational and rotational average quantum numbers is shown in fig.5.18 for both the quantum and the quasiclassical approach. In the same way as for the reactive cross sections in fig.5.7, at low collision energy (approximately below ~ 0.5 eV) the agreement between the results is good for H_2 as well as for HD, while it tends to get worse as the energy is raised. In the case of H_2 it is interesting to notice that beyond the threshold of ~ 2 eV, namely where the collision induced desorption starts to take place, the quasiclassical H_2 molecules show an average vibrational quantum number $\langle v \rangle$ higher that the corresponding quantum data. This is consistent with the picture emerging from fig.5.7, namely that the quasiclassical approach compared to the quantum approach predicts a higher reactive cross section, likely related to a less efficient collision induced desorption. In this way, the formation of highly excited QCT

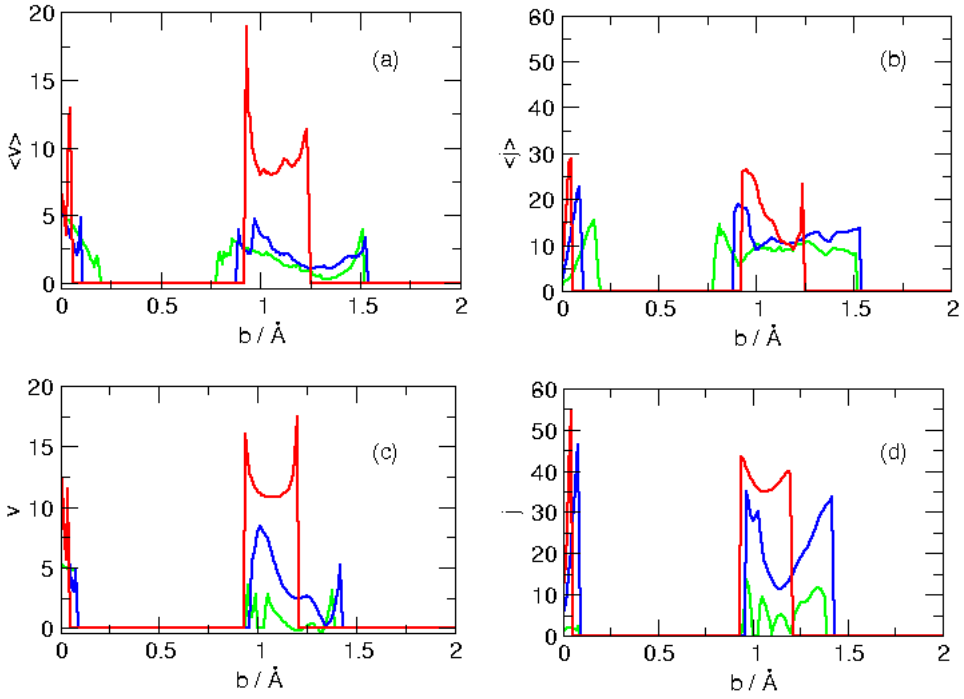

Figure 5.17: average vibrational (a) and rotational (b) quantum numbers as a function of the impact parameter from quasiclassical ($v = 0$) calculations. Vibrational (c) and rotational (d) quantum numbers from classical calculations. Results refer to different collision energies, namely E_{coll} =0.1 eV (green line), E_{coll} =1 eV (blue line) and E_{coll} =4 eV (red line).

molecules may possibly be explained. On the other hand, the good agreement on the $\langle j \rangle$ values proves that the vibrational excitation of these molecules in the quasiclassical study is not associated to a parallel increase in the average rotational excitation.

5.6.2 H_2 molecules in AIMD

The distribution of the H_2 molecules into rotational states in the interval $j = 0 - 14$ is reported in fig.5.18 as a function of the vibrational excitation of the molecules themselves at different collision energies of the incident atom. In all the cases, most of the molecules form in the ground vibrational state and there is a decreasing probability to find molecules in the higher excited states; on the other hand, the rotational excitation is quite relevant at all the energies considered. This last observation suggests that the formation of H_2 molecules mainly occurs with a noncollinear mechanism, namely when the incident atom proceeds towards the surface at a certain distance ρ (in the xy plane) from the target atom. The point is that the incoming hydrogen moves towards the silver surface along the normal direction and, except for very low collision energies, it only weakly deviates towards the target; in this way the projectile gets close to the surface before forming the molecule. Once on the surface at an appropriate distance from the target, a molecule may form that likely rotates around the normal to the surface (in the so-called *helicopter* fashion, opposed to *cartwheel* fashion in which

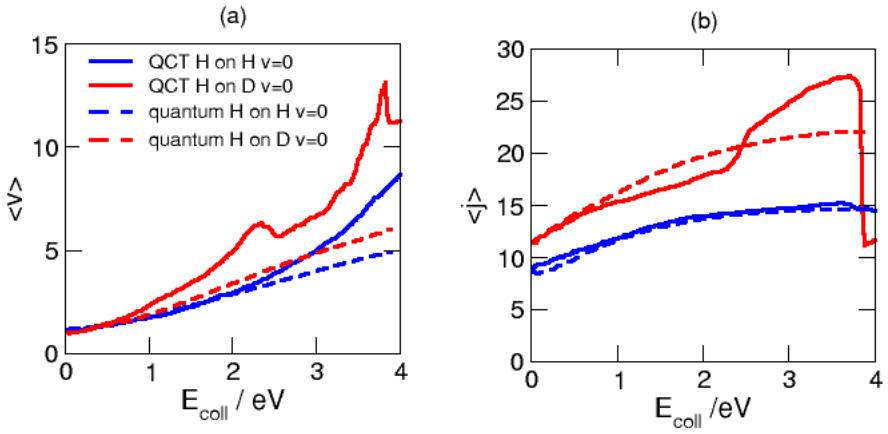

Figure 5.18: analysis of H_2 and HD product molecules: comparison between the average (a) vibrational and (b) rotational quantum numbers obtained from quasiclassical and quantum calculations with the target atom originally in $v = 0$.

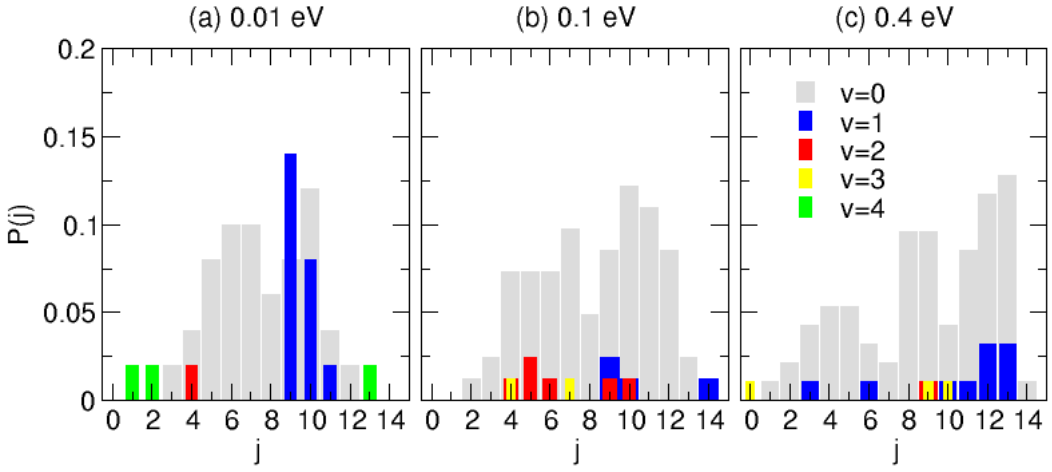

Figure 5.19: normalized probability $P(j)$ as a function of the rotational quantum number j in different vibrational states as indicated by the colours at collision energies (a)$E_{coll} = 0.01$ eV, (b)$E_{coll} = 0.1$ eV and (c)$E_{coll} = 0.4$ eV.

the molecule rotates around an axis parallel to the surface). In this limit, the main interest is in the projection of $\mathbf{r}$ and $\mathbf{v}$ in the xy plane, and a large $\mathbf{r}$ is associated to a large j[8]. Moreover, also the low vibrational excitation is consistent with this picture, as high vibrational states become likely populated when the reaction occurs upon a direct encounter between the two atoms, namely in the quasicollinear region or in the noncollinear region if the projectile is strongly deviated towards the target, before reaching the surface.

[8] This follows from the relation

$$|J^2| \propto j(j+1)$$

with the angular momentum vector J defined as $J = \mathbf{r} \times \mu \mathbf{v}$, where μ is the reduced mass of the two atoms and v is the angular velocity.

5.6.2.1 Comparison with classical trajectory results

We compared the H_2 molecules that form by modeling the Eley-Rideal reaction with ab initio molecular dynamics and in the classical trajectory scheme. To this end we consider the average vibrational and rotational quantum numbers as a function of the collision energy of the incoming atom in the interval between 0.01-0.4 eV. Due to the high computational cost of AIMD, one may afford only a small number of trajectories for each energy and we found that 400 trajectories generated in the surface sector described in sec.5.4.1 were sufficient to get converged reactive cross sections. Anyway, the number of reactive trajectories was found to be too small (less than $\sim$ 100/400) at any collision energy to produce accurate results in the analysis of the product molecules. In this way, the $\langle v \rangle$ values of H_2 molecules from AIMD trajectories in fig.5.19a do not show the clear increasing tendency associated to the quasiclassical results, anyway this may not even be ruled out due to the uncertainty in the AIMD data. Moreover, the AIMD data are enough to show that the Eley-Rideal reaction on the Ag(111) surface forms H_2 molecules in a low vibrational state. In the same fashion also the $\langle j \rangle$ values in fig.5.19b emerging from the AIMD study are not accurate, even if also in this case they are enough to confirm that these product molecules are characterized by a high rotational excitation. On a qualitative level, the lower vibrational excitation, compared to the CT results, may be a consequence of two facts: first, the incoming atom usually bounces on the surface, before reacting, and in this way it may dissipate part of its energy into the surface phonons; anyway, though possible, the effectiveness of this dissipative channel is limited by the mass mismatch between hydrogen and silver atoms. Second, due to the surface corrugation, the incident atom transfers part of its kinetic energy, initially associated to the motion along the surface normal, in the motion parallel to the surface, thereby reducing the amount of energy available to form vibrationally excited molecules. In the end, this kinetic energy accounting for the motion in the xy plane may in turn be transferred to the product molecules in the form of rotational excitation, thereby explaining the higher rotational excitation of the AIMD molecules compared to the ones obtained within the flat surface approximation.

5.7 Conclusions

We studied the formation of hydrogen molecules on the Ag(111) surface in the single-adsorbate case, by using (quasi)classical dynamics on a reference potential[20] and ab initio molecular dynamics. Beyond the inherent differences in the two methods, initially pointed out, we obtained large cross-sections for the Eley-Rideal reaction and product molecules with relatively low vibrational and high rotational excitation. Such distribution of the internal energy of molecules was found to be indicative of the reactive scheme, mainly based on a non-collinear geometry, with only a small quasi-collinear reactivity. Moreover, the reaction was found to occur typically upon a bounce of the incident atom on the surface. In this way, the energy exchange between the incident atom and the surface, allowed

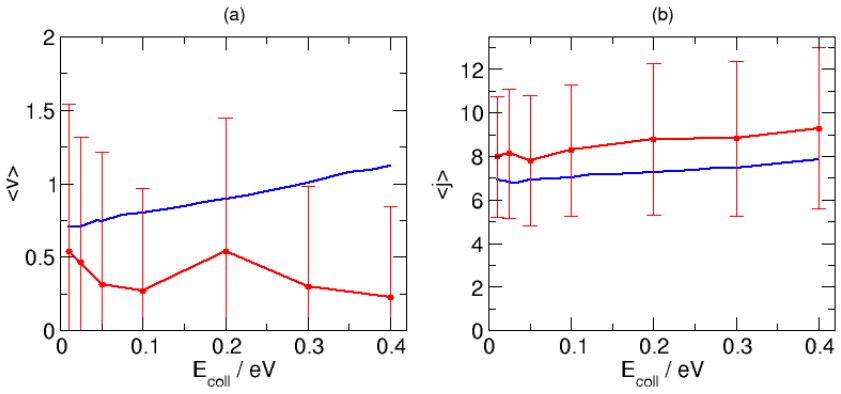

Figure 5.20: comparison between average (a) vibrational and (b) rotational quantum numbers of the H_2 molecules obtained in AIMD (red line with standard deviation) and in the classical trajectory method (blue line).

in the ab initio MD study while ignored in (quasi)classical study due to the model PES adopted, becomes relevant to determine the final outcome of each trajectory. The comparison between the two methods has been done in the low energy regime, between 0.01-0.4 eV, where we could safely ignore the target vibration. In this way we could evaluate the effect of the surface corrugation on the reaction and we found that the specific potential energy surface used in the QCT study leads in any case to an overestimate of the real cross section. As well we compared our results with the experimental work in ref.[52], in which the cross section was computed in the case of the D by H abstraction at different D coverages. By decreasing the surface coverage, it was found that the reaction cross section raises, up to $\sigma = 4.5\,\text{Å}^2$ at the lowest coverage considered (~ 0.03 ML), upon admitting a polychromatic flux of H atoms (with no indication on the temperature of the beam) at the surface temperature of 80 K. As the experimental conditions are somewhat different from those used in our simulations, we could compare the experimental cross section with our theoretical results only at a qualitative level. In this way we found some differences suggesting that the final outcome may be likely influenced by the surface temperature, the incident angle of the incoming particles and the surface precoverage, in addition to the dependence on the collision energy, the surface relaxation and the vibrational excitation of the adsorbed atom already investigated in our study.

Appendix A

The Jahn-Teller theory

A.1 The adiabatic approximation

In order to introduce the basic concepts of the Jahn-Teller theory[12**?**], we first consider the basic expressions for the changes in the electron-nuclear interactions due to nuclear motions, i.e. vibronic interactions, in degenerate and non-degenerate electronic states.
From the Schrödinger equation, the electron-nuclear interaction is treated by:

$$(\mathcal{H} - E)\,\Psi(r, Q) = 0 \tag{A.1}$$

where $\Psi(r, Q)$ is the full wavefunction, r represents the whole set of coordinates of the electrons r_i with $i = 1, 2...n$ and Q is the whole set of nuclear coordinates Q_α with $\alpha = 1, 2...N$, $\mathcal{H}$ is the hamiltonian operator and E is the total energy of the system. Except for very simple systems, composed by few nuclei and electrons, the exact solution of eq.(A.1) is extremely difficult and one has usually to look for approximate solutions, resulting from simplified descriptions of the original system. Among these, one of the most successful, as both conceptually simple and widely applicable, is the *adiabatic approximation*, based on the inequality between electrons and nuclei masses, that reflects in a substantial difference in their relative speeds. Accordingly, one may assume that a relaxed distribution of the electronic cloud $\Psi(r, Q)$ follows each istantaneous configuration Q of the nuclei, meaning that the nuclei move in the average field of the electrons. This allows to split the search of the energy of the system into two steps: first the electronic part of the Schrödinger equation is computed for each of the fixed Q coordinates, then the obtained mean electron energy is used as the potential energy in which nuclear displacements take place. Thereby, the global hamiltonian in eq.(A.1) is divided in:

$$\mathcal{H} = \mathcal{H}_r + \mathcal{H}_Q + V(r, Q)\,, \tag{A.2}$$

where $\mathcal{H}_r$ is the electronic part and includes the kinetic energy of the electrons and the electron-electron interactions, $\mathcal{H}_Q$ is the nuclear part including the kinetic energy of the nuclei and $V(r, Q)$ is the potential energy including the internuclear repulsion and the interaction between electrons

and nuclei. The $V(r,Q)$ operator can be expanded as a series about the reference position $Q_\alpha = Q_{\alpha 0} = 0$, where $\{Q_\alpha\}$ is the set of symmetrized displacements described later.

$$V(r,Q) = V(r,0) + \sum_\alpha \left(\partial V/\partial Q_\alpha\right)_0 Q_\alpha + \frac{1}{2}\sum_{\alpha,\beta}\left(\partial^2 V/\partial Q_\alpha \partial Q_\beta\right)_0 Q_\alpha Q_\beta + ... \tag{A.3}$$

By assuming only the first term of this expansion as the potential energy of the electrons in the field of nuclei fixed at $Q_\alpha = 0$, one can solve the electronic part of the Schrödinger equation:

$$\left(\mathcal{H}_r + V(r,0) - \varepsilon_k^{'}\right)\varphi_k(r) = 0 \tag{A.4}$$

where $\varepsilon_k^{'}$ and $\varphi_k(r)$ are respectively the energy and the eigenfunction of the electronic state k in the given nuclear configuration $Q_\alpha = 0$. Then the full Schrödinger equation is considered to account for the effects of the nuclear motion on the solutions of eq.A.4. To this end, the total wavefuction $\Psi(r,Q)$ is rewritten in terms of the electronic functions $\varphi_k(r)$:

$$\Psi(r,Q) = \sum_k \chi_k(Q)\,\varphi_k(r) \tag{A.5}$$

where the coeffients $\chi_k(Q)$ depend on the Q coordinates. After some simple transformations, the Schrödinger equation becomes:

$$\left(\mathcal{H}_Q + \varepsilon_k(Q) - E\right)\chi_k(Q) + \sum_{m\neq k} W_{km}(Q)\,\chi_m(Q) = 0 \tag{A.6}$$

where $W_{km}(Q)$ is the electronic matrix element

$$W_{km}(Q) = \langle \varphi_k(r)\,|W(r,Q)|\,\varphi_m(r)\rangle \tag{A.7}$$

representing the vibronic interactions, *i.e.* the part of $V(r,Q)$ which depends on Q only, since the dependence on r has been ruled out by integration. Indeed:

$$W(r,Q) = V(r,Q) - V(r,0) = \sum_\alpha \left(\partial V/\partial Q_\alpha\right)_0 Q_\alpha + \frac{1}{2}\sum_{\alpha,\beta}\left(\partial^2 V/\partial Q_\alpha \partial Q_\beta\right)_0 Q_\alpha Q_\beta + ... \tag{A.8}$$

and $\varepsilon_k(Q) = \varepsilon_k^{'} + W_{kk}(Q)$ is the potential energy of the nuclei in the mean field on electrons in the state $\varphi_k(r)$. If the vibronic mixing, namely the coupling between electronic states due to the nuclear motion here represented by W_{km} in eq.(A.6), may be set down to zero, then the system of equation decouples and it decomposes in a simple set of equations:

$$\left(\mathcal{H}_Q + \varepsilon_k(Q) - E\right)\chi_k(Q) = 0 \qquad\qquad k = 1,2,3... \tag{A.9}$$

This is the *crude adiabatic approximation* known as the Born-Oppenheimer approximation and $\varepsilon_k(Q)$ is the adiabatic potential energy surface (APES) of each state k. Of course, such description

is valid only as far as the vibronic mixing of different electronic states can be ignored, that is

$$\hbar\omega \ll \left|\varepsilon_m^{'} - \varepsilon_k^{'}\right| \tag{A.10}$$

where $\hbar\omega$ is the energy quantum of vibrations in the electronic state under consideration (k or m) and $\varepsilon_m^{'}, \varepsilon_k^{'}$ are solutions of eq. A.4. This is a criterion of validity of the adiabatic approximation, that applies to stable electronic states with localized vibrations; obviously it does not hold with degenerate or pseudodegenerate electronic states.

In the limit of non-interacting electronic states, a more accurate description is given by the *full adiabatic approximation*. In this case the electronic part of the Schrödinger equation includes the electron-nuclear interactions in the whole range of nuclear coordinates, thus modifying eq.(A.4) as follows:

$$\left(\mathcal{H}_r + V(r,Q) - \varepsilon_k^{'}(Q)\right)\varphi_k(r,Q) = 0 \tag{A.11}$$

with the electronic eigenfunction no more independent on Q. The global wavefunction is now $\Psi(r,Q) = \sum_k \varphi_k(r,Q)\,\chi_k(Q)$ and, instead of W_{km} in eq.(A.6), one gets the operator of nonadiabacity Λ_{km} basically due to the fact that the kinetic operator $\mathcal{H}_Q$ now applies to $\varphi(r,Q)$ too,

$$\left(\mathcal{H}_Q + \varepsilon_k(Q) - E\right)\chi_k(Q) + \sum_{m\neq k}\Lambda_{km}\chi_m(Q) = 0 \tag{A.12}$$

with

$$\Lambda_{km} = -\frac{\hbar^2}{2}\sum_\alpha\left(\frac{1}{M_\alpha}2\left\langle\varphi_k\left|\nabla\right|\varphi_m\right\rangle\nabla + \left\langle\varphi_k\left|\nabla^2\right|\varphi_m\right\rangle\right)\chi_m(Q) = 0 \tag{A.13}$$

and M_α the nuclear mass. If the electronic state is nondegenerate and the condition in eq.(A.10) applies, the vibronic coupling terms may be neglected and only Λ_{kk} terms survive: this is the case of the full adiabatic approximation. On the other hand, if such condition is not satisfied, the vibronic coupling terms included in Λ_{km} may not be ignored. They are related to the kinetic operator $\mathcal{H}_Q$ and they account for the rate at which the wavefuction changes due to nuclear displacements Q_α, that is higher in the regions where the energies of the two electronic states are closer. Anyway, for strong vibronic coupling the electronic wavefunctions and, as a consequence, the off-diagonal nonadiabatic corrections may have singularities which complicate the solution of (A.12), thus making it useful to apply an adiabatic-to-diabatic matrix transformation. This is chosen in such a way to generate smooth wavefuctions with respect to Q that are no longer solutions of the electronic problem, a diagonal matrix form for the kinetic energy and off-diagonal elements for potential energy, which vary smoothly with Q.

However, when the adiabacity criterion does not hold and the adiabatic approximation is not valid, as in the presence of (pseudo)degenerate or strongly interacting states, the criterion in eq.(A.10) may not be retained and the Jahn-Teller theory comes into play. The basic lines of this theory will be presented in the following section, upon choosing as appropriate starting point the set of equations in eq.(A.6) with W_{km} instead of Λ_{km}.

A.2 Vibronic interactions and vibronic coupling constants

The original formulation of the Jahn-Teller (JT) effect as proposed by the authors of the paper in 1937[45] is: "...the nuclear configuration of any nonlinear polyatomic system in a degenerate electronic state is unstable with respect to nuclear displacements that lower the symmetry and remove the degeneracy." This former statement has been further refined during the years, but what has remained is the idea that degeneracy or pseudodegeneracy produce a strong interaction between the electronic and nuclear motion that result in series of observable effects known as JT vibronic coupling effects. A more rigourous formulation reads as: "..If the APES of a polyatomic system has two or more branches that intersect in one point (degeneracy point $Q_\alpha = 0$) then at least one of them has no extremum at this point." And finally, a further general formulation states: "..the necessary and sufficient condition of instability (lack of minimum on the APES) of the high-symmetry configuration of any polyatomic system is the presence of two or more electronic states that are either degenerate in this configuration, or non-degenerate but sufficiently strongly interacting under the nuclear displacements in the direction of instability".

In the limit in which these definitions apply, that is for strongly interacting (possibly degenerate or pseudodegenerate) solutions of the electronic Schrödinger equation within the Born-Oppenheimer approximation, the mixing interactions among the electronic states are included as W_{km} in eq.(A.6). Linear and quadratic terms of the expansion in eq.(A.8) are usually enough to properly describe the system provided a suitable reference configuration has been chosen. In general, the reference configuration corresponds to the highly symmetric nuclear arrangement in which the electronic term is degenerate; similarly, also for pseudodegenerate states the high symmetry of the nuclear positions remains a good criterion. Starting from the reference geometry, the nuclear displacements are depicted by normal coordinates that are in turn related to the symmetrized coordinates, namely collective nuclear displacements that transform into each other under the group operations[1]. A symmetrized displacement is effectively a normal coordinate if it spans an irreducible representation that occurs only once in the given molecular point group; otherwise, if the symmetrized displacement spans an irreducible representation (irrep) that occurs more than once in that point group (for instance $T_2^{'}$ and $T_2^{''}$ in the T_d group) then the normal coordinate is a linear combination of symmetrized displacements spanning the same irreps.

The operator of vibronic interactions in normal coordinates reads as

$$W(r,Q) = \sum_{\Gamma\gamma} \left(\partial V/\partial Q_{\Gamma\gamma}\right)_0 Q_{\Gamma\gamma} + \sum_{\Gamma'\gamma',\Gamma''\gamma''} \left(\partial^2 V/\partial Q_{\Gamma'\gamma'}\partial Q_{\Gamma''\gamma''}\right)_0 Q_{\Gamma'\gamma'}Q_{\Gamma''\gamma''} + ... \qquad \text{(A.14)}$$

where Γ is the irreducible representation defining a generic nuclear displacement, f-fold degenerate, where the subscript γ is the 'line' of matrix $f \times f$ and thus the f-th component of the normal coordinate. As shown in eq.(A.7), the linear vibronic coupling costants are given by the matrix

[1] It is well known that in a system of N atoms, the number of vibrational degrees of freedom as well as of symmetrized displacement is $3N-6$ or $3N-5$ for linear arrangements.

elements of $W(r,Q)$. Following from the Wigner-Eckart theorem the general formulation is

$$F_{\overline{\Gamma\gamma}}^{(\Gamma\gamma\Gamma'\gamma')} = \left\langle \Gamma\gamma \left| \left(\partial V/\partial Q_{\overline{\Gamma\gamma}}\right)_0 \right| \Gamma'\gamma' \right\rangle = F_{\overline{\Gamma}}^{(\Gamma\Gamma')} \left\langle \overline{\Gamma\gamma}\Gamma'\gamma'|\Gamma\gamma \right\rangle \tag{A.15}$$

where $\left\langle \overline{\Gamma\gamma}\Gamma'\gamma'|\Gamma\gamma \right\rangle$ is a Clebsh-Gordan coefficient available from tabular data. In this way, if at least one linear vibronic constant is known, all the other can be easily calculated. Of course, if Γ and Γ' are nondegenerate, the general expression in eq.(A.15) reduces to

$$F_{\overline{\Gamma}}^{(\Gamma\Gamma')} = \left\langle \Gamma \left| \left(\partial V/\partial Q_{\overline{\Gamma}}\right)_0 \right| \Gamma' \right\rangle . \tag{A.16}$$

Irrespective of the degeneracy, the group theory predicts that:

- the off-diagonal terms ($\Gamma \neq \Gamma'$) are nonzero if and only if $\Gamma \times \Gamma' = \overline{\Gamma}$,
- the diagonal terms ($\Gamma = \Gamma'$) are nonzero if the symmetric product $[\Gamma \times \Gamma]$ contains $\overline{\Gamma}$, i.e. $\overline{\Gamma} \in [\Gamma \times \Gamma]$.

Anyway, within this scenario the degeneracy plays a fundamental role. For nondegenerate states, since $[\Gamma \times \Gamma] = \Gamma \times \Gamma = A_1$, the electrons can induce nuclear displacements only in the direction of the total symmetric mode, thus without affecting the symmetry of the system. In case Γ or Γ' or both of them are degenerate, also $\overline{\Gamma}$ may be degenerate and the symmetric product contains nontotally symmetric representations in addition to symmetric one. For instance, in D_{3h} and D_{4h} point symmetry groups for the E irrep the symmetric products read as $[E \times E] \rightarrow A_1 + E$ and $[E \times E] \rightarrow A_1 + B_1 + B_2$, respectively. This implies that a symmetric nuclear configuration undergoes nontotally symmetric distortions, driven by the electrons in a degenerate state. Note that this is exactly the prediction of the Jahn-Teller theorem.

In principle one can introduce in a way similar to eqs.(A.15)-(A.16) also the quadratic coupling constants, $G_{\overline{\Gamma\gamma}}^{\Gamma\Gamma'}$, but a full derivation of such terms is beyond the aim of this appendix. However, it is interesting to point out that some of these constants, usually referred to as force constants, represent the curvature of the APES and they are defined as follows:

$$G_{\overline{\Gamma}}^{\Gamma\Gamma} = K_{0\overline{\Gamma}}^{\Gamma\Gamma} = \frac{1}{2} \left\langle \Gamma \left| \left(\partial^2 V/\partial Q_{\overline{\Gamma}}^2\right)_0 \right| \Gamma \right\rangle \tag{A.17}$$

A.3 The Jahn-Teller theorem

Whenever by solving the Schrödinger equation in eq.(A.4), one finds f-fold degenerate solutions, i.e. f states $\varphi_k(r)$ with $k = 1, 2...f$ and energy $\varepsilon'_k = \varepsilon_0$, the adiabatic approximation no longer applies. As a consequence, the energy levels ε'_k are expected to vary under the nuclear displacements $Q_{\Gamma\gamma} \neq 0$, as predicted on a semiquantitative level by the Jahn-Teller theorem. This relies on a perturbative approach and, for sufficiently small nuclear displacements $Q_{\Gamma\gamma}$, it returns $\varepsilon_k(Q)$, solutions of the

secular equation:

$$\begin{vmatrix} W_{11}-\varepsilon & W_{12} & ... & W_{1f} \\ W_{21} & W_{22}-\varepsilon & ... & W_{2f} \\ \vdots & \vdots & \vdots & \vdots \\ W_{f1} & W_{f2} & ... & W_{ff}-\varepsilon \end{vmatrix} = 0 \tag{A.18}$$

where W_{ij} are the matrix elements of the operator in eq.(A.14) calculated with the wavefunctions of the degenerate term. Here only the nuclear displacements that lower the global symmetry of the system are taken into accounts, thus the totally symmetric displacement is not included. As well, by truncating the expansion in eq.(A.14) at the first order in the assumption that higher contributions are irrelevant for small displacements $Q_{\Gamma\gamma}$, it results

$$W_{ij} = \sum_{\Gamma\gamma} \left\langle i \left| \left(\partial V/\partial Q_{\Gamma\gamma}\right)_0 \right| j \right\rangle Q_{\Gamma\gamma} \tag{A.19}$$

that according to eq.(A.15) reads as:

$$W_{\Gamma\gamma\Gamma\gamma'} = \sum_{\Gamma\gamma} \left\langle \Gamma \left| \left(\partial V/\partial Q_{\overline{\Gamma}}\right)_0 \right| \Gamma \right\rangle \left\langle \overline{\Gamma\gamma}\Gamma\gamma' \mid \Gamma\gamma \right\rangle Q_{\overline{\Gamma\gamma}} = \sum_{\Gamma\gamma} F_{\overline{\Gamma}}^{\Gamma\Gamma} \left\langle \overline{\Gamma\gamma}\Gamma\gamma' \mid \Gamma\gamma \right\rangle Q_{\overline{\Gamma\gamma}}. \tag{A.20}$$

If at least one of the linear vibronic constants F is nonzero, then at least one of the roots of the secular equation contains linear terms in the displacement $Q_{\Gamma\gamma}$ and the APES $\varepsilon_k(Q)$ has no minimum at the point $Q_{\Gamma\gamma} = 0$. It is worth noticing that the lack of a minimum along the $Q_{\Gamma\gamma}$ coordinate, does not directly implies the instability of the nuclear configuration; in the same way the nonzero F term may not be associated to a distorting force along the Q direction. In fact, close to the point of degeneracy, the adiabatic approximation is no longer valid and $\varepsilon(Q)$ looses the meaning of potential energy surface of the nuclei in the mean field of electrons. Thereby, in principle the lack of a minimum results in a variety of effects where the structural distortion is one of the most important.

Every time the Jahn-Teller theorem applies, namely for polyatomic systems in degenerate electronic states that can vibronically couple to one or several types of nuclear displacements, one refers to as a Jahn-Teller problem. Upon predicting the JT-active displacements for the electronic state under investigation, one may find the stable configuration of the nuclei and their dynamics in the presence of the JT effect by computing the $\varepsilon_k(Q)$ values. These are defined as follows (omitting the symmetry label Γ of the electronic state):

$$\varepsilon_k(Q) = \frac{1}{2} \sum_{\Gamma\gamma} K_\Gamma Q_{\Gamma\gamma}^2 + \varepsilon_k^v(Q) \tag{A.21}$$

where a more comprehensive description is given here by including up to the second order terms in eq.(A.14). The $\varepsilon_k^v(Q)$ values are the roots of the secular equation ($\left\| W_{\gamma\gamma'}^v - \varepsilon^v I \right\| = 0$, with $\gamma, \gamma' = 1, 2...f$) from which the K_Γ terms, known as force constants and defined in eq.(A.17), have been separated. In the region of nuclear configurations far from the point of degeneracy,

especially near the minima of the APES, the energy gap between different branches of the APES can be sufficiently large even for strong vibronic coupling. Thereby in this case the adiabatic approximation holds and one may look at the nuclei as moving along the potential energy surface. Note that this qualitative picture is often in very good agreement with the numerical solutions of the vibronic equations in eq.(A.6).

A.3.1 The $E \otimes e$ problem

Consider now the specific Jahn-Teller problem $E \otimes e$, where E indicates the electronic state and e refers to the nuclear displacement. This applies to systems with a symmetry axis of third-order in which doubly degenerate electronic states E are possible and for which the group theory predicts $[E \times E] = A_1 + E$. From eq.(A.2), the electronic part of the total hamiltonian is given by

$$\mathcal{H}^{el} = \mathcal{H}_0 + \sum_{\alpha=1}^{2} W_\alpha Q_\alpha + \frac{1}{2} \sum_{\alpha,\beta=1}^{2} W_{\alpha\beta} Q_\alpha Q_\beta \tag{A.22}$$

where $Q_\alpha = \{Q_1, Q_2\}$ are the symmetrized coordinates, $W_\alpha = (\partial V/\partial Q_\alpha)_0$, $W_{\alpha\beta} = \left(\partial^2 V/\partial Q_\alpha \partial Q_\beta\right)_0$, $Q_{\alpha\beta} = Q_\alpha Q_\beta$ and $\mathcal{H}_0 = \mathcal{H}_r + V(r,0)$. Close to the high symmetry point at $Q_\alpha = 0$, a doubly degenerate electronic state is described by the eigenvalues $\varepsilon_{k=1,2}(Q)$ of the (second order) matrix

$$\begin{aligned}
\mathcal{H} = &\left| \begin{array}{cc} \varepsilon_1' & 0 \\ 0 & \varepsilon_2' \end{array} \right| + \\
&+ \left| \begin{array}{cc} \sum_\alpha \langle 1|W_\alpha|1\rangle Q_\alpha + \frac{1}{2}\sum_{\alpha\beta} \langle 1|W_{\alpha\beta}|1\rangle Q_{\alpha\beta} & \sum_\alpha \langle 1|W_\alpha|2\rangle Q_\alpha + \frac{1}{2}\sum_{\alpha\beta} \langle 1|W_{\alpha\beta}|2\rangle Q_{\alpha\beta} \\ \sum_\alpha \langle 2|W_\alpha|1\rangle Q_\alpha + \frac{1}{2}\sum_{\alpha\beta} \langle 2|W_{\alpha\beta}|1\rangle Q_{\alpha\beta} & \sum_\alpha \langle 2|W_\alpha|2\rangle Q_\alpha + \frac{1}{2}\sum_{\alpha\beta} \langle 2|W_{\alpha\beta}|2\rangle Q_{\alpha\beta} \end{array} \right|
\end{aligned} \tag{A.23}$$

where $\{|1\rangle, |2\rangle\}$ are the electronic states, that form the basis of the irreducible representation Γ_E. If there are nonzero linear terms in the matrix in eq.(A.23), the reference configuration is not stationary. This occurs for $\Gamma_\alpha \in \Gamma_{[E\times E]}$, where $\Gamma_{[E\times E]}$ is the set of irreducible representations arising from the symmetric product of the electronic wavefuction at the reference configuration. By properly choosing $\{|1\rangle, |2\rangle\}$ it follows:

$$\begin{aligned}
F_E &= \langle 1|W_1|1\rangle = -\langle 2|W_1|2\rangle = -\langle 1|W_2|2\rangle \\
K_E &= \frac{1}{2}\langle 1|W_{11} + W_{22}|1\rangle = \frac{1}{2}\langle 2|W_{11} + W_{22}|2\rangle \\
G_E &= \frac{1}{2}\langle 1|W_{12}|2\rangle = \frac{1}{4}\langle 1|W_{11} - W_{22}|1\rangle = -\frac{1}{4}\langle 2|W_{11} - W_{22}|2\rangle \\
\langle 1|W_2|1\rangle &= \langle 2|W_2|2\rangle = \langle 1|W_1|2\rangle = 0 \\
\langle 1|W_{12}|1\rangle &= \langle 2|W_{12}|2\rangle = 0 \\
\langle 1|W_{11}|2\rangle &= \langle 1|W_{22}|2\rangle = 0
\end{aligned}$$

And therefore,

$$\langle 1|W_{11}|1\rangle = \langle 2|W_{22}|2\rangle = K_E + 2G_E$$

$$\langle 1\,|W_{22}|\,1\rangle = \langle 2\,|W_{11}|\,2\rangle = K_E - 2G_E$$

Finally, it results

$$H = \varepsilon' I + \begin{vmatrix} F_E Q_1 + \frac{1}{2}AQ_1^2 + \frac{1}{2}BQ_2^2 & -F_E Q_2 + 2G_E Q_1 Q_2 \\ -F_E Q_2 + 2G_E Q_1 & -F_E Q_1 + \frac{1}{2}BQ_1^2 + \frac{1}{2}AQ_2^2 \end{vmatrix} \tag{A.24}$$

with $A = K_E + 2G_E$ and $B = K_E - 2G_E$, thus

$$= \left(\varepsilon' + \frac{1}{2}K_E\left(Q_1^2 + Q_2^2\right)\right) I + \begin{vmatrix} F_E Q_1 + G_E\left(Q_1^2 - Q_2^2\right) & -F_E Q_2 + 2G_E Q_1 Q_2 \\ -F_E Q_2 + 2G_E Q_1 Q_2 & -F_E Q_1 - G_E\left(Q_1^2 - Q_2^2\right) \end{vmatrix} \tag{A.25}$$

By transforming the cartesian coordinates $\{Q_1, Q_2\}$ into polar coordinates, namely $Q_1 = \rho\cos\phi$ and $Q_2 = \rho\sin\phi$, the eigenvalues of the perturbation become

$$\varepsilon_\pm(\rho,\phi) = \frac{1}{2}K_E\rho^2 \pm \rho\sqrt{F_E^2 + G_E^2\rho^2 + 2F_E G_E \rho\cos(3\phi)} \tag{A.26}$$

and two possibilities arise in the limit of

- $\cos(3\phi) = +1$ and $\phi = 0,\ \frac{2}{3}\pi,\ \frac{4}{3}\pi$
- $\cos(3\phi) = -1$ and $\phi = \frac{\pi}{3},\ \pi,\ \frac{5}{3}\pi$.

For $F_E G_E > 0$, $\phi = 0,\ \frac{2}{3}\pi,\ \frac{4}{3}\pi$ indicate the directions of three equivalent minima on the APES and $\phi = \frac{\pi}{3},\ \pi,\ \frac{5}{3}\pi$ indicate the direction of three equivalent saddle points; for $F_E G_E < 0$ the opposite holds.

Consider now the specific case of $\phi = 0,\ \frac{\pi}{3}$ to get the position of the two non-equivalent stationary points and their energy. Along $\phi = 0$, for $F_E G_E > 0$, the eigenvalues are

$$\varepsilon_+(\rho,0) = \frac{1}{2}\left(K_E + 2G_E\right)\rho^2 + F_E\rho; \qquad \varepsilon_-(\rho,0) = \frac{1}{2}\left(K_E - 2G_E\right)\rho^2 - F_E\rho \tag{A.27}$$

For $\rho > 0$ only the lowest branch of the APES has a minimum, provided $K_E > 2G_E$

$$\frac{\partial\varepsilon_-(\rho,0)}{\partial\rho} = \left(K_E - 2G_E\right)\rho - F_E \tag{A.28}$$

$$\rho_{min} = \frac{F_E}{K_E - 2G_E}; \qquad \varepsilon_-(\rho_{min},0) = -\frac{F_E^2}{2\left(K_E - 2G_E\right)}. \tag{A.29}$$

This defines the Jahn-Teller stabilization energy as

$$E_{JT} = \frac{F_E^2}{2\left(K_E - 2G_E\right)} = \frac{F_E^2}{2k_-^0} \tag{A.30}$$

where $k_-^0 = K_E - 2G_E = \frac{\partial^2\varepsilon_-(\rho,0)}{\partial\rho^2}$. Hence, knowing k_-^0 and E_{JT} means to know F_E.

Looking now along $\phi = \pi/3$ for $F_E G_E > 0$,

$$\varepsilon_\pm(\rho,\pi/3) = \frac{1}{2}K_E\rho^2 \pm \rho\sqrt{F_E^2 + G_E^2\rho^2 - 2F_E G_E\rho} = \frac{1}{2}K_E\rho^2 \pm \rho\left|F_E - G_E\rho\right| \tag{A.31}$$

and two cases appear depending on ρ

$$\varepsilon_+(\rho,\pi/3)=\begin{cases}\frac{1}{2}(K_E+2G_E)\rho^2-\rho F_E & \rho>F_E/G_E\\ \frac{1}{2}(K_E-2G_E)\rho^2+\rho F_E & \rho<F_E/G_E\end{cases} \tag{A.32}$$

$$\varepsilon_-(\rho,\pi/3)=\begin{cases}\frac{1}{2}(K_E-2G_E)\rho^2+\rho F_E & \rho>F_E/G_E\\ \frac{1}{2}(K_E+2G_E)\rho^2-\rho F_E & \rho<F_E/G_E\end{cases} \tag{A.33}$$

Consider $\overline{\rho}=F_E/G_E$ large enough and look at $\rho<\overline{\rho}$, without dealing with the additional conical intersection developing at the point $\overline{\rho}$; thus the lowest sheet has a minimum at

$$\rho_{min}=\frac{F_E}{K_E+2G_E} \tag{A.34}$$

$$\varepsilon_{min}=\varepsilon_-(\rho_{min},\pi/3)=-\frac{F_E^2}{2(K_E+2G_E)} \tag{A.35}$$

The saddle point energy thus has a separation δ from the minimum at $\phi=0$

$$\delta=-\frac{F_E^2}{2(K_E-2G_E)}+\frac{F_E^2}{2(K_E+2G_E)}=\frac{4G_EF_E^2}{2(K_E^2-4G_E^2)}=\frac{4G_EE_{JT}}{K_E+2G_E}=\frac{4G_EE_{JT}}{k_-^{\pi/3}} \tag{A.36}$$

where $k_-^{\pi/3}=K_E+2G_E=\frac{\partial^2\varepsilon_-(\rho,\pi/3)}{\partial\rho^2}$ is the radial curvature of the APES along this direction. Note that the knowledge of k_-^0, $k_-^{\pi/3}$and E_{JT} allows one to determine the vibronic constants (F_E,G_E,K_E) and hence all the branches of the energy surface:

$$F_E=\sqrt{2k_-^0E_{JT}}\qquad G_E=\frac{k_-^{\pi/3}-k_-^0}{4}\qquad K_E=\frac{k_-^{\pi/3}+k_-^0}{2} \tag{A.37}$$

Some conclusions can be drawn by looking at $\varepsilon_-(Q_1,0)=\frac{1}{2}K_EQ_1^2-|Q_1|\,|F_E+G_EQ_1|$, and especially that:

$$\varepsilon_-(Q_1,0)=\begin{cases}\frac{1}{2}(K_E-2G_E)Q_1^2-Q_1F_E & Q_1>0\\ \frac{1}{2}(K_E+2G_E)Q_1^2+Q_1F_E & -\frac{F_E}{G_E}<Q_1<0\\ \frac{1}{2}(K_E-2G_E)Q_1^2-Q_1F_E & Q_1<-\frac{F_E}{G_E}\end{cases} \tag{A.38}$$

The behaviour of $\varepsilon_-(Q_1,0)$ is summarized in fig.(A.1).

A.4 The pseudo Jahn-Teller effect

In this section a brief introduction on the pseudo Jahn-Teller effect is given that may take place, in principle, for any system without a priori limitations. For the sake of simplicity, the case of a nondegenerate ground state vibronically coupled to nondegenerate excited states is considered. Here the coupling is still enclosed in the $W_{km}(Q)$ term in eq.(A.6); for small couplings it can safely be ignored, thus restoring the usual adiabatic approximation. Anyway in many cases the vibronic

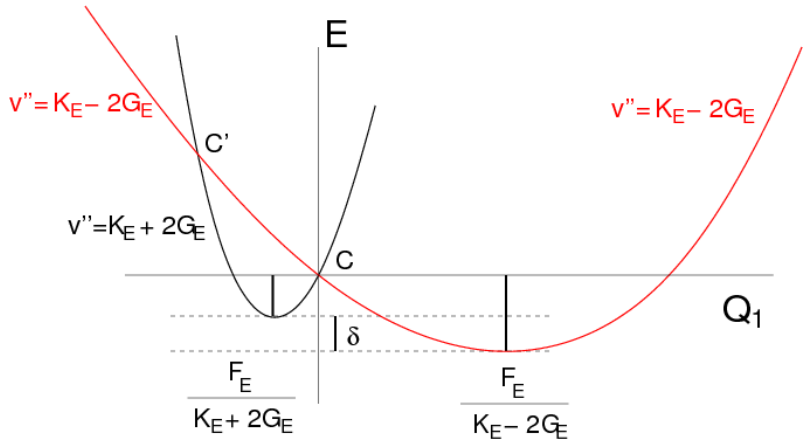

Figure A.1: The APES along the Q_1 coordinate. The red curve shows a minimum for $Q_1 > 0$ (for $\phi = 0$) and it is a global minimum on the surface. The black curve shows a minimum for $Q_1 < 0$ (for $\phi = \pi$) and it is a saddle point on the surface. The three regions in (A.38) appear clearly: v'' is the curvature of the lower curve $\varepsilon_-(Q_1, 0)$; C and C' label respectively the 'main' and the 'additional' conical intersection; δ is the energy difference between the two minima.

coupling is sufficiently strong to make the ground-state unstable, within the pseudo Jahn-Teller scheme. Consider for instance the case of two nondegenerate states Γ and Γ' separated by an energy gap 2Δ where the vibronic contributions $\varepsilon_k^v(Q)$ are obtained by solving the secular equation ($\left\| W^v_{\gamma\gamma'} - \varepsilon^v I \right\| = 0$, with $\gamma, \gamma' = 1, 2...f$). Assuming that only one coordinate $Q_{\overline{\Gamma}}$ satisfies the criterion $\overline{\Gamma} = \Gamma \times \Gamma'$ and including only linear terms in the vibronic interaction, one gets

$$W = \begin{vmatrix} -\Delta & FQ \\ FQ & \Delta \end{vmatrix} \tag{A.39}$$

where F is the off-diagonal linear vibronic constant $F = \langle \Gamma \left| \left(\partial V / \partial Q_{\overline{\Gamma}}\right)_0 \right| \Gamma' \rangle$. After solving the secular equation and assuming $K_0 = K_0^{\Gamma} = K_0^{\Gamma'}$, from eq.(A.21) it follows

$$\varepsilon_k(Q) = \frac{1}{2} K_0 Q^2 \pm \left(\Delta^2 + F^2 Q^2\right)^{\frac{1}{2}}. \tag{A.40}$$

Then expanding the second term[2] in Q,

$$\varepsilon_k(Q) = \frac{1}{2}\left(K_0 \pm F^2/\Delta\right) Q^2 \pm \Delta \mp \frac{1}{8}\left(F^4/\Delta^3\right) Q^4 \pm ... \tag{A.41}$$

From this expression it is evident that the vibronic coupling changes the curvature (the term in Q^2) in different ways for the two states: it increases in the upper level, while it decreases in the lower one. Anyway until the curvature is positive, i.e. $\Delta > F^2/K_0$ the minima of both states are at $Q = 0$ as in the absence of vibronic mixing: this is the weak pseudo Jahn-Teller effect. Instead, if $\Delta < F^2/K_0$ the curvature of the lower curve becomes negative and the system becomes unstable with respect to displacements along Q. This is the strong pseudo Jahn-Teller effect, that gives an

[2] $(1+x)^{1/2} = 1 + \frac{1}{2}x - \frac{1}{8}x^2 + ...$

APES with two minima at

$$\pm Q_0 = \sqrt{2}\left[\left(F^2/K_0^2\right) - \left(\Delta^2/F^2\right)\right]^{\frac{1}{2}}, \tag{A.42}$$

the JT stabilization energy is

$$E_{JT} = \frac{F^2}{K_0} - \Delta\left(1 - \frac{\Delta K_0}{F^2}\right) \tag{A.43}$$

and the curvature at this two minima points is

$$K = K_0\left[1 - \left(\frac{\Delta K_0}{F^2}\right)^2\right]. \tag{A.44}$$

Note that when $\Delta = F^2/K_0$, the curvature is zero everywhere. Considering now the case where $K_{0\Gamma} \neq K_{0\Gamma'}$, we get the following two expressions for the curvature in the lower and upper curve respectively

$$K_{\overline{\Gamma}}^{\Gamma} = K_{0\overline{\Gamma}}^{\Gamma} - \left|F_{\overline{\Gamma}}^{\Gamma\Gamma'}\right|^2/\Delta \tag{A.45}$$

$$K_{\overline{\Gamma}}^{\Gamma'} = K_{0\overline{\Gamma}}^{\Gamma'} + \left|F_{\overline{\Gamma}}^{\Gamma\Gamma'}\right|^2/\Delta \tag{A.46}$$

The F term is nonzero only if $\overline{\Gamma} \in \Gamma \times \Gamma'$ and thus only selected excited states can couple with the groundstate (or more generally with lower energy states) leading to instability. Including all the excited states with the suitable symmetry, the condition of instability becomes as follows:

$$\sum_{\Gamma'}\left|F_{\overline{\Gamma}}^{\Gamma\Gamma'}\right|^2/\Delta_{\Gamma\Gamma'} > K_{0\overline{\Gamma}}^{\Gamma}. \tag{A.47}$$

When degenerate states are involved, the pseudo Jahn-Teller problem becomes more complicated, as it basically turns into a *Jahn-Teller plus pseudo-Jahn-Teller* one. Consider as an example a system with trigonal symmetry D_{3h}, in which a ground state with E'' symmetry and an nondegenerate excited state with symmetry A_1' are coupled by a vibration with e'' symmetry. The pseudo Jahn-Teller problem associated to this case is $(E'' + A_1') \otimes e''$. It is actually composed by a JT problem $E'' \otimes (a_1' + e')$ for the ground state and PJT problem $(E'' + A_1') \otimes e''$. In conclusion the PJT problem for this system is $(E'' + A_1') \otimes (a_1' + e' + e'')$.

Appendix B

Group theory

B.1 Basic concepts on the linear representation theory of finite groups

A group $\mathcal{G}$ is an abstract mathematical object composed by a set of elements together with an operation, the group law. To form a group the generic group operation and the elements must satisfy four conditions: closure, associativity, identity and invertiblity. They are defined as:

- *closure*: for all a, b in $\mathcal{G}$, the result of the operation, $a \cdot b$, is also in $\mathcal{G}$;
- *associativity*: for all a, b and c in $\mathcal{G}$, $(a \cdot b) \cdot c = a \cdot (b \cdot c)$;
- *identity element*: there exists an element (and it is unique) e in $\mathcal{G}$, such that for every element a in $\mathcal{G}$, the equation $e \cdot a = a \cdot e = a$ holds;
- *inverse element*: for each a in $\mathcal{G}$, there exists an element a^{-1} in $\mathcal{G}$ such that $a \cdot a^{-1} = a^{-1} \cdot a = e$.

This appendix deals in particular with finite groups that are composed by a finite set of elements; the number of elements is the *order* of the group. Moreover a group can be partionned into non overlapping subsets of elements that form *conjugate classes*. In general for any two elements a and b of the group, the equation $a \cdot b = b \cdot a$ may not be true. Groups, for which $a \cdot b = b \cdot a$ always holds, are called abelian.
In mathematics, group representations allow to describe abstract groups in terms of linear transformations of vector spaces; in particular, they can be used to represent the elements of a group as matrices. In this way the operation of the group can be represented by matrix multiplication. Some basic definitions need to be introduced at this point[78].

B.1.1 General definitions

Isomorphism Two groups $\mathcal{G}_1$ and $\mathcal{G}_2$ with elements $\{G_i\}$ and with certain group operations are isomorphic if there exists a *one to one* correspondence T between the elements of $\mathcal{G}_1$ and the elements of $\mathcal{G}_2$, i.e. $T : \mathcal{G}_1 \to \mathcal{G}_2$,

$$G_a \in \mathcal{G}_1 \rightsquigarrow T(G_a) \in \mathcal{G}_2 \tag{B.1}$$

and this correspondence preserves the group operations, namely multiplying and then mapping gives the same result as first mapping and then multiplying

$$T(G_a G_b) = T(G_a)\, T(G_b) \tag{B.2}$$

Homomorphism $\mathcal{G}_1$ is homomorphic to $\mathcal{G}_2$ if there exists a *many to one* correspondence T that preserves the group operations and satisfies the assumptions in eqs.B.1,B.2. Note that here for any element of $\mathcal{G}_1$ there must be one and only one element of $\mathcal{G}_2$, but the inverse is not required. In fact for a given element $F \in \mathcal{G}_2$ there can be more than one element in $\mathcal{G}_1$; if this is not the case, then the homomorphism is an isomorphism. Notice that any group is homomorphic to the simplest group $E \equiv \{1\}$ containing only the identity.

The set of non-singular $n \times n$ matrices M_n forms a group where important subgroups are the set of real matrices, unitary matrices and orthogonal matrices. These M_n matrices are also morphisms, as they map the non-singular transformations of vectors from a n-dimensional space ε_n to another. These vectors are defined in a chosen basis $\{|e_i\rangle\}$ in the space ε_n; each matrix $\hat{M} \in M_n$ operating on them produces an isomorphism of ε_n with itself, namely an automorphism,

$$\hat{M}\,|e_i\rangle = \sum_{j=1}^{n} |e_j\rangle\, M_{ji} \tag{B.3}$$

where $\hat{M}\varepsilon_n \simeq \varepsilon_n$ means that the transformed space is isomorphic to ε_n, while $\hat{M}\varepsilon_n = \varepsilon_n$ means that the transformed space is exactly ε_n, as in eq.B.3 where the transformed vectors are combination of the original vectors and M is non-singular. Unitary matrices represent automorphism of Hilbert spaces, as they preserve both the linear structure and the scalar products; real matrices refer to real vector spaces and orthogonal matrices to real Hilbert spaces.

Representations Formally, a *representation* means a homomorphism from a group to the group of automorphism of an object. If the object is a vector space, then one has a linear representation. Accordingly, the representation Γ is a homomorphism from the group $\mathcal{G}$ to the group of matrices M_n, automorphisms of the space ε_n. This reads as

$$\Gamma :\ \mathcal{G} \to M_n \tag{B.4}$$

$$G_a \rightsquigarrow \Gamma(G_a) = M_a \tag{B.5}$$

$$G_a G_b = G_c \Rightarrow M_a M_b = M_c \tag{B.6}$$

where $\Gamma(1) = I$. In other words, any n-dimensional space ε_n where M_n is a group of automorphisms forms a vector space where $\mathcal{G}$ applies. Since the matrices M_n are defined on a basis, one looks for a basis of the representation. More generally, for a given representation, one identifies a set of generic

operators $\mathcal{O}$ operating in the space ε_n, where they define an automorphism. They are related to the matrices M_n as,

$$\hat{\Gamma} : \mathcal{G} \to \mathcal{O}(\varepsilon_n) \tag{B.7}$$

$$G_a \rightsquigarrow \hat{\Gamma}(G_a) = \hat{M}_a \tag{B.8}$$

where by applying $\hat{M}_a$ on some preferred basis, one obtains

$$\hat{M}_a |e_i\rangle = \sum_{j=1}^{n} |e_j\rangle (M_a)_{ij} \tag{B.9}$$

A change of basis amounts to a transformation of Γ into an equivalent representation Γ' according to

$$\Gamma' = O^{-1}\Gamma O \tag{B.10}$$

where O is the matrix for the change of basis and B.9 holds for any element of the representation. Thus, the homomorphism $\hat{\Gamma}$ can be fixed once and for all for a given ε_n irrespective of the basis where M_n is defined.
The trace of a representation matrix

$$\mathrm{Tr}\{M(G)\} = \sum_{j=1}^{n} (M)_{jj}(G) = \chi(G) \tag{B.11}$$

is the character of G. The traces of all the matrices $\mathrm{Tr}\{M(G)\}$ of a representation defines the character as a fuction over the group. It can be shown that (i) the character of a representation $M(G)$ is invariant to basis transformation; (ii) it is the same for all the elements of a conjugate class; (iii) the character of the identity is equal to the dimension of the space associated to the representation n.

Direct sum of vector spaces Given ε_1 and ε_2 two vector spaces, one may form a third space called the direct sum and denoted as $\varepsilon_1 \oplus \varepsilon_2$ by setting:

$$\varepsilon_1 \oplus \varepsilon_2 \ni |u\rangle = (|u_1\rangle, |u_2\rangle) \qquad \forall |u_1\rangle \in \varepsilon_1;\ \forall |u_2\rangle \in \varepsilon_2 \tag{B.12}$$

and

$$(|u_1\rangle, |u_2\rangle) + (|v_1\rangle, |v_2\rangle) = (|u_1\rangle + |v_1\rangle, |u_2\rangle + |v_2\rangle) \tag{B.13}$$

$$\lambda(|u_1\rangle, |u_2\rangle) = (\lambda|u_1\rangle, \lambda|u_2\rangle). \tag{B.14}$$

Note that $(0_1, 0_2)$ is the zero of $\varepsilon_1 \oplus \varepsilon_2$. For convenience one can write $|u\rangle = |u_1\rangle \oplus |u_2\rangle$, since the properties in eqs.B.13,B.14 are similar to those satisfied by an ordinary sum operation.

Direct sum of operators If $\hat{M}_1$ and $\hat{M}_2$ are operators acting in ε_1 and ε_2 respectively, the direct sum $\hat{M} = \hat{M}_1 \oplus \hat{M}_2$ can be formed, which is an operator in the direct sum space $\varepsilon_1 \oplus \varepsilon_2$ defined as

$$\left(\hat{M}_1 \oplus \hat{M}_2\right) |u_1\rangle \oplus |u_2\rangle = \hat{M}_1 |u_1\rangle \oplus \hat{M}_2 |u_2\rangle \tag{B.15}$$

from which follows that $\hat{M}_1 \oplus \hat{M}_2$ is linear.

Direct sum of representations Given two representations $\hat{\Gamma}_1$ and $\hat{\Gamma}_2$ of a group $\mathcal{G}$ into the automorphisms $\mathcal{O}(\varepsilon_1)$, $\mathcal{O}(\varepsilon_2)$ of two vector spaces ε_1 and ε_2, the sum of the representations is defined element by element as direct sum of operators:

$$\left(\hat{\Gamma}_1 \oplus \hat{\Gamma}_2\right)(G) = \hat{\Gamma}_1(G) \oplus \hat{\Gamma}_2(G) \qquad \forall G \in \mathcal{G} \tag{B.16}$$

This defines a novel representation $\hat{\Gamma}$ of $\mathcal{G}$ into the automorphisms $\mathcal{O}(\varepsilon_1 \oplus \varepsilon_2)$ of $\varepsilon_1 \oplus \varepsilon_2$.

B.1.2 Irreducible representations

By definition a representation $\hat{\Gamma}$ of a group $\mathcal{G}$ requires a vector space ε which is invariant under the group, symbolically as $\mathcal{G}\varepsilon = \varepsilon$. Note that what actually operates on the elements of ε is an operator $\hat{\Gamma}(G)$ related to $G \in \mathcal{G}$ and not $\mathcal{G}$ itself. The representation $\hat{\Gamma}$ is reducible if the space ε can be decoupled into invariant subspaces ε_1, $\varepsilon_2, ...\varepsilon_k$, as follows[1]:

$$\varepsilon = \sum\nolimits_{\alpha}^{\oplus} \varepsilon_\alpha \tag{B.17}$$

$$\mathcal{G}\varepsilon_\alpha = \varepsilon_\alpha \tag{B.18}$$

The set of subspaces $\{\varepsilon_\alpha\}$ performs a decomposition if and only if

$$\{\varepsilon_\alpha\} \cap \{\varepsilon_\beta\} = \{0\} \qquad \alpha \neq \beta \tag{B.19}$$

and $\text{span}\{\cup_\alpha \varepsilon_\alpha\} = \text{span}\{\varepsilon\} = \varepsilon$, provided ε_α are linear spaces. The representation $\hat{\Gamma}$ is irreducible if the only invariant subspaces are $\{0\}$ and ε itself. On the other hand, the matrix representation of a reducible representation takes a block diagonal form

$$\hat{\Gamma} = \begin{bmatrix} \hat{\Gamma}_1 & 0 & 0 & 0 \\ 0 & \hat{\Gamma}_2 & 0 & 0 \\ 0 & 0 & \ddots & 0 \\ 0 & 0 & 0 & \hat{\Gamma}_k \end{bmatrix} \tag{B.20}$$

[1] The sum $\oplus$ in eq.B.17 is the internal direct sum, i.e. the sum of subobjects of a common object, as opposite to the external one, i.e. the sum of objects that are not subobjects of a common object. Anyway they are essentially equivalent.

and the reduction procedure amounts to find a basis $\{|e_{i,\alpha}\rangle\}_{i,\alpha}$ such as

$$\{|e_{i,\alpha}\rangle\}_{i,\alpha} = \cup_\alpha \{|e_{i,\alpha}\rangle\}_i^{f_\alpha} \tag{B.21}$$

$$\text{span}\,\{|e_{i,\alpha}\rangle\}_i^{f_\alpha} = \varepsilon_\alpha$$

where α is the index of the irreducible representation; i goes from 1 to f_α, f_α being the dimensionality of the space for the α representation. Note that the same $\hat{\Gamma}_\alpha$ may occurr more then once in a given decomposition. Hence, generally

$$\hat{\Gamma} = \sum_\alpha^\oplus n_\alpha \hat{\Gamma}_\alpha \tag{B.22}$$

where n_α is the number of equivalent $\hat{\Gamma}_\alpha$ contained in the decomposition of $\hat{\Gamma}$ into irreducible representations.

B.1.3 Schur's lemma (I) and (II)

Schur's lemma (I): if $\hat{\Gamma}_\alpha$ and $\hat{\Gamma}_\beta$ are two irreducible representations of the group $\mathcal{G}$ and S is a map from ε_b to ε_a, such as

$$\hat{\Gamma}_\alpha S = S\hat{\Gamma}_\beta \tag{B.23}$$

which means as usual $\hat{\Gamma}_\alpha(G)\,S = S\hat{\Gamma}_\beta(G)$ for any $G \in \mathcal{G}$, then this implies: $S = 0$ or S not singular.
Proof: let $\tilde{\varepsilon}$ be the kernel of S, i.e. $S\tilde{\varepsilon} = \{0\}$. Adding $\tilde{\varepsilon}$ on both sides of eq.B.23, it follows

$$\hat{\Gamma}_\alpha S\tilde{\varepsilon} = \hat{\Gamma}_\alpha\{0\} = \{0\} \equiv S\left(\hat{\Gamma}_\beta\tilde{\varepsilon}\right) \tag{B.24}$$

which requires $\hat{\Gamma}_\beta\tilde{\varepsilon} = \tilde{\varepsilon}$ to be valid. This means that $\tilde{\varepsilon}$ is an invariant subspace of ε_b and thus $\tilde{\varepsilon} = \varepsilon_b$ or $\tilde{\varepsilon} = \{0\}$ since $\hat{\Gamma}_\beta$ is irreducible. In the first case $\ker S$ coincides with ε_b thus $\text{Im}S = \{0\}$; it follows that there is no mapping between ε_a and ε_b thus $S = 0$. In the second case S is invertible and there exists S^{-1}: $\text{Im}S \subset \varepsilon_a \to \varepsilon_b$ such that $\forall y \in \text{Im}S$ it follows that $S^{-1}y = x$ and thus $Sx = y$.
Corollary: if $\hat{\Gamma}_\alpha$ and $\hat{\Gamma}_\beta$ are two irreducible representations of the group $\mathcal{G}$ and there exists a nonzero S that maps from ε_b to ε_a and obeys $\hat{\Gamma}_\alpha S = S\hat{\Gamma}_\beta$, then the two representations are equivalent $\hat{\Gamma}_\alpha \equiv \hat{\Gamma}_\beta$.
Proof: adding ε_b on both sides of eq.B.23, it follows

$$\hat{\Gamma}_\alpha(S\varepsilon_b) = S\hat{\Gamma}_\beta\varepsilon_b \equiv S\varepsilon_b \tag{B.25}$$

this implies that $S\varepsilon_b$ is invariant thus, except for $S = 0$, $S\varepsilon_b \equiv \varepsilon_a$ follows from the fact that $\hat{\Gamma}_\alpha$ is irreducible; in this case $\text{Im}S \equiv \varepsilon_a$. Hence for $S \neq 0$, $\hat{\Gamma}_\alpha$ is equivalent to $\hat{\Gamma}_\beta$.
In conclusion from the Schur's lemma (I) and the corollary, it results that: $S = 0$, if $\hat{\Gamma}_\alpha$ is not equivalent to $\hat{\Gamma}_\beta$; $S = 0$ or $S \neq 0$ (not singular), if $\hat{\Gamma}_\alpha \equiv \hat{\Gamma}_\beta$.

Schur's lemma (II): given two equivalent irreducible representations $\hat{\Gamma}_\alpha \equiv \hat{\Gamma}_\beta$ and $\hat{\Gamma}_\alpha S = \hat{\Gamma}_\beta S$, then either $S = 0$ or $S = \lambda 1$, $\lambda \in \mathbb{C}$.

Proof: adding $-\lambda\Gamma_\alpha$ to both sides of eq.B.23 with $\lambda \in \mathbb{C}$ one obtains,

$$\hat{\Gamma}_\alpha S - \lambda\hat{\Gamma}_\alpha = S\Gamma_\beta - \lambda\Gamma_\alpha \tag{B.26}$$

Since $\hat{\Gamma}_\alpha \equiv \hat{\Gamma}_\beta$,

$$\hat{\Gamma}_\alpha (S - \lambda) = (S - \lambda)\Gamma_\alpha. \tag{B.27}$$

Consider now λ an eigenvalue of S and V_λ its eigenspace,

$$\hat{\Gamma}_\alpha (S - \lambda) V_\lambda = \hat{\Gamma}_\alpha \{0\} = \{0\} = (S - \lambda)\left(\hat{\Gamma}_\alpha V_\lambda\right) \tag{B.28}$$

Thus $\hat{\Gamma}_\alpha V_\lambda \subset V_\lambda$, which means that V_λ is an invariant subspace. It follows that either $V_\lambda = \{0\}$ or $V_\lambda = \varepsilon_\alpha$ since $\hat{\Gamma}_\alpha$ is irreducible. The first case is not possible since V_λ is by hypothesis an eigenspace and thus the equation is satisfied only if $S \equiv \lambda 1_\alpha$. One only assumes that an eigenvalue exists but this is always guaranteed in finite-dimensional spaces.

B.1.4 Orthogonality theorems

Consider the two matrix representations Γ^α and Γ^β of the finite group $\mathcal{G}$ and suppose for simplicity that they are both unitary. This can always be realized in the Hilbert spaces ε_α and ε_β by introducing orthonormal basis. Let $\gamma_k^\alpha(G)$ be the column vector

$$\gamma_k^\alpha(G) = \begin{bmatrix} \Gamma_{1k}^\alpha(G) \\ \Gamma_{2k}^\alpha(G) \\ \vdots \\ \Gamma_{f_\alpha k}^\alpha(G) \end{bmatrix} = \{\Gamma_{ik}^\alpha(G)\}_{i=1}^{f_\alpha} \tag{B.29}$$

where, k is the column index of the matrix representation, G is an element of the group and f_α is the dimensionality of the irreducible representation α. In the same way $\gamma_l^\beta(G)$ is generated with the help of the β representation. Hence,

$$\Gamma^\alpha(G)\gamma_k^\alpha\left(G'\right) = \left\{\left(\Gamma^\alpha(G)\Gamma^\alpha\left(G'\right)\right)_{ik}\right\}_{i=1}^{f_\alpha} = \left\{\Gamma_{ik}^\alpha\left(G''\right)\right\}_{i=1}^{f_\alpha} \equiv \gamma_k^\alpha\left(G''\right) \tag{B.30}$$

where $G'' = GG'$. Analogously,

$$\gamma_l^{\beta\dagger}\left(G'\right)\Gamma^{\beta\dagger}(G) = \gamma_l^{\beta\dagger}\left(G'\right)\Gamma^\beta\left(G^{-1}\right) = \gamma_l^{\beta\dagger}\left(GG'\right). \tag{B.31}$$

Let then S^{kl} be the $f_\alpha \times f_\beta$ matrix

$$S^{kl} = \sum_G \gamma_k(G)\gamma_l^\dagger(G). \tag{B.32}$$

Then,

$$\begin{aligned}\hat{\Gamma}^{\alpha}(G) S^{kl} &= \sum_{G'} \hat{\Gamma}^{\alpha}(G) \gamma_k^{\alpha}\left(G'\right) \gamma_l^{\beta\dagger}\left(G'\right) = \sum_{G''} \gamma_k^{\alpha}\left(G''\right) \gamma_l^{\beta\dagger}\left(G^{-1}G''\right) = \\ &= \sum_{G''} \gamma_k^{\alpha}\left(G''\right) \gamma_l^{\beta\dagger}\left(G''\right) \hat{\Gamma}^{\beta}(G) \equiv S^{kl}\hat{\Gamma}^{\beta}(G)\end{aligned} \tag{B.33}$$

for any $G \in \mathcal{G}$. From Schur's lemma (I) it follows that for two non equivalent irreducible representations, i.e. $\alpha \neq \beta$

$$S_{ij}^{kl} = \sum_{G} \Gamma_{ik}^{\alpha}(G) \Gamma_{jl}^{\beta *}(G) = 0 \tag{B.34}$$

For $\alpha = \beta$, that is $\Gamma^{\alpha} \equiv \Gamma^{\beta}$, the Schur's lemma (II) predicts that $S^{kl} = \lambda_{kl} 1_{\alpha}$ and in particular

$$\mathrm{tr} S^{kl} = \lambda_{kl} f_{\alpha}. \tag{B.35}$$

The trace reads as

$$\begin{aligned}\mathrm{tr} S^{kl} &= \mathrm{tr}\left\{\sum_{G} \Gamma_{ik}^{\alpha}(G) \Gamma_{lj}^{\alpha}\left(G^{-1}\right)\right\} = \sum_{i}\sum_{G} \Gamma_{li}^{\alpha}\left(G^{-1}\right) \Gamma_{ik}^{\alpha}(G) = \\ &= \left(\sum_{G} \Gamma^{\alpha}\left(G^{-1}\right) \Gamma^{\alpha}(G)\right)_{lk} = \sum_{G} 1_{\alpha}\delta_{lk} \equiv g\delta_{lk}\end{aligned} \tag{B.36}$$

where g is the order of the group. Hence $\lambda_{kl} \equiv g/f_{\alpha}\delta_{lk}$. For $\alpha = \beta$ it follows

$$S_{ij}^{kl} = \sum_{G} \Gamma_{ik}^{\alpha}(G) \Gamma_{jl}^{\alpha *}(G) = \frac{g}{f_{\alpha}} \delta_{ij}\delta_{kl} \tag{B.37}$$

This leads to the so called Orthogonality Theorem,

$$\sum_{G} \Gamma_{ik}^{\alpha}(G) \Gamma_{jl}^{\beta *}(G) = \frac{g}{f_{\alpha}} \delta_{\alpha\beta}\delta_{ij}\delta_{kl}. \tag{B.38}$$

Finally by defining the character χ of the representation α for each element G according to eq.B.11, one has

$$\chi^{\alpha}(G) = \mathrm{tr}\left(\Gamma^{\alpha}(G)\right) = \sum_{k} \Gamma_{kk}^{\alpha}(G) \tag{B.39}$$

$$\sum_{G} \chi^{\alpha}(G) \chi^{\beta *}(G) = \frac{g}{f_{\alpha}} \delta_{\alpha\beta} \sum_{k,l} \delta_{kl}\delta_{kl} \equiv g\delta_{\alpha\beta} \tag{B.40}$$

For a chosen representation Γ^{α}, according to eq.B.39, one may calculate the character of each element of the group thus defining the vector of characters. From eq.B.40 it follows that in non equivalent irreducible representations the vectors of characters are orthogonal; while equivalent irreducible representations share the same vector of characters. Moreover for each element of the group one may build a vector of characters in all the available irreducible representations of the group. Elements with the same vector of character through all the irreducible representations form a *conjugate class*. The total number of elements in the group corresponds to the order of the group g; while the number of conjugate classes gives to the number of non equivalent irreducible

representations.

By using the vectors of characters one may also rewrite the relation in eq.B.22 in a more practical way. Indeed the vector of characters of a reducible representation is simply the sum of the vectors of characters of the irreducible representations from which it originates. Thus it is easy to decompose a reducible representation Γ into its corresponding Γ^{α} components, by projecting the vector of characters of the reducible representation on the basis vectors of the irreducible representations. In this case the contribution n_{α} of Γ_{α} is given by:

$$n_{\alpha} = \frac{1}{g} \sum_{G \in \mathcal{G}} \chi_{\alpha}^{*}(G) \chi(G) \tag{B.41}$$

where g is the order of the group and $\chi(G)$ is the trace of the G-th element of the reducible representation. Note that this process is known as spectral analysis of representations.

B.1.5 Symmetric and antisymmentric products

When $\alpha = \beta$ the product representation $\zeta_{ij} = \psi_i^{\alpha} \phi_j^{\alpha}$ naturally splits into

$$[\zeta_{ij}] = \psi_i^{\alpha} \phi_j^{\alpha} + \psi_j^{\alpha} \phi_i^{\alpha} = [\zeta_{ji}] \tag{B.42}$$

and

$$\{\zeta_{ij}\} = \psi_i^{\alpha} \phi_j^{\alpha} - \psi_j^{\alpha} \phi_i^{\alpha} = -\{\zeta_{ji}\} \tag{B.43}$$

where $\{\psi_i\}$, $\{\phi_i\}$ are basis functions for the representation α. The former eq.B.42 represents the symmetric product, while the latter eq.B.43 is the antisymmetric product and it makes sense only when $\psi_i \neq \phi_j$. Then applying a group operation $\hat{\Gamma}(G)$ to eq.B.42 gives

$$\hat{\Gamma}(G)[\zeta_{ij}] = \sum_{k,l} \left(\psi_k^{\alpha} \phi_l^{\alpha} \Gamma_{ki}(G) \Gamma_{lj}(G) + \psi_l^{\alpha} \phi_k^{\alpha} \Gamma_{lj}(G) \Gamma_{ki}(G)\right) = \sum_{k,l} [\zeta_{kl}] \Gamma_{ki}(G) \Gamma_{lj}(G) \tag{B.44}$$

where $\Gamma_{ki,lj}(G)$ are elements of the matrix representation for each G in the group. Analogously

$$\hat{\Gamma}(G)\{\zeta_{ij}\} = \sum_{k,l} \{\zeta_{kl}\} \Gamma_{ki}(G) \Gamma_{lj}(G) \tag{B.45}$$

From eqs.B.42,B.43 it follows,

$$\begin{aligned} \hat{\Gamma}(G)[\zeta_{ij}] &= \sum_{k,l} [\zeta_{kl}] \Gamma_{ki}(G) \Gamma_{lj}(G) = \sum_{l,k} [\zeta_{lk}] \Gamma_{lj}(G) \Gamma_{ki}(G) = \\ &= \sum_{k,l} [\zeta_{kl}] \Gamma_{kj}(G) \Gamma_{li}(G) = \hat{\Gamma}(G)[\zeta_{ji}] \end{aligned} \tag{B.46}$$

and

$$\begin{aligned} \hat{\Gamma}(G)\{\zeta_{ij}\} &= \sum_{k,l} \{\zeta_{kl}\} \Gamma_{ki}(G) \Gamma_{lj}(G) = \sum_{l,k} \{\zeta_{lk}\} \Gamma_{lj}(G) \Gamma_{ki}(G) = \\ &= -\sum_{k,l} \{\zeta_{kl}\} \Gamma_{kj}(G) \Gamma_{li}(G) = -\hat{\Gamma}(G)\{\zeta_{ji}\} \end{aligned} \tag{B.47}$$

Hence

$$\hat{\Gamma}(G)[\zeta_{ij}] = \sum_{k,l}[\zeta_{kl}]\frac{\Gamma_{ki}(G)\Gamma_{lj}(G)+\Gamma_{kj}(G)\Gamma_{li}(G)}{2} \tag{B.48}$$

$$\hat{\Gamma}(G)\{\zeta_{ij}\} = \sum_{k,l}\{\zeta_{kl}\}\frac{\Gamma_{ki}(G)\Gamma_{lj}(G)-\Gamma_{kj}(G)\Gamma_{li}(G)}{2} \tag{B.49}$$

$$[\chi\otimes\chi](G) = \sum_{i,j}\frac{\Gamma_{ii}(G)\Gamma_{jj}(G)+\Gamma_{ij}(G)\Gamma_{ji}(G)}{2} = \frac{\left(\chi^2(G)+\chi\left(G^2\right)\right)}{2} \tag{B.50}$$

$$\{\chi\otimes\chi\}(G) = \sum_{i,j}\frac{\Gamma_{ii}(G)\Gamma_{jj}(G)-\Gamma_{ij}(G)\Gamma_{ji}(G)}{2} = \frac{\left(\chi^2(G)-\chi\left(G^2\right)\right)}{2} \tag{B.51}$$

B.1.6 Projectors

For a representation in a chosen space, one then has to determine a suitable basis formed by elements that transform under the group elements in the chosen representation. These basis elements are linearly independent in the case of irreducible representations. Now let be Γ^{α} the *unitary* matrix irreducible representation of the group $\mathcal{G}$ and $\hat{\Gamma}^{\alpha}$ its corresponding operator representation in a given Hilbert space. Consider the operator

$$\hat{\Omega}^{\alpha}_{ij} = \sum_{G}\Gamma^{\alpha *}_{ij}(G)\hat{\Gamma}(G) = \sum_{G}\Gamma^{\alpha}_{ij}\left(G^{-1}\right)\hat{\Gamma}(G) \tag{B.52}$$

Upon applying $\hat{\Gamma}(G)$, it follows

$$\begin{array}{l}\hat{\Gamma}(G)\hat{\Omega}^{\alpha}_{ij} = \sum_{G'}\Gamma^{\alpha *}_{ij}\left(G'\right)\hat{\Gamma}(G)\hat{\Gamma}\left(G'\right) = \sum_{G''}\Gamma^{\alpha *}_{ij}\left(G^{-1}G''\right)\hat{\Gamma}\left(G''\right) \equiv \\ \equiv \sum_{m}\sum_{G''}\Gamma^{\alpha *}_{im}\left(G^{-1}\right)\Gamma^{\alpha *}_{mj}\left(G''\right)\hat{\Gamma}\left(G''\right) = \sum_{m}\Gamma^{\alpha}_{im}(G)\hat{\Omega}^{\alpha}_{mj}.\end{array} \tag{B.53}$$

Then by using the orthogonality theorem one obtains

$$\begin{array}{l}\hat{\Omega}^{\beta}_{kl}\hat{\Omega}^{\alpha}_{ij} = \sum_{G}\Gamma^{\beta *}_{kl}(G)\hat{\Gamma}(G)\sum_{G'}\Gamma^{\alpha *}_{ij}\left(G'\right)\hat{\Gamma}\left(G'\right) = \\ = \sum_{G,G''}\Gamma^{\beta *}_{kl}(G)\hat{\Gamma}\left(G''\right)\Gamma^{\alpha *}_{ij}\left(G^{-1}G''\right) = \\ = \sum_{m}\sum_{G,G''}\Gamma^{\beta *}_{kl}(G)\Gamma^{\alpha *}_{im}\left(G^{-1}\right)\Gamma^{\alpha *}_{mj}\left(G''\right)\hat{\Gamma}\left(G''\right) = \\ = \sum_{m}\sum_{G}\Gamma^{\beta *}_{kl}(G)\Gamma^{\alpha}_{im}(G)\hat{\Omega}^{\alpha}_{mj} = \frac{g}{f_{\alpha}}\sum_{m}\delta_{\alpha\beta}\delta_{lm}\delta_{ki}\hat{\Omega}^{\alpha}_{mj} = \frac{g}{f_{\alpha}}\delta_{\alpha\beta}\delta_{ki}\hat{\Omega}^{\alpha}_{lj}\end{array} \tag{B.54}$$

In the case of the irreducible representation Γ^{α}, the diagonal elements of eq.B.54 are

$$\hat{\Omega}^{\alpha}_{kk}\hat{\Omega}^{\alpha}_{ii} = \frac{g}{f_{\alpha}}\delta_{ki}\hat{\Omega}^{\alpha}_{ik} \tag{B.55}$$

from which derives $\hat{\Omega}^{\alpha}_{kk} = \frac{g}{f_{\alpha}}$ and one can prove

$$\sum_{\alpha=1}^{d}\sum_{k=1}^{f_{\alpha}}\frac{f_{\alpha}}{g}\hat{\Omega}^{\alpha}_{kk} = 1 \tag{B.56}$$

meaning that each element can be decomposed in terms of the different irreducible representations. In the Hilbert space, the operators $\hat{\Omega}^{\alpha}_{mj}$ form a unitary matrix[2]: the columns of this matrix applied on a fixed object φ provide the basis functions of the representation. This means that for any fixed i, the operators $\left\{\hat{\Omega}^{\alpha}_{1i}, \hat{\Omega}^{\alpha}_{2i}, ...\hat{\Omega}^{\alpha}_{f_\alpha i}\right\}$ can be applied on φ to generate f_α basis fuctions with the appropriate symmetry

$$\begin{aligned} \Phi^{\alpha}_{1} &= \hat{\Omega}^{\alpha}_{1i}\varphi = \textstyle\sum_G \Gamma_{1i}\left(G^{-1}\right)\hat{\Gamma}\left(G\right)\varphi \\ &\vdots \\ \Phi^{\alpha}_{f_\alpha} &= \hat{\Omega}^{\alpha}_{f_\alpha i}\varphi = \textstyle\sum_G \Gamma_{f_\alpha i}\left(G^{-1}\right)\hat{\Gamma}\left(G\right)\varphi \end{aligned} \tag{B.57}$$

thus forming a basis of the irreducible f_α-dimensional representation Γ^{α}. Once the basis functions are available, one may generate new functions with the proper symmetry simply by applying the group elements,

$$\hat{\Gamma}\left(G\right)\hat{\Omega}^{\alpha}_{ij}\varphi = \sum_m \Gamma^{\alpha}_{im}\left(G\right)\hat{\Omega}^{\alpha}_{mj}\varphi. \tag{B.58}$$

B.2 Analysis of the group of symmetry D_{3h}

This part shows how to recover information on a given symmetry group by analysing the corresponding character table that contains the values of the characters of the irreducible representations of the group as obtained from eq.B.39. For any finite group, the columns of the table are labeled by the conjugate classes, while the rows by the irreducible representations. These tables are square, meaning that the number of independent irreducible representations equals that of conjugate classes. Note that for point symmetry groups the table often contains additional information that it is useful when dealing with molecular applications. Here is described the case of the D_{3h} point symmentry group and its character table is shown in table B.1. For further examples see ref.[7] and ref.[21].
From the character table, the order of the group g can be easily obtained. According to the definition given in eq.B.40, g is equal to the sum of $\left(\chi^{\alpha}\left(G\right)\right)^2$ for any α belonging to the group. By the choice of $\alpha = A_1^{'}$, it follows:

$$\begin{aligned} &g = 1\cdot\chi^2\left(E\right) + 2\cdot\chi^2\left(C_3\right) + 3\cdot\chi^2\left(C_2\right) + 1\cdot\chi^2\left(\sigma_h\right) + 2\cdot\chi^2\left(S_3\right) + 3\cdot\chi^2\left(\sigma_v\right) = \\ &= 1+2+3+1+2+3 = 12 \end{aligned} \tag{B.59}$$

As a consenquence of the fact that the elements of the group are distributed into conjugate classes, each term $\left(\chi^{\alpha}\left(G\right)\right)^2$ is multiplied by a factor corresponding to the number of elements in the class.

[2] In general for non unitary matrices, eq.B.52 reads as

$$\hat{\Omega}^{\alpha}_{ij} = \sum_G \Gamma^{\alpha *}_{ij}\left(G\right)\hat{\Gamma}\left(G\right) = \sum_G \Gamma^{\alpha}_{ji}\left(G^{-1}\right)\hat{\Gamma}\left(G\right);$$

accordingly eq.B.53 is

$$\hat{\Gamma}\left(G\right)\hat{\Omega}^{\alpha}_{ij} = \sum_m \Gamma^{\alpha}_{mi}\left(G\right)\hat{\Omega}^{\alpha}_{mj}$$

and eq.B.54 is

$$\hat{\Omega}^{\beta}_{kl}\hat{\Omega}^{\alpha}_{ij} = \frac{g}{f_\alpha}\delta_{\alpha\beta}\delta_{li}\hat{\Omega}^{\alpha}_{kj}$$

D_{3h}	E	$2C_3$	$3C_2$	σ_h	$2S_3$	$3\sigma_v$	$g = 12$
$A_1^{'}$	1	1	1	1	1	1	
$A_2^{'}$	1	1	-1	1	1	-1	R_z
$E^{'}$	2	-1	0	2	-1	0	(x, y)
$A_1^{''}$	1	1	1	-1	-1	-1	
$A_2^{''}$	1	1	-1	-1	-1	1	z
$E^{''}$	2	-1	0	-2	1	0	(R_x, R_y)

Table B.1: Character table for the D_{3h} point group.

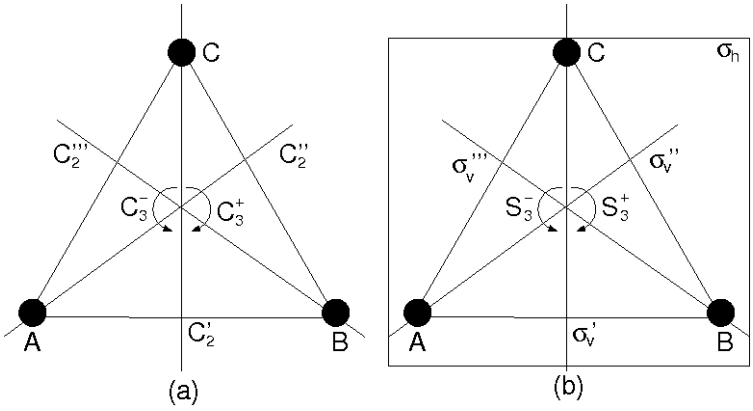

Figure B.1: Symmetry elements of the D_{3h} point group. (a) axis, (b) planes and roto-reflection axis.

The simplest system belonging to the D_{3h} symmetry group is the equilater triangle. The group operations are defined as in fig.B.1.

By applying some simple concepts of the group theory, one may generate basis functions with the desired symmetry starting from a chosen set of functions; here the case of a simple triangular molecule is considered and it is shown how to create appropriate basis functions by linear combination of the functions in a certain set. Molecular orbitals, that span irreducible representations of the point group, generally result from the linear combination of atomic orbitals. Moreover, molecular vibrations are represented by basis functions, the so called normal modes, that are constructed from unit vectors aligned along the x, y, z axis. In a similar way also the molecular rotations are obtained. In the end, it is shown how to find the electronic state for a given orbital occupation; this is also related to the electronic spin orientation that determines the final spin state.

B.2.1 Basis functions of s atomic orbitals

First of all consider the set of functions $\{\phi_A, \phi_B, \phi_C\}$, corresponding to three s-orbitals located at the vertices of the triangle. Under the symmetry operations, they behave as follows (each orbital contributes +1 if it remains in its original position, 0 otherwise):

E	$2C_3$	$3C_2$	σ_h	$2S_3$	$3\sigma_v$
3	0	1	3	0	1

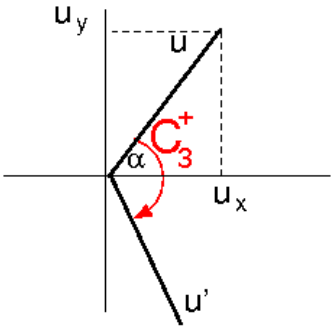

Figure B.2: Representation of the C_3^+rotation in the (x, y) plane.

This is a reducible representation Γ for the D_{3h} point group and it can be decomposed in a direct sum of irreducible representations Γ^α by applying eq.B.22 and eq.B.41. In this case, one finds that

$$\Gamma = \Gamma^{A_1^{'}} \oplus \Gamma^{E^{'}}. \tag{B.60}$$

Now one has to linearly combine the set of atomic orbitals $\{\phi_A, \phi_B, \phi_C\}$ to generate the basis functions with symmetry $A_1^{'}$ and $E^{'}$ respectively. To this extent eq.B.57 has to be used, hence one first applies the symmetry operations to ϕ_C chosen as *generator* and it results:

E	C_3^+	C_3^-	$C_2^{'}$	$C_2^{''}$	$C_2^{'''}$	σ_h	S_3^+	S_3^-	$\sigma_v^{'}$	$\sigma_v^{''}$	$\sigma_v^{'''}$
ϕ_C	ϕ_A	ϕ_B	ϕ_C	ϕ_A	ϕ_B	ϕ_C	ϕ_A	ϕ_B	ϕ_C	ϕ_A	ϕ_B

Then these functions are multiplied by the $\Gamma_{ij}^\alpha\left(G^{-1}\right)$ according to eq.B.57; within the D_{3h} point group such coefficients belong to unitary matrices with real elements thus the following holds

$$\Gamma_{ij}^\alpha\left(G^{-1}\right) = \Gamma_{ij}^{\alpha *}\left(G\right) = \Gamma_{ij}^\alpha\left(G\right)$$

Note that if α is a one-dimensional irreducible representation, then

$$\Gamma_{ij}^\alpha\left(G\right) = \chi^\alpha\left(G\right). \tag{B.61}$$

The basis function with $A_1^{'}$ symmetry finally reads as:

$$\Phi^{A_1^{'}} = \frac{1}{\sqrt{3}}\left(\phi_A + \phi_B + \phi_C\right). \tag{B.62}$$

Consider now the $E^{'}$ symmetry. The matrix representation of this two-dimensional irreducible representation is in the plane (x, y) and thus it describes how these vectors transform under the symmetry operations. By way of example, here the matrix representation for the C_3^+ (clockwise) rotation is shown in fig.B.2.
Hence, by applying C_3^+

$$\begin{aligned} u_x = \cos\alpha \rightarrow \cos\left(\alpha - \tfrac{2}{3}\pi\right) = -\tfrac{1}{2}\cos\alpha + \tfrac{\sqrt{3}}{2}\sin\alpha \\ u_y = \sin\alpha \rightarrow \sin\left(\alpha - \tfrac{2}{3}\pi\right) = -\tfrac{1}{2}\sin\alpha - \tfrac{\sqrt{3}}{2}\cos\alpha \end{aligned} \tag{B.63}$$

Thus,

$$\begin{vmatrix} -\frac{1}{2} & \frac{\sqrt{3}}{2} \\ -\frac{\sqrt{3}}{2} & -\frac{1}{2} \end{vmatrix}_{C_3^+}$$

In the same way all the other matrices can be obtained:

$$\begin{matrix} \begin{vmatrix} 1 & 0 \\ 0 & 1 \end{vmatrix}_{E,\sigma_h} & \begin{vmatrix} -\frac{1}{2} & \frac{\sqrt{3}}{2} \\ -\frac{\sqrt{3}}{2} & -\frac{1}{2} \end{vmatrix}_{C_3^+,S_3^+} & \begin{vmatrix} -\frac{1}{2} & -\frac{\sqrt{3}}{2} \\ \frac{\sqrt{3}}{2} & -\frac{1}{2} \end{vmatrix}_{C_3^-,S_3^-} \\ \begin{vmatrix} -1 & 0 \\ 0 & 1 \end{vmatrix}_{C_2',\sigma_v'} & \begin{vmatrix} \frac{1}{2} & \frac{\sqrt{3}}{2} \\ \frac{\sqrt{3}}{2} & -\frac{1}{2} \end{vmatrix}_{C_2'',\sigma_v''} & \begin{vmatrix} \frac{1}{2} & -\frac{\sqrt{3}}{2} \\ -\frac{\sqrt{3}}{2} & -\frac{1}{2} \end{vmatrix}_{C_2''',\sigma_v'''} \end{matrix} \tag{B.64}$$

As shown in eq.B.64, normally one may deal with only the symmetry elements E, C_3^+, C_3^-, C_2', C_2'',C_2''' as the remaining behave in the same way in the (x, y) plane. However, to generate basis functions with symmetry $E^{'}$, one needs the row vectors $\Gamma_{ij}^{E^{'}}(G)$; thus by choosing the first row of matrices in eq.B.64, namely $i = 1$ and $j = 1,\ 2$, it results

G	E	C_3^+	C_3^-	C_2'	C_2''	C_2'''
$\hat{\Gamma}(G)$	ϕ_C	ϕ_A	ϕ_B	ϕ_C	ϕ_A	ϕ_B
$\Gamma_{11}^{E^{'}}(G)$	1	$-\frac{1}{2}$	$-\frac{1}{2}$	-1	$\frac{1}{2}$	$\frac{1}{2}$
$\Gamma_{12}^{E^{'}}(G)$	0	$\frac{\sqrt{3}}{2}$	$-\frac{\sqrt{3}}{2}$	0	$\frac{\sqrt{3}}{2}$	$-\frac{\sqrt{3}}{2}$

and the sum over all G results in:

$$\begin{aligned} \Gamma_{11}^{E^{'}}: &\quad \Phi_1^{E^{'}} = 0 \\ \Gamma_{12}^{E^{'}}: &\quad \Phi_2^{E^{'}} = \sqrt{3}\,(\phi_A - \phi_B) \end{aligned} \tag{B.65}$$

The linear combination goes to zero for $\Gamma_{11}^{E^{'}}$, thus one may try with the second row of matrices in eq.B.64. Hence,

G	E	C_3^+	C_3^-	C_2'	C_2''	C_2'''
$\hat{\Gamma}(G)$	ϕ_C	ϕ_A	ϕ_B	ϕ_C	ϕ_A	ϕ_B
$\Gamma_{21}^{E^{'}}(G)$	0	$\frac{\sqrt{3}}{2}$	$-\frac{\sqrt{3}}{2}$	0	$\frac{\sqrt{3}}{2}$	$-\frac{\sqrt{3}}{2}$
$\Gamma_{22}^{E^{'}}(G)$	1	$-\frac{1}{2}$	$-\frac{1}{2}$	1	$-\frac{1}{2}$	$-\frac{1}{2}$

and again, the sum over G gives:

$$\begin{aligned} \Gamma_{21}^{E^{'}}: &\quad \Phi_1^{E^{'}} = \sqrt{3}\,(\phi_A - \phi_B) \\ \Gamma_{22}^{E^{'}}: &\quad \Phi_2^{E^{'}} = 2\phi_C - \phi_B - \phi_A \end{aligned} \tag{B.66}$$

Once normalized, the two basis function with symmetry $E^{'}$ appear as:

$$\begin{aligned} \Gamma_{21}^{E^{'}}: &\quad \Phi_1^{E^{'}} = \tfrac{1}{\sqrt{2}}\,(\phi_A - \phi_B) \\ \Gamma_{22}^{E^{'}}: &\quad \Phi_2^{E^{'}} = \tfrac{1}{\sqrt{6}}\,(2\phi_C - \phi_B - \phi_A) \end{aligned} \tag{B.67}$$

In fig.B.3 the basis functions for the *s*-orbitals are reported.

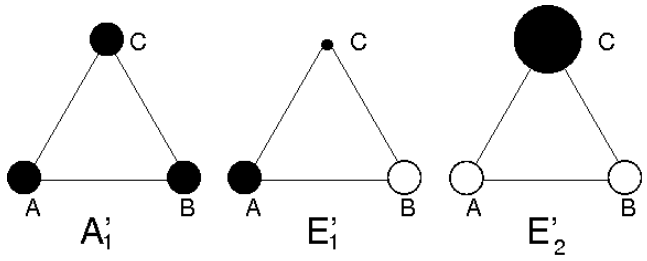

Figure B.3: Basis functions arising from the linear combination of s-orbitals for a triatomic system within the D_{3h} point group.

B.2.2 Basis functions of p_z atomic orbitals

In the same way, upon choosing a set of functions $\{\phi_A,\ \phi_B,\ \phi_C\}$, corresponding to three p_z-orbitals located at the vertices of the triangle, one first has to check how they behave under the symmetry operations,

E	$2C_3$	$3C_2$	σ_h	$2S_3$	$3\sigma_v$
3	0	-1	-3	0	1

Note that each orbital contributes +1 or -1 if it remains in its original position with respectively the same or opposite sign, 0 otherwise. This reducible representation can be decomposed in the following direct sum,

$$\Gamma = \Gamma^{A_2''} \oplus \Gamma^{E''}. \tag{B.68}$$

To generate the basis functions with symmetry A_2'' and E'' one has to linearly combine the set of atomic orbitals $\{\phi_A,\ \phi_B,\ \phi_C\}$ as shown in eq.B.57. By applying the symmetry operations to ϕ_C chosen as generator, it results:

E	C_3^+	C_3^-	C_2'	C_2''	C_2'''	σ_h	S_3^+	S_3^-	σ_v'	σ_v''	σ_v'''
ϕ_C	ϕ_A	ϕ_B	$-\phi_C$	$-\phi_A$	$-\phi_B$	$-\phi_C$	$-\phi_A$	$-\phi_B$	ϕ_C	ϕ_A	ϕ_B

Then these functions are multiplied by $\Gamma_{ij}^{\alpha}(G)$. Following from eq.B.61, the basis function with A_2'' symmetry is

$$\Phi^{A_2''} = \frac{1}{\sqrt{3}}\left(\phi_A + \phi_B + \phi_C\right). \tag{B.69}$$

To generate the two basis functions of E'' symmetry one can still use the 2×2 matrices for the (x, y) transformations under the symmetry operations in eq.B.64. Note that these matrices span the E' irreducible representation, thus they need to be 'adapted' to the E'' case. This can be simply done multiplying by -1 those matrices in E'' with 'opposite' character compared to E'. Now performing the steps described above for $i = 1$, one first gets

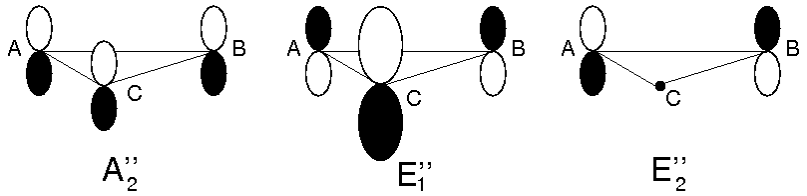

Figure B.4: Basis functions arising from the linear combination of p_z-orbitals for a triatomic system within the D_{3h} point group.

G	E	C_3^+	C_3^-	C_2'	C_2''	C_2'''	σ_h	S_3^+	S_3^-	σ_v'	σ_v''	σ_v'''
$\hat{\Gamma}(G)$	ϕ_C	ϕ_A	ϕ_B	$-\phi_C$	$-\phi_A$	$-\phi_B$	$-\phi_C$	$-\phi_A$	$-\phi_B$	ϕ_C	ϕ_A	ϕ_B
$\Gamma_{11}^{E''}(G)$	1	$-\frac{1}{2}$	$-\frac{1}{2}$	-1	$\frac{1}{2}$	$\frac{1}{2}$	-1	$\frac{1}{2}$	$\frac{1}{2}$	1	$-\frac{1}{2}$	$-\frac{1}{2}$
$\Gamma_{12}^{E''}(G)$	0	$\frac{\sqrt{3}}{2}$	$-\frac{\sqrt{3}}{2}$	0	$\frac{\sqrt{3}}{2}$	$-\frac{\sqrt{3}}{2}$	0	$\frac{\sqrt{3}}{2}$	$-\frac{\sqrt{3}}{2}$	0	$-\frac{\sqrt{3}}{2}$	$\frac{\sqrt{3}}{2}$

and then making the sum over all the G and normalizing:

$$\begin{array}{ll} \Gamma_{11}^{E''}: & \Phi_1^{E''} = 2\phi_C - \phi_B - \phi_A \rightarrow \frac{1}{\sqrt{6}}(2\phi_C - \phi_B - \phi_A) \\ \Gamma_{12}^{E''}: & \Phi_2^{E''} = \frac{1}{\sqrt{2}}(\phi_A - \phi_B) \end{array} \tag{B.70}$$

In fig.B.4 the basis functions for the p_z-orbitals are reported.

B.2.3 Basis functions of vibrational, rotational and translational modes

Also the analysis of the normal modes is based on eq.B.57. In this case, the natural choice is a set of unitary vectors $\{e_i^A, e_i^B, e_i^C\}_{i=1}^3$ aligned along x, y, z and centered respectively at the vertices A, B, C. At first, one has to describe the behaviour of these vectors under the symmetry operations,

E	$2C_3$	$3C_2$	σ_h	$2S_3$	$3\sigma_v$
9	0	-1	3	0	1

then this reducible representation needs to be decomposed in the following direct sum,

$$\Gamma = \Gamma^{A_1'} \oplus \Gamma^{A_2'} \oplus 2\Gamma^{E'} \oplus \Gamma^{A_2''} \oplus \Gamma^{E''}. \tag{B.71}$$

It contains not only the vibrational normal modes, but also translations and rotations. With the help of the table of characters it is possible to distinguish among them. The rotations, labeled as R_x, R_y and R_z in table B.1, span respectively the irreducible representation E'' and A_2'; the translations, labeled as x, y and z in table B.1, span respectively the irreducible representation E' and A_2''. In conclusion in addition to three rotational and three translational modes, three normal (vibrational) modes remain and they have A_1' and E' symmetry[3]. To generate basis functions with

[3]The number of normal modes in nonlinear molecules is $3N-6$ where N is the total number of atoms, three are the degree of freedom of each atom along the x, y, z, axis and six are the possible rigid rotations and translations of the molecule along the x, y, z, axis. In case of linear molecules, the number of normal modes is given by $3N-5$.

the appropriate symmetry one has to proceed in the same way as for s and p_z orbitals. Thus, at first a generator is chosen, in this case the vector e_1^C, and then it is transformed under the symmetry operations of the group. It belongs to the plane (x, y) and it is therefore expected to transform according to the matrices $E^{'}$ in eq.B.64. Again one may deal only with the first six symmetry elements since the last are exactly equivalent in the (x, y) plane and then obtain:

G	E	C_3^+	C_3^-	$C_2^{'}$	$C_2^{''}$	$C_2^{'''}$
$\hat{\Gamma}(G)$	e_1^C	$-\frac{1}{2}e_1^B - \frac{\sqrt{3}}{2}e_2^B$	$-\frac{1}{2}e_1^A + \frac{\sqrt{3}}{2}e_2^A$	$-e_1^C$	$\frac{1}{2}e_1^B + \frac{\sqrt{3}}{2}e_2^B$	$\frac{1}{2}e_1^A - \frac{\sqrt{3}}{2}e_2^A$

These elements are now multiplied by the corresponding character in the $A_1^{'}$ representation, $\chi^{A_1^{'}}(G)$; then they are summed over G and finally give $\Phi^{A_1^{'}} = 0$. This simply means that e_1^C is not a good generator for this irreducible representation, hence one tries e_2^C and proceed as before. Note that the choice of e_2^C actually implies to choose the second column in the matrices $E^{'}$ in eq.B.64

G	E	C_3^+	C_3^-	$C_2^{'}$	$C_2^{''}$	$C_2^{'''}$
$\hat{\Gamma}(G)$	e_2^C	$\frac{\sqrt{3}}{2}e_1^B - \frac{1}{2}e_2^B$	$-\frac{\sqrt{3}}{2}e_1^A - \frac{1}{2}e_2^A$	e_2^C	$\frac{\sqrt{3}}{2}e_1^B - \frac{1}{2}e_2^B$	$-\frac{\sqrt{3}}{2}e_1^A - \frac{1}{2}e_2^A$

Hence,

$$\Phi^{A_1^{'}} = 2e_2^C + \sqrt{3}e_1^B - e_2^B - \sqrt{3}e_1^A - e_2^A. \tag{B.72}$$

After normalization,

$$\Phi^{A_1^{'}} = \frac{1}{\sqrt{12}}\left(2e_2^C + \sqrt{3}e_1^B - e_2^B - \sqrt{3}e_1^A - e_2^A\right). \tag{B.73}$$

For basis functions with $E^{'}$symmetry, one refers to the matrices in eq.B.64 and uses coefficients from the first row when the generator is e_1^C,

G	E	C_3^+	C_3^-	$C_2^{'}$	$C_2^{''}$	$C_2^{'''}$
$\hat{\Gamma}(G)$	e_1^C	$-\frac{1}{2}e_1^B - \frac{\sqrt{3}}{2}e_2^B$	$-\frac{1}{2}e_1^A + \frac{\sqrt{3}}{2}e_2^A$	$-e_1^C$	$\frac{1}{2}e_1^B + \frac{\sqrt{3}}{2}e_2^B$	$\frac{1}{2}e_1^A - \frac{\sqrt{3}}{2}e_2^A$
$\Gamma_{11}^{E^{'}}(G)$	1	$-\frac{1}{2}$	$-\frac{1}{2}$	-1	$\frac{1}{2}$	$\frac{1}{2}$
$\Gamma_{12}^{E^{'}}(G)$	0	$\frac{\sqrt{3}}{2}$	$-\frac{\sqrt{3}}{2}$	0	$\frac{\sqrt{3}}{2}$	$-\frac{\sqrt{3}}{2}$

Then the sum over all G reads as:

$$\begin{aligned}\Phi_1^{E^{'}} &= 2e_1^C + \tfrac{1}{2}e_1^B + \tfrac{\sqrt{3}}{2}e_2^B + \tfrac{1}{2}e_1^A - \tfrac{\sqrt{3}}{2}e_2^A \\ \Phi_2^{E^{'}} &= 0\end{aligned} \tag{B.74}$$

Again since $\Phi_2^{E^{'}} = 0$, one adopts the coefficients from the second row in eq.B.64 and thus uses the vector e_2^C as generator. From this choice, it follows

G	E	C_3^+	C_3^-	$C_2^{'}$	$C_2^{''}$	$C_2^{'''}$
$\hat{\Gamma}(G)$	e_2^C	$\frac{\sqrt{3}}{2}e_1^B - \frac{1}{2}e_2^B$	$-\frac{\sqrt{3}}{2}e_1^A - \frac{1}{2}e_2^A$	e_2^C	$\frac{\sqrt{3}}{2}e_1^B - \frac{1}{2}e_2^B$	$-\frac{\sqrt{3}}{2}e_1^A - \frac{1}{2}e_2^A$
$\Gamma_{21}^{E^{'}}(G)$	0	$\frac{\sqrt{3}}{2}$	$-\frac{\sqrt{3}}{2}$	0	$\frac{\sqrt{3}}{2}$	$-\frac{\sqrt{3}}{2}$
$\Gamma_{22}^{E^{'}}(G)$	1	$-\frac{1}{2}$	$-\frac{1}{2}$	1	$-\frac{1}{2}$	$-\frac{1}{2}$

$$\begin{aligned}\Phi_1^{E'} &= \tfrac{3}{2}e_1^B - \tfrac{\sqrt{3}}{2}e_2^B + \tfrac{3}{2}e_1^A + \tfrac{\sqrt{3}}{2}e_2^A \\ \Phi_2^{E'} &= 2e_2^C - \tfrac{\sqrt{3}}{2}e_1^B + \tfrac{1}{2}e_2^B + \tfrac{\sqrt{3}}{2}e_1^A + \tfrac{1}{2}e_2^A\end{aligned} \tag{B.75}$$

These two vibrational coordinates transform into each other but contain also translations along x and y axis, since they span the same irreducible representation E'. Therefore, they are of the form

$$\Phi_i = \alpha\Phi_i^V + \beta\Phi_i^T \tag{B.76}$$

where $\left(\Phi_1^T, \Phi_2^T\right)$ are translational coordinates, α and β are coefficients independent on i. The latter reads as

$$\Phi_1^T = \frac{1}{\sqrt{3}}\left(e_1^A + e_1^B + e_1^C\right) \tag{B.77}$$

$$\Phi_2^T = \frac{1}{\sqrt{3}}\left(e_2^A + e_2^B + e_2^C\right) \tag{B.78}$$

Using the scalar product in the configuration space ($\mathbb{R}^6$ in plane or $\mathbb{R}^9$ in general), it results

$$\beta = \Phi_1^*\Phi_1^T = \frac{3}{2\sqrt{3}} + \frac{3}{2\sqrt{3}} = \sqrt{3} \equiv \Phi_2^*\Phi_2^T \tag{B.79}$$

Hence,

$$\alpha\Phi_1^V = \Phi_1 - \sqrt{3}\Phi_1^T = \frac{1}{2}e_1^A + \frac{\sqrt{3}}{2}e_2^A + \frac{1}{2}e_1^B - \frac{\sqrt{3}}{2}e_2^B - e_1^C \tag{B.80}$$

$$\alpha\Phi_2^V = \Phi_2 - \sqrt{3}\Phi_2^T = \frac{\sqrt{3}}{2}e_1^A - \frac{1}{2}e_2^A - \frac{\sqrt{3}}{2}e_1^B - \frac{1}{2}e_2^B + e_2^C \tag{B.81}$$

These are the unnormalized vibrational coordinates; after normalization, they read as

$$\tilde{\Phi}_1^V = \frac{1}{\sqrt{3}}\left\{\frac{1}{2}e_1^A + \frac{\sqrt{3}}{2}e_2^A + \frac{1}{2}e_1^B - \frac{\sqrt{3}}{2}e_2^B - e_1^C\right\} = \frac{1}{\sqrt{3}}\begin{pmatrix} \frac{1}{2} \\ \frac{\sqrt{3}}{2} \\ \frac{1}{2} \\ -\frac{\sqrt{3}}{2} \\ -1 \\ 0 \end{pmatrix} \tag{B.82}$$

$$\tilde{\Phi}_2^V = \frac{1}{\sqrt{3}}\left\{\frac{\sqrt{3}}{2}e_1^A - \frac{1}{2}e_2^A - \frac{\sqrt{3}}{2}e_1^B - \frac{1}{2}e_2^B + e_2^C\right\} = \frac{1}{\sqrt{3}}\begin{pmatrix} \frac{\sqrt{3}}{2} \\ -\frac{1}{2} \\ -\frac{\sqrt{3}}{2} \\ -\frac{1}{2} \\ 0 \\ 1 \end{pmatrix} \tag{B.83}$$

where the latter are unit vectors in the six-dimensional configuration space appropriate for the triatomic system in $2D$, here modeled by the equilater triangle. The three normal modes are summarized in fig.B.5.

Up to here only the translational coordinates for displacements along the x and y axis within E'

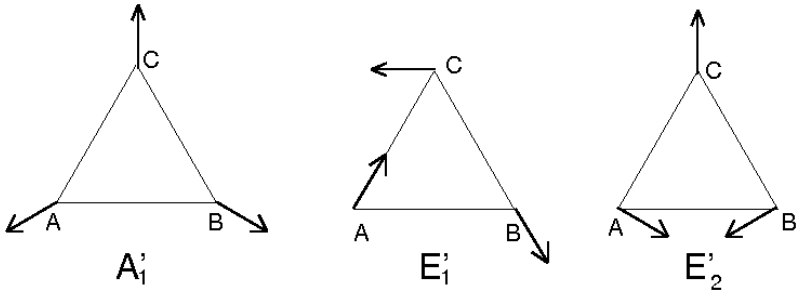

Figure B.5: Normal modes for a triatomic system with D_{3h} symmetry.

have been introduced. The displacement along the z axis spans the irreducible representation $A_2^{''}$. The choice of e_3^C as generator gives

G	E	C_3^+	C_3^-	$C_2^{'}$	$C_2^{''}$	$C_2^{'''}$	σ_h	S_3^+	S_3^-	$\sigma_v^{'}$	$\sigma_v^{''}$	$\sigma_v^{'''}$
$\hat{\Gamma}(G)$	e_3^C	e_3^B	e_3^A	$-e_3^C$	$-e_3^B$	$-e_3^A$	$-e_3^C$	$-e_3^B$	$-e_3^A$	e_3^C	e_3^B	e_3^A
$\chi^{A_2^{''}}(G)$	1	1	1	-1	-1	-1	-1	-1	-1	1	1	1

and the final normalized result is

$$\Phi_{T_z}^{A_2^{''}} = \frac{1}{\sqrt{3}}\left(e_3^C + e_3^B + e_3^A\right) \tag{B.84}$$

Finally the rotational coordinates are considered, that span the irreducible representations $A_2^{'}$, for the rotation around the z axis (R_z), and $E^{''}$, for the rotations around the x and y axis (R_x, R_y). For $A_2^{'}$ we choose again e_1^C as generator, since the rotation around the z axis takes place in the (x, y) plane. The behaviour of e_1^C under the symmetry operations reads as

G	E	C_3^+	C_3^-	$C_2^{'}$	$C_2^{''}$	$C_2^{'''}$
$\hat{\Gamma}(G)$	e_1^C	$-\frac{1}{2}e_1^B - \frac{\sqrt{3}}{2}e_2^B$	$-\frac{1}{2}e_1^A + \frac{\sqrt{3}}{2}e_2^A$	$-e_1^C$	$\frac{1}{2}e_1^B + \frac{\sqrt{3}}{2}e_2^B$	$\frac{1}{2}e_1^A - \frac{\sqrt{3}}{2}e_2^A$
$\chi^{A_2^{'}}(G)$	1	1	1	-1	-1	-1

Multiplying by the characters of $A_2^{'}$ and then summing, the rotation along z reads as,

$$\Phi_{R_z}^{A_2^{'}} = 2e_1^C - e_1^B - \sqrt{3}e_2^B - e_1^A + \sqrt{3}e_2^A \tag{B.85}$$

The two basis functions for the rotations R_x, R_y belong to the $E^{''}$ irreducible representation and, both have a component along the z axis. In this case, by selecting e_3^C as generator, one obtains

G	E	C_3^+	C_3^-	$C_2^{'}$	$C_2^{''}$	$C_2^{'''}$	σ_h	S_3^+	S_3^-	$\sigma_v^{'}$	$\sigma_v^{''}$	$\sigma_v^{'''}$
$\hat{\Gamma}(G)$	e_3^C	e_3^B	e_3^A	$-e_3^C$	$-e_3^B$	$-e_3^A$	$-e_3^C$	$-e_3^B$	$-e_3^A$	e_3^C	e_3^B	e_3^A
$\Gamma_{11}^{E^{''}}(G)$	1	$-\frac{1}{2}$	$-\frac{1}{2}$	-1	$\frac{1}{2}$	$\frac{1}{2}$	-1	$\frac{1}{2}$	$\frac{1}{2}$	-1	$\frac{1}{2}$	$\frac{1}{2}$
$\Gamma_{12}^{E^{''}}(G)$	0	$\frac{\sqrt{3}}{2}$	$-\frac{\sqrt{3}}{2}$	0	$\frac{\sqrt{3}}{2}$	$-\frac{\sqrt{3}}{2}$	0	$-\frac{\sqrt{3}}{2}$	$\frac{\sqrt{3}}{2}$	0	$\frac{\sqrt{3}}{2}$	$-\frac{\sqrt{3}}{2}$

$$\Phi_1^{E^{''}} = 2e_3^C - e_3^B - e_3^A \qquad \Phi_2^{E^{''}} = \sqrt{3}\left(e_3^B - e_3^A\right) \tag{B.86}$$

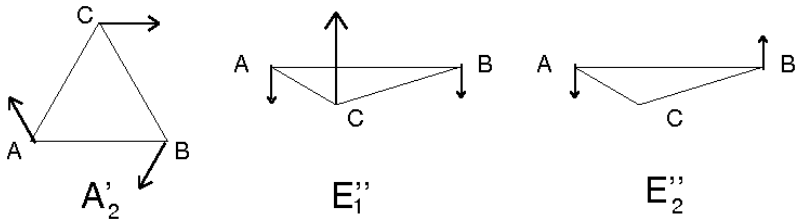

Figure B.6: Rotations for a triatomic system with D_{3h} symmetry.

After normalization,

$$\Phi_1^{E''} = \frac{1}{\sqrt{6}}\left(2e_3^C - e_3^B - e_3^A\right) \qquad \Phi_2^{E''} = \frac{1}{\sqrt{2}}\left(e_3^B - e_3^A\right). \tag{B.87}$$

In fig.B.6 all the rotations are summarized.

Some further comments can be done on the analysis just performed. For example, to get the contributions of the two degenerate vibrational coordinates (E') to a given distorted configuration, one refers to the vectors $\{u_A, u_B, u_C\}$ giving the displacement in the (x, y) plane of the atom A, B, and C respectively. They are defined as

$$u = \begin{pmatrix} u_A \\ u_B \\ u_C \end{pmatrix} = \begin{bmatrix} e_1^A - e_1^{A\star} \\ e_2^A - e_2^{A\star} \\ e_1^B - e_1^{B\star} \\ e_2^B - e_2^{B\star} \\ e_1^C - e_1^{C\star} \\ e_2^C - e_2^{C\star} \end{bmatrix} \tag{B.88}$$

where $\left(e_1^{A\star},\, e_2^{A\star},\, e_1^{B\star},\, e_2^{B\star},\, e_1^{C\star},\, e_2^{C\star}\right)$ is a reference symmetric configuration. Given u, the two contributions come from the scalar product between u itself and the vector corresponding to each vibration:

$$Q_1 = \left(\tilde{\Phi}_1^V\right)^t u \qquad Q_2 = \left(\tilde{\Phi}_2^V\right)^t u \tag{B.89}$$

The path $u(q)$, where $q \in \mathbb{R}$ depends on all the coordinates affecting the system, has thus a projection on the E' plane generated by the two orthogonal vibrations $\tilde{\Phi}_1^V$ and $\tilde{\Phi}_2^V$

$$u_{E'}(q) = Q_1(q)\,\tilde{\Phi}_1^V + Q_2(q)\,\tilde{\Phi}_2^V \tag{B.90}$$

Note that the symmetric displacement with symmetry A_1' gives $u_{E'}(q) = 0$, namely its projection onto the E' plane of the two non-symmetric normal modes is null. More generally, $Q_\perp$ is any other coordinate orthogonal to the space E'spanned by the two vibrations, hence it can be the symmetric stretching (A_1'), a rotation around the x or y axis (E''), a rotation (A_2') or a translation around the z axis (A_2''). For a triatomic system only the symmetric stretching may affect the energy. This

possibility implies that many different curves could be obtained for the same path, depending on the values of the other coordinates (in this case the components $Q_\perp$ representing the symmetric stretching). In particular one is often interested in the conical intersection point, which is placed at the crossing of the two axis Q_1 and Q_2. The position of this point may result by minimizing the energy of the system with respect to all the coordinates $Q_\perp$ for $Q_1 = Q_2 = 0$.

B.2.4 Spin state symmetry

A slightly more subtle question is how to predict the spin state of an electronic system with a certain spatial symmetry, depending of course on the orbitals occupied but also on the presence of degeneracy. In general the overall electronic state is obtained by the direct product among the irreducible representations correponding to occupied orbitals. This procedure is straightforward if no degenerate orbitals are included, otherwise it is rather more complicated. A concrete example may help to clarify this concept. Consider again the triatomic system with D_{3h} symmetry and suppose it has four electrons distributed in the orbitals as follows

$$a_1^{'}(2)e^{'}(n_1)a_2^{''}(n_2) \tag{B.91}$$

where $a_1^{'}$ and $e^{'}$ are the in plane σ orbitals derived respectively in eq.B.62 and eq.B.67, $a_2^{''}$ is the lowest lying π orbital derived in eq.B.69, and n_1 and n_2 are integers giving the orbital occupation. Three different scenarios can arise from eq.B.91: (i) $n_1 = n_2 = 1$; (ii) $n_1 = 0$ and $n_2 = 2$; (iii) $n_1 = 2$ and $n_2 = 0$. The direct product of close-shell orbitals (doubly occupied) gives always the totally symmetric representation $A_1^{'}$, thus the electronic configuration is simply determined by the partially occupied orbitals. In the first case,

$$n_1 = n_2 = 1 \longrightarrow e^{'}a_2^{''} = E^{''} \tag{B.92}$$

the two electrons may align with parallel or antiparallel spin and finally give the electronic spin state $^{1,3}E^{''}$. The second scenario reduces to a close-shell case, indeed no fractional occupation is present, and as expected it turns out to be

$$n_1 = 0,\ n_2 = 2 \longrightarrow \left(a_2^{''}\right)^2 = A_1^{'} \tag{B.93}$$

where only the singlet alignment is allowed, $^1A_1^{'}$. The last case shows degenerate orbitals with a partial occupation, where the direct product $e^{'}e^{'}$ generates a reducible representation Γ,

D_{3h}	E	$2C_3$	$3C_2$	σ_h	$2S_3$	$3\sigma_v$
$e^{'}$	2	-1	0	2	-1	0
$\left(e^{'}\right)^2$	4	1	0	4	1	0

that can be decomposed into pure symmetry components by using eq.B.41

$$\Gamma = \Gamma^{A_1^{'}} \oplus \Gamma^{A_2^{'}} \oplus \Gamma^{E^{'}}. \tag{B.94}$$

To attribute the correct spin state (singlet or triplet) to the spatial simmetries $A_1^{'}$, $A_2^{'}$ and $E^{'}$, we need to use a projector $\hat{P}$, similar to that already introduced in eq.B.57

$$\hat{P}_{\Gamma_\alpha} = \sum_G \chi_{\Gamma^\alpha}(G)\,\hat{\Gamma}(G) \tag{B.95}$$

This projector, applied to a determinantal function of the form $|\phi_i\phi_j|$, generates a sum of determinants with coefficients given by the corresponding matrix representation for α:

$$\hat{P}_{\Gamma_\alpha}|\phi_i\phi_j| = \sum_G \sum_{kl} \chi_{\Gamma^\alpha}(G)\,\Gamma_{ik}(G)\,\Gamma_{jl}(G)\,|\phi_k\phi_l|\,. \tag{B.96}$$

Coming back to the $e^{'}e^{'}$ problem, we start investigating the triplet case applying the projector to $\left|e_1^{'}\alpha e_2^{'}\alpha\right|$:

$$\begin{aligned}\hat{P}_{\Gamma_\alpha}\left|e_1^{'}\alpha e_2^{'}\alpha\right| = \sum_G \chi_{\Gamma^\alpha}(G)\Big\{&\Gamma_{11}(G)\,\Gamma_{21}(G)\left|e_1^{'}\alpha e_1^{'}\alpha\right| + \Gamma_{11}(G)\,\Gamma_{22}(G)\left|e_1^{'}\alpha e_2^{'}\alpha\right| + \\ &+\Gamma_{12}(G)\,\Gamma_{21}(G)\left|e_2^{'}\alpha e_1^{'}\alpha\right| + +\Gamma_{12}(G)\,\Gamma_{22}(G)\left|e_2^{'}\alpha e_2^{'}\alpha\right|\Big\}\end{aligned} \tag{B.97}$$

Thus, excluding the first and the last term because of the Pauli exclusion principle, eq.B.97 reduces to

$$\hat{P}_{\Gamma_\alpha}\left|e_1^{'}\alpha e_2^{'}\alpha\right| = \sum_G \chi_{\Gamma^\alpha}(G)\left(\Gamma_{11}(G)\,\Gamma_{22}(G) - \Gamma_{12}(G)\,\Gamma_{21}(G)\right)\left|e_1^{'}\alpha e_2^{'}\alpha\right|. \tag{B.98}$$

In a similar way, the projector applied on $\left|e_1^{'}\beta e_2^{'}\beta\right|$ gives

$$\hat{P}_{\Gamma_\alpha}\left|e_1^{'}\beta e_2^{'}\beta\right| = \sum_G \chi_{\Gamma^\alpha}(G)\left(\Gamma_{11}(G)\,\Gamma_{22}(G) - \Gamma_{12}(G)\,\Gamma_{21}(G)\right)\left|e_1^{'}\beta e_2^{'}\beta\right|. \tag{B.99}$$

Finally the use of $\frac{1}{\sqrt{2}}\left\{\left|e_1^{'}\alpha e_2^{'}\beta\right| + \left|e_1^{'}\beta e_2^{'}\alpha\right|\right\}$ as generator gives

$$\begin{aligned}&\hat{P}_{\Gamma_\alpha}\tfrac{1}{\sqrt{2}}\left\{\left|e_1^{'}\alpha e_2^{'}\beta\right| + \left|e_1^{'}\beta e_2^{'}\alpha\right|\right\} = \\ &\textstyle\sum_G \chi_{\Gamma^\alpha}(G)\left(\Gamma_{11}(G)\,\Gamma_{22}(G) - \Gamma_{12}(G)\,\Gamma_{21}(G)\right)\tfrac{1}{\sqrt{2}}\left\{\left|e_1^{'}\alpha e_2^{'}\beta\right| + \left|e_1^{'}\beta e_2^{'}\alpha\right|\right\}\end{aligned} \tag{B.100}$$

Now, looking at the matrix elements within the $E^{'}$ irreducible representation in eq.B.64, one computes the coefficients for each symmetry operations in the triplet wavefunctions. Setting $A(G) = \Gamma_{11}(G)\,\Gamma_{22}(G)$ and $B(G) = \Gamma_{12}(G)\,\Gamma_{21}(G)$, it results

G	E	C_3^+	C_3^-	$C_2^{'}$	$C_2^{''}$	$C_2^{'''}$
A	1	$\frac{1}{4}$	$\frac{1}{4}$	-1	$-\frac{1}{4}$	$-\frac{1}{4}$
B	0	$-\frac{3}{4}$	$-\frac{3}{4}$	0	$\frac{3}{4}$	$\frac{3}{4}$
$A-B$	1	1	1	-1	-1	-1

Then multiplying the quantity $A(G) - B(G)$ by the characters of the irreducible representations $A_1^{'}$, $A_2^{'}$ and $E^{'}$, it follows

G	E	$2C_3$	$3C_2$	σ_h	$2S_3$	$3\sigma_v$	Sum
$A-B$	1	1	-1	1	1	-1	
$\chi^{A_1^{'}}(A-B)$	1	1	-1	1	1	-1	0
$\chi^{A_2^{'}}(A-B)$	1	1	1	1	1	1	12
$\chi^{E^{'}}(A-B)$	2	-1	0	2	-1	0	0

and a nonzero coefficient results only for $A_2^{'}$. This allows to conclude that the triplet function is of pure ${}^3A_2^{'}$ symmetry and after normalization it becomes

$$\Phi^{A_2^{'}} = \frac{1}{\sqrt{2}}\left\{\left|e_1^{'}\alpha e_2^{'}\beta\right| + \left|e_1^{'}\beta e_2^{'}\alpha\right|\right\} \tag{B.101}$$

Now the singlet state is studied, starting with $\left|e_1^{'}\alpha e_1^{'}\beta\right|$ as generator,

$$\begin{aligned}\hat{P}_{\Gamma_\alpha}\left|e_1^{'}\alpha e_1^{'}\beta\right| = \sum_G \chi^{\Gamma^\alpha}(G)\Big\{&\Gamma_{11}(G)\,\Gamma_{11}(G)\left|e_1^{'}\alpha e_1^{'}\beta\right| + \\ &+\Gamma_{12}(G)\,\Gamma_{12}(G)\left|e_2^{'}\alpha e_2^{'}\beta\right| + \Gamma_{11}(G)\,\Gamma_{12}(G)\left(\left|e_1^{'}\alpha e_2^{'}\beta\right| - \left|e_1^{'}\beta e_2^{'}\alpha\right|\right)\Big\}\end{aligned} \tag{B.102}$$

then with $\left|e_2^{'}\alpha e_2^{'}\beta\right|$,

$$\begin{aligned}\hat{P}_{\Gamma_\alpha}\left|e_2^{'}\alpha e_2^{'}\beta\right| = \sum_G \chi^{\Gamma^\alpha}(G)\Big\{&\Gamma_{21}(G)\,\Gamma_{21}(G)\left|e_1^{'}\alpha e_1^{'}\beta\right| + \\ &\Gamma_{22}(G)\,\Gamma_{22}(G)\left|e_2^{'}\alpha e_2^{'}\beta\right| + \Gamma_{22}(G)\,\Gamma_{21}(G)\left(\left|e_1^{'}\alpha e_2^{'}\beta\right| - \left|e_1^{'}\beta e_2^{'}\alpha\right|\right)\Big\}\end{aligned} \tag{B.103}$$

and finally with $\frac{1}{\sqrt{2}}\left(\left|e_1^{'}\alpha e_2^{'}\beta\right| - \left|e_1^{'}\beta e_2^{'}\alpha\right|\right)$

$$\begin{aligned}&\hat{P}_{\Gamma_\alpha}\tfrac{1}{\sqrt{2}}\left\{\left|e_1^{'}\alpha e_2^{'}\beta\right| - \left|e_1^{'}\beta e_2^{'}\alpha\right|\right\} = \\ &= \textstyle\sum_G \chi^{\Gamma^\alpha}(G)\Big\{\sqrt{2}\Gamma_{11}(G)\,\Gamma_{21}(G)\left|e_1^{'}\alpha e_1^{'}\beta\right| + \sqrt{2}\Gamma_{12}(G)\,\Gamma_{22}(G)\left|e_2^{'}\alpha e_2^{'}\beta\right| + \\ &+\tfrac{1}{\sqrt{2}}\left(\Gamma_{11}(G)\,\Gamma_{22}(G) + \Gamma_{12}(G)\,\Gamma_{21}(G)\right)\left(\left|e_1^{'}\alpha e_2^{'}\beta\right| - \left|e_1^{'}\beta e_2^{'}\alpha\right|\right)\Big\}.\end{aligned} \tag{B.104}$$

Afterwards, proceeding as before, one looks at the three singlet wavefuctions. In the first case, it is

G	E	C_3^+	C_3^-	$C_2^{'}$	$C_2^{''}$	$C_2^{'''}$
Γ_{11}^2	1	$\frac{1}{4}$	$\frac{1}{4}$	1	$\frac{1}{4}$	$\frac{1}{4}$
Γ_{12}^2	0	$\frac{3}{4}$	$\frac{3}{4}$	0	$\frac{3}{4}$	$\frac{3}{4}$
$\Gamma_{11}\Gamma_{12}$	0	$-\frac{\sqrt{3}}{4}$	$\frac{\sqrt{3}}{4}$	0	$\frac{\sqrt{3}}{4}$	$-\frac{\sqrt{3}}{4}$

then by multiplication with the characters of the irreducible representations $A_1^{'}$, $A_2^{'}$ and $E^{'}$, it follows

G	E	C_3^+	C_3^-	C_2'	C_2''	C_2'''	$2 \cdot Sum$
$\chi^{A_1'}\Gamma_{11}^2$	1	$\frac{1}{4}$	$\frac{1}{4}$	1	$\frac{1}{4}$	$\frac{1}{4}$	6
$\chi^{A_1'}\Gamma_{12}^2$	0	$\frac{3}{4}$	$\frac{3}{4}$	0	$\frac{3}{4}$	$\frac{3}{4}$	6
$\chi^{A_1'}\Gamma_{11}\Gamma_{12}$	0	$-\frac{\sqrt{3}}{4}$	$\frac{\sqrt{3}}{4}$	0	$\frac{\sqrt{3}}{4}$	-$\frac{\sqrt{3}}{4}$	0

G	E	C_3^+	C_3^-	C_2'	C_2''	C_2'''	$2 \cdot Sum$
$\chi^{A_2'}\Gamma_{11}^2$	1	$\frac{1}{4}$	$\frac{1}{4}$	-1	$-\frac{1}{4}$	$-\frac{1}{4}$	0
$\chi^{A_2'}\Gamma_{12}^2$	0	$\frac{3}{4}$	$\frac{3}{4}$	0	$-\frac{3}{4}$	$-\frac{3}{4}$	0
$\chi^{A_2'}\Gamma_{11}\Gamma_{12}$	0	$-\frac{\sqrt{3}}{4}$	$\frac{\sqrt{3}}{4}$	0	$-\frac{\sqrt{3}}{4}$	$\frac{\sqrt{3}}{4}$	0

G	E	C_3^+	C_3^-	C_2'	C_2''	C_2'''	$2 \cdot Sum$
$\chi^{E'}\Gamma_{11}^2$	2	$-\frac{1}{4}$	$-\frac{1}{4}$	1	0	0	3
$\chi^{E'}\Gamma_{12}^2$	0	$-\frac{3}{4}$	$-\frac{3}{4}$	0	0	0	-3
$\chi^{E'}\Gamma_{11}\Gamma_{12}$	0	$\frac{\sqrt{3}}{4}$	$-\frac{\sqrt{3}}{4}$	0	0	0	0

Note that the final sum is multiplied by a factor of two just to account for the remaining six symmetry elements. Nonzero coefficients have been found for the irreducible representations A_1' and E', which can thus be labeled as ${}^1A_1'$ and ${}^1E'$. After normalization they can be written as

$$\Phi^{A_1'} = \frac{1}{\sqrt{2}}\left\{\left|e_1'\alpha e_1'\beta\right| + \left|e_2'\alpha e_2'\beta\right|\right\} \tag{B.105}$$

$$\Phi^{E'} = \frac{1}{\sqrt{2}}\left\{\left|e_1'\alpha e_1'\beta\right| - \left|e_2'\alpha e_2'\beta\right|\right\} \tag{B.106}$$

Likewise, for the second case one finds nonzero coefficients only for the irreducible representations A_1' and E', which can thus be labeled as ${}^1A_1'$ and ${}^1E'$. After normalization the functions can be written as

$$\Phi^{A_1'} = \frac{1}{\sqrt{2}}\left\{\left|e_1'\alpha e_1'\beta\right| + \left|e_2'\alpha e_2'\beta\right|\right\} \tag{B.107}$$

$$\Phi_1^{E'} = \frac{1}{\sqrt{2}}\left\{\left|e_2'\alpha e_2'\beta\right| - \left|e_1'\alpha e_1'\beta\right|\right\} \tag{B.108}$$

In the end, the last singlet fuctions gives,

G	E	C_3^+	C_3^-	C_2'	C_2''	C_2'''
$\Gamma_{11}\Gamma_{21}$	0	$\frac{\sqrt{3}}{4}$	$-\frac{\sqrt{3}}{4}$	0	$\frac{\sqrt{3}}{4}$	$-\frac{\sqrt{3}}{4}$
$\Gamma_{22}\Gamma_{12}$	0	$-\frac{\sqrt{3}}{4}$	$\frac{\sqrt{3}}{4}$	0	$-\frac{\sqrt{3}}{4}$	$\frac{\sqrt{3}}{4}$
$\Gamma_{11}\Gamma_{22}$	1	$\frac{1}{4}$	$\frac{1}{4}$	-1	$-\frac{1}{4}$	$-\frac{1}{4}$
$\Gamma_{12}\Gamma_{21}$	0	$-\frac{3}{4}$	$-\frac{3}{4}$	0	$\frac{3}{4}$	$\frac{3}{4}$

then by multiplication with the characters of the irreducible representations $A_1^{'}$, $A_2^{'}$ and $E^{'}$

G	E	C_3^+	C_3^-	$C_2^{'}$	$C_2^{''}$	$C_2^{'''}$	$2 \cdot Sum$
$\chi^{A_1^{'}}\Gamma_{11}\Gamma_{21}$	0	$\frac{\sqrt{3}}{4}$	$-\frac{\sqrt{3}}{4}$	0	$\frac{\sqrt{3}}{4}$	$-\frac{\sqrt{3}}{4}$	0
$\chi^{A_1^{'}}\Gamma_{22}\Gamma_{12}$	0	$-\frac{\sqrt{3}}{4}$	$\frac{\sqrt{3}}{4}$	0	$-\frac{\sqrt{3}}{4}$	$\frac{\sqrt{3}}{4}$	0
$\chi^{A_1^{'}}\Gamma_{11}\Gamma_{22}$	1	$\frac{1}{4}$	$\frac{1}{4}$	-1	$-\frac{1}{4}$	$-\frac{1}{4}$	0
$\chi^{A_1^{'}}\Gamma_{12}\Gamma_{21}$	0	$-\frac{3}{4}$	$-\frac{3}{4}$	0	$\frac{3}{4}$	$\frac{3}{4}$	0

G	E	C_3^+	C_3^-	$C_2^{'}$	$C_2^{''}$	$C_2^{'''}$	$2 \cdot Sum$
$\chi^{A_2^{'}}\Gamma_{11}\Gamma_{21}$	0	$\frac{\sqrt{3}}{4}$	$-\frac{\sqrt{3}}{4}$	0	$-\frac{\sqrt{3}}{4}$	$\frac{\sqrt{3}}{4}$	0
$\chi^{A_2^{'}}\Gamma_{22}\Gamma_{12}$	0	$-\frac{\sqrt{3}}{4}$	$\frac{\sqrt{3}}{4}$	0	$\frac{\sqrt{3}}{4}$	$-\frac{\sqrt{3}}{4}$	0
$\chi^{A_2^{'}}\Gamma_{11}\Gamma_{22}$	1	$\frac{1}{4}$	$\frac{1}{4}$	1	$\frac{1}{4}$	$\frac{1}{4}$	6
$\chi^{A_2^{'}}\Gamma_{12}\Gamma_{21}$	0	$-\frac{3}{4}$	$-\frac{3}{4}$	0	$-\frac{3}{4}$	$-\frac{3}{4}$	-6

G	E	C_3^+	C_3^-	$C_2^{'}$	$C_2^{''}$	$C_2^{'''}$	$2 \cdot Sum$
$\chi^{E^{'}}\Gamma_{11}\Gamma_{21}$	0	$-\frac{\sqrt{3}}{4}$	$\frac{\sqrt{3}}{4}$	0	0	0	0
$\chi^{E^{'}}\Gamma_{22}\Gamma_{12}$	0	$\frac{\sqrt{3}}{4}$	$-\frac{\sqrt{3}}{4}$	0	0	0	0
$\chi^{E^{'}}\Gamma_{11}\Gamma_{22}$	2	$\frac{1}{4}$	$\frac{1}{4}$	0	0	0	3
$\chi^{E^{'}}\Gamma_{12}\Gamma_{21}$	0	$\frac{3}{4}$	$\frac{3}{4}$	0	0	0	3

Nonzero coefficients have been found for the irreducible representations $A_2^{'}$ and $E^{'}$. But in the first case the function vanishes as the two coefficients cancel, thus after normalization the function reads as

$$\Phi_2^{E^{'}} = \frac{1}{\sqrt{2}} \left\{ \left| e_1^{'} \alpha e_2^{'} \beta \right| - \left| e_1^{'} \beta e_2^{'} \alpha \right| \right\} \tag{B.109}$$

thus again one finds[1] $E^{'}$.

In summary the application of the projector in eq.B.96 to suitable determinantal functions gives, for the triplet state

- ${}^3A_2^{'} = \left\{ \left| e_1^{'} \alpha e_2^{'} \alpha \right| ; \left| e_1^{'} \beta e_2^{'} \beta \right| ; \frac{1}{\sqrt{2}} \left[\left| e_1^{'} \alpha e_2^{'} \beta \right| + \left| e_1^{'} \beta e_2^{'} \alpha \right| \right] \right\}$

while for the singlet state

- ${}^1A_1^{'} = \frac{1}{\sqrt{2}} \left[\left| e_1^{'} \alpha e_1^{'} \beta \right| + \left| e_2^{'} \alpha e_2^{'} \beta \right| \right]$
- ${}^1E^{'} = \frac{1}{\sqrt{2}} \left[\left| e_1^{'} \alpha e_1^{'} \beta \right| - \left| e_2^{'} \alpha e_2^{'} \beta \right| \right]$ $\qquad$ ${}^1E^{''} = \frac{1}{\sqrt{2}} \left[\left| e_1^{'} \alpha e_2^{'} \beta \right| - \left| e_1^{'} \beta e_2^{'} \alpha \right| \right]$.

In conclusion, this section showed the scheme to generate determinantal wavefuctions with the correct spatial and spin symmetry in the presence of partially occupied degenerate orbitals. In the first step, one has to perform the direct product of the open shell orbitals, that gives rise to a

configuration spanning the Γ representation. This is reducible, thus the second step is the spectral analysis of Γ to find the spatial symmetry components, namely the irreducible representations that form Γ. Finally, once the possible spatial symmetries are known, one has to form determinantal wavefunctions for each spin state. Note that not all the space-spin symmetry combinations are allowed, indeed some vanish due to the antisymmetry as embodied in the determinants. This is indeed the case of the above example where the ${}^1A_2'$, ${}^3A_1'$, ${}^3E'$ configurations do not appear. However, when non equivalent sets of degenerate orbitals are used, e.g. orbitals with symmetry e' and e'', none option is excluded, thus the spatial symmetries in the direct product may sustain any spin configurations.

Appendix C

ab initio molecular dynamics

Molecular dynamics (MD) simulations allow one to follow the time evolution of a given system and thus to get a description at atomic level of the processes that occur, like chemical reactions and physical transformations. The crucial point in any molecular dynamics scheme is the description of the interatomic interactions. Typically the full potential is splitted in a sum of many terms, accounting for two-body and many-body interactions, short-range and long-range interactions, electrostatic and non-electrostatic interactions, ... The traditional route in molecular dynamics is to determine these terms in advance, before starting the simulation. Anyway one has to be aware that the use of a fixed predefined potential implies serious drawbacks especially in dealing with *chemically complex* systems, that are made by many different types of atoms and molecules, with a huge number of interactions to parameterize. Moreover, if modifications in the electronic structure as well as in the bonding pattern occur during the course of the simulation, the initial parameters may turn out to be uncorrect. Similarly, any small modification of the system, for instance the substitution of one atomic species, usually is accompained by huge efforts to update the potential terms, as the potential parameters are defined for a specific system.

Another point of view in the traditional molecular dynamics is given by a class of methodologies where a global potential energy surface is built in a first step either empirically, semi-empirically or based on electronic structure calculations. Then it is fitted to a suitable analytical form and finally the dynamics evolution of the nuclei along this surface is generated according to a classical, quasi-classical or quantum-mechanical model. The main task within this framework is the construction of the potential energy surface which is done by mapping the space of the coordinates and may be extremely demanding from the computational point view. In principle given an unconstrained N body system, 3N-6 degrees of freedom need to be investigated; by including at least 10 points along each coordinate, the number of calculations required is in the order of 10^{3N-6}.

The field of traditional molecular dynamics was extended by a family of techniques known as *ab initio* molecular dynamics (AIMD). The novelty in AIMD relies on the way to handle the potential energy. Indeed in this case the dynamics of the system is not guided by a predefined potential but the forces acting on the nuclei are determined on-the-fly via electronic structure calculations as the trajectory is generated. In this way the electronic variables become active degrees of freedom

with interaction potentials computed at each step of the simulation. This allows one to follow the evolution of chemically complex systems as well as of those which drastically change their electronic structure during the dynamics. Anyway this also implies that the approximation is shifted from the way to introduce the potential terms to the way to solve the electronic structure. In fact AIMD makes the connection between classical molecular dynamics based on the Newton's equations and *ab initio* electronic structure calculations based on the approximated solution of the Schrodinger equation mainly via Hartree-Fock or density functional theory schemes. Apart from its clear advantages, the *ab initio* foundation of molecular dynamics comes along with shorter correlation lenghts and relaxation times compared to the ones affordable in the classical framework; furthermore it excludes the possibility to get a clear physical picture as well as to drive the processes by playing with the potential parameters. On the other hand, the lack of a predefined physical model allows one to see the real physics of a system with possibly unforeseen phenomena.
In many cases a rough estimate of the computational cost of a dynamics simulation can be useful to evaluate wheter it is convenient or not the use of one method rather another one. To this end suppose that in an AIMD simulation 10^n independent trajectories are necessary to statistically sample over the initial conditions; in addition 10^M steps are needed for each trajectory. It thus results that 10^{M+n} steps have to be done. Then, in the assumption that a single step in AIMD costs (computationally) as much as a single-point electronic structure calculation, it is possible to compare AIMD and molecular dynamics methods based on the preliminary construction of the potential energy surface. Naturally, the size of the system, i.e. the number of atoms N, is the decisive factor in the construction of a potential energy surface: for large N, this can be done only by lowering the dimensionality of the surface, thus reducing the number of degrees of freedom through the introduction of some constraints. On the other hand, in ab initio molecular dynamics the computational time is imposed by the statistical accuracy in terms of number of trajectories and number of steps in each trajectory. In summary for sufficiently small systems, computing the potential energy surface is preferable than following trajectories on-the-fly and it scales as 10^{M+n}; by contrast for systems large and complex enough, AIMD is favoured by a factor of $\sim 10^N$.

C.1 Derivation of classical molecular dynamics

The aim of this section is to show how the basic concepts of *classical* molecular dynamics, namely the Newton's equation and the potential energy in which nuclei move, may be derived from the Schrödinger equation. Note that two alternative approaches may be followed in such derivation and in both of them nuclei need to be approximated as classical particles. The starting point is the non-relativistic time-dependent Schrödinger equation

$$i\hbar\frac{\partial}{\partial t}\Phi\left(\mathbf{r},\mathbf{R},t\right)=\mathcal{H}\Phi\left(\mathbf{r},\mathbf{R},t\right) \tag{C.1}$$

where the wavefunction Φ depends on the electronic and nuclear coordinates, carried by the vectors $\mathbf{r}$ and $\mathbf{R}$, and on the time t. The full hamiltonian operator $\mathcal{H}$ is defined as

$$\mathcal{H} = -\sum_{I}^{N_{at}} \frac{1}{2M_I}\nabla_I^2 + \mathcal{E}\left(\mathbf{R}\right) \tag{C.2}$$

where the first term provides the kinetic energy of the nuclei in the potential $\mathcal{E}\left(\mathbf{R}\right)$. The total electronic energy $\mathcal{E}$ is evaluated for a given nuclear configuration by applying the electronic hamiltonian operator[1]. The exact solution of the corresponding time-independent electronic Schrödinger equation

$$\mathcal{H}_e\Psi_k\left(\mathbf{r},\mathbf{R}\right) = \mathcal{E}_k\left(\mathbf{R}\right)\Psi_k\left(\mathbf{r},\mathbf{R}\right) \tag{C.3}$$

is known for clamped nuclei at position $\{\mathbf{R}\}$. Here the spectrum of $\mathcal{H}_e$ is assumed to be descrete and the eigenfunctions to be orthonormalized. Once known all the adiabatic functions at all the nuclear coordinates $\{\mathbf{R}\}$, the total wavefunction can be expanded in terms of the complete set of eigenfunctions $\{\Psi_l\}$ of $\mathcal{H}_e$,

$$\Phi\left(\mathbf{r},\mathbf{R},t\right) = \sum_{l=0}^{\infty}\Psi_l\left(\mathbf{r},\mathbf{R}\right)\chi_l\left(\mathbf{R},t\right) \tag{C.4}$$

where the nuclear wavefunctions $\{\chi_l\}$ may be interpreted as time-dependent weighting coefficients. By using eq.C.4 in the time-dependent Schröndinger equation, after multiplication by $\Psi_k^*\left(\mathbf{r},\mathbf{R}\right)$ and integration over the electronic coordinates $\mathbf{r}$, a set of coupled equations is obtained

$$\left[-\sum_{I}^{N_{at}}\frac{1}{2M_I}\nabla_I^2 + \mathcal{E}_k\left(\mathbf{R}\right)\right]\chi_k + \sum_{l}C_{kl}\chi_l = i\hbar\frac{\partial}{\partial t}\chi_k \tag{C.5}$$

where $\mathcal{E}_k$ includes the electronic energy and the nuclear repulsion for a given configuration, and C_{kl} is the exact nonadiabatic coupling operator[2]. If one considers only the diagonal term C_{kk}, the coupling between different electronic terms vanishes and eq.C.5 results in the *adiabatic approximation*, where C_{kk} depends only on the single curve Ψ_k and thus it simply represents a correction to the adiabatic eigenvalue $\mathcal{E}_k$. Correspondingly the coupled wavefunction in eq.C.4 becomes simply the direct product of an electronic and a nuclear wavefunction[3]. In the ultimate simplification also the diagonal

[1] The electronic hamiltonian operator $\mathcal{H}_e$,

$$\mathcal{H}_e\left(\mathbf{r},\mathbf{R}\right) = -\frac{1}{2}\sum_{i}^{N_{el}}\nabla_i^2 - \sum_{I}^{N_{at}}\sum_{i}^{N_{el}}\frac{Z_I}{|\mathbf{R}_I-\mathbf{r}_i|} + \sum_{i<j}^{N_{el}}\frac{1}{|\mathbf{r}_i-\mathbf{r}_j|} + \sum_{I<J}^{N_{at}}\frac{Z_IZ_J}{|\mathbf{R}_I-\mathbf{R}_J|}.$$

depends explicitly on the electronic coordinates and parametrically on the nuclear ones. Here the four components respectively represent the electronic kinetic energy, the electron-nuclear attraction, the electron-electron repulsion and the nuclear-nuclear repulsion. Note that for a given configuration the last term is a constant contribution.

[2] $C_{kl} = \int\Psi_k^*\left[-\sum_I\frac{1}{2M_I}\nabla_I^2\right]\Psi_l d\mathbf{r} + \sum_I\frac{1}{M_I}\left\{\int\Psi_k^*\left[-\nabla_I\right]\Psi_l d\mathbf{r}\right\}\nabla_I$

[3]
$$\left[-\sum_{I}^{N_{at}}\frac{1}{2M_I}\nabla_I^2 + \mathcal{E}_k\left(\mathbf{R}\right) + C_{kk}\right]\chi_k = i\hbar\frac{\partial}{\partial t}\chi_k \qquad \text{and} \qquad \Phi\left(\mathbf{r},\mathbf{R},t\right)\approx\Psi_k\left(\mathbf{r},\mathbf{R}\right)\chi_k\left(\mathbf{R},t\right)$$

coupling term is neglected, thereby generating the famous *Born-Oppenheimer approximation*[4].

C.1.1 Time-independent Schrödinger equation: Born-Oppenheimer MD

Once stated the Born-Oppenheimer approximation, which works safely in many physical situations, in the next step the nuclei have to be represented as classical particles. This is a change of perspective in view of the application of the classical equations of motion. To this end, the nuclear wavefunction is conveniently rewritten as

$$\chi_k(\mathbf{R},t) = A_k(\mathbf{R},t)\, e^{iS_k(\mathbf{R},t)/\hbar} \tag{C.6}$$

in terms of amplitude A_k and phase S_k. Note that both of them are real. After transforming the nuclear wavefunction in the BO approximation accordingly to the definition in eq.C.6, two equations result corresponding to the real and the imaginary part:

$$Re: \frac{\partial S_k}{\partial t} + \sum_I \frac{1}{2M_I}(\nabla_I S_k)^2 + \mathcal{E}_k = \hbar^2 \sum_I \frac{1}{2M_I}\frac{\nabla_I^2 A_k}{A_k} \tag{C.7}$$

$$Im: \frac{\partial A_k}{\partial t} + \sum_I \frac{1}{2M_I} A_k\left(\nabla_I^2 S_k\right) + \sum_I \frac{1}{M_I}(\nabla_I A_k)(\nabla_I S_k) = 0 \tag{C.8}$$

After multiplication by $2A_k$, the relation for the amplitude in eq.C.8 may be rewritten as a continuity equation

$$\frac{\partial \rho_k}{\partial t} + \sum_I \nabla_I \mathbf{J}_{k,I} = 0 \tag{C.9}$$

with $\rho_k = |\chi_k|^2 \equiv A_k^2$ and the current density $\mathbf{J}_{k,I} = A_k^2(\nabla_I S_k)/M_I$. This equation ensures locally the conservation of the particle probability density $|\chi_k|^2$ of the nuclei in the presence of a flux.
The relation of the phase in eq.C.7 will now be analysed. By eliminating the term multiplied by $\hbar^2$ within the classical limit $\hbar \to 0$, the equation becomes isomorphic to the equation of motion in the Hamilton-Jacobi formulation of classical mechanics:

$$\frac{\partial S_k}{\partial t} + H_k(\mathbf{R}, \{\nabla_I S_k\}) = 0 \tag{C.10}$$

with the classical Hamilton function in terms of generalized nuclear coordinates and conjugate momenta

$$H_k(\mathbf{R},\mathbf{P}) = T(\mathbf{P}) + V_k(\mathbf{R}) \tag{C.11}$$

with T and V_k representing the kinetic and the potential contribution. To fulfill the energy conservation requirement,

$$\frac{\partial S_k}{\partial t} = -(T + \mathcal{E}_k) = -\mathcal{E}_k^{tot} = constant \tag{C.12}$$

[4]It is also known as the *crude adiabatic approximation*,

$$\left[-\sum_I^{N_{at}} \frac{1}{2M_I}\nabla_I^2 + \mathcal{E}_k(\mathbf{R})\right]\chi_k = i\hbar\frac{\partial}{\partial t}\chi_k$$

Following from $\mathbf{P}_I \equiv \nabla_I S_k = M_I \mathbf{J}_{k,I}/\rho_k$ and the relation between S_k and the total energy in eq.C.12, the Newton's motion equation $\dot{\mathbf{P}}_I = -\nabla_I V_k(\mathbf{R})$ may be written as

$$\dot{\mathbf{P}}_I = -\nabla_I \mathcal{E}_k \qquad \text{or} \qquad M_I \ddot{\mathbf{R}}_I(t) = -\nabla_I V_k^{BO}(\mathbf{R}(t)) \tag{C.13}$$

for each decoupled electronic state k. This means that the nuclei move according to classical mechanics feeling the effective Born-Oppenheimer potential V_k^{BO}, namely they move along the adiabatic potential energy surface $\mathcal{E}_k$. Such surface has been determined quantum mechanically by solving the time-independent electronic Schrödinger equation for a given set of nuclear coordinates, $\mathbf{R}$. Thus, this means that the time dependence of the electronic structure is imposed by the nuclear classical dynamics as the electronic hamiltonian parametrically depends on the nuclear configuration. Note that V_k^{BO} is obtained as the minimum of the expectation value $\langle \mathcal{H}_e \rangle$ at each step of the nuclear propagation[5]. As the forces acting on the nuclei are determined from the BO energies, this branch of ab initio molecular dynamics is also known as Born-Oppenheimer MD.

C.1.2 Time-dependent Schrödinger equation: Ehrenfest MD

An alternative derivation deals with the electronic problem by solving the time-dependent Schrödinger equation. At variance with Born-Oppenheimer MD, this implies that the electronic structure does not just depend on the nuclear configuration at time t, but electrons have their intrinsic dynamics. In this case the total wavefunction $\Phi(\mathbf{r}, \mathbf{R}, t)$ is separated as

$$\Phi(\mathbf{r}, \mathbf{R}, t) \approx \Psi(\mathbf{r}, t)\, \chi(\mathbf{R}, t) \exp\left[\frac{i}{\hbar} \int_{t_0}^{t} \tilde{E}_e\left(t'\right) dt'\right] \tag{C.14}$$

where the electronic and nuclear wavefunctions are orthonormal at each time t; the last term is a phase factor introduced to get simple final equations. Note that, independently from the phase factor, the product description of the total wavefunction is different from the Born expression even in terms of a single adiabatic state Ψ_k. The total hamiltonian operator applied to the wavefuction in eq.C.14, after multipling by Ψ^* and χ^* and integrating over the electronic and nuclear coordinates, finally yields the equations for the electronic and nuclear motion. These set of equations consti-

[5] Considering the ground state Ψ_0, the electronic structure and the nuclear propagation are described as

$$\mathcal{H}_e \Psi_0 = \mathcal{E}_0 \Psi_0 \qquad \text{and} \qquad M_I \ddot{\mathbf{R}}_I(t) = -\nabla_I \min_{\Psi_0} \{\langle \Psi_0 | \mathcal{H}_e | \Psi_0 \rangle\}.$$

If the ground state wavefunction is described within the Hartree-Fock approximation as a single Slater determinant $\Psi_0 = 1/\sqrt{N!} \det\{\phi_i\}$, the two equations become

$$\mathcal{H}_e^{HF} \phi_i = \sum_{ij} \Lambda_{ij} \phi_j \qquad \text{and} \qquad M_I \ddot{\mathbf{R}}_I(t) = -\nabla_I \min_{\{\phi_i\}} \left\{\langle \Psi_0 | \mathcal{H}_e^{HF} | \Psi_0 \rangle\right\}$$

and analogously within the Kohn-Sham density functional theory

$$\mathcal{H}_e^{KS} \phi_i = \sum_{ij} \Lambda_{ij} \phi_j \qquad \text{and} \qquad M_I \ddot{\mathbf{R}}_I(t) = -\nabla_I \min_{\{\phi_i\}} \left\{\langle \Psi_0 | \mathcal{H}_e^{KS} | \Psi_0 \rangle\right\}.$$

tute the basis of the time-dependent self-consistent field (TDSCF) method introduced by Dirac in 1930[23].

$$i\hbar\frac{\partial\Psi}{\partial t} = -\sum_i \frac{\hbar^2}{2m_e}\nabla_i^2\Psi + \left\{\int \chi^*(\mathbf{R},t)\, V_{e-n}(\mathbf{r},\mathbf{R})\, \chi(\mathbf{R},t)\, d\mathbf{R}\right\}\Psi = \mathcal{H}_e\Psi \tag{C.15}$$

$$i\hbar\frac{\partial\chi}{\partial t} = -\sum_I \frac{\hbar^2}{2M_I}\nabla_I^2\chi + \left\{\int \Psi^*(\mathbf{r},t)\, \mathcal{H}_e(\mathbf{r},\mathbf{R})\, \Psi(\mathbf{r},t)\, d\mathbf{r}\right\}\chi \tag{C.16}$$

It results that both electrons and nuclei move in time-dependent effective potentials, where electronic motion is determined by the mean-field potential generated by nuclei and the opposite holds for the nuclear motion. At this point, nuclei have again to be approximated as classical particles, but now in the presence of electrons which are quantum particles moving in time. This can be done following the same approach already used to derive Born-Oppenheimer molecular dynamics. Accordingly the nuclear wavefunction is conveniently rewritten as in eq.C.6; then the full hamiltonian of eq.C.2 applies and two equations are carried out in terms of amplitude and phase of the nuclear wavefunction χ. In the classical limit $\hbar \to 0$, the phase expression is

$$\frac{\partial S}{\partial t} + \sum_I \frac{1}{2M_I}(\nabla_I S)^2 + \int \Psi^*\mathcal{H}_e\Psi d\mathbf{r} = 0. \tag{C.17}$$

Correspondigly, the Newton's equations of motion of the classical nuclei are

$$\dot{\mathbf{P}}_I = -\nabla_I \int \Psi^*\mathcal{H}_e\Psi d\mathbf{r} \qquad \text{or} \qquad M_I\ddot{\mathbf{R}}_I(t) = -\nabla_I V_e^E(\mathbf{R}(t)) \tag{C.18}$$

where the nuclei behave as classical particles and move according to the classical mechanics in an effective potential V_e^E known as Ehrenfest potential. This is the solution of the time-dependent electronic Schrödinger equation and it represents the mean-field potential averaged over the electronic degrees of freedom in which nuclei move, $V_e^E = \langle\Psi|\mathcal{H}_e|\Psi\rangle$. Note that it is computed on-the-fly for each nuclear configuration $\mathbf{R}(t)$. The TDSCF equation that describes the electronic motion has still a quantum appearence, as it contains the nuclear wavefunction $\chi(\mathbf{R},t)$ instead of just the nuclear positions $\mathbf{R}(t)$. Anyway, by replacing $|\chi(\mathbf{R},t)|^2$ with $\prod_I \delta(\mathbf{R}_I - \mathbf{R}_I(t))$ in the classical limit $\hbar \to 0$, the electronic time-dependent wavefunction becomes

$$i\hbar\frac{\partial\Psi}{\partial t} = -\sum_i \frac{\hbar^2}{2m_e}\nabla_i^2\Psi + V_{e-n}(\mathbf{r},\mathbf{R}(t))\,\Psi = \mathcal{H}_e(\mathbf{r},\mathbf{R}(t))\,\Psi(\mathbf{r},\mathbf{R},t). \tag{C.19}$$

Note that upon the classical reduction, $\mathcal{H}_e$ depends parametrically on the classical nuclear positions at time t, $\mathbf{R}(t)$.

C.1.3 Overview of the two methods

Here the ab initio molecular dynamics approach has been presented as based on the simultaneous solution of the Newton's equation for the nuclei and the Schrödinger equation for the electrons. This is a mixed quantum-classical approach as the electrons behave like quantum objects while

nuclei have been approximated by classical particles. Two alternatives derivations have been shown that differ in some aspects. In the case of the Born-Oppenheimer MD approach, (i) the electronic structure is described within the time-independent Schrödinger equation and (ii) the expectation value of the electronic hamiltonian has to be minimized at each step in the nuclear propagation; moreover (iii) transitions between electronic states are not contemplated. On the other hand, in the Ehrenfest MD version, (i) the electronic system evolves in time according to the time-dependent Schrödinger equation; (ii) a wavefunction that minimizes $\langle \mathcal{H}_e \rangle$ in the initial configuration will stay in its ground state as the nuclei move, due to the unitarity of the wavefunction propagation; finally, (iii) transitions between electronic states are taken into account and the electronic wave function may be expanded as a sum over the electronic states weigthed by time-dependent coefficients,

$$\Psi\left(\mathbf{r},\mathbf{R},t\right)=\sum_{l=0}^{\infty}c_l\left(t\right)\Psi_l\left(\mathbf{r},\mathbf{R}\right). \tag{C.20}$$

Typically a suitable set of basis functions $\{\Psi_l\}$ consists of the eigenfunctions generated by solving the Schrödinger equation within the Born-Oppenheimer approximation for nuclei at $\mathbf{R}$ at time t. Accordingly the quantum-classical coupled equations for electron-nuclear dynamics may be rewritten as,

$$M_I\ddot{\mathbf{R}}_I\left(t\right)=-\nabla_I\sum_k\left|c_k\left(t\right)\right|^2E_k=-\sum_k\left|c_k\left(t\right)\right|^2\nabla_IE_k+\sum_{k,l}c_k^*c_l\left(E_k-E_l\right)\int\Psi_k^*\nabla_I\Psi_l d\mathbf{r} \tag{C.21}$$

$$i\hbar\frac{\partial\Psi}{\partial t}=i\hbar\frac{\partial c_k\left(t\right)}{\partial t}+\sum_l c_l\left(t\right)\int\Psi_k^*\frac{\partial}{\partial t}\Psi_l d\mathbf{r}=E_kc_k\left(t\right) \tag{C.22}$$

where the coupling between different electronic states is taken into account. Note that if only the ground state wavefunction is included in the expansion for $\Psi\left(\mathbf{r},\mathbf{R},t\right)$ then the Ehrenfest potential exactly reduces to the ground state Born-Oppenheimer potential[6] and the equations of motion become

$$M_I\ddot{\mathbf{R}}_I\left(t\right)=-\nabla_I\left\langle\Psi_0\right|\mathcal{H}_e\left|\Psi_0\right\rangle\qquad\text{and}\qquad i\hbar\frac{\partial\Psi}{\partial t}=\mathcal{H}_e\Psi_0. \tag{C.23}$$

In Ehrenfest dynamics the time scale and thus the time step to integrate the equations of motion is determined by the intrinsic dynamics of the electrons, which are faster than nuclei. The time step has to be as large as possible, allowing at the same time to properly integrate the electronic equations of motion. Contrary to that, in Born-Oppenheimer dynamics there is no electronic intrinsic dynamics

[6]The possibility to fully decouple the electronic and the nuclear problem justifies the classical (as well as quasi-classical and quantum) molecular dynamics approach based on the global potential energy surface. Indeed, as the electronic and nuclear dynamics are fully decoupled, one may think at first to solve the Schrödinger equation for many different nuclear configurations; then fit the data to yield an analytical form of the global potential energy surface; finally use the forces associated to such surface to propagate the nuclei, starting from many different initial conditions. Anyway the construction of a global potential energy surface may turn out to be prohibitively costly for large systems. In this case the global potential can be approximated by a truncated expansion of many-body contributions depending on the nuclear coordinates. This potential is usually named *force-field*. It introduces a relevant simplication as the electronic degrees of freedom are replaced by a set of interaction potentials, typically two or three-body terms. As a consequence the problem reduces to purely classical mechanics and the dimensionality bottleneck is circumvented. Anyway the new potential provides a less realistic picture of chemical situations.

and thus the length of the time step is fully determined by the nuclear motion. As nuclei move slower than electrons, a larger time step may be used. However this means that the electronic structure problem has to be solved self-consistently at each molecular dynamics step, whereas this is avoided in the Ehrenfest dynamics where the wavefunction is automatically kept at its minimum as the nuclei are propagated. From the above considerations one may conclude that the *ideal* ab initio molecular dynamics method should: integrate the equations of motion on a (long) time scale set by the nuclear dynamics and avoid the self-consistent minimization step to get the electronic structure for each given nuclear arrangement. This may be done by exploiting the smooth time evolution of the wavefunction in the case of electrons with intrinsic dynamics.

C.1.4 Car-Parrinello molecular dynamics

Car-Parrinello molecular dynamics is here very shortly presented as a non-obvious method which combines the better features of both Ehrenfest and Born-Oppenheimer molecular dynamics. The basic idea of the Car-Parrinello approach is to take advantage of the different time scale on which electronic and nuclear dynamics take place. The quantum-classical problem is mapped on a purely classical system with two different energy scales, loosing in this way the physical time information of the quantum electron dynamics. An important aspect derives from the fact that the electronic energy is not only a function of the nuclear coodinates $\mathbf{R}$, but it is also a functional of Ψ_0 and thus of the basis functions $\{\phi_i\}$ used to construct Ψ_0, e.g. the set of spin-orbitals in a Slater determinant. This suggests the idea that a functional derivative with respect to the functions $\{\phi_i\}$ may be read as the force acting on the orbitals, analogously to the case of classical mechanics where the derivative of a suitable Lagrangian with respect to the nuclear positions gives the forces acting on the nuclei. By including some possible constraints, the general Lagrangian reads as

$$\mathcal{L}_{CP} = \sum_I \frac{1}{2} M_I \dot{\mathbf{R}}_I^2 + \sum_i \mu \left\langle \dot{\phi}_i | \dot{\phi}_i \right\rangle - \langle \Psi_0 | \mathcal{H}_e | \Psi_0 \rangle + constraints \tag{C.24}$$

where the first term gives the kinetic energy of the nuclei; the second one refers to the kinetic energy of orbitals and the fictitious mass μ has been assigned to the orbital degrees of freedom; finally the third one is the potential energy. In the derivation of $\mathcal{L}_{CP}$ with respect to nuclear and orbitals positions the following holds $\frac{\partial \mathcal{L}_{CP}}{\partial \mathbf{R}_I} = \frac{d}{dt} \frac{\partial \mathcal{L}_{CP}}{\partial \dot{\mathbf{R}}_I}$ and $\frac{\delta \mathcal{L}_{CP}}{\delta \phi_i *} = \frac{d}{dt} \frac{\delta \mathcal{L}_{CP}}{\delta \dot{\phi}_i *}$. Accordingly the generic Car-Parrinello equations of motion are obtained

$$M_I \ddot{\mathbf{R}}_I(t) = -\frac{\partial}{\partial \mathbf{R}_I} \langle \Psi_0 | \mathcal{H}_e | \Psi_0 \rangle + \frac{\partial}{\partial \mathbf{R}_I} \{constraints\} \tag{C.25}$$

$$\mu \ddot{\phi}_i(t) = -\frac{\delta}{\delta \phi_i^*} \langle \Psi_0 | \mathcal{H}_e | \Psi_0 \rangle + \frac{\delta}{\delta \phi_i^*} \{constraints\} \tag{C.26}$$

As in general the constraints depend on the nuclear coordinates as well as on the set of orbitals, the above equations lead in the end to constrained forces.

In the Car-Parrinello dynamics, nuclei propagate with an istantaneous real temperature that is proportional to their kinetic energy $\propto \sum_I M_I \dot{\mathbf{R}}_I^2$; in the same way the orbitals evolve in time

at a fictitious temperature $\propto \sum_i \mu \left\langle \dot{\phi}_i | \dot{\phi}_i \right\rangle$. In this model the electronic temperature indicates how far is the electronic system from its istantaneous minimum energy; thereby the electronic wavefunction will remain close to the ground state, namely the initial condition, provided the fictitious temperature remains low during the simulation. Typically this case is characterized by *bound* oscillations of the fictitious kinetic energy around a constant value. The physical reason for such behaviour is that the nuclei and electrons are dynamically separated, their vibrational states do not overlap and thus the energy transfer between them is prohibitively slow. In practice this aspect is controlled by the fictitious mass μ which indeed appears in the expression for the fictious temperature. The choice of μ is strictly connected to the choice of the time step and it results as a compromise between two aspects: (i) the need to stay close to the Born-Oppenheimer surface, that implies a low fictitious temperature, $\mu \to 0$ and a small time step to follow such a fast dynamics and (ii) the need to use a time step as large as possible to integrate the nuclear equation.

C.2 Forces acting on the nuclei

All dynamics studies rely on the calculation of the forces that act on the nuclei and drive their propagation. The accurate evaluation of such forces is crucial to get reliable dynamics results. The numerical evaluation of the force

$$F_I = -\nabla_I \langle \Psi_0 | \mathcal{H}_e | \Psi_0 \rangle \tag{C.27}$$

as finite-differences of the total electronic energy it too costly and too inaccurate for molecular dynamics. Thus the analytical approach is followed and the force turns out to be the sum of three contributions,

$$\nabla_I \langle \Psi_0 | \mathcal{H}_e | \Psi_0 \rangle = \langle \nabla_I \Psi_0 | \mathcal{H}_e | \Psi_0 \rangle + \langle \Psi_0 | \nabla_I \mathcal{H}_e | \Psi_0 \rangle + \langle \Psi_0 | \mathcal{H}_e | \nabla_I \Psi_0 \rangle . \tag{C.28}$$

If the wavefunction is an exact eigenfunction of the hamiltonian operator and it is expanded in a *complete* basis set, the Hellmann-Feynman theorem applies and the force becomes

$$F_I^{HFT} = - \langle \Psi_0 | \nabla_I \mathcal{H}_e | \Psi_0 \rangle . \tag{C.29}$$

It holds also for variational wavefunctions, such as Hartree-Fock or Kohn-Sham wavefunctions, provided a complete basis set is used. If one considers a single Slater determinant, $\Psi_0 = 1/\sqrt{N!} \det \{\phi_i\}$, the spin orbitals ϕ_i can be expanded in terms of a set of basis functions $\{f_\nu\}$ as $\phi_i = \sum_\nu c_{i\nu} f_\nu (\mathbf{r}, \mathbf{R})$. The basis functions might depend explicitly on the nuclear positions as in the case of atom-centered orbitals, whereas the expansion coefficients always have an implicit dependence. As a consequence the derivative of the orbitals reads as

$$\nabla_I \phi_i = \sum_\nu \left(\nabla_I c_{i\nu} \right) f_\nu (\mathbf{r}, \mathbf{R}) + \sum_\nu c_{i\nu} \left(\nabla_I f_\nu (\mathbf{r}, \mathbf{R}) \right) . \tag{C.30}$$

AIMD	Localized basis	Originless basis
BO	$F_I^{HFT} + F_I^{IBS} + F_I^{NSC}$	$F_I^{HFT} + F_I^{NSC}$
E	$F_I^{HFT} + F_I^{IBS}$	F_I^{HFT}
CP	$F_I^{HFT} + F_I^{IBS}$	F_I^{HFT}

Table C.1: forces acting on the nuclei in Born-Oppenheimer (BO), Ehrenfest (E) and Car-Parrinello (CP) molecular dynamics scheme for different basis sets.

Following from eq.C.30, the contributions to the force coming from the derivative of the wavefunction in eq.C.28 can be seen as two terms. The first is the *incomplete-basis-set* correction and it contains the gradients of the basis functions. It is usually named Pulay force and it reads as

$$F_I^{IBS} = \sum_{i\mu\nu} \left(\langle \nabla_I f_\nu | \, \mathcal{H}_e^{NSC} - \varepsilon_i \, | f_\mu \rangle + \langle f_\nu | \, \mathcal{H}_e^{NSC} - \varepsilon_i \, | \nabla_I f_\mu \rangle \right) \tag{C.31}$$

where $\mathcal{H}_e^{NSC}$ is the non-self consistent one-particle Hamiltonian. The second term is the *non-self-consistency* correction to the force,

$$F_I^{NSC} = - \int d\mathbf{r} \, (\nabla_I n) \left(V^{SCF} - V^{NSC} \right). \tag{C.32}$$

which depends on the difference between the self-consistent and the non-self consistent potential energy and on the charge density n. In conclusion the total force needed for dynamics calculations is $F_I = F_I^{HFT} + F_I^{IBS} + F_I^{NSC}$. Note that the Pulay force in eq.C.31 would be zero in the limit of a complete basis set; anyway it also vanishes with originless basis functions, like plane waves, if the number of such functions is kept fixed. The point related to the *non-self-consistency* correction in eq.C.32 is more subtle. This term vanishes only if self-consistency is reached, that is only if the wavefunction Ψ_0 is an eigenfunction of the hamiltonian within the given *finite* basis set; as in numerical calculations this can never occur, the correction F_I^{NSC} can never be suppressed. Anyway in Car-Parrinello as well as in Ehrenfest molecular dynamics schemes the self-consistency is never required: indeed, to compute the forces acting on the nuclei, one merely needs to evaluate the expression$\langle \Psi_0 | \, \mathcal{H}_e \, | \Psi_0 \rangle$, where Ψ_0 is just a wavefunction of the Hamiltonian at time t. As a consequence, the non-self consistency correction to the force turns out to be irrelevant in these two methods. Of course, this is not the case in Born-Oppenheimer molecular dynamics, where the expectation value of $\mathcal{H}_e$ has to be minimized with respect to Ψ_0 for each nuclear configuration before computing the forces. All these considerations are summarized in table C.1.

C.2.1 The Hellmann-Feynman theorem

Under the hypothesis of a wavefunction which is defined in a complete basis set and it is eigenfunction of the hamiltonian operator, the Hellmann-Feynmann theorem may be easily derived. Indeed given the generic hamiltonian operator $\hat{H}_\lambda$ that depends on the parameter λ and its eigenfunction $\Psi(\lambda)$ that depends implicitly on the same parameter λ, the energy derivative is

$$\frac{dE}{d\lambda} = \left\{ \frac{d\left\langle \Psi\left(\lambda'\right)\right|}{d\lambda'}\hat{H}_\lambda\left|\Psi\left(\lambda'\right)\right\rangle + \left\langle \Psi\left(\lambda\right)\left|\frac{d\hat{H}_\lambda}{d\lambda}\right|\Psi\left(\lambda\right)\right\rangle + \left\langle \Psi\left(\lambda'\right)\right|\hat{H}_\lambda\frac{d\left|\Psi\left(\lambda'\right)\right\rangle}{d\lambda'} \right\}_{\lambda=\lambda'} \tag{C.33}$$

If the Hamiltonian is hermitian, one may write

$$\begin{aligned} &= \left\{ \left\langle \Psi\left(\lambda\right)\left|\frac{d\hat{H}_\lambda}{d\lambda}\right|\Psi\left(\lambda\right)\right\rangle + E_\lambda\left(\frac{d\left\langle \Psi\left(\lambda'\right)\right|}{d\lambda'}\left|\Psi\left(\lambda'\right)\right\rangle + \left\langle \Psi\left(\lambda'\right)\right|\frac{d\left|\Psi\left(\lambda'\right)\right\rangle}{d\lambda'}\right) \right\}_{\lambda=\lambda'} = \\ &= \left\{ \left\langle \Psi\left(\lambda\right)\left|\frac{d\hat{H}_\lambda}{d\lambda}\right|\Psi\left(\lambda\right)\right\rangle + E_\lambda\frac{d}{d\lambda'}\left\langle \Psi\left(\lambda'\right)\mid\Psi\left(\lambda'\right)\right\rangle \right\}_{\lambda=\lambda'} \end{aligned} \tag{C.34}$$

The second term in C.34 vanishes, because $\left\langle \Psi\left(\lambda'\right)\mid\Psi\left(\lambda'\right)\right\rangle$ is a normalization constant and the only term retained gives the Hellmann-Feynman force

$$F_\lambda^{HFT} = -\left\langle \Psi\left(\lambda\right)\left|\frac{d\hat{H}_\lambda}{d\lambda}\right|\Psi\left(\lambda\right)\right\rangle. \tag{C.35}$$

The Hellmann-Feynman theorem has its natural application in computing the forces that act on the nuclei. Thus it is typically invoked in the search of the minimum on a potential energy surface and in ab initio molecular dynamics. In the first case the nuclei move along the potential energy surface up to reach the equilibrium position where the forces are ideally null; instead in AIMD the nuclei are usually propagated until the outcome of the trajectory is clear. This means until the event occurred is clearly classifiable; for instance in gas-surface systems one may encounter many alternatives processes, namely reaction, dissociation, scattering, adsorption, etc... Basically in both the cases the procedure consists of (i) a preliminary step in which the total energy is minimised with respect to the electronic wavefunction for the initial configuration of the nuclei $\{\mathbf{R}_I\}$; followed by (ii) the computation of the forces acting on the nuclei. Then (iii) according to these forces the nuclei are moved in the new configuration $\left\{\mathbf{R}'_I\right\}$ by using a chosen algorithm. After that for any following nuclear arrangement $\left\{\mathbf{R}'_I\right\}$, this procedure repeats. Note that the total energy has to be minimised with respect to the electronic wavefunction for each configuration $\left\{\mathbf{R}'_I\right\} \neq \{\mathbf{R}_I\}$ if a Born-Oppenheimer MD or a geometry optimisation is performed, while in Car-Parrinello and Ehrenfest MD the energy minimisation is required only at the very first step. Here the generic parameter λ corresponds to the coordinates of the nuclei. Given the hamiltonian operator

$$\hat{H} = \hat{T} + \hat{V}_{ee} - \sum_i^{N_{el}}\sum_\alpha^{N_{at}}\frac{Z_\alpha}{|\mathbf{r}_i - \mathbf{R}_\alpha|} + \sum_\alpha^{N_{at}}\sum_{\beta>\alpha}^{N_{at}}\frac{Z_\alpha Z_\beta}{|\mathbf{R}_\alpha - \mathbf{R}_\beta|} \tag{C.36}$$

the force acting on the nucleus I along the x-direction is given by

$$F_I = -\frac{\partial E}{\partial X_I} = \left\langle \Psi\left|\frac{d\hat{H}}{dX_I}\right|\Psi\right\rangle \tag{C.37}$$

where only the electron-nucleus and nucleus-nucleus interactions in the hamiltonian contributes to its derivative,

$$\frac{d\hat{H}}{dX_I} = Z_I \sum_i^{N_{el}} \frac{x_i - X_I}{|\mathbf{r}_i - \mathbf{R}_I|^3} - Z_I \sum_{J \neq I}^{N_{at}} Z_J \frac{(X_J - X_{I\gamma})}{|\mathbf{R}_J - \mathbf{R}_I|^3} \tag{C.38}$$

Finally, inserting eq.C.38 into eq.C.35, one gets the force acting on the I nucleus in term of the electron density $\rho(r)$, the atomic coordinates and nuclear charges:

$$F_I = Z_I \int \frac{x - X_I}{|\mathbf{r} - \mathbf{R}_I|^3} \rho(\mathbf{r})\, d\mathbf{r} - Z_I \sum_{J \neq I}^{N_{at}} Z_J \frac{(X_J - X_I)}{|\mathbf{R}_J - \mathbf{R}_I|^3} \tag{C.39}$$

C.3 The Verlet algorithm

In molecular dynamics the nuclei of a given system move due to the forces that act on them. Time dependent properties can be obtained by integrating the equations of motion for the particles in the system. In the simplest cases a good description of the time evolution of the system under investigation may be given by the Newton's law, that reads as

$$\ddot{\mathbf{R}}_I = -\nabla V_I(\{\mathbf{R}_I\})/M_I \tag{C.40}$$

Anyway this means that one has to solve a set of first and second order differential equations to get the time evolution of the positions and momenta of every particle in the system. Except for very small system, the analytical integration of the equations of motion is a very difficult task, thus one typically prefers a numerical method. In this case the derivatives involved are discretized, namely they are estimated using the finite differences method. Consider here the generic function f that is a function of time and choose a step δt to follow its evolution. The value of the function at time $t + \delta t$ and $t - \delta t$, read as

$$\begin{aligned} f(t + \delta t) &= f(t) + \delta t f'(t) + \frac{(\delta t)^2}{2} f''(t) + ... \\ f(t - \delta t) &= f(t) - \delta t f'(t) + \frac{(\delta t)^2}{2} f''(t) + ... \end{aligned} \tag{C.41}$$

By summing the two equations in eq.C.41, one finally gets

$$f(t + \delta t) = 2f(t) - f(t - \delta t) + (\delta t)^2 f''(t) + \mathcal{O}\left((\delta t)^4\right) \tag{C.42}$$

In molecular dynamics one wants to know the position of each nucleus as a function of the time; thus the function R_I is introduced that gives the position of atom I at different times. The eq.C.42 now reads as

$$R_I(t + \delta t) = 2R_I(t) - R_I(t - \delta t) + (\delta t)^2 \ddot{R}_I(t) + \mathcal{O}\left((\delta t)^4\right) \tag{C.43}$$

and, by inserting eq.C.43 in the Newton's equations of motion, one gets

$$\frac{R_I(t+\delta t)+R_I(t-\delta t)-2R_I(t)}{(\delta t)^2} \simeq -\nabla V_I\left(\{\mathbf{R}_I(t)\}\right)/M_I = a_I(t) \tag{C.44}$$

or alternatively

$$R_I(t+\delta t) \simeq 2R_I(t) - R_I(t-\delta t) + a_I(t)(\delta t)^2 \tag{C.45}$$

that gives the position of the particle I-th at time $t+\delta t$ provided the positions at time t and $t-\delta t$ as well as the force acting on the particle at time t are known. This is the *Verlet algorithm* that actually represents one of the most widely used propagation scheme in molecular dynamics simulations. This approach has many useful features indeed it is robust and it conserves the linear momentum; it is centered, since $t+\delta t$ and $t-\delta t$ play the same role; and it is time reversible, namely one may come back to the origin following the very same trajectory by reverting the sign of time and momentum. A limit in this algorithm is that velocities are not computed as they are not necessary for the algorithm to work. To evaluate the time evolution of velocity dependent properties or the average kinetic energy, one can estimate the velocity

$$v_I(t) \simeq \frac{R_I(t+\delta t)-R_I(t-\delta t)}{2\delta t}. \tag{C.46}$$

Anyway note that here the velocity belongs to the time step prior to the one used for the position. A possible solution is apported by the so called *velocity Verlet algorithm* that is mathematically identical to the original Verlet algorithm in the sense that it generates the same trajectory. It is based on

$$\begin{aligned} R_I(t+\delta t) &= R_I(t) + v_I(t)\,\delta t + \frac{a_I(t)}{2}(\delta t)^2 \\ v_I(t+\delta t) &= v_I(t) + \frac{a_I(t)+a_I(t+\delta t)}{2}\delta t \end{aligned} \tag{C.47}$$

Schematically, the velocity Verlet algorithm proceeds as follows: first, the new position at time $t+\delta t$ is calculated; then the acceleration at time $t+\delta t$ is evaluated from the force according to eq.C.40; finally the velocity at time $t+\delta t$ is computed. Once all the quantities are known, one restarts from the first stage.

Before concluding it is important to point out that the time step δt is an important parameter in the setup of a molecular dynamics simulation. For this reason it has to be properly chosen in such way to be (i) as small as possible, so that to generate a small error (even if possibly additive) at each step of the dynamics and (ii) as large as possible, so that to reduce the number of steps, thus the computational cost, needed to conclude a trajectory.

Bibliography

[1] http://webbook.nist.gov. NIST Chemistry Webbook.

[2] C. P. Ewels M. I. Heggie A. A. El-Barbary, R. H. Telling and P. R. Briddon. *Phys. Rev. B*, 68:144107, 2003.

[3] A. Kumar N.-G. Shang A. Ney, P. Papakonstantinou and N. Peng. *Appl. Phys. Lett.*, 99:102504, 2011.

[4] D. S. L. Abergel, V. Apalkov, J. Berashevich, K. Ziegler, and T. Chakraborty. *Advances in physics*, 59:261–482, 2010.

[5] B. L. Altshuler, A. G. Aronov, and P. A. Lee. *Phys. Rev. Lett.*, 44:1288–1291, 1980.

[6] N. W. Ashcroft and N. D. Mermin. *Solid state physics*. Saunders College, 1976.

[7] P. W. Atkins and R. S. Friedman. *Molecular quantum mechanics*. Oxford University Press, 1997.

[8] G. B. Bachelet, D. R. Hamann, and M. Schlüter. *Phys. Rev. B*, 26:4199–4228, 1982.

[9] T. Bally and W. Thatcher Borden. *Rev. Computational Chemistry*, 13, 2007.

[10] J. Barzola-Quiquia, P. Esquinazi, M. Rothermel, D. Spemann, T. Butz, and N. Garcia. *Phys. Rev. B*, 76:161403, 2007.

[11] M. Batzil. *Surf. Sci. Rep.*, 67:83–115, 2012.

[12] I. B. Bersuker. *Chem. Rev.*, 101:1067–1114, 2001.

[13] I. B. Bersuker. *The Jahn-Teller effect*. Cambridge University Press, 2006.

[14] P. E. Blöchl. *Phys. Rev. B*, 50:17953, 1994.

[15] S. Béchu, D. Lemoine, M. Bacal, A. Bès, and J. Pelletier. *AIP Conf. Proc.*, 1097:74, 2009.

[16] S. Casolo, O. M. Løvvik, R. Martinazzo, and G. F. Tantardini. *J. Chem. Phys.*, 130:054704, 2009.

[17] A. H. Castro Neto, F. Guinea, N. M. R. Peres, K. S. Novoselov, and A. K. Geim. *Rev. Mod. Phys.*, 81:109, 2009.

[18] P Celani and H J Werner. *J. Chem. Phys.*, 112:5546, 2000.

[19] D. M. Ceperley and B. J. Adler. *Phys. Rev. Lett.*, 45:566, 1980.

[20] S. Chabbal, S. Nave, and D. Lemoine. Unprecedented, very large Eley-Rideal reactivity between hydrogen atoms on a metal surface: the Ag(111) case. *to be submitted.*

[21] A. D. Simon D. A. McQuarrie. *Physical chemistry. A molecular approach.* University Science Books, 1997.

[22] M.W.C. Dharma-wardana and Marek Z. Zgierski. *Physica E*, 41:80 – 83, 2008.

[23] P. A. M. Dirac. *Proc. of the Cambridge phylosophical society*, 26:376–385, 1930.

[24] R. M. Dreizler and E. K. U. Gross. *Density Functional Theory.* Springer, Heidelberg, 1990.

[25] J. C. Tully E. K. Grimmelmann and M. J. Cardillo. *J. Chem. Phys.*, 72:1039, 1980.

[26] D. D. Eley and E. K. Rideal. *Nature*, 146:401, 1940.

[27] A. B. Elkowitz, J. H. McCreery, and G. Wolken. *J. Chem. Phys.*, 17:423, 1976.

[28] P. Esquinazi, A. Setzer, R. Höhne, C. Semmelhack, Y. Kopelevich, D. Spemann, T. Butz, B. Kohlstrunk, and M. Lösche. *Phys. Rev. B*, 66:024429, 2002.

[29] P. Esquinazi, D. Spemann, R. Höhne, A. Setzer, K.-H. Han, and T. Butz. *Phys. Rev. Lett.*, 91:227201, 2003.

[30] J. Kotakoski F. Banhart and A. V. Krasheninnikov. *ACS Nano*, 5:26–41, 2011.

[31] S. Fajtlowicz, P. E. John, and H. Sachs. *Croat. Chem. Acta*, 78:195, 2005.

[32] A. Filippetti, A. Satta, D. Vanderbilt, and W. Zhong. *International Journal of quantum Chemistry*, 61:421–427, 1997.

[33] A. Filippetti, D. Vanderbilt, W. Zhong, Y. cai, and G. B. Bachelet. *Phys. Rev. B*, 52:11793–11804, 1995.

[34] Antoine Georges, Gabriel Kotliar, Werner Krauth, and Marcelo J. Rozenberg. *Rev. Mod. Phys.*, 68:13–125, Jan 1996.

[35] A Gross. *Theoretical surface science: a microscopic perspective.* Springer, 2003.

[36] D. R. Hamann, M. Schlüter, and C. Chiang. *Phys. Rev. Lett.*, 43:1494–1497, 1979.

[37] B. Hammer and J. K. Norskov. *Nature*, 376:238, 1995.

[38] B. Hammer and J. K. Norskov. *Surf. Sci.*, 343:211, 1995.

[39] K. Held. *Advances in Physics*, 56:829–926, Dec 2007.

[40] L. Hornekær, E. Rauls, W. Xu, Ž. Šljivančanin, R. Otero, I. Stensgaard, E. Lægsgaard, B. Hammer, and F. Besenbacher. *Phys. Rev. Lett.*, 97:186102, 2006.

[41] M. Inui, S. A. Trugman, and E. Abrahams. *Phys. Rev. B*, 49:3190, 1994.

[42] W. G. Cullen E. D. Williams J.-H. Chen, L. Li and M. S. Fuhrer. *Nature Phys.*, 7:535, 2011.

[43] W. G. Cullen E. D. Williams J.-H. Chen, L. Li and M. S. Fuhrer. *Nature Phys.*, 8:353, 2012.

[44] B. Jackson and D. Lemoine. *J. Chem. Phys.*, 114:474, 2001.

[45] H. A. Jahn and E. Teller. *Proc. R. Soc. Lond. A*, 161:220–235, 1937.

[46] Q. G. Jiang, Z. M. Ao, W. T. Zheng, S. Li, and Q. Jiang. *Phys. Chem. Chem. Phys.*, 15:21016, 2013.

[47] J. Jobst and H. B. Weber. *Nature Phys.*, 8:352, 2012.

[48] Johannes Jobst, Daniel Waldmann, Igor V. Gornyi, Alexander D. Mirlin, and Heiko B. Weber. *Phys. Rev. Lett.*, 108:106601, 2012.

[49] H. Jonsson, G. Mills, and K. W. Jacobsen. *Nudged Elastic Band Method for Finding Minimum Energy Paths of Transitions, in Classical and Quantum Dynamics in Condensed Phase Simulations.* World Scientific, 1998.

[50] M. Katsnelson. *Graphene: Carbon in Two Dimensions.* Cambridge University Press, 2012.

[51] Peter J. Knowles and H.-J. Werner. *Chem. Phys. Letters*, 115:259–267, 1985.

[52] D. Kolovos-Vellianitis and J. Kuppers. *Surface Science*, 548:67, 2004.

[53] G. Kotliar, S. Y. Savrasov, K. Haule, V. S. Oudovenko, O. Parcollet, and C. A. Marianetti. *Rev. Mod. Phys.*, 78:865–951, Aug 2006.

[54] A. V. Krasheninnikov and K. Nordlund. *J. Appl. Phys.*, 107:071301, 2010.

[55] G. Kresse and J. Furthmüller. *Phys. Rev. B*, 54:11169, 1996.

[56] G. Kresse and J. Hafner. *Phys. Rev. B*, 47:558, 1993.

[57] G. Kresse and J. Hafner. *Phys. Rev. B*, 49:14251, 1994.

[58] G. Kresse and D. Joubert. *Phys. Rev. B*, 59:1758, 1999.

[59] J. G. Kushmerick, K. F. Kelly, H.-P. Rust, N. J. Halas, and P. S. Weiss. *J. Phys. Chem. B*, 103:1619, 1999.

[60] N. D. Lang and W. Kohn. *Phys. Rev. B*, 1:4555, 1970.

[61] N. D. Lang and A. Williams. *Phys. Rev. B*, 18:616, 1978.

[62] D. Lemoine and B. Jackson. *Comput. Phys. Commun.*, 137:415, 2001.

[63] P. O. Lethinen, A. S. Foster, Y. Ma, A. V. Krasheninnikov, and R. M. Nieminen. *Phys. Rev. Lett.*, 93:187202, 2004.

[64] E. H. Lieb. *Phys. Rev. Lett.*, 62:1201, 1989.

[65] M. Lischka and A. Gross. *Phys. Rev. B*, 65:075420, 2002.

[66] F. Guinea M. A. Cazalilla, A. Iucci and A. H. Castro Neto. *arXiv:1207.3135*, 2012.

[67] G. F. Tantardini A. Ponti M. Bonfanti, S. Casolo and R. Martinazzo. *J. Chem. Phys.*, 135:164701, 2011.

[68] F. Guinea M. M. Ugeda, I. Brihuega and J. M. Gomez-Rodriguez. *Phys. Rev. Lett.*, 104:096804, 2010.

[69] I. Brihuega P. Pou A. J. Martínez-Galera R. Pérez M. M. Ugeda, D. Fernández-Torre and J. M. Gómez-Rodríguez. *Phys. Rev. Lett.*, 107:116803, 2011.

[70] R. Martinazzo, S. Assoni, G. Marinoni, and G. F. Tantardini. *J. Chem. Phys.*, 120:8761, 2004.

[71] G. Mills, H. Jonsson, and G. K. Schenter. *Surf. Sci.*, 324:305, 1995.

[72] A. K. Mitchell and L. Fritz. *arXiv:1212.2631*, 2012.

[73] J. E. Muller. *Phys. Rev. Lett.*, 65:3021, 1990.

[74] R. R. Nair, M. Sepioni, I-Ling Tsai, O. Lehtinen, J. Keinonen, A. V. Krasheninnikov, T. Thomson, A. K. Geim, and I. V. Grigorieva. *Nature Phys.*, 8:199, 2012.

[75] R. R. Nair, I-Ling Tsai, M. Sepioni, O. Lehtinen, J. Keinonen, A. V. Krasheninnikov, A. H. Castro Neto, M. I. Katsnelso, A. K. Geim, and I. V. Grigorieva. *Nature Comm*, 4:2010, 2013.

[76] A. H. Castro Neto and K. Novoselov. *Rep. Prog. Phys.*, 74:082501, 2011.

[77] K. S. Novoselov, A. K. Geim, S. V. Morozov, D. Jiang, Y. Zhang, S. V. Dubonos, I. V. Grigorieva, and A. A. Firsov. *Science*, 306:666, 2004.

[78] Y. Öhrn. *Elements of molecular symmetry.* Wiley, John and Sons, incorporated, 2000.

[79] T. Pruschke H. Ochoa P. Haase, S. Fuchs and F. Guinea. *Phys. Rev. B*, 83:241408(R), 2011.

[80] J. J. Palacios and F. Yndurain. *Phys. Rev. B*, 85:245443, 2012.

[81] R. G. Parr and W. Yang. *Density-Functional Theory of atoms and molecules.* Oxford University Press, 1989.

[82] L. Pauling. *The Nature of the Chemical Bond.* Cornell University Press, Ithaca, N.Y., 1972.

[83] V. I. Pazzi, P. H. T. Philipsen, E. Baerends, and G. F. Tantardini. *Surf. Sci.*, 443:1, 1999.

[84] J. P. Perdew, K. Burke, and M. Ernzerhof. *Phys. Rev. Lett.*, 77:3865, 1996.

[85] J. P. Perdew, K. Burke, and M. Ernzerhof. *Phys. Rev. Lett.*, 78:1396, 1997.

[86] J. P. Perdew, J. A. Chevary, S. H. Vosko, K. A. Jackson, M. R. Pederson, D. J. Singh, and C. Fiolhais. *Phys. Rev. B*, 46:6671, 1992.

[87] J. P. Perdew and S. Kurth. Density functionals for non-relativistic coulomb systems. In *A primer in density functional theory*, Lecture notes in physics. Springer, Heidelberg, 2003.

[88] V. M. Pereira, F. Guinea, J.M.B. Lopes dos Santos, N.M.R. Peres, and A.H. Castro Neto. *Phys. Rev. Lett.*, 96:036801, 2006.

[89] V. M. Pereira, J. M. B. Lopes dos Santos, and A. H. Castro Neto. *Phys. Rev. B*, 77:115109, 2008.

[90] M. Persson and B. Jackson. *J. Chem. Phys.*, 102:1078, 1995.

[91] J. G. Quattrucci, B. Jackson, and D. Lemoine. *J. Chem. Phys.*, 118:2537, 2003.

[92] C. T. Rettner and D. J. Auerbach. *Science*, 263:365, 1994.

[93] M Riccó, D. Pontiroli, M. Mazzani, M. Choucair, J. A. Stride, and O. V. Yazyev. *Nano. Lett.*, 11:4919, 2011.

[94] A. W. Robertson, B. Montanari, K. He, C. S. Allen, Y. A. Wu, N. E. Harrison, A. I. Kirkland, and J. H. Warner. *ACS Nano*, 7:4495, 2013.

[95] B. O. Roos. *Ab initio methods in quantum chemistry*, page 399, 1987.

[96] A. N. Rudenko, F. J. Keil, M. I. Katsnelson, and A. I. Lichtenstein. *Phys. Rev. B*, 86:075422, Aug 2012.

[97] S. Sato. *Nippon Kagaku Zasshi*, 77:1202, 1956.

[98] M. W. Schmidt and M. S. Gordon. *Annu. Rev. Phys. Chem.*, 49:233–66, 1998.

[99] M. Sepioni, R. R. Nair, S. Rablen, J. Narayanan, F. Tuna, R. Winpenny, A. K. Geim, and I. V. Grigorieva. *Phys. Rev. Lett.*, 105:207205, 2010.

[100] M. Sepioni, R.R. Nair, I.-Ling Tsai, A. K. Geim, and I. V. Grigorieva. *EPL*, 97:47001, 2012.

[101] X. Sha, B. Jackson, and D. Lemoine. *J. Chem. Phys.*, 116:7158, 2002.

[102] G. Somorjai and Y. Li. *Introduction to surface chemistry and catalysis.* Wiley, 2010.

[103] A. Szabo and N. S. Ostlund. *Modern quantum chemistry: introduction to advanced electronic structure theory.* Dover publications, inc., 1996.

[104] G. F. Tantardini and M. Simonetta. *Surf. Sci.*, 105:577, 1981.

[105] M. Teter. *Phys. Rev. B*, 48:5031–5041, 1993.

[106] Jr. Thom H. Dunning. *J. Chem. Phys.*, 90(2):1007–1023, 1989.

[107] D. Vanderbilt. *Phys. Rev. B*, 41:7892, 1990.

[108] P. R. Wallace. *Phys. Rev.*, 71:622, 1947.

[109] Y. Wang, Y. Huang, Y. Song, X. Zhang, Y. Ma, J. Liang, and Y. Chen. *Nano Lett.*, 9:220, 2009.

[110] H J Werner. *Mol. Phys.*, 89:645, 1996.

[111] H.-J. Werner, P. J. Knowles, G. Knizia, F. R. Manby, M. Schütz, et al., 2010.

[112] H.-J. Werner and Peter J. Knowles. *J. Chem. Phys.*, 82:5053, 1985.

[113] M. H. Xie Y. N. Tang Y. H. Li X. Q. Dai, J. H. Zhao and B.Zhao. *Eur. Phys. J. B*, 80:343–349, 2011.

[114] O. V. Yazyev. *Rep. Prog. Phys.*, 73:056501, 2010.

[115] Oleg V. Yazyev and Lothar Helm. *Phys. Rev. B*, 75:125408, 2007.

[116] T. Zecho, A. Güttler, X. Sha, D. Lemoine, B. Jackson, and J. Küppers. *Chem. Phys. Lett.*, 366:188, 2002.